A THESIS

FOR THE DEGREE OF DOCTOR OF PHILOSOPHY

Development of Nanostructured Electrode Materials for Self-Charging Supercapacitor Power Cell

SURJIT SAHOO

DEPARTMENT OF MECHATRONICS ENGINEERING

GRADUATE SCHOOL
JEJU NATIONAL UNIVERSITY

February 2020

Development of Nanostructured Electrode Materials for Self-Charging Supercapacitor Power Cell

Surjit Sahoo

(Supervised by Professor Sang-Jae Kim)

A thesis submitted in partial fulfilment of the requirement for the degree of

Doctor of Philosophy

2019.12

The thesis has been examined and approved.

……

Prof. Kwang-Man Lee, Professor, Department of Electronic Engineering, College of Engineering, Jeju National University.
Thesis Director

……

Prof. Nam-Jin Kim, Professor, Department of Nuclear & Energy Engineering, College of Engineering, Jeju National University.
Thesis Committee Member

……

Prof. Hyomin Lee, Assistant Professor, Department of Chemical & Biological Engineering, College of Engineering, Jeju National University.
Thesis Committee Member

……

Prof. Woo Young Kim, Assistant Professor, Department of Electronic Engineering, College of Engineering, Jeju National University.
Thesis Committee Member

……

Prof. Sang -Jae Kim, Professor, Department of Mechatronics Engineering, College of Engineering, Jeju National University.
Thesis Committee Member and Supervisor

December, 2019

DEPARTMENT OF MECHATRONICS ENGINEERING
GRADUATE SCHOOL
JEJU NATIONAL UNIVERSITY
REPUBLIC OF KOREA

Dedicated to my father, mother, my Family members, all my teachers and friends

ACKNOWLEDGEMENT

Foremost, I would like to express my sincere cheers to the almighty for his support and making me stood in all challenging times and mastered me to tackle situations peacefully. My mother **Mrs. Sukanti Sahoo** my first teacher and her irrepealable love, my father **Mr. Surendra Nath Sahoo** my first guide, who made me to think and feel happy always. Appreciations to the kindhearted well-wishers, all my family members who made me to reach this extent in my life. My sincere thanks to my advisor **Prof. Sang-Jae Kim** for his continuous support throughout my Ph.D. and motivation towards research. His patience, motivation, and immense knowledge is unparalleled. His guidance helped me in every other means during time of research until the completion of thesis to mold myself in a better way.

I express my sincere and the most heartful gratitude to **Dr. Karthikeyan Krishnamoorthy**, who is not only a mentor in my professional life but also a well-wisher in my personal life. I would extend my deep appreciativeness to **Dr. Parthiban Pazhamalai** for mentoring and handling me as his brother. I also would like to thank all of my colleagues Dr. Nagamalleswara Rao Alluri, Dr. Arunkumar Chandrasekhar, Dr. Sophia Selvarajan, Dr. Yuvasree Purusothaman Mr. Vivekanathan Venkateswaran, Mrs. Kausalya Ganesan, Mr. Vimal kumar Mariappan, Ms. Sindhuja Manoharan, Mr. Rajagopal Pandey, Mr. Gaurav Khandelwal, Mr. Nirmal, Mr. Woo Joong Kim, Mr. Divakar, Mr. Abishek, Mr. Dhanasekar, Dr. Deepak, Dr. Natraj,Mr. Swapnil, Mr. Prashanth, Ms. Aparna, Mr .Arunprasath, Mr. Sugato, Ms. Manisha, who made my time in the lab as memorable.

I would also like to thank my friends outside the laboratory especially Dr.MSP Sudhakaran, Dr. Srikanth, Ms. Karthika Muthuramalingam, Mr. Gnanaselvan, Mr. Sravan Kumar, and Mr. Vikram for the beautiful reminiscences to cherish during my stay in Jeju.

I am grateful to the instrumentation facilities provided by Jeju National University to handle the sole operation of the instruments. I am thankful to Barain Korea 21 (BK-21) for funds provided for my research work.

I would like to extend my ovations to my friends who have been supported and making me feel good in my difficult times. Impeccable gratitude to all the well-wishers who lend their hands directly or indirectly during my entire stay in Jeju.

Surjit Sahoo

TABLE OF CONTENTS

CHAPTER-4

CHAPTER-7

High performance self-charging supercapacitor using porous PVDF-ionic liquid electrolyte sandwiched between two-dimensional graphene electrodes

Nomenclature

AC	Activated Carbon
BET	Brunauer-Emmet-Teller
CV	Cyclic voltammetry
CNT	Carbon nanotube
CT	Conductive textile
DI	De-ionized
ECD	Electrochemical deposition
ECs	Electrochemical capacitors
EDLC	Electrochemical double layer capacitor
EDS	Energy dispersive X-ray Spectroscopy
EIS	Electrochemical Impedance spectroscopy
ESR	Equivalent series resistance
FE- SEM	Field-emission scanning electron microscopy
FT-IR	Fourier transform infrared spectrometer
GCD	Galvanostatic charge discharge
GO	Graphene Oxide
HT	Heat treatment

HR-TEM	High resolution transmission electron microscopy
RGO	Reduced graphene oxide
SCs	Supercapacitors
SS	Stainless steel
TEM	Transmission electron microscope
XRD	X-ray diffraction
XPS	X-ray phonon spectroscopy

LIST OF TABLES

LIST OF FIGURES

ABSTRACT-HANGUL

사람이 생활하는 데에는 에너지가 필수적이다. 석유 같은 재생이 힘든 에너지원들이 고갈되어 감과 지구 온난화 및 기술의 발전에 의해 인류는 에너지 부족을 야기하고 있다. 이로 인해, 친환경적이면서 고성능인 에너지 수확, 저장 및 변환 장치에 대한 요구가 증가하고 있다. 전기화학적 에너지는 청정에너지와 관련하여 빠질 수 없는 부분이다. 수퍼커패시터, 연료 전지 및 배터리 같은 기존의 에너지장치는 전기화학적 반응을 통해 화학에너지를 전기에너지로 변환함으로써 다양한 휴대용 전자장치 및 전기 자동차 등에 사용되어왔다. 슈퍼커패시터 중에는 친환경적이며 빠른 충 방전 시간, 초고전력 등 다양한 휴대용 전자장치의 전력 공급원으로서 훌륭한 특성으로 인해 많은 주목을 받고 있는 것이 있다. 하지만, 충분치 않은 에너지 양 등이 수퍼커패시터의 실적용에 관하여 문제로 남아있다. 지난 10 년간 수퍼커패시터의 특정 전력, 특정 에너지 및 장시간 사용 안정성 등 과 같은 성능을 향상시키기 위해 여러 그룹에서 연구 작업이 진행되었다. 고성능을 위해 수퍼커패시터 장치를 위한 주요독립소자를 찾아야 한다. 수퍼커패시터 장치의 독립소자를 고려하면 전도성 기판, 전해질 및 전극 재료는 수퍼커패시터의 전기화학적 성능에 중요한 부분을 제공한다. 다양한 유형의 전극 재료

중에서, 나노입자, 나노시트 및 나노와이어 같은 나노구조 전극재료는 짧은 전극, 이온 수송 경로 및 높은 비표면적에 대한 접근성으로 인해 향상된 전기화학적 성능을 보인다.

수퍼커패시터 장치의 실적용 관점에서, 에너지 변환 및 저장은 휴대용 및 착용 가능한 전자 장치의 전원 공급을 위해 단일 시스템 안에서 이루어져야 한다. 전통적으로, 에너지 저장과 에너지 수확은 별개의 작업 메커니즘 및 독립적 물리장치를 사용하는 것으로 잘 알려진 현상이다. 자가충전 수퍼커패시터 파워셀은 외부에서 가해진 기계적 에너지를 “압전-전기화학적 공정”을 통해 전기적 에너지로 변환하고 배터리 혹은 수퍼커패시터 장치에 저장할 수 있는 가능성을 갖고 있다. SCSPC 장치의 자가충전 전압 및 에너지 변환 효율은 전원 공급 전자 장치를 위한 중요한 기준을 충족하기 위해 향상되어야 한다. 따라서 SCSPC 장치의 성능 개선은 지속 가능한 에너지원과 관련하여 상당한 관심을 끌고 있다. 에너지 저장 장치 및 SCSPC 장치와 관련하여 모든 기능을 고려하여, 이 논문은 주로 성능이 개선된 수퍼커패시터 및 자가 충전 수퍼커패시터 파워셀을 위한 나노구조 전극 재료에 집중되었다.

챕터 3 에서는 전이 금속 셀레나이드 (α-MnSe) 나노 입자의 합성을 설명하고 3 전극 시스템 및 대칭형 수퍼커패시터 장치에서 수퍼커패시터 응용을 위한 양극 재료로써의 전기화학적 분석을 하였다. 챕터 4 에서는 수열공정을 통하여 구리 몰리브덴

황화물 (Cu_2MoS_4) 나노 입자의 합성을 나타내고 3 전극 셋업 및 대칭형 수퍼커패시터 (SSC) 장치에서 수퍼커패시터 전극으로서 전기화학적 분석을 하였다. Cu_2MoS_4 전극은 약 127 F / g 의 비중 측정 커패시턴스를 보였고 SSC 는 탁월한 주기 안정성으로 28.25 F / g 의 비중 커패시턴스를 나타냈다. 또한 챕터 5 에서 Cu_2MoS_4 의 슈퍼 용량 특성을 개선하기 위해, Cu_2MoS_4-rGO 복합 재료는 열 수법을 통해 제조되고 슈퍼 용량 성능이 확인되었다. Cu_2MoS_4-rGO 복합 전극은 노출된 Cu_2MoS_4 전극에 비해 더 우수한 비정전 용량 (231.51 F g^{-1})을 나타낸다. Cu_2MoS_4-rGO 복합 전극의 전기 화학적 성능의 향상은 Cu_2MoS_4 나노 입자와 rGO 시트 사이의 화학적 상호 작용과 관련 될 수 있으며, 이는 전기 화학적 공정을 위한 더 활성화된 부위를 생성한다. 열악한 환경에서 수퍼커패시터를 적용하는 관점에서, 수성 Na_2SO_4 전해질의 25 ° C ~ 80 ° C 의 온도 범위에서 Cu_2MoS_4-rGO 복합 전극에 대한 자세한 온도 의존적 수퍼커패시터 연구가 수행되었다. Cu_2MoS_4 전극의 중량 커패시턴스 및 비 에너지를 보다 향상시키기 위해, 바인더가 없는 전극 제조 전략이 챕터 6 에서 선택되었다. Cu_2MoS_4 나노 구조의 직접 성장은 열 수법을 사용하여 Ni 폼에서 발생하였고 그들의 수퍼커패시티브 특성을 분석하였다. 3 극 시스템에서 바인더가 없는 Cu_2MoS_4 전극에 대해 2278.83 F / g 의 비중 측정 커패시턴스가 달성되었다. Cu_2MoS_4 SSC 장치 (바인더 프리)는 탁월한 비 에너지 (23.61 Wh / kg)로 265.62 F / g 의 커패시턴스를

전달하였다. Ni 폼 전극에 고정된 바인더 프리 Cu_2MoS_4는 이온 전달 경로가 짧고 독특한 구조의 뛰어난 전자 전도성으로 인해 바인더 기반 Cu_2MoS_4 전극 및 Cu_2MoS_4-rGO 복합 전극에 비해 우수한 수퍼커패시티브 특성을 보여준다. 마지막으로, 수퍼커패시터의 실제 적용을 고려하여, 챕터 7 에서 SCSPC 가 제조 및 논의되었다. SCSPC 는 에너지 저장 장치를 위한 고유 전극 (그래핀 시트) 및 $TEABF_4$ 전해질이 통합된 압전 분리기 (table salt derived porous PVDF) 를 사용하여 제조되었다. 다공성 PVDF (table salt derived) 압전 분리기는 20N 의 인가된 힘에서 약 11V 의 전압을 발생시켰다. 유사하게, 그래핀 SCSPC 의 전기 화학적 성능은 35.58Wh / kg 의 에너지 밀도와 함께 약 28.46F / g 의 장치 특정 중량 커패시턴스를 갖는다. 그래핀 SCSPC 는 112mV 까지 자가충전 되었으며 이는 탄소 SCSPC 를 기반으로 한 과거의 연구보다 높다.

실험적 증거는 다공성 PVDF (table salt derived) 압전 분리기를 사용하여 기계적 에너지를 전기 에너지로 변환하고 그래핀 SCSPC 장치를 사용한 에너지 저장을 보여주었으며, 결과적으로 휴대용 및 착용 가능한 전자 장치에 전력을 공급하기 위한 차세대 자체 전원 장치 개발에 대한 관심을 고려하였다.

사람이 생활하는 데에는 에너지가 필수적이다. 석유 같은 재생이 힘든 에너지원들이 고갈되어 감과 지구 온난화 및 기술의 발전에 의해 인류는 에너지 부족을

야기하고 있다. 이로 인해, 친환경적이면서 고성능인 에너지 수확, 저장 및 변환 장치에 대한 요구가 증가하고 있다. 전기화학적 에너지는 청정에너지와 관련하여 빠질 수 없는 부분이다. 수퍼커패시터, 연료 전지 및 배터리 같은 기존의 에너지장치는 전기화학적 반응을 통해 화학에너지를 전기에너지로 변환함으로써 다양한 휴대용 전자장치 및 전기 자동차 등에 사용되어왔다. 슈퍼커패시터 중에는 친환경적이며 빠른 충 방전 시간, 초고전력 등 다양한 휴대용 전자장치의 전력 공급원으로서 훌륭한 특성으로 인해 많은 주목을 받고 있는 것이 있다. 하지만, 충분치 않은 에너지 양 등이 수퍼커패시터의 실적용에 관하여 문제로 남아있다. 지난 10 년간 수퍼커패시터의 특정 전력, 특정 에너지 및 장시간 사용 안정성 등 과 같은 성능을 향상시키기 위해 여러 그룹에서 연구 작업이 진행되었다. 고성능을 위해 수퍼커패시터 장치를 위한 주요독립소자를 찾아야 한다. 수퍼커패시터 장치의 독립소자를 고려하면 전도성 기판, 전해질 및 전극 재료는 수퍼커패시터의 전기화학적 성능에 중요한 부분을 제공한다. 다양한 유형의 전극 재료 중에서, 나노입자, 나노시트 및 나노와이어 같은 나노구조 전극재료는 짧은 전극, 이온 수송 경로 및 높은 비표면적에 대한 접근성으로 인해 향상된 전기화학적 성능을 보인다.

수퍼커패시터 장치의 실적용 관점에서, 에너지 변환 및 저장은 휴대용 및 착용 가능한 전자 장치의 전원 공급을 위해 단일 시스템 안에서 이루어져야 한다. 전통적으로,

에너지 저장과 에너지 수확은 별개의 작업 메커니즘 및 독립적 물리장치를 사용하는 것으로 잘 알려진 현상이다. 자가충전 수퍼커패시터 파워셀은 외부에서 가해진 기계적 에너지를 “압전-전기화학적 공정”을 통해 전기적 에너지로 변환하고 배터리 혹은 수퍼커패시터 장치에 저장할 수 있는 가능성을 갖고 있다. SCSPC 장치의 자가충전 전압 및 에너지 변환 효율은 전원 공급 전자 장치를 위한 중요한 기준을 충족하기 위해 향상되어야 한다. 따라서 SCSPC 장치의 성능 개선은 지속 가능한 에너지원과 관련하여 상당한 관심을 끌고 있다. 에너지 저장 장치 및 SCSPC 장치와 관련하여 모든 기능을 고려하여, 이 논문은 주로 성능이 개선된 수퍼커패시터 및 자가 충전 수퍼커패시터 파워셀을 위한 나노구조 전극 재료에 집중되었다.

챕터 3 에서는 전이 금속 셀레나이드 (α-MnSe) 나노 입자의 합성을 설명하고 3 전극 시스템 및 대칭형 수퍼커패시터 장치에서 수퍼커패시터 응용을 위한 양극 재료로써의 전기화학적 분석을 하였다. 챕터 4 에서는 수열공정을 통하여 구리 몰리브덴 황화물 (Cu_2MoS_4) 나노 입자의 합성을 나타내고 3 전극 셋업 및 대칭형 수퍼커패시터 (SSC) 장치에서 수퍼커패시터 전극으로서 전기화학적 분석을 하였다. Cu_2MoS_4 전극은 약 127 F / g 의 비중 측정 커패시턴스를 보였고 SSC 는 탁월한 주기 안정성으로 28.25 F / g 의 비중 커패시턴스를 나타냈다. 또한 챕터 5 에서 Cu_2MoS_4 의 슈퍼 용량 특성을 개선하기

위해, Cu_2MoS_4-rGO 복합 재료는 열 수법을 통해 제조되고 슈퍼 용량 성능이 확인되었다. Cu_2MoS_4-rGO 복합 전극은 노출된 Cu_2MoS_4 전극에 비해 더 우수한 비정전 용량 (231.51 F g^{-1})을 나타낸다. Cu_2MoS_4-rGO 복합 전극의 전기 화학적 성능의 향상은 Cu_2MoS_4 나노 입자와 rGO 시트 사이의 화학적 상호 작용과 관련 될 수 있으며, 이는 전기 화학적 공정을 위한 더 활성화된 부위를 생성한다. 열악한 환경에서 수퍼커패시터를 적용하는 관점에서, 수성 Na_2SO_4 전해질의 25 ° C ~ 80 ° C 의 온도 범위에서 Cu_2MoS_4-rGO 복합 전극에 대한 자세한 온도 의존적 수퍼커패시터 연구가 수행되었다. Cu_2MoS_4 전극의 중량 커패시턴스 및 비 에너지를 보다 향상시키기 위해, 바인더가 없는 전극 제조 전략이 챕터 6 에서 선택되었다. Cu_2MoS_4 나노 구조의 직접 성장은 열 수법을 사용하여 Ni 폼에서 발생하였고 그들의 수퍼커패시티브 특성을 분석하였다. 3 극 시스템에서 바인더가 없는 Cu_2MoS_4 전극에 대해 2278.83 F / g 의 비중 측정 커패시턴스가 달성되었다. Cu_2MoS_4 SSC 장치 (바인더 프리)는 탁월한 비 에너지 (23.61 Wh / kg)로 265.62 F / g 의 커패시턴스를 전달하였다. Ni 폼 전극에 고정된 바인더 프리 Cu_2MoS_4 는 이온 전달 경로가 짧고 독특한 구조의 뛰어난 전자 전도성으로 인해 바인더 기반 Cu_2MoS_4 전극 및 Cu_2MoS_4-rGO 복합 전극에 비해 우수한 수퍼커패시티브 특성을 보여준다. 마지막으로, 수퍼커패시터의 실제 적용을 고려하여, 챕터 7 에서 SCSPC 가 제조 및 논의되었다. SCSPC 는 에너지 저장

장치를 위한 고유 전극 (그래핀 시트) 및 $TEABF_4$ 전해질이 통합된 압전 분리기 (table salt derived porous PVDF) 를 사용하여 제조되었다. 다공성 PVDF (table salt derived) 압전 분리기는 20N 의 인가된 힘에서 약 11V 의 전압을 발생시켰다. 유사하게, 그래핀 SCSPC 의 전기 화학적 성능은 35.58Wh / kg 의 에너지 밀도와 함께 약 28.46F / g 의 장치 특정 중량 커패시턴스를 갖는다. 그래핀 SCSPC 는 112mV 까지 자가충전 되었으며 이는 탄소 SCSPC 를 기반으로 한 과거의 연구보다 높다.

실험적 증거는 다공성 PVDF (table salt derived) 압전 분리기를 사용하여 기계적 에너지를 전기 에너지로 변환하고 그래핀 SCSPC 장치를 사용한 에너지 저장을 보여주었으며, 결과적으로 휴대용 및 착용 가능한 전자 장치에 전력을 공급하기 위한 차세대 자체 전원 장치 개발에 대한 관심을 고려하였다.

ABSTRACT

Energy is indispensable for human establishment. Insufficient sources of non-renewable energy along with an increase in global warming and evolution in technology put human beings under the nose of an energy crisis. So, there has been an increasing requirement for environment-friendly, high-performance energy harvesting, storing and conversion devices. Electrochemical energy is an unpreventable fragment of the clean energy portfolio. Unconventional energy devices, such as supercapacitors, fuel cells, and batteries, have been used in various portable electronic devices and electric vehicles due to the conversion of chemical energy into electrical energy via electrochemical reactions. Amongst supercapacitor has gained much attention due to their admirable characteristics, including eco-friendly nature, rapid charging/discharging time, and ultrahigh specific power, which are immensely anticipated as an auspicious contender to meet the demands to supply power for various portable electronic devices. However, extensive implementations of supercapacitors remain a question, with unfulfilled energy demands. Several research works were carried out by several research groups to enhance the performance metrics like specific power, specific energy, and long cyclic stability of supercapacitors through last decade. The choosing of significant independent elements for the supercapacitor devices is extremely required to acquire high performance. Taking into consideration of independent elements of supercapacitor devices, the conducting substrate, electrolyte, and electrode material provides a crucial part in the electrochemical performances of supercapacitor. Among various types of electrode materials, nanostructured electrode materials like nanoparticle, nanosheet, and nanowire exhibit enhanced electrochemical performance due to their accessibility of short electron and ion transport pathways and high specific surface area.

In the view of the practical application of a supercapacitor device, the energy conversion and storage should be in a single system to power up portable and wearable electronic devices.

Traditionally, energy storage and energy harvesting are two well-known phenomena using distinct working mechanisms and independent physical units. The self-charging supercapacitor power cell (SCSPC) has the potential to convert mechanical energy from applied stress/force to electrical energy and stores them in battery or supercapacitor device via "piezo-electrochemical process". The self-charging voltage and energy conversion efficiency of SCSPC devices are needed to be enhanced to meet out the significant criterions for power up electronic devices. Hence the improvement in the performance of SCSPC device attract considerable attention considering the emergence of sustainable energy sources. Taking all the features into consideration with respect to energy storage device and SCSPC device, this thesis is mostly concentrated on nanostructured electrode materials towards supercapacitor and self-charging supercapacitor power cell with improved performance.

Chapter-3 of this thesis presents the synthesis of transition metal selenide (α-MnSe) nanoparticle and performed electrochemical analysis as a positive electrode material for supercapacitor applications in three-electrode system and symmetric supercapacitor devices. Chapter-4 of this thesis represents the synthesis of copper molybdenum sulfide (Cu_2MoS_4) nanoparticles using the hydrothermal process and performed the electrochemical analysis as supercapacitor electrode in both three-electrode setup and symmetric supercapacitor (SSC) device. The Cu_2MoS_4 electrode showed specific gravimetric capacitance of about 127 F/g and SSC exhibited a specific capacitance of 28.25 F/g with superb cyclic stability. Further to improve supercapacitive properties of Cu_2MoS_4, Cu_2MoS_4-rGO composite material is prepared via hydrothermal method and performed supercapacitive performance in chapter-5. The Cu_2MoS_4-rGO composite electrode exhibits better specific capacitance (231.51 F g^{-1}) compare to the bare Cu_2MoS_4 electrode. The enhancement in the electrochemical performance of Cu_2MoS_4-rGO composite electrode can be associated with the chemical interaction between Cu_2MoS_4

nanoparticles, and rGO sheets, which producing more active sites for the electrochemical process. In the view of application of supercapacitor in the harsh environment, the detailed temperature-dependent supercapacitor study occurred for Cu_2MoS_4-rGO composite electrode in the applied temperature range of 25 °C to 80 °C in aqueous Na_2SO_4 electrolyte. For more improving the gravimetric capacitance and the specific energy of Cu_2MoS_4 electrode, a binder free electrode fabrication strategy has been chosen in chapter-6. The direct growth of Cu_2MoS_4 nanostructures occurred on Ni foam using hydrothermal method and analyzed their supercapacitive properties. The specific gravimetric capacitance of 2278.83 F/g was achieved for binder-free Cu_2MoS_4 electrode in three electrode system. The Cu_2MoS_4 SSC device (binder-free) delivered capacitance of 265.62 F/g with excellent specific energy (23.61 Wh/kg). The binder free Cu_2MoS_4 anchored on Ni foam electrode shows better supercapacitive properties compare to binder based Cu_2MoS_4 electrode and Cu_2MoS_4-rGO composite electrode due to their short ion transport pathways, and superb electronic conductivity of unique architecture. Finally, in view of practical application of supercapacitor, a SCSPC was fabricated and discussed in chapter-7. A SCSPC was fabricated using unique electrodes (graphene sheets) for energy storage device, and piezo-separator (table salt derived porous PVDF) incorporated with $TEABF_4$ electrolyte. The porous PVDF (table salt derived) piezo-separator generated a voltage of about 11 V at an applied force of 20 N. Similarly, electrochemical performance of graphene SCSPC possesses device specific gravimetric capacitance of about 28.46 F/g with energy density of 35.58 Wh/kg. The graphene SCSPC was self-charged up to 112 mV, which is higher than the past works based on carbon SCSPC. The experimental evidence demonstrated the conversion of mechanical energy into electrical energy using porous PVDF (table salt derived) piezo-separator and storage using the graphene SCSPC device, consequently considering the attention towards the development of future-generation self-powered devices for powering up portable and wearable electronics.

CHAPTER 1

INTRODUCTION

1.1. Background

Energy conversion and energy storage have become a worldwide concern in current days because of rapid consumption of available energy resources and global warming issues. In an effort to fight the rising greenhouse gases emission caused by the burning of these limited conventional natural resources, human society is moving towards developing renewable energy sources, such as solar-, wind-, hydropower-, and geothermal- energy that offer justifiable energy in environmentally friendly manner[1–5]. At the same time the destruction of environmental hazards like nuclear waste from non-renewable sources from the nuclear plants. Additionally, over past few decades the market price of fossil fuels has rapidly increasing day by day which makes more pressure on economic progress of the developing and developed countries [6]. Hence the fabrication of an efficient energy or power source device using renewable resources (solar, wind, hydropower etc.) that offer sustainable energy without losing the environmental quality. Therefore, these inadequate energy resources mainly depend on natural conditions (e.g., rain-, wind-, sunshine-, and location); thus, innovative technology is essential to convert the off-peak electricity into various forms of energy conversion and storage system to fill the energy shortages during the on-peak period [7].

1.2. Significance of electrochemical energy storage devices

To retain an equilibrium amid the desires of predominant energy demands and the ecological issues, investment in electrochemical energy storage (EES) is needed to accompany in a green energy future[8]. Electrochemical energy storage- and conversion- systems with good performance, such as metal–air batteries (MABs), lithium-ion batteries (LIBs), sodium-ion

batteries (SIBs), supercapacitors (SCs), and water-splitting, are very encouraging technologies for conquering the universal energy challenges [9–13]. The EES has fascinated among various classes of energy storing systems due to its numerous merits such as ultra-high efficiency conversion rate, direct energy conversion without intermediate step, miniaturization, portability, convenience to scale up and minimum pollution. The SCs and LIBs are at the frontier of this research due to extensively uses in our day to day life, powering various advanced electronic devices and new electric vehicles. However, the crucial tasks and problem headed for the commercialization of EES system, have been broadly considered in different fields of technology basically on electrode materials and electrolyte. Along with some practical problems and when selecting the SCs and LIBs, the usage with lower cost electrode material is a major issue.

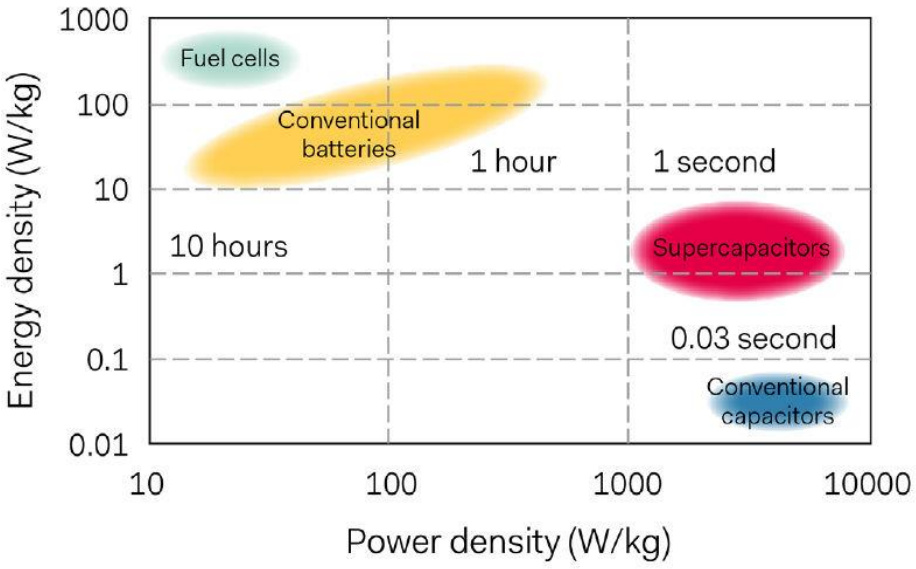

Figure 1.2 Evaluation of energy storage devices by Ragone plot.

Amongst the EES systems, supercapacitors (SCs) have captivated substantial interest in both academia and industry because of their unique properties such as superior power density induced due to a fast charge-discharge rates and a long-life cycle in comparison with batteries and fuel-

cells. Practically, SCs have maximal power (kW kg^{-1}) than batteries which are theoretically very low as shown in Figure 1.1.Hence, SCs are most auspicious candidate for alternative energy storage systems with longer life time and lighter weight than other energy storage devices [14]. Currently, due to ultrahigh power densities SCs are used in verities of applications such as in industrial power and energy management, memory back-up systems, portable electronics[15].

1.3 CLASSIFICATION OF SUPERCAPACITORS

Based on the charge storage process and existing R & D technologies, SCs can be categorized as electrochemical dual-layer capacitors (EDLCs), pseudo-capacitors and hybrid-ion capacitors [16]. The categorization of SCs is acquired in the Figure 1.3.

1.3.1 ELECTROCHEMICAL DOUBLE- LAYER CAPACITORS (EDLC)

The charge-storage process in EDLCs is depending on the electrostatic adsorption of the electrolyte-ions on the electroactive materials surface. Thus, the significant thing is to achieve high capacitance of EDLCs is in employing a highly available surface area and electrically conducting electrodes. Nanostructured carbonaceous materials possessing a larger surface area and decent electrical conductivity are the materials of excellent-choice for EDLCs.

Carbonaceous materials like as graphene and their derivatives, carbon-nanotubes, activated carbon, carbon in various forms (nanocoils-, nanohorns-, onions-), carbon fabrics, carbon fibers, zeolite-templated carbons, carbon aerogels, carbide-derived carbons, and porous carbons having electrical conductivity, electrochemical stability, and highly accessible surface area along with low-cost could manage all the necessities for SCs application[17]. The EDLC nature of the carbonaceous electrode is mainly ruled by their structure along with the porosity and specific surface area. The charge storage process in the EDLC succeeds through the electrostatic adsorption of ions (EDLC), at the interface between the electrolyte and electrode by employing the applied cell voltage. In the 19^{th} century, the idea of EDL was first proposed by

Helmholtz when he explored the scattering of opposite charges at interface on colloidal microparticles. The Helmholtz double layer model describes that the two layers of opposite charge appear at the electrolyte/electrode interface and the layers are separated by an atomic distance.

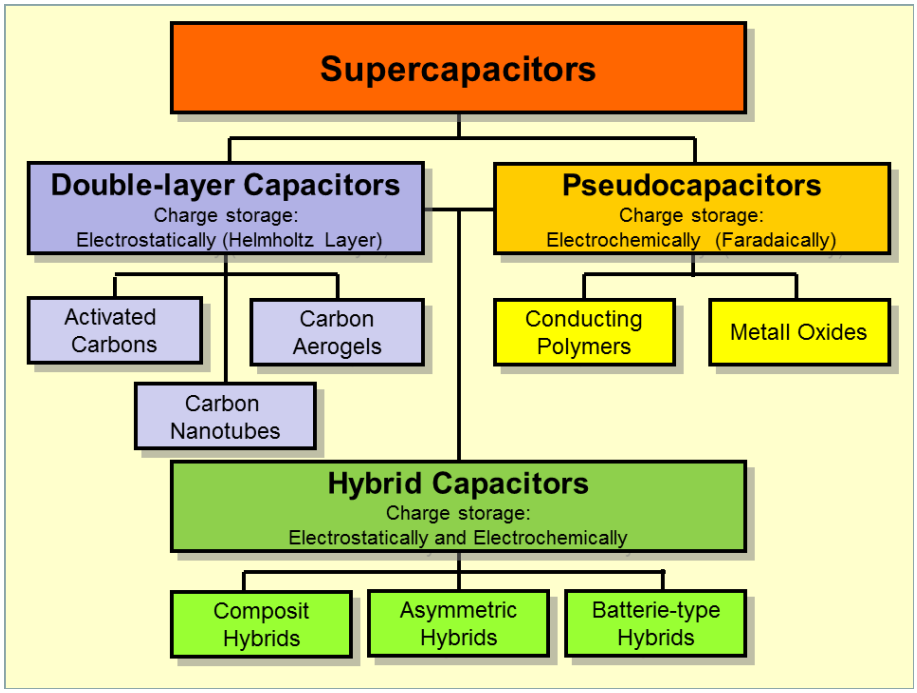

Figure 1.3 Categorization of SCs.

Later, Gouy and Chapman modified the Helmholtz double layer model to study the thermal motion of ions closer to a charged surface, which is denoted as diffuse layer. The perception of EDLC is a grouping of two regions; (i) the inner and (ii) the diffuse layer. Therefore, the entire capacitance (C) can be stated by the following relation [18]:

$$1/C = 1/C_i + 1/C_d \quad \ldots\ldots\ldots\ldots\ldots\ldots\ldots\ldots\ldots\ldots \quad (2)$$

Where C_i is the inner (Helmholtz) layer capacitance self-governing of the surface-inactive electrolyte concentration, and C_d is the intercalative capacitance according to Gouy–

Chapman theory. Classically, carbon-based materials and their derivatives are used in EDLCs behavior (graphene, porous carbon, activated carbon and carbon nanotubes (CNTs)).

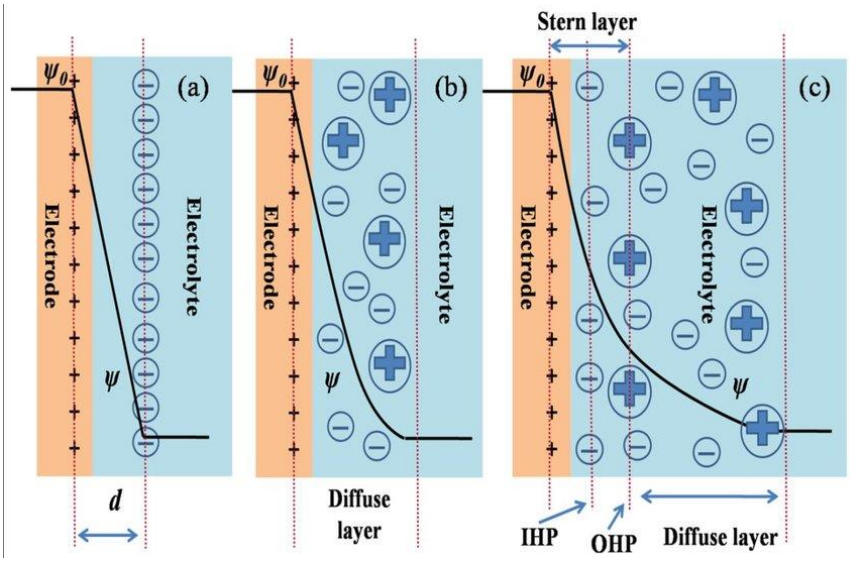

Figure 1.3.1 Representations of the EDLC at a positively charged surface: (a) Helmholtz model, (b) Gouy–Chapman (GC) model, and (c) Stern model, representing the (i) inner and (ii) outer Helmholtz planes.

1.3.2 PSEUDOCAPACITORS

In pseudo-capacitors, the charge storage process arisen between electrode and electrolyte interface which result in bulk oxidation in anode and reduction in cathode (i.e. oxidation-reduction reactions or redox reaction or faradic reaction[19,20]).The faradaic mechanism can be categorized as different electrochemical features: (1) under-potential deposition (UD), (2) redox pseudo-capacitance (example: transition metal oxides), and (3) intercalation pseudo-capacitance. Under-potential (UD) is created when the adsorbents of metal-ions at a distinct metal's surface which is well above their redox potential. One typical illustration of UD is that of Pb on the surface of an Au electrode. Redox pseudocapacitance/diffusion capacitance rises while ions are electrochemically adsorbed onto the surface/near surface of an electrode material with the allied phase charge-transfer. As well, another kind of capacitance called

intercalation/diffusion capacitance arises due to the diffusioin of ions into the layers/channel of an electrode material in the company of a phase charge-transfer with absence of crystallographic phase alteration. It worthy to note that these three kind of mechanisms occurs due to the different materials and various physio-chemical process; the resemblance in the electrochemical signs rises because of the connection between potential (voltage difference) and the amount of charge that grows as a result of EDLC processes at the electrolyte/electrode interface (EEI) /within the internal surface of a material[21]. These processes are described in Figure 1.3.2**.**

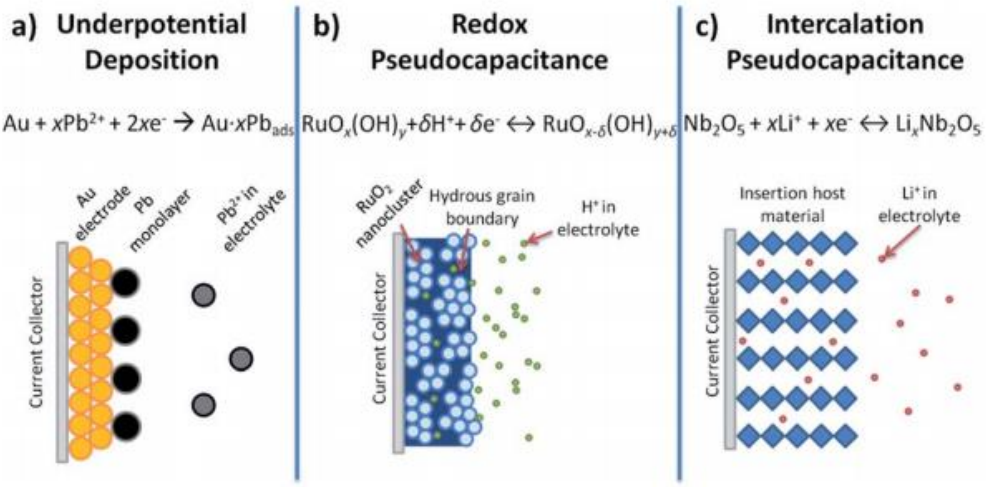

Figure 1.3.2 Reversible redox mechanisms: (a) under-potential deposition (UD), (b) redox pseudo-capacitance, and (c) intercalation pseudo-capacitance.

Transition metal oxides (e.g. MnO_2, Fe_3O_4, and RuO_2), transition metal sulfides/selenides (e.g. MoS_2, $MoSe_2$), carbon nanomaterials holding oxygen related surface functional groups, and conducting polymers (e.g. polyaniline (PANi), polypyrrole (PPy), and polythiophene (PT)) [22–24] are generally being used as a pseudo-capacitor materials.

1.3.3 HYBRID SUPERCAPACITORS

Current research efforts on SCs displays that new strategies must be applied to achieve a high energy density as compared to the lithium-ion batteries with different attempts. Later, a new strategy is proposed using the combination both Faradaic and non-Faradaic processes in order to store charge in hybrid capacitors to accomplish a higher energy and power densities than the lithium-ion batteries.

The phrase “hybrid” in SC can be used if pairing the two electrodes with diverse charge storage properties, i.e., one faradaic and one capacitive, that characteristics lie in between a SC and a battery device. While, “asymmetric supercapacitor” employs an extensive range of electrode combinations since it can be utilized electrodes of the same nature but with various mass loading, or in the combination of two electrodes using different materials. Brousse et al., recently stated that the term “asymmetric” should be used only when pseudocapacitive or capacitive electrodes are involved so as to evade confusion with true “hybrid” devices [25–27]. There are many literatures on the usage of faradaic electrode materials for electrochemical capacitor applications including our published reports. Sadly, few of these materials are denoted as “pseudocapacitive” materials although the reason that their electrochemical nature (i.e., charge/discharge curve and cyclic voltammogram) is akin to that of “battery electrodes”. Generally, positive electrodes for hybrid supercapacitors are based on same faradaic reaction as we discussed in previous section. But it is potential independent charge storage behavior which should be denoted as “battery like electrodes” of faradaic electrodes. Hybrid SCs devices compose of asymmetric cells. In hybrid SCs devices, numerous charge-storage mechanisms are applied in the positive and negative electrode. For instance, one electrode uses the EDLC mechanism (that is, carbon based electrode) whereas the further charge storage by means of pseudo-capacitive reactions, that is, as happens in transition oxides, except MnO_2, RuO_2[28,29].

1.3.4 Electrode materials

Generally, electrode materials and electrolytes play key roles to decide the specific capacitance, which has been getting more attention from research and academia. It is demonstrated that monitoring the structure and physical property of electrode materials are deciding factors to improve the performance SCs including good specific capacitance, better rate capability and cyclic life [30]. Overall, the electrode materials of supercapacitor can be categorized as: (1) carbon-based materials, (2) metal oxides, (3) polymers, and (4) transition metal chalcogenides.

1.3.4.1 Carbon based electrode materials

Carbon materials store charges electrostatically on their surfaces by means of reversible adsorption/desorption of ions of the electrolyte onto active electrode materials. Carbon-based materials have been broadly investigated as electrode materials for SCs due to a unique combination of physical features such as good surface area, lightweight, good electrical conductivity, controlled pore size distribution, and compatibility with other materials.

(i) Activated carbons (ACs): Activated carbon (AC) is a non-graphitic carbon (i.e. disordered carbon) and holding the property of high-porosity nature[31]. It can be seen from the interplanar spacing (0.335 nm) of activated carbon which is smaller than the graphite interplanar spacing (0.34-0.35 nm) and also this AC consist of several number of disorder graphene layers or basal layer, branded as turbostatic carbon. ACs are extensively utilized electrode materials owing to their high surface area, relatively good electrical properties and reasonable cost. ACs are usually can be generated from physical (thermal) and/or chemical activation of numerous types of carbonaceous materials (e.g. wood, coal, nutshell, etc.) [18,32].

(ii) Carbon nanotubes (CNTs): CNTs displays high advantages of exceptional inter-connected mesoporous structure, high electronic conductivity, good mechanical and thermal stability [33]. These excellent properties of CNTs make them an interesting electrode material for EDLCs.

CNTs can be classified as single-walled carbon nanotubes (SWNTs) and multi-walled carbon nanotubes (MWNTs), both of which have been investigated as high energy storage electrode materials [34].

(iii) Graphene: Graphene is a one-atom thick sheet combined of sp^2 bonded carbon atoms in a polyaromatic honeycomb crystal lattice. Graphene is appropriate for high performance energy storage systems because of their high rate, cycle stability, improved capacity and exceptional physiochemical properties [35]. Many techniques like thermal reduction, chemical reduction, electrochemical reduction, microwave assisted reduction and multistep reduction methods etc. have been utilized to synthesize graphene-based electrode materials.

1.3.4.2 Metal oxides:

Metal oxides generally possess a high specific capacitance and good conductivity, which causes them appropriate for electrode fabrication that induces to focus to achieve high energy and high-power supercapacitors[36]. Ruthenium oxide (RuO_2) is one of the most investigated electrode materials because of its advantages over than other materials. RuO_2 has the best specific capacitance amongst pseudocapacitive materials, about 1000 F g^{-1} [37]. Since ruthenium oxide is too expensive, there are several reports studied on combining it with other low-priced materials. Now, low-cost metal oxides such as MnO_2, MoO_3, and WO_3 are employed for supercapacitor application[38].

1.3.4.3 Conducting polymers (CPs):

In general, CPs are gifted electrode materials for supercapacitors for three main motives: (i) good specific capacitance due to doping process includes the entire polymer mass (ii) high conductivity in the charged state and (iii) doping/un-doping process is generally fast, hence, SCs devices with lesser ESR and better specific power are feasible, in addition conventional CPs are low-cost [39]. The classic cyclic voltammogram of a polymer electrode is non-rectangular shape,

as expected for a capacitor, but displays a current peak at redox potential of the polymer, whereas metal oxide can display a series of redox reactions, showing an approximately rectangular cyclic voltammogram shape [40].

1.3.4.4 Transition metal chalcogenides:

Recently, two-dimensional (2D) nanomaterials, predominantly layered transition metal chalcogenides (TMDs), are evolving as a class of vital electrode materials in electro-chemistry and electronics because of their intriguing physical and chemical properties and hence, grasp great promise for various applications such as electrocatalysts, electronics devices and energy storage [41,42]. Generally, sulfide materials are classified as semiconductors owing their significant refractive indices, and good electrical conductivity. An essential property that discriminates sulfide materials from oxide is the band gap; the energy separation between the filled valence-band made mostly from the sulfur p-orbital, and the empty conduction band constructed mostly from the empty cation orbitals. Transition metal sulfides are also known to be active electrode materials for supercapacitor, but to date very few metal sulfides such as NiS, CoS, WS_2, $MoSe_2$, and MoS_2, have been used to fabricate SCs devices due to their high conductivity and surface area [43–45]. Although binary metal sulfides have been used for various applications because of their high thermoelectric properties, now, low-priced, low-toxicity, and easy-to-work on binary metal sulfides have captivated rising interest in current decades as energy materials. Until now, there are inadequate reports on preparation of Cu_2MoS_4, $CoMoS_4$, $CuSbS_2$, $ZnCo_2S_4$, $Cdln_2S_4$, $FeMo_4S_6$, $CuCo_2S_4$, etc., and their applications as supercapacitor electrode[46–49].

1.4. Energy harvesting: Nanogenerator

In current years, the urging for fossil fuels, such as coal, petroleum, and natural gas, is growing with fast development and industrial growth. Though, fossil-fuels are non-renewable energy resources, and a huge amount of impurities and waste are produced from their use. Hence,

it is enormously vital to develop a novel energy sources as replacements to outdated fossil fuels[50]. The energy harvesting from ambient atmosphere such as solar-, thermal-, wind-,mechanical- and chemical- energy has fascinated massive attention in the researcher due to the independent and sustainable operating of such systems without the usage of a battery [51,52]. Amongst, harvesting machine-driven energy from our active environment is broadly evaluated to be one of the gifted approaches to offer a green and clean energy source for self-powered system, such as implanted medical devices, wireless sensor networks, nanorobotics, and wearable electronics. The mechanical energy that converts mechanical to electrical energy using triboelectric, piezoelectric, and electromagnetic principles[53–56].

Among various energy conversion approaches, piezo/tribo-nanogenerator has been engrossed towards the wearable electronics due to their conversion of mechanical to electrical energy at low frequency [57]. Even though conversion rate of mechanical to electrical energy is low it has huge impact to operate smart devices with the asset of power source without external power supply. Basically, piezoelectric nanogenerator performances depends on the several factors such as externally applied force, usage of piezoelectric material and device design. Since, piezoelectric nanogenerator have been established to efficiently convert biomechanical energy into electrical output and used as power source for various applications [58].

1.4.1. Mechanism of piezoelectric nanogenerator

The phenomenon of piezoelectricity, where electricity is produced through the mechanical impact can be utilized as an energy harvesting technique for miniaturized devices. The free ions or electrons are attracted to the oppositely charged surface of the material due to the existence of polarization with oriented or aligned dipole which has been diagrammatically shown in the Figure 1.4.1(a) where the observance of material polarization is there along with the bounded surface charge. Under the absence of stress, there will not be a current flow when

the electric load is connected along the material surface. The mechanism of piezoelectricity arises from the fact that the surface charges will be created owing to the changes in polarization level under repeated compression. The decrement in polarization level due to the repeated stress makes the current to flow on the application of electric load along the surface of the material as picturized in Figure 1.4.1(b). In contrast, the current will flow in opposite direction if the stress is applied in tensile direction owing to the increase in polarization level as shown in Figure 1.4.1(c). Obviously, AC current will be generated through the application of alternating stress on the material.

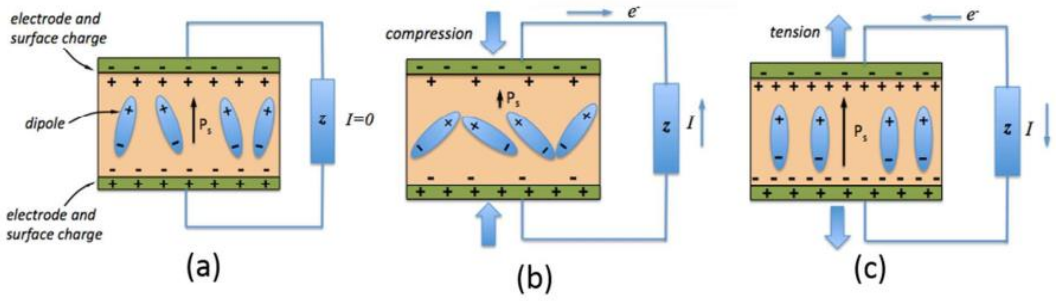

Figure 1.4.1 Mechanism of the piezoelectric nanogenerator.

1.4.2. Piezo-materials

Till now, plenty of researchers have attempted to fabricate the piezoelectric nanogenerators through different materials and designs to improve its performance. The materials such as zinc oxide, cadmium sulfide, PZT [59], barium titanate [60], GaN, poly (vinylidene fluoride)[61] and PTFE, and polymers have been successfully transformed into different nano-architectures to realize their piezoelectric behavior in order to utilize in self-driven power source applications[62]. The materials with wurtzite structure such as CdS, ZnO, and GaN have been studied enormously because of their feasibility in terms of cost and production.

1.5. Objectives and scope of thesis

Supercapacitor is the thing which cannot be neglected in the energy industries due their contribution through their enormous power density value, prolonged life cycle, and feasibility to integrate intrinsically and extrinsically with other energy conversion devices in the current scenario and future. Owing to their poor energy storing capacity, low operating window followed by self-discharge characteristics, supercapacitors are mostly used as a complementary aid not an alternative to batteries. The surface area, electrical conductivity and mobility of ions through the electroactive surface of the electrode determines the performance metrices of a typical supercapacitor. The well-known charge storage mechanisms of a supercapacitors comprise of electric double-layer formation (EDLCs) employing ion adsorption & desorption (carbon-based materials), pseudo-capacitance, (metal oxides, metal chalcogenides, and conducting polymer) using rapid faradaic reactions. The electrode materials play a vital role in deciding the energy storage mechanism regardless the type of supercapacitors. TM sulfides possess superior electrical conductivity, and temperature withstanding ability than MOs (Metal Oxides) and MOHs(Metal Hydroxides). The high electronegativity of the sulfur ions makes them to produce more flexible structures than oxygen ions leads to better electrochemical redox reactions in metal sulfides. Therefore, this thesis aims to develop TMCs (transition metal chalcogenides) such as α-MnSe, Cu_2MoS_4 and $CuFeS_2$ with different nanostructures and their composites to overcome the drawbacks of currently using supercapacitors. The objectives of this work are briefly outlined as follows:

- To synthesize nanostructured transition metal chalcogenides by hydrothermal method.
- The physical characterization of as prepared electrode materials was performed using FTIR- Fourier transform Infrared spectroscopy, XRD- X-ray diffraction, FESEM-scanning electron microscopy, XPS- X-ray photoelectron spectroscopy, transmission

electron microscopy (HRTEM), Raman spectroscopy and N_2 adsorption/desorption method.

- The energy storage performances of the designed electrode materials were determined through three-electrode system and symmetric device configuration in different organic and aqueous electrolytes.
- Finally, the thesis aimed to develop a self-charging power cell through intrinsic integration of graphene electrodes as supercapacitor and porous PVDF as piezo-separator.

It is envisaged that the results presented in this thesis will provide simple and effective methodologies to tailor the structure of TMCs for energy storage application. In addition, the graphene-based self-powered cell provide a new horizon in the field of biomedical engineering to implement the integrated energy harvesting and storage materials as a single device inside the patient's body.

1.6. Structure of this thesis

The thesis is summarized into five chapters,

Chapter-1 describes that the detailed introduction about the energy storage systems, electrochemical capacitors, mechanism of the different types of electrochemical capacitors, materials used in the different electrochemical capacitors and energy harvesting system (piezoelectric nanogenerator).

Chapter-2 provides details of the chemicals and reagents, experimental setups and methods used in the thesis. Also deals with the different characterization engaged in the analysis of materials properties like structural, optical, composition, morphological and electrochemical properties. The details about the cell and working electrodes fabrication using aqueous or gel electrolyte and analysis of electrochemical data.

Chapter-3 presents the synthesis of transition metal selenide α-MnSe and their structural and electrochemical properties as a positive electrode material for supercapacitor applications.

Chapter-4 describes the synthesis of Cu_2MoS_4 as a negative electrode material for supercapacitor applications in both three-electrode system and symmetric supercapacitor device.

Chapter-5 presents the synthesis of Cu_2MoS_4-rGO composite as electrode material for supercapacitor applications. Also, we performed the temperature dependent electrochemical analysis of Cu_2MoS_4-rGO composite electrode.

Chapter-6 emphasize the improved electrochemical performance of Cu_2MoS_4 by binder-free approach and performed supercapacitor analysis in both three-electrode and symmetric supercapacitor device in aqueous electrolyte.

Chapter-7 describes the fabrication of Self-Charging Supercapacitor Power Cell (SCSPC) using porous PVDF as a piezo-separator and graphene as electrochemically active materials for positive and negative electrodes, respectively for the first time. The fabrication and working mechanism of a SCSPC was discussed in detail. The SCSPC provide a new auspicious path in the supercapacitor research for the development of future generation self-powered power source for wearable and flexible electronic devices.

Chapter-8 summarizes the salient features of the present study and outlined some suggestions for future work.

1.7 References

1 E. Skoplaki and J. A. Palyvos, *Solar Energy*, 2009, **83**, 614–624.

2 T. T. Chow, *Applied Energy*, 2010, **87**, 365–379.

3 K. Liu, M. Yu and W. Zhu, *Renewable Energy*, 2019, **140**, 912–927.

4 Q. Schiermeier, J. Tollefson, T. Scully, A. Witze and O. Morton, *Nature*, 2008, **454**, 816–823.

5 S. Chu and A. Majumdar, *Nature*, 2012, **488**, 294–303.

6 R. J. P. Schmitt, N. Kittner, G. M. Kondolf and D. M. Kammen, *Nature*, 2019, **569**, 330–332.

7 S. P. S. Badwal, S. S. Giddey, C. Munnings, A. I. Bhatt and A. F. Hollenkamp, *Frontiers in Chemistry*, , DOI:10.3389/fchem.2014.00079.

8 H. Wei, D. Cui, J. Ma, L. Chu, X. Zhao, H. Song, H. Liu, T. Liu, N. Wang and Z. Guo, *Journal of Materials Chemistry A*, 2017, **5**, 1873–1894.

9 B. Dunn, H. Kamath and J.-M. Tarascon, *Science*, 2011, **334**, 928–935.

10 M. D. Slater, D. Kim, E. Lee and C. S. Johnson, *Advanced Functional Materials*, 2013, **23**, 947–958.

11 J.-M. Tarascon and M. Armand, *Nature*, 2001, **414**, 359–367.

12 L. Järup, *British Medical Bulletin*, 2003, **68**, 167–182.

13 M. Winter and R. J. Brodd, *Chemical Reviews*, 2004, **104**, 4245–4270.

14 G. Wang, L. Zhang and J. Zhang, *Chem. Soc. Rev.*, 2012, **41**, 797–828.

15 L. L. Zhang and X. S. Zhao, *Chemical Society Reviews*, 2009, **38**, 2520.

16 W. Zuo, R. Li, C. Zhou, Y. Li, J. Xia and J. Liu, *Advanced Science*, 2017, **4**, 1600539.

17 I. Tanahashi, A. Yoshida and A. Nishino, *Bulletin of the Chemical Society of Japan*, 1990, **63**, 3611–3614.

18 C. Sc, C. Ramirez-Castro, M. Oljaca, S. Passerini, M. Winter and A. Balducci, *Journal of The Electrochemical Society*, 2015, **162**, 44–51.

19 H. Pan, Y. Shao, P. Yan, Y. Cheng, K. S. Han, Z. Nie, C. Wang, J. Yang, X. Li, P. Bhattacharya, K. T. Mueller and J. Liu, *Nature Energy*, 2016, **1**, 16039.

20 K. Krishnamoorthy, P. Pazhamalai, S. Sahoo and S.-J. Kim, *J. Mater. Chem. A*, 2017, **5**, 5726–5736.

21 V. Augustyn, P. Simon and B. Dunn, *Energy & Environmental Science*, 2014, **7**, 1597.

22 P. SIMON and Y. GOGOTSI, in *Nanoscience and Technology*, Co-Published with Macmillan Publishers Ltd, UK, 2009, pp. 320–329.

23 G. A. Snook, C. Peng, D. J. Fray and G. Z. Chen, *Electrochemistry Communications*, 2007, **9**, 83–88.

24 Q. Abbas, M. Mirzaeian and A. A. Ogwu, *International Journal of Hydrogen Energy*, 2017, **42**, 25588–25597.

25 A. Borenstein, O. Hanna, R. Attias, S. Luski, T. Brousse and D. Aurbach, *J. Mater. Chem. A*, 2017, **5**, 12653–12672.

26 Y. Gogotsi and R. M. Penner, *ACS Nano*, 2018, **12**, 2081–2083.

27 A. González, E. Goikolea, J. A. Barrena and R. Mysyk, *Renewable and Sustainable Energy Reviews*, 2016, **58**, 1189–1206.

28 A. Leela Mohana Reddy, F. Estaline Amitha, I. Jafri and S. Ramaprabhu, *Nanoscale Research Letters*, 2008, **3**, 145–151.

29 A. K. Cuentas Gallegos and M. E. Rincón, *Journal of Power Sources*, 2006, **162**, 743–747.

30 L. L. Zhang and X. S. Zhao, *Chemical Society Reviews*, 2009, **38**, 2520.

31 P. Simon and A. Burke, *Electrochemical Society Interface*, 2008, **17**, 38–43.

32 A. Alfarra, E. Frackowiak and F. B??guin, *Applied Surface Science*, 2004, **228**, 84–92.

33 C. W. Liew, S. Ramesh and A. K. Arof, *International Journal of Hydrogen Energy*, 2015, **40**, 852–862.

34 S.-B. Yoon, J.-P. Jegal, K. C. Roh and K.-B. Kim, *Journal of the Electrochemical Society*, 2014, **161**, H207–H213.

35 D. A. C. Brownson and C. E. Banks, *The Handbook of Graphene Electrochemistry*,

Springer London, London, 2014.

36 K. M. Deen and E. Asselin, *Electrochimica Acta*, 2016, **212**, 979–991.

37 W. Yong-gang and Z. Xiao-gang, *Electrochimica Acta*, 2004, **49**, 1957–1962.

38 C. Xu, F. Kang, B. Li and H. Du, *Journal of Materials Research*, 2010, **25**, 1421–1432.

39 G. A. Snook, P. Kao and A. S. Best, *Journal of Power Sources*, 2011, **196**, 1–12.

40 B. E. Conway, *Journal of The Electrochemical Society*, 1991, **138**, 1539.

41 H. Fang, M. Tosun, G. Seol, T. C. Chang, K. Takei, J. Guo and A. Javey, *Nano Letters*, 2013, **13**, 1991–1995.

42 G. A. Muller, J. B. Cook, H.-S. Kim, S. H. Tolbert and B. Dunn, *Nano Letters*, 2015, **15**, 1911–1917.

43 B. T. Zhu, Z. Wang, S. Ding, J. S. Chen and X. W. (David) Lou, *RSC Advances*, 2011, **1**, 397.

44 D. Zhang, *International Journal of Electrochemical Science*, 2016, 6791–6798.

45 M. Pumera, Z. Sofer and A. Ambrosi, *J. Mater. Chem. A*, 2014, **2**, 8981–8987.

46 B. Yang, L. Wang, J. Han, Y. Zhou, H. Song, S. Chen, J. Zhong, L. Lv, D. Niu and J. Tang, *Chemistry of Materials*, 2014, **26**, 3135–3143.

47 S. Hong, D. P. Kumar, D. A. Reddy, J. Choi and T. K. Kim, *Applied Surface Science*, 2017, **396**, 421–429.

48 A. Pramanik, S. Maiti, T. Dhawa, M. Sreemany and S. Mahanty, *Materials Today Energy*, 2018, **9**, 416–427.

49 X. Zhang, P. Ding, Y. Sun and J. Guo, *Materials Letters*, 2016, **183**, 1–4.

50 Y. Chen, J. Ma, B. Han, P. Zhang, H. Hua, H. Chen and X. Su, *Journal of Traffic and Transportation Engineering (English Edition)*, 2018, **5**, 318–334.

51 S. P. Beeby, M. J. Tudor and N. M. White, *Measurement Science and Technology*, 2006,

17, R175–R195.

52 X. Wang, J. Song, J. Liu and Z. L. Wang, *Science*, 2007, **316**, 102–105.

53 F.-R. Fan, Z.-Q. Tian and Z. Lin Wang, *Nano Energy*, 2012, **1**, 328–334.

54 H. Klauk, U. Zschieschang, J. Pflaum and M. Halik, *Nature*, 2007, **445**, 745–748.

55 A. I. Hochbaum and P. Yang, *Chemical Reviews*, 2010, **110**, 527–546.

56 S. P. Beeby, R. N. Torah, M. J. Tudor, P. Glynne-Jones, T. O'Donnell, C. R. Saha and S. Roy, *Journal of Micromechanics and Microengineering*, 2007, **17**, 1257–1265.

57 Z. L. Wang, *Materials Science and Engineering: R: Reports*, 2009, **64**, 33–71.

58 Z. L. Wang, *Advanced Functional Materials*, 2008, **18**, 3553–3567.

59 Y. Gao and Z. L. Wang, *Nano Letters*, 2007, **7**, 2499–2505.

60 T. Takenaka, K. Maruyama and K. Sakata, *Japanese Journal of Applied Physics*, 1991, **30**, 2236–2239.

61 P. Singh, H. Borkar, B. P. Singh, V. N. Singh and A. Kumar, *AIP Advances*, 2014, **4**, 0–11.

62 G. H. Haertling, *Journal of the American Ceramic Society*, 1999, **82**, 797–818.

CHAPTER 2

CHEMICALS, SYNTHESIS METHODS, PHYSICAL CHARACTERIZATION, ELECTRODE FABRICATION TECHNIQUES AND ELECTROCHEMICAL CHARACTERIZATION

This section describes the comprehensive information regarding the materials, synthesis method, physical characterization, electrode fabrication technique and electrochemical characterization which are acquired for the study of this present work. To fulfill the research aim, experimental work was performed in the laboratory, followed by physicochemical characterization and investigation of the electrochemical features of the as prepared materials. This chapter explains the experimental evidences including the chemicals and instruments used in the research work. The distinctive materials preparation methods such as hydrothermal, sonochemical, film casting and modified hummers method (used for synthesis of graphene oxide) was used in this study. The elementary materials characterization techniques such as morphology, crystal structure, composition, optical properties and surface area are also discussed. The electrode fabrication, cell assembly, and electrochemical evaluation is explored briefly.

2.1 Chemicals and Equipment's

All chemicals used in this thesis experiments were of analytical-grade, and were used as acquired with-out additional purification. The list of chemicals and solvents utilized in this thesis are given in Table 2.1

Table 2.1 Chemicals and solvents used in this thesis.

Chemicals	Formula	Purity (check)	Supplier
Manganese acetate tetrahydrate	$Mn(CH_2COO)_2.4H_2O$	98%	Daejung Chemicals & Metals Co. Ltd, South Korea
Lithium sulfate	Li_2SO_4	97%	
Copper (II) sulfate pentahydrate	$CuSO_4.5H_2O$	99%	
Thioacetamide	CH_3CSNH_2	99.3%	
Sodium molybdate	$Na_2MoO_4.2H_2O$	98%	
Sodium sulfate	Na_2SO_4	99.9%	
Cupric chloride di-hydrate	$CuCl_2 \cdot 2H_2O$	97%	
Ferrous chloride tetra-hydrate	$FeCl_2 \cdot 4H_2O$	99%	
Thiourea	CH_4N_2S	98%	
Lithium hydroxide	LiOH	98.5%	
Hydrogen peroxide	H_2O_2	30%	
Hydrazine hydrate	$N_2H_4.H_2O$	80%	
N-Methyl-2-pyrrolidone	NMP	99.7%	
Sulphuric acid	H_2SO_4	98%	
Hydrochloric acid	HCl	35%	
Ethylene glycol	$C_2H_6O_2$	98%	
Dimethyl formamide (DMF)	C3H7NO	99.8%	
Graphite powder	C	75%	Sigma Aldrich Ltd, South Korea
Calcium silicide	$CaSi_2$	-	
Polyvinylidene fluoride	PVDF	-	
Sodium selenite	Na_2SeO_3	98%	Alfa Aesar Chemicals, South Korea
Tetraethylammonium tetrafluoroborate	$TEABF_4$	99%	
Carbon black	-	99.5%	

The equipment's used for materials synthesis, characterization and electrochemical measurements are given Table 2.2.

Table 2.2 Equipment's used in the research project

Apparatus	Model or Specification	Manufacturer
Hot-plate & Magnetic stirrer	MS300HS	M TOPS
Autoclave	PTFE container	XI ' AN FENG YU INDUSTRY CO,.LTD
Oven	OF-02 GW	JEIO Tech
Microwave	MW-202BG	LG
Centrifuge	GYROZEN -1580 MG	Gyrozen
Ultrosonicator	SONIC-VCX 500 model (20 kHz, 500 W)	Sonics Materials, Inc.
Ultrasonic cleaner	Elmasonic P 30H	ELMA
Balance	AUW220D	Shimadzu
Electrochemical work station	AUTOLAB PGSTAT302N	Eco Chemie
Keithley Nano voltmeter& picoammeter	2182A & 6485	Keithley
Furnace	CRF-M15	Ceber
Glove box	KK-011AS	Korea Kiyon
Coin-cell crimping and disassembling machine	MSK-160D	MTI, Korea

2.2 Material preparation

The synthesis of nanomaterials with controlled shape and size have captivated more interest for many practical and technological applications. To achieve the research work, the materials were mainly synthesized using following methods such as hydrothermal, sonochemical, and film casting, etc.,

2.2.1 Hydrothermal method

Hydrothermal method is one of the significant approaches among various synthesis method that has many advantages such as low-priced, environmentally friendly, exceptional morphology, and the feasibility of getting high accessible active sites. Hydrothermal method is not restricted to the preparation and growth of traditional and advanced materials but also take a very wide shape, covering numerous interdisciplinary branches of science. This method has been considered as one of the popular promising approaches for preparing nanomaterials with different morphologies and also direct of materials on the substrate[1,2]. The synthesis process utilizes homo- or heterogeneous or metastable precursors in aqueous medium at the pressure more than 1 atm and at the temperature above 100 ℃ and the precursors endure recrystallization of metastable precursors (RMP) reaction because of consequence of temperature and pressure inner of the stainless-steel hydrothermal reactor which results to the formation of crystallize nanostructured materials directly from precursor solution. The reduced graphene oxide, manganese selenide, copper molybdenum sulfide, copper molybdenum sulfide-reduced graphene oxide composite, chalcopyrite, and binder-free Cu_2MoS_4 on Ni foam (CMS/Ni), were prepared through hydrothermal technique as presented in this thesis.

2.2.2 Sonochemical method

Sonochemical process becomes more auspicious in the preparation of various type nanomaterials including nano chalcogenides, and metal oxide nanoparticles[3]. The formation of particle with such properties is due to the chemical-effects of ultrasound raised from acoustic cavitation which results in the evolution, growth, and implosive collapse of bubbles in a liquid medium. The formed implosive collapse of the bubbles produces a confined hotspot via adiabatic compression with passing temperatures of ~4000 K, pressures of 1700 atm, and cooling rates in excess of 1010 K s^{-1}. The sonochemical approach can be more appropriate for the reduction of GO because of the enormous reaction conditions such as excessive pressure,

temperature, and rapid cooling process which allows to a range of chemical reaction usually not accessible in the traditional synthesis processes.

2.2.3. Film casting

The film-casting method is utilized mechanically to manufacture thin flat sheets or films. In film casting and particulate leaching, a polymer is liquified in an organic solvent. Particles, mostly salts, with specific dimensions are then mixed to the solution. The mixture is formed into its final geometry. For instance, it can be cast onto a glass plate or petri-dish to fabricate a membrane or in a three-dimensional mold to create a scaffold. While the solvent dry out, it generates a structure of composite material containing of the particles together with the polymer[4].

2.2.4 Graphene oxide synthesis by modified Hummer's method

Graphene oxide was successfully synthesized from graphite powder using modified Hummer's method[5]. Initially, 2g of graphite powder was stirred in 40 mL H_2SO_4 (98%) for 2 h. After 2 h of stirring, 6 g of $KMnO_4$ was slowly added to the stirring solution in a time period of 1 h. The reaction bath should be maintained at 15 °C during the addition of $KMnO_4$ to reduce the excess heat generation. Followed by addition of $KMnO_4$ the solution is allowed to stir for 1 h and then the subsequent solution was diluted by addition of 90 mL of water. The suspension was additionally reacted by adding 30% H_2O_2 solution (10 mL) and 150 mL of distilled water. The subsequent suspension solution was cleaned by centrifugation process with 5% HCl aqueous solution and after that with DI water until the pH of the final solution became neutral. The obtained GO was obtained by adding 150 mL of DI water to the developing graphite oxide precipitate and were exposed to ultrasound irradiation for 2 h using probe type sonicator for exfoliation of graphitic oxide into a GO monolayer.

2.3. Materials characterization

The as prepared nanomaterials were characterized using various techniques to identify the morphology, microstructure, phase, crystallinity, chemical composition and specific surface area. The comprehensive experimental conditions are given below.

2.3.1. X-ray diffraction (XRD)

X-ray powder diffraction (XRD) is a fast-analytical method mainly used for phase recognition of material and can deliver information on unit cell dimensions. The investigated material is superbly ground, homogenized, and regular bulk composition is determined [6]. The synthesized samples were analyzed by using Rigaku X-ray diffractometer (Rigaku Instruments Co, Tokyo, Japan) and Empyrean X-ray diffractometer instrument (Malvern Panalytical, UK) equipped with Cu-Kα detector (λ = 1.54184 Å) under a voltage of 40 kV and a current of 40 mA with of range 2θ angle of 10-80° with a step of 0.02°.

Figure 2.3.1 Image of X-Ray diffractometer for the powder analysis.

2.3.2. Field-emission scanning electron microscopy (FE-SEM)

The morphology and particle size of the prepared material is very important to investigate the electrochemical reaction and it was easily identified using the Field emission scanning electron microscope (FE-SEM). Here we utilized FE-SEM (TESCAN, MIRA3) coupled with an energy-dispersive x-ray spectroscopy (EDS) analyzer for the morphological and

elemental analysis of prepared sample. The elemental composition of the prepared samples was measured using EDS instrumentation. Prior to analysis, the as-prepared samples were fixed onto a double-sided conducted-tape mounted on a metal stud and coated with platinum using a sputter coater.

Figure 2.3.2 Image of FE-SEM instrument.

2.3.3. Laser Raman spectroscopy

Raman Spectroscopy is a non-damaging physico-chemical analysis procedure which delivers thorough information regarding crystal structure, phase and polymorph, crystallinity and molecular interactions. It is based upon the interface of light with the chemical bonds within a prepared material. Raman is a light scattering measurement technique, by which a molecule scatters upon incident light from an extreme intensity laser light source. Raman spectra for the prepared samples in this thesis were studied using a LabRam HR800 micro Raman spectroscope (manufacturer: Horiba Jobin-Yvon, France). The Raman spectrum was functioned at an excitation wavelength of 514 nm at the different laser power using Ar^{+} ion laser. The spectral region of 100-4000 cm^{-1} was used to collect the data were using an acquisition time of 10 s data point.

Figure 2.3.3 Image of Micro Raman Spectroscopy system.

2.3.4. Fourier transform infrared (FT-IR) spectrometer

The use of Fourier transform infrared (FTIR) spectroscopy has been counted to be one of the most effective techniques to analyze the chemical and surface chemistry in different types solid, liquid or gas. The FT-IR spectra were measured at room temperature with an FT-IR spectrometer (Thermo Scientific Systems, Nicolet- 6700) using KBr palletizer method in the range of 4000 to 400 cm^{-1} [7,8].

Figure 2.3.4 Image of Fourier transform Spectrophotometer system.

2.3.5. X-ray photoelectron spectroscopy (XPS)

X-ray photoelectron spectroscopy (XPS), well-known as electron spectroscopy for analysis the chemical state (ESCA), of a material. XPS can analyze the elemental composition, chemical state, empirical formula, and electronic state of the elements within a material. The X-

ray photoelectron spectroscopy (XPS) techniques using ESCA- 2000, VG Microtech Ltd and Theta Probe AR-XPS system (Thermo Fisher Scientific, U.K) is used to measure the chemical composition and the state of elements present in the outermost part of samples. In XPS a monochromatic X-ray beam source at 1486.6 eV (Aluminum anode at 14 kV) was utilized to scan upon the sample surface. A high flux X-ray source was used for X-ray production, and a quartz crystal monochromatic was used to focus and scan the X-ray beam on the prepared sample surface.

Figure 2.3.5 Image of X-ray photoelectron spectrometer system.

2.3.6. Brunauer, Emmett and Teller (BET) surface area analysis

The nitrogen (N_2) adsorption-desorption isotherm measurement was carried out to find out the pore-volume, pore-size and, surface-area distribution of the as-prepared samples. The Brunauer-Emmett-Teller (BET) analysis was performed with Quantachrome RASiQwin™ c 1994-2012, Quantachrome Instruments v2.02 and nitrogen (N_2) gas was used as an adsorptive for the determination of the above parameters. The surface-area of the prepared samples was calculated by using the multiple-point BET model. The pore size distributions were obtained from the adsorption-desorption isotherm by the Horvath-Kawazae (HK) method. The pore-

volume was calculated from the volume of nitrogen adsorbed at a relative pressure of P/Po =0.95 [9].

2.3.7. UV-Vis spectrophotometer (UV-Vis)

The optical properties of the NPs were analyzed using UV–Vis spectroscopy (UV/VIS/NIR spectrophotometer (Cary 5G)) with a quartz cuvette path length of 1 cm. The data was obtained in the range of wavelength 200 to 850 nm[10].

2.4 Fabrication of electrode

The working electrodes were fabricated via slurry coating method. Briefly, the active material (prepared samples), carbon black, and polyvinylidene difluoride (PVDF) were mixed in an appropriate mass ratio of 80:15:5 or 85:10:5 using N-methyl pyrrolidone (NMP) as solvent and grinded well to form uniform homogeneous paste/slurry. The resulting paste was coated on to the current collector substrate and dried in the oven at 80 °C for 12 h. For hierarchical grow of nanostructures, the active material is directly grown on the Ni foam. The electroactive mass of the active material on the current collector was obtained from the differentiation between the specific-mass of the current collector before and after loading of active material using a dual-range semi microbalance (AUW-220D, Shimadzu) with an estimate to five decimal places[11–13].

2.5 Device fabrication

This study mainly focusses on the improvement of the energy storage performance metrics, we developed the fabrication of symmetric supercapacitor device using aqueous electrolyte and ionic/organic electrolyte[14].

2.5.1 Coin-cell symmetric supercapacitor

The symmetric supercapacitor was assembled in CR2032 coin-cell set-up using active material coated stainless-steel substrates with an area of 1.86/1.54 cm^2 as coated electrodes separated by a Celgard membrane and $TEABF_4$ /AN or $EMIMBF_4$ as the electrolyte[12,15]. The

assembled coin-cell device was crimped using an electric coin cell crimping and disassembling machine (MTI, Korea). Device fabrication and electrolyte handling were performed in glove box with below 1 ppm of moisture and oxygen[13,16].

2.6 Electrochemical characterization

To understand the capacitive nature and calculate the specific capacity, specific capacitance of the fabricated electrodes and devices, cyclic-voltammetry (CV), and galvanostatic-charge/discharge (GCD) and electrochemical impedance spectroscopy (EIS) tests were carried out. All of the electrochemical characterizations were investigated using an AUTOLAB PGSTAT302N electrochemical work station. A classic three-electrode configuration was equipped with a working electrode, platinum served as the counter electrode, Ag/AgCl as reference electrode. Three electrode systems are familiar in basic research where it permits one electrode to be investigated in isolation, without difficulties from the electrochemistry of the other electrodes.

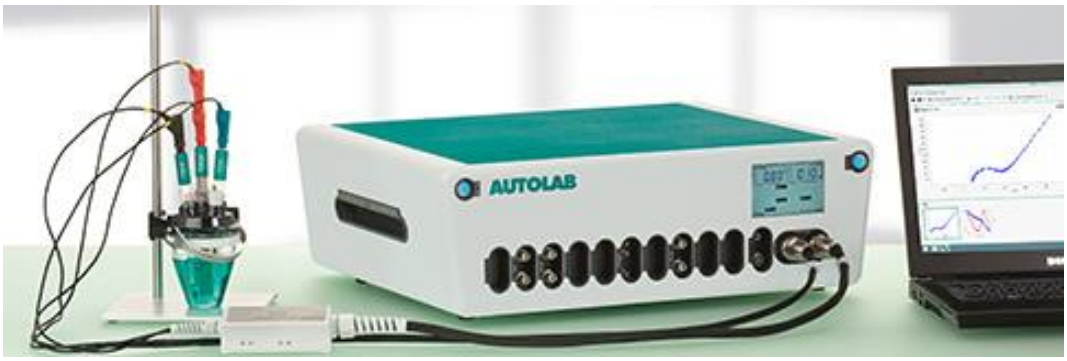

Figure 2.6 Image of Electrochemical work station.

For measuring packaged supercapacitors (two electrode cell configuration), both reference and counter electrode leads are joined to the negative (-) terminal of the capacitor. The working electrode and working sense leads are connected to the positive (+) terminal[13,14].

2.6.1 Cyclic voltammetry (CV)

CV measurement is popularly known to be a suitable tool for evaluating the difference between capacitor type EDLC behaviors, battery like faradaic nature in an electrochemical process. In CV quantifying, the ranges of voltage scan rates have been given from a lower to an upper limit at constant voltage. The evolution of current was measured as voltage function. The characteristics of the linear sweep voltammogram measured depend on a rate of the electron transfer process, chemical reactivity of the electro-active materials and the voltage scan rate. The CV measurement of the electrodes were received by using the changing of scan rates: 5 to 1000 mV s^{-1}.

2.6.2 Galvanostatic charge/discharge (GCD)

The GCD technique are the most essential and direct strategy to investigate the applicability of energy storage devices. A repetitive loop of charge and discharge is denoted as a cycle. Principally, charge-discharge are measured at a single current density until the reach of set potential. The GCD curves were produced at the different current densities.

2.6.3 Electrochemical impedance spectroscopy (EIS)

EIS is a most useful and non-destructive tool to evaluate the capacitive nature and resistance for the surface of the electrode material. This makes the possibility for further electrochemical measurements. EIS is the common method for measuring the equivalent series resistance of energy storage devices. It also permits developing models to annotate, fundamental reaction mechanisms. Using these models, capacitor non-idealities can be found. A sinusoidal alternate current (AC) excitation signal is applied throughout an EIS experiment to the investigated system and AC response is measured. Scanning of frequency in a wide range from lower to higher creates the reaction ways with different rate constants, such as charge transfer, mass transport, and chemical reaction. In the study, EIS experiment for prepared electrodes was conducted between the frequency ranges of 0.1 Hz or 0.01 Hz and 100 kHz. Nyquist plot was

used to analyze the data and, are the plotted with the real component (Z′) against imaginary part (-Z′′) which show the response of frequency for the electrode/electrolyte system[19].

2.6.4. Calculation of electrochemical parameters

The electrochemical criterions, such as the specific capacitance, energy density (E), Coulombic efficiency (η), and power density (P) are important criterions for the analysis of the capacitive behavior of electrochemical cells.

2.6.4.1 Determination of specific capacitance from CV analysis:

The specific capacitance was calculated from the CV profiles using the relation[20]:

$$C_G = [\int IdV / (s \times \Delta V \times M)] \quad \text{..... (1)}$$

$$C_A = [\int IdV / (s \times \Delta V \times A)] \quad \text{..... (2)}$$

Here "C_A and C_G" represents the specific areal capacitance (F cm^{-2}) and gravimetric capacitance (F g^{-1}), "∫ IdV" is the integral area, "s" is the scan rate, "A" is the area of the electroactive material, "M" is the electroactive mass, and "ΔV" is the potential window.

2.6.4.2 Determination of specific capacitance from GCD analysis:

The specific capacitance was calculated from the GCD profiles using the relation[21,22]:

$$C_A = (I \times T_d) / (A \times \Delta V) \quad \text{..... (3)}$$

$$C_G = (I \times T_d) / (M \times \Delta V) \quad \text{..... (4)}$$

Here "C_A and C_G" represents the specific areal capacitance (F cm^{-2}) and gravimetric capacitance (F g^{-1}), "I" is the discharge current, "T_d" is the time required for discharge, "A" is the area of the electroactive material, "M" is the electroactive mass, and "ΔV" is the potential window.

2.6.4.3 Determination of Columbic efficiency (η%), Energy and power density:

The energy and power density are calculated in terms of using the relations given below[23]:

$$\eta\% = T_d / T_c \times 100 \quad \text{..... (5)}$$

$$E = [C \times \Delta V^2] / 2 \text{..... (6)}$$

$$P = E / T_d \text{ ..... (7)}$$

Here “E” and “P” are the energy-density and power-density of the device, “C” is the specific capacitance, “ΔV” is the potential window, and “T_c” is the charging time and “T_d” is the discharge time

2.6.4.4 Determination of specific capacitance from EIS analysis:

The specific capacitance with respect to applied frequency found from the EIS analysis using the relation[24]:

$$C = 1/ (2\pi f z'') \text{……..……(8)}$$

Here “C” is the specific capacitance of the supercapacitor device, and “f” is the applied frequency, and “z″” is the imaginary part of impedance.

2.6.4.5 Determination of real and imaginary components of capacitance from EIS analysis

The variability of real and imaginary capacitance with concerning to the applied range of frequencies was obtained using the relation (9) and (10) respectively[24,25]:

$$C'_\omega = -Z''_\omega /(\omega|Z_\omega|^2) \text{……..… (9)}$$

$$C''_\omega = Z'_\omega /(\omega|Z_\omega|^2) \text{……..… (10)}$$

Here, “C'_ω” and “C''_ω” represents the real and imaginary components of capacitance that resembles to the stored-energy and irreversible energy-loses, respectively.

2.7 References:

1 C. Burda, X. Chen, R. Narayanan and M. A. El-Sayed, *Chemical Reviews*, 2005, **105**, 1025–1102.

2 B. L. Cushing, V. L. Kolesnichenko and C. J. O’Connor, *Chemical Reviews*, 2004, **104**, 3893–3946.

3 K. Krishnamoorthy, G.-S. Kim and S. J. Kim, *Ultrasonics Sonochemistry*, 2013, **20**, 644–649.

4 P. LeBaron, *Applied Clay Science*, 1999, **15**, 11–29.

5 K. Krishnamoorthy, M. Veerapandian, K. Yun and S.-J. Kim, *Carbon*, 2013, **53**, 38–49.

6 K. M. Deen and E. Asselin, *Electrochimica Acta*, 2016, **212**, 979–991.

7 Y. Bormashenko, R. Pogreb, O. Stanevsky and E. Bormashenko, *Polymer Testing*, 2004, **23**, 791–796.

8 P. Martins, A. C. Lopes and S. Lanceros-Mendez, *Progress in Polymer Science*, 2014, **39**, 683–706.

9 D. J. K. Ross and R. Marc Bustin, *Marine and Petroleum Geology*, 2009, **26**, 916–927.

10 L. Wu, J. C. Yu and X. Fu, *Journal of Molecular Catalysis A: Chemical*, 2006, **244**, 25–32.

11 P. Pazhamalai, K. Krishnamoorthy, M. S. P. Sudhakaran and S. J. Kim, *ChemElectroChem*, 2017, **4**, 396–403.

12 G. K. Veerasubramani, K. Krishnamoorthy, P. Pazhamalai and S. J. Kim, *Carbon*, 2016, **105**, 638–648.

13 K. Krishnamoorthy, P. Pazhamalai and S. J. Kim, *Energy and Environmental Science*, 2018, **11**, 1595–1602.

14 P. Pazhamalai, K. Krishnamoorthy, V. K. Mariappan, S. Sahoo, S. Manoharan and S. J. Kim, *Advanced Materials Interfaces*, , DOI:10.1002/admi.201800055.

15 S. Sahoo, K. Krishnamoorthy, P. Pazhamalai, V. K. Mariappan, S. Manoharan and S.-J. Kim, *Journal of Materials Chemistry A*, 2019, **7**, 21693–21703.

16 G. K. Veerasubramani, K. Krishnamoorthy and S. J. Kim, *RSC Adv.*, 2015, **5**, 16319–16327.

17 D. P. Dubal, N. R. Chodankar, D. H. Kim and P. Gomez-Romero, *Chemical Society Reviews*, 2018, **47**, 2065–2129.

18 G. A. Muller, J. B. Cook, H.-S. Kim, S. H. Tolbert and B. Dunn, *Nano Letters*, 2015, **15**, 1911–1917.

19 K. Krishnamoorthy, P. Pazhamalai, G. K. Veerasubramani and S. J. Kim, *Journal of Power Sources*, 2016, **321**, 112–119.

20 P. Pazhamalai, K. Krishnamoorthy, S. Sahoo and S.-J. Kim, *Journal of Alloys and Compounds*, 2018, **765**, 1041–1048.

21 K. Krishnamoorthy, P. Pazhamalai, S. Sahoo and S.-J. Kim, *Journal of Materials Chemistry A*, 2017, **5**, 5726–5736.

22 K. Krishnamoorthy, P. Pazhamalai and S.-J. Kim, *Energy & Environmental Science*, 2018, **11**, 1595–1602.

23 P. Pazhamalai, K. Krishnamoorthy, V. K. Mariappan and S.-J. Kim, *Journal of Industrial and Engineering Chemistry*, 2018, **64**, 134–142.

24 P. Pazhamalai, K. Krishnamoorthy, V. K. Mariappan and S.-J. Kim, *Journal of Colloid and Interface Science*, 2019, **536**, 62–70.

25 K. Krishnamoorthy, P. Pazhamalai and S. J. Kim, *Electrochimica Acta*, 2017, **227**, 85–94.

CHAPTER – 3

Hydrothermally prepared α-MnSe nanoparticles as a new pseudocapacitive electrode material for supercapacitor

Highlights

- Transition metal chalcogenides become emerging materials as electrodes for electrochemical energy storage devices.
- In this study, we are reporting the preparation of α-MnSe nanoparticles using a one-pot hydrothermal method and examined its use as an electrode material for supercapacitors. Physico-chemical characterizations such as X-ray diffraction, laser Raman, and field emission scanning electron microscopic analyses revealed the formation of α-MnSe nanoparticles.
- The electrochemical analysis such as cyclic voltammetry and electrochemical impedance spectroscopy suggested the mechanism of charge-storage is due to the pseudocapacitive nature of α-MnSe electrode.
- The α-MnSe electrode delivered a specific capacitance of 96.76 F g^{-1} from galvanostatic charge-discharge obtained at a constant current density of 0.1 mA cm^{-2} with a corresponding energy density of 8.60 Wh kg^{-1} and better cyclic stability over 2000 cycles.
- Further, the electrochemical performance of the α-MnSe symmetric supercapacitor device shows that the specific capacitance of the device is about 23.44 F g^{-1} at a current density of 0.1 mA cm^{-2}, with a potential window of 0.8 V.

3.1. Introduction

Among energy storage devices, electrochemical capacitors or supercapacitors show superior characteristics, including high-power densities (> 10 kW kg^{-1}), fast charging/discharging (within seconds), and long cyclic stabilities (> 10^5 cycles) [1,2]. These properties make supercapacitors a promising candidate for powering applications in portable electronic devices and electric vehicles [3]. An increasing focus on reducing inefficient use of conventional non-renewable energy resources has led to substantial interest in electrode materials that demonstrate excellent energy storage performance, through either ion adsorption/desorption (electric double layer capacitor, EDLC) or fast faradic redox reactions (pseudocapacitors) [4]. EDLC uses carbon-based electrodes such as graphene, activated carbon, carbon nanotubes, and carbon nanodots which store charge via electrostatic adsorption and desorption of ions at the electrode surface but are limited by low specific capacitance[5]. Pseudocapacitors utilizes the advantages of fast faradic redox reactions using transition-metal-oxide, metal chalcogenides, and conducting-polymer-based electrode materials which exhibit higher specific capacitances than EDLC [6]. In recent years, transition metal chalcogenides have emerged as high-performance electrode materials compared to transition metal hydroxides/oxide due to their relatively high electrical conductivity, multiple available oxidation states, which promote rapid redox reactions and excellent electrochemical properties [7,8]. Therefore, transition metal chalcogenides are considered as a potential candidate for high-performance electrode materials for energy storage devices [9,10].

Selenium (Se)-based electroactive materials have attracted considerable attention for electrochemical hydrogen evolution and storage, fuel-cell catalysts, batteries, and supercapacitors [11,12]. Selenium is in Group VI of the periodic table, along with sulfur and oxygen, which demonstrates superior metallic and electrical properties compared to sulfur and oxygen.

The electrical conductivity of Se (1×10^{-3} S m^{-1}) is much greater than that of sulfur (5×10^{-28} S m^{-1}) [13] and demonstrating excellent supercapacitive properties than sulfur [14]. Wang et al. synthesized $GeSe_2$ by chemical vapor deposition (CVD) and investigated their supercapacitive properties (300 F g^{-1} at 1 A g^{-1}) [15]. Zhang et al. prepared SnSe nanosheets as an electrode for energy storage applications (228 F g^{-1} at 0.5 A g^{-1}) using a high-temperature refluxing process[16]. Marri et al. prepared a VSe_2-RGO composite using a hydrothermal method that exhibits a high specific capacitance of 680 F g^{-1} [17]. Patil et al. electrodeposited selenium thin films on a stainless steel substrate for supercapacitor applications (29.25 F g^{-1} at 5 mV s^{-1}) [18]. Patil et al. also reported the supercapacitive properties of La_2Se_3 nanoflakes prepared by chemical-bath deposition (331 F g^{-1} at 5 mV s^{-1}) [19]. Mn-based oxides, hydroxides, and sulfide materials have been used as the pseudocapacitive electrode materials due to their superior electrochemical behavior, low cost, and low environmental toxicity [20]. Chodankar et al. investigated the electrochemical behavior of MnO_2 thin films prepared via chemical bath deposition for supercapacitor (643 F g^{-1} at 5 mV s^{-1}) [21]. Anandan et al. synthesized $Mn(OH)_2$ using the sonochemical method and reported a specific capacitance of 127 F g^{-1} for the electrode material [22]. Pujari et al. prepared MnS by chemical bath deposition and proposed its application towards supercapacitor application (747 F g^{-1} at 1 mA cm^{-2}) [23]. Hence, transition metal selenides, composed of Mn and Se, can provide efficient transport of ions and electrons leading to excellent electrochemical performance. Manganese selenide (MnSe) is a low-cost semiconducting and eco-friendly material with applications in lithium storage and oxygen reduction catalysis [24,25]. However, there have been no reports on the electrochemical investigation of manganese selenide. Hence, in this study, we synthesized α-MnSe nanoparticles via the one-step hydrothermal method and investigated their electrochemical performances via three-electrode and two-electrode configuration for supercapacitor applications.

3.2. Experimental section

3.2.1. Materials

Manganese acetate tetrahydrate ($Mn(CH_2COO)_2.4H_2O$), hydrazine monohydrate ($N_2H_4.H_2O$), N-methyl pyrrolidone (NMP), and lithium sulfate (Li_2SO_4) were purchased from Daejung Chemicals Ltd., South Korea. Sodium selenite (Na_2SeO_3) and carbon black were purchased from Alfa Aesar, South Korea. Polyvinylidene fluoride (PVDF) was purchased from Sigma Aldrich, South Korea.

3.2.2. Preparation of manganese selenide (α-MnSe) nanoparticles

A one-pot hydrothermal method was used for the preparation of α-MnSe nanoparticles using manganese acetate and sodium selenite as a starting precursor. Briefly, manganese acetate (0.196 g) and sodium selenite (0.069 g) precursors were taken in the molar ratio of 2:1 and dissolved in 60 mL of double distilled water using magnetic stirring. Then, an appropriate amount of hydrazine hydrate was added to the above solution, and the resulting mixture was transferred to a 100 mL stainless steel autoclave and kept at 180 ℃ for 24 h. After completion of the reaction, the autoclave was then left to cool naturally to room temperature, and the precipitates were collected by centrifugation using water and ethanol. The centrifugation process was repeated until the removal of any residues, and the final precipitate was allowed to dry at 60 ℃ in a hot air oven for overnight.

3.2.3. Instrumentation

The crystalline nature and phase purity of the prepared α-MnSe sample were obtained using a Rigaku X-ray diffractometer instrument at 40 kV and 40 mA with Cu-Kα radiation (λ = 1.54184 Å). The Raman spectrum for the α-MnSe sample was measured on a LabRam HR

Evolution Raman spectrometer (Horiba Jobin-Yvon, France) with a laser excitation source of wavelength 514 nm and laser power of 10 mW. The surface morphology of the as-prepared α-MnSe was analysed using field-emission scanning electron microscopy (FE-SEM; JSM-6700F, JEOL Ltd.) under different magnifications.

3.2.4. Electrochemical analysis of α-MnSe nanoparticles

The working electrode was prepared using the slurry coating method as reported in our earlier works [26]. Briefly, the working electrode was prepared by grinding the active material α-MnSe nanoparticles (40 mg), conductive filler carbon black (7.5 mg), and binder PVDF (2.5 mg) in the weight ratio of 80:15:5 with an appropriate amount of NMP solvent in an agate-mortar until a uniform slurry was obtained. Then, the as-prepared slurry was coated on a pre-cleaned stainless-steel substrate (1×1 cm^2) and allowed to dry at 60 °C in an oven overnight. The electrochemical performance of the α-MnSe electrode was tested in a three-electrode and two-electrode (symmetric supercapacitor device) configuration on an Autolab PGSTAT302 N workstation (Metrohm Autolab) using an aqueous solution of 1M Li_2SO_4 as the electrolyte. Electrochemical characterizations such as cyclic voltammetry (CV), galvanostatic charge-discharge (CD), and electrochemical impedance spectroscopy (EIS) were carried for the α-MnSe electrode both in three-electrode and two electrode configuration. For the three-electrode configuration, α-MnSe is used as the working electrode, platinum as the counter electrode, and Ag/AgCl as the reference electrode. The symmetric device was fabricated by sandwiching polypropylene separated in between two α-MnSe electrodes. The mass of the active material loaded onto the stainless-steel substrate was measured to be 0.85 mg. The specific capacitance (C_{sp}) from CV and CD analyses using the following relations [27,28]**:**

$$C_{sp} = [(\int IdV) / (s \times \Delta V \times m)] \quad \text{.....(1)}$$

$$C_{sp} = [(I \times \Delta t) / (\Delta V \times m)] \ldots\ldots\ldots\ldots\ldots\ldots\ldots\ldots \quad (2)$$

Here, "$\int IdV$" is the integral area under the CV curve, "*m"* is the mass of the electrode, "*s"* is the scan rate, "*I" is* the discharge current and "ΔV*"* is the potential window, and "Δt*"* is the discharge time. The energy density (*E*) and power density (*P*) of the α-MnSe electrode and device were calculated using the relations [26]:

$$E = (I \times \Delta t \times \Delta V) / (7.2 \times m) \ldots\ldots\ldots\ldots\ldots\ldots\ldots (3)$$

$$P = (3.6 \times E) / \Delta t \ldots\ldots\ldots\ldots\ldots\ldots\ldots\ldots\ldots\ldots (4)$$

3.3. Results and discussion:

This study employed a facile hydrothermal method for the synthesis of α-MnSe nanoparticles using Na_2SeO_3 as the Se source, $Mn(CH_2COO).4H_2O$ as Mn source and $N_2H_4.H_2O$ as the reducing agent. The possible chemical reactions occurring in the formation of α-MnSe nanoparticles during the hydrothermal reaction are [29,30]:

$$Na_2SeO_3 + Mn^{2+} \rightarrow 2Na^{2+} + MnSeO_3 (\downarrow) \ldots\ldots\ldots\ldots (5)$$

$$MnSeO_3 \leftrightarrow Mn^{2+} + SeO_3^{2-} \ldots\ldots\ldots\ldots\ldots\ldots\ldots (6)$$

$$SeO_3^{2-} + N_2H_4 \rightarrow Se (\downarrow) + N_2 (\uparrow) + H_2O + 2OH^- \ldots\ldots\ldots (7)$$

$$3Se + 6OH^- \rightarrow 2Se^{2-} + SeO_3^{2-} + 3\ H_2O \ldots\ldots\ldots\ldots\ldots (8)$$

$$Se^{2-} + Se + Mn^{2+} \rightarrow MnSe_2 (\downarrow) \ldots\ldots\ldots\ldots\ldots\ldots\ldots (9)$$

$$Se^{2-} + Mn^{2+} \rightarrow MnSe (\downarrow) \ldots\ldots\ldots\ldots\ldots\ldots\ldots\ldots (10)$$

Figure 3.1(a) shows X-ray diffraction (XRD) pattern for the as-prepared α-MnSe material which confirms that the hydrothermally prepared sample corresponds to a face-centered cubic phase of α-MnSe and in good agreement with the standard diffraction pattern of α-MnSe (JCPDS No: 73-1741) with the space symmetry group *Fm3m*. The obtained diffraction peaks can be assigned to the characteristic peaks of face-centered cubic α-MnSe without any impurities

(e.g., Mn_3O_4, MnS or SeO). The sharp diffraction peaks at 2θ = 28.39, 32.90, 47.21, 56.02, 58.74, 68.99, 76.22, 78.58, and 87.84° correspond to the diffraction planes (111), (200), (220), (311), (222), (400), (331), (420), and (422), respectively with high degree of crystallinity. The laser Raman spectrum was used to investigate the vibrational and rotational modes of the material. Figure 3.1(b) shows a typical Raman spectrum of the α-MnSe nanoparticles. The sharp and strong peak located at ~ 636 cm^{-1} can be assigned to the Mn-Se stretching mode and in close agreement with previous studies on manganese based metal chalcogenides systems [31,32]. FE-SEM measurements were performed to investigate the surface morphologies of the α-MnSe and shown in Figure 3.1 (c, and d). FE-SEM micrograph shown in Figure 3.1(c) depicts the formation of MnSe nanoparticles as a result of the hydrothermal reaction. The high-resolution FE-SEM micrograph (Figure 3.1(d)) revealed that the formed MnSe nanoparticles having an average size distribution in the range of 20–30 nm.

The electrochemical performance of the α-MnSe nanoparticles was initially investigated using the three-electrode configuration in an aqueous solution containing 1 M Li_2SO_4 as the electrolyte. Figure 3.2(a and b) shows the CV profiles of the α-MnSe electrode obtained at a scan rate of 1 mV s^{-1} and with different scan rates from 5 to 100 mV s^{-1}, respectively within the potential range of 0.0 to 0.8 V. To understand the mechanism of charge storage in detail, the CV profiles were measured in a range of 0.2 V potential window as shown in Figure 3.2(a) which highlights the contribution of capacitive current in the range of 0.1 to 0.7 V whereas the presence of pseudocapacitive current has been observed in the range of 0.0 to 0.1 V, and 0.7 to 0.8 V.

Figure 3.2(b) shows the CV profiles recorded using different scan rate from 5 to 100 mV s^{-1}. It shows the presence of typical rectangular shaped curves at a scan rate of 5 mV s^{-1} and the shape of the CV curves is distorted little with an increase in scan rate from 5 to 100 mV s^{-1}

which might be due to the limited diffusion of electrolyte ions into the electroactive surface of the MnSe electrode [33].

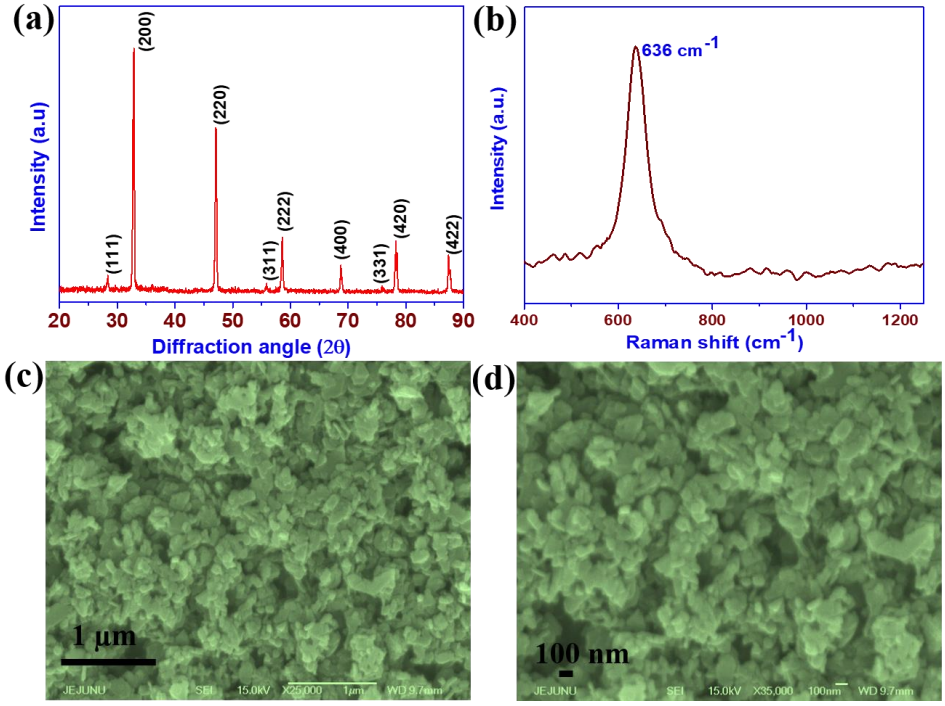

Figure 3.1 (a) X-ray diffraction pattern of α-MnSe and (b) laser Raman spectrum of α-MnSe. Field emission scanning electron micrographs of α-MnSe nanoparticles measured at different magnifications (c) 1 µm and (d) 100 nm.

Future studies using *in-situ* X-ray photoelectron spectroscopic analysis are needed to elucidate for understanding the transition of the oxidation state of Mn in the electrode material [34,35]. Further, there are no noticeable redox peaks obtained in the CV profiles measured at different scan rates, thus, indicating that the α-MnSe electrode is electrochemically charged and discharged at a pseudoconstant rate over the complete CV cycle [6,33].

To understand the fundamental charge-transfer behavior and capacitive nature of the α-MnSe electrode, EIS measurements were performed in the frequency range of 0.01 Hz–100 kHz at an amplitude of 10 mV with different fixed electrode potentials and the results are analyzed using Nyquist and Bode plots as given in Figure 2(c and d). The Nyquist plot indicates the

presence of a small semicircle in the high-frequency region (resistive part) and a straight line in the low-frequency region (capacitive part) [6]. The inset of Figure 2(c) shows an equivalent circuit model fitted using NOVA software which shows the presence of three resistive components (such as solution resistance (R_s), charge-transfer resistance (R_{ct}), and leakage resistance (R_L) with the presence of Warburg and two constant phase elements (CPE) [36]. The presence of two CPEs in the equivalent circuit model is due to the surface capacitive nature of the electrode and the semi-infinite transport of ions diffusion kinetics [2,37]. There are no significant changes observed in the solution resistance of the α-MnSe electrode measured at different potentials whereas the charge-transfer resistance decreases with an increase in potential suggesting the potential dependent charge-transfer process according to the classical equality [38,39]. The increase in potential from 0 to 0.8 V shows a clear deviation in the Warburg line, and the electrode is capacitive over the potential from 0.2 to 0.6 V since the Warburg line is moving closer to the imaginary axis whereas the α-MnSe electrode shows pseudocapacitive nature with potential of 0 and 0.8 V. This finding agrees with the previous finding of pseudocapacitive nature of CeO_2 [37]. The similar behavior is also observed in Bode phase angle plots shown in Fig. 2(d). The phase angle obtained at the tail of 0.0, 0.2,0.4,0.6, 0.8 V electrode potentials are found to be 62.74°, 71.72°, 72.74°, 76.84° and 67.51° which indicates the presence of pseudocapacitive nature in α-MnSe electrode at the potential of 0 and 0.8 V. This finding is in close agreement with the CV profiles shown in Figure 3.2(a).

Galvanostatic CD profiles were obtained at different current densities for the α-MnSe electrode in the same potential range of 0.0 to 0.8 V to further examine the charge storage mechanism and behavior. Typical CD curves of the α-MnSe electrode measured at a different constant current density of 0.1 to 1.0 mA cm^{-2} (Figure 3.3(a)) shows the symmetric triangular-shaped curves indicate the good capacitive nature of α-MnSe electrode. The linear CD

characteristic was retained in the CD profiles obtained at different current densities for the α-MnSe electrode. Figure 3.3(b) shows the corresponding specific capacitance as a function of current density for the α-MnSe electrode in which the specific capacitance is decreasing with increasing current density which is due to the time constraints faced by the electrolyte ions to effectively utilize the electrode material at higher current density [40,41]. A specific capacitance of about 96.76 F g^{-1} was obtained from the CD profile at a current density of 0.1 mA cm^{-2}, higher than recently reported electrode materials, as shown in Table 3.1 [42–46].

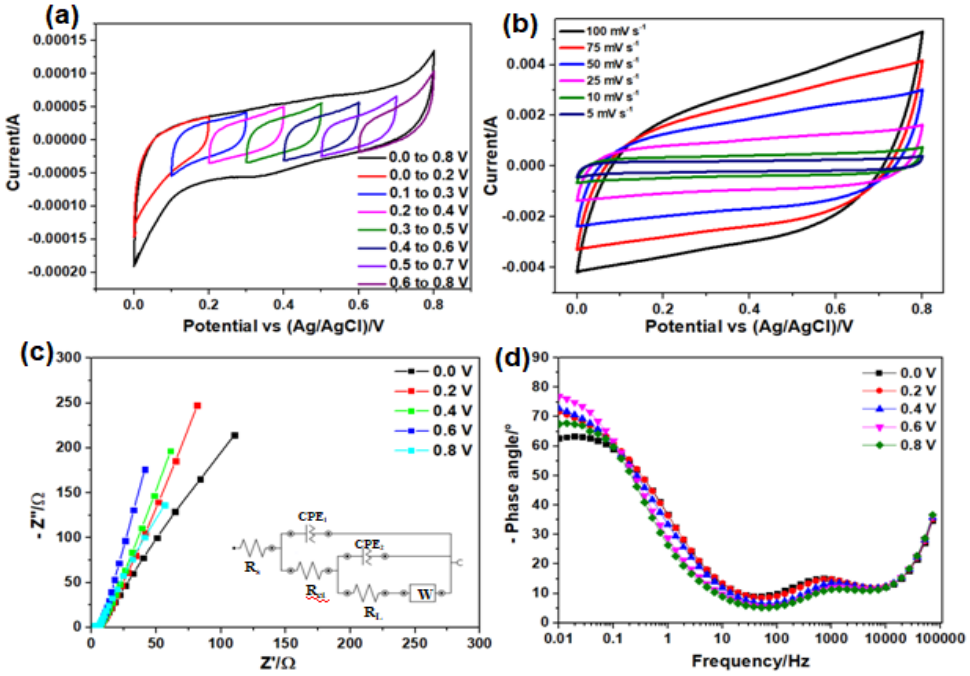

Figure 3.2 (a) Cyclic voltammetric profile of α-MnSe electrode measured at low scan rate (1 mV s^{-1}), (b) cyclic voltammetric profiles measured at different scan rates ranging from 5 to 100 mV s^{-1}), (c) Nyquist plot and (d) Bode phase angle plot. This data was obtained using three-electrode configuration.

The observed increase in R_{ct} of 1.9 Ω after cyclic tests are still is low compared with the recently reported literature [41,47]. The excellent electrochemical performance and cyclic stability of α-MnSe electrode are due to (a) fast reaction and ionic diffusion kinetics of nano-sized particles of α-MnSe, and (b) the well-crystallized nanoparticles and the structural robustness of

α-MnSe nanoparticles. Figure 3.3(d) shows the Ragone plot for the α-MnSe electrode, and indicates an energy density of the electrode of about 8.60 Wh kg^{-1}, with a corresponding power density of about 47.05 W kg^{-1} at a constant discharge current density of 0.1 mA cm^{-2}.

Figure 3.3(c) shows the long-term cyclic stability performance of the α-MnSe electrode measured using CD analysis at a constant current density of 2 mA cm^{-2} over 2,000 cycles. The specific capacitance of the α-MnSe electrode increased slightly (103.40%) after 2,000 cycles, possibly due to late activation of the electrode material and better contact between the electrolyte and electrode [40]. Figure 3.3(c) inset displays the FESEM micrograph of the electrode before and after cyclic stability. The FESEM micrograph after 2000 cycles revealed that there is very less aggregation of nanoparticles. The inset of Figure 3.3(d) shows Nyquist plots for the α-MnSe electrode before and after cyclic stability test which showed an increase in the charge-transfer resistance from 9 to 10.9 Ω for the α-MnSe electrode after 2000 continuous CD cycles. The observed slight increase in the charge-transfer resistance (R_{ct}) is mainly due to the late activation process of electrolyte ions onto the interior surface of the α-MnSe electrode leading to a better diffusion channel during prolonged cycles [48].. The energy density of the α-MnSe electrode was higher than the reported energy density values of other electrode materials, such as chemically activated carbon (8.5 Wh kg^{-1}) [49], RuO_2 (4.6 Wh kg^{-1}) [50], carbon microspheres (4.89 Wh kg^{-1}) [51], single-walled carbon nanotubes (7 Wh kg^{-1}) [52], and ultrafine CuS nanoneedles (4.22 Wh kg^{-1}) [53].

To further investigate practical applications, the electrochemical performance of α-MnSe nanoparticles in symmetric devices is performed, which provides a real indication of electrode material properties [26,54]. Therefore, symmetric supercapacitor device was fabricated using the α-MnSe electrode, separated using polypropylene separator in an aqueous solution of 1 M Li_2SO_4 as the electrolyte. Figure 3.4(a) shows the CV profile of the symmetric α-MnSe symmetric device recorded at a constant scan rate of 5 mV s^{-1}, which represent the ideal

capacitive behavior of the α-MnSe symmetric supercapacitor device. Similarly, the CV profile of the α-MnSe symmetric device measured at different scan rates in the range 2.5 to 100 mV s^{-1} over the potential range 0.0 to 0.8 V is shown in Figure 3.4(b). The CV curves of the α-MnSe symmetric device exhibited a typical rectangular behavior, suggesting that the mechanism of charge storage can be attributed to the presence of a pseudocapacitive nature, as in a MnO_2 symmetric cell [55]. The shape of the CV profiles was symmetric even at high scan rates, indicating the high reversibility of the α-MnSe symmetric device. Figure 3.4(c) shows the effect of scan rate on the specific capacitance of the α-MnSe symmetric device. The optimum specific capacitance observed in the α-MnSe symmetric device was 21.69 F g^{-1}. The Nyquist plot of the as-fabricated α-MnSe device is shown in Figure 3.4(d), elucidates that the presence of solution resistance (R_s = 0.46 Ω), charge transfer resistance (R_{ct} = 123 Ω), and the Warburg line in the low-frequency region which is due to the diffusive resistance of electrolyte ions within the α-MnSe symmetric device.

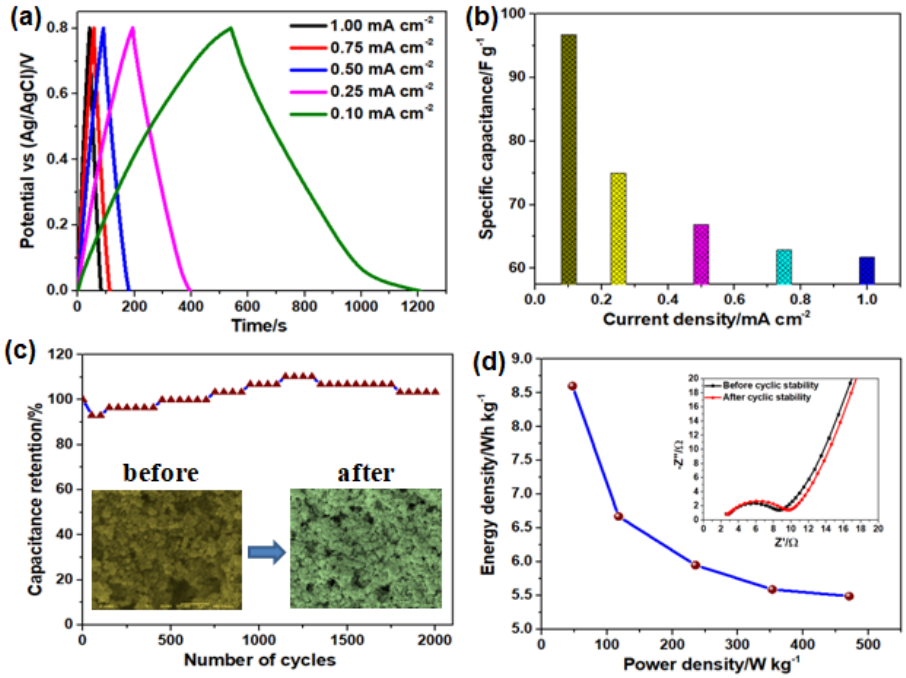

Figure 3.3 (a) Charge-discharge profile of α-MnSe electrode measured at different current densities, (b) effect of current density on the specific capacitance of α-MnSe electrodes, and (c) the cyclic stability test of α-MnSe electrodes over 2000 cycles and the inset shows the FESEM image of electrode before and after electrochemical performance, and (d) Ragone plot of α-MnSe electrodes (data obtained using half-cell configuration) and inset shows the Nyquist plot before and after cyclic stability.

Figure 3.5(a) shows the CD profile of the α-MnSe symmetric device at a constant current density of 0.5 mA cm^{-2}, and shows the linear region of constant slope in the potential range, indicating capacitive behavior [54]. The galvanostatic CD curves for the α-MnSe symmetric device at different current densities (0.1 to 1 mA cm^{-2}) are shown in Figure 3.5(b). During the beginning of discharge cycle, there is the existence of ohmic drop or IR drop about 0.07 V (at a current density of 0.1 mA cm^{-2}) for the symmetric device. The observed ohmic drop value gradually decreases with a decrease in current density. The ohmic drop arises due to the internal resistance of the active electrode material and the contact resistance between the electrode and electrolyte solution [56].

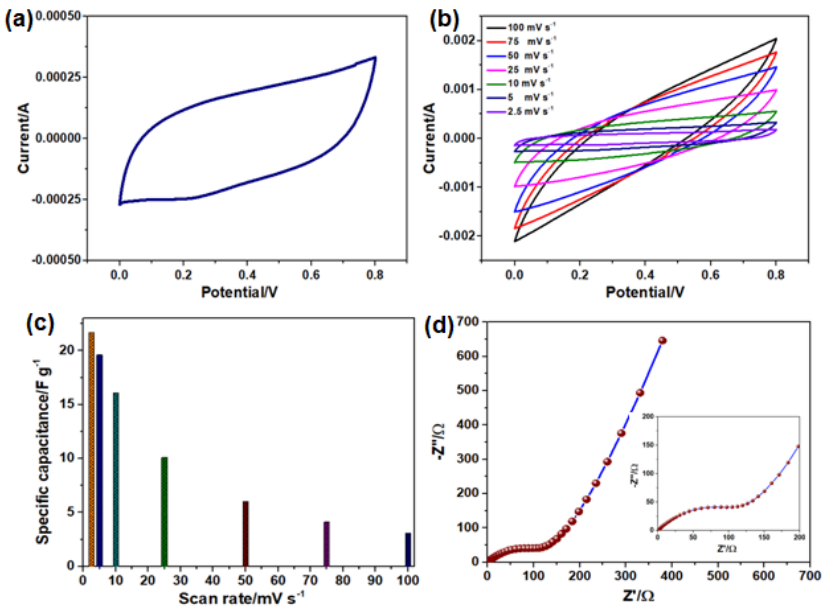

Figure 3.4. Electrochemical performance of α-MnSe based symmetric supercapacitor device (a) cyclic voltammetric profile measured at low scan rate (5 mV s^{-1}), (b) cyclic voltammetric profiles at different scan rates, (c) effect of scan

rate on the specific capacitance of α-MnSe symmetric supercapacitor device, and (d) Nyquist plot of α-MnSe symmetric supercapacitor device. The inset shown in Figure 3.4 (d) represents the enlarged portion of the Nyquist plot of the α-MnSe device in the high-frequency region.

The effect of current density on the specific capacitance of the fabricated α-MnSe symmetric device is summarised in Figure 3.5(c). The device delivered the highest specific capacitance of 23.44 F g^{-1} at a current density of 0.1 mA cm^{-2}. The acquired specific capacitance of the α-MnSe symmetric device was higher than that reported in previous work on hydrothermally prepared $ZnCo_2O_4$ nanorods on Ni wire (10.9 F g^{-1}) [57], carbon nanofibers (3.5 F g^{-1}) [58], RuS_2 (17 F g^{-1}) [26], TiS_2 (4.6 F g^{-1}), and $MoSe_2$ (2.57 F g^{-1}) [59]. To evaluate the supercapacitor performance of the symmetric cell, the typical Ragone plot for a α-MnSe symmetric device for different current densities is shown in Figure 3.5(d). The α-MnSe symmetric device delivered the highest energy density of 2.08 Wh kg^{-1} at a corresponding power density of 25 W kg^{-1}, measured at a constant current density of 0.1 mA cm^{-2}. The active material here provides a unique structure that should be investigated further in future energy storage study. The synergistic effect of a novel structure and a metal selenide containing both manganese and selenium can provide efficient transport of ions and electrons leading to excellent electrochemical performance for next-generation energy storage devices.

Table 3.1 Summary of electrochemical performances of the α-MnSe electrode and recently reported electrode materials using three-electrode configurations.

Material	**Preparation method**	**Specific capacitance/ F g^{-1}**	**Reference**
ZnS	Solvothermal	32.8	[42]
Graphdiyne	Cross-coupling reaction	71.4	[43]
WS_2	Chemical exfoliation	40	[44]

Thermally reduced graphene	Thermal expansion	47.5	[45]
MoS_2	Mechanical delamination	89.02	[46]
α-MnSe	Hydrothermal	96.76	This work

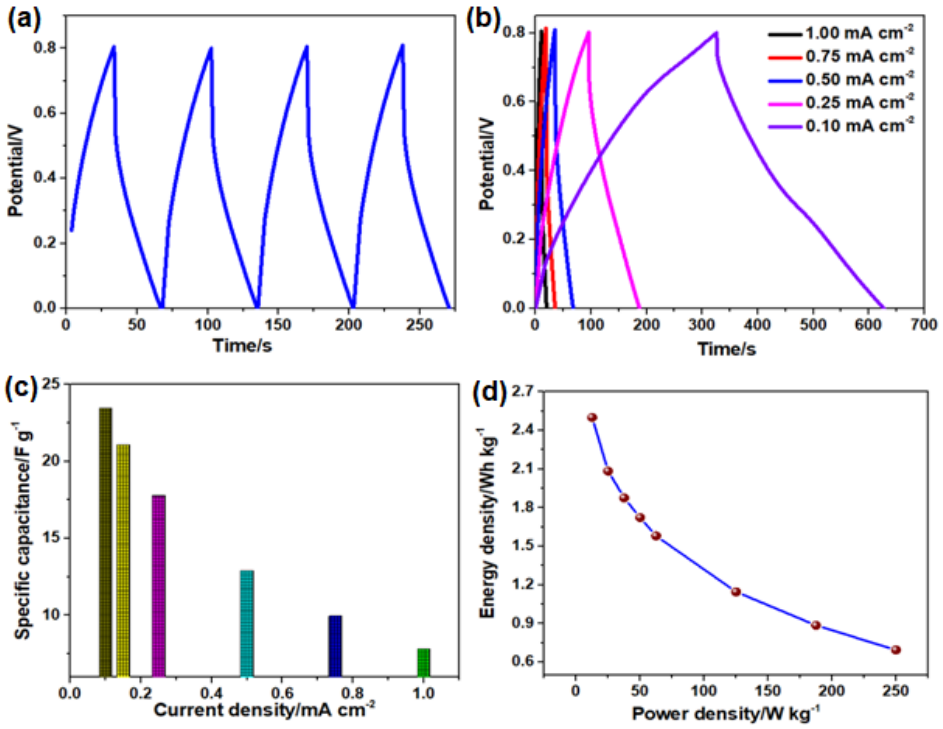

Figure 3.5 (a) Charge-discharge profile of α-MnSe symmetric supercapacitor device measured at a constant current density of 0.5 mA cm^{-2}, (b) charge-discharge profiles measured at different current densities, (c) effect of current density on specific capacitance of α-MnSe symmetric supercapacitor device and (d) Ragone plot of α-MnSe symmetric supercapacitor device.

3.4. Conclusions

In conclusion, we successfully prepared α-MnSe nanoparticles using a facile hydrothermal method and investigated their performance as a supercapacitor electrode using a

three-electrode configuration and symmetric device. In the three-electrode configuration, the CV curves are broadly rectangular in shape, indicating the pseudocapacitive nature of α-MnSe, similar to that of MnO_2. CD analysis showed that the α-MnSe electrode possessed a high specific capacitance of 96.76 F g^{-1} at a current density of 0.1 mA cm^{-2} with an energy density of 8.60 Wh kg^{-1}. Furthermore, the α-MnSe electrode exhibited excellent cyclic stability (103.40%) after 2,000 CD cycles. Similarly, the fabricated α-MnSe symmetric device delivered a maximum specific capacitance of 23.44 F g^{-1} at a current density of 0.1 mA cm^{-2} in the potential window of 0.8 V. Collectively, the electrochemical performances suggest that α-MnSe nanoparticles as a promising candidate for an electrode material for energy storage devices.

3.5. References

1 D. P. Dubal, G. S. Gund, R. Holze, H. S. Jadhav, C. D. Lokhande and C.-J. Park, *Electrochim. Acta*, 2013, **103**, 103–109.

2 K. Krishnamoorthy, P. Pazhamalai, S. Sahoo and S.-J. Kim, *J. Mater. Chem. A*, 2017, **5**, 5726–5736.

3 Z. Wu, Y. Zhu and X. Ji, *J. Mater. Chem. A*, 2014, **2**, 14759–14772.

4 N. Garg, M. Basu and A. K. Ganguli, *J. Phys. Chem. C*, 2014, **118**, 17332–17341.

5 S. Sahoo, K. K. Naik, D. J. Late and C. S. Rout, *J. Alloys Compd.*, 2017, **695**, 154–161.

6 K. Krishnamoorthy, G. K. Veerasubramani, P. Pazhamalai and S. J. Kim, *Electrochim. Acta*, 2016, **190**, 305–312.

7 S. Sahoo, K. K. Naik and C. S. Rout, *Nanotechnology*, 2015, **26**, 455401.

8 S. Ratha and C. S. Rout, *ACS Appl. Mater. Interfaces*, 2013, **5**, 11427–11433.

9 G. A. Muller, J. B. Cook, H.-S. Kim, S. H. Tolbert and B. Dunn, *Nano Lett.*, 2015, **15**, 1911–1917.

10 J.-C. Xing, Y.-L. Zhu, Q.-W. Zhou, X.-D. Zheng and Q.-J. Jiao, *Electrochim. Acta*, 2014, **136**, 550–556.

11 N. S. Arul and J. I. Han, *Mater. Lett.*, 2016, **181**, 345–349.

12 H. Chen, S. Chen, M. Fan, C. Li, D. Chen, G. Tian and K. Shu, *J. Mater. Chem. A*, 2015, **3**, 23653–23659.

13 G. Nagaraju, S. M. Cha, S. C. Sekhar and J. S. Yu, *Adv. Energy Mater.*, 2017, **7**, 1601362.

14 Y.-P. Gao, X. Wu, K.-J. Huang, L.-L. Xing, Y.-Y. Zhang and L. Liu, *CrystEngComm*, 2017, **19**, 404–418.

15 X. Wang, B. Liu, Q. Wang, W. Song, X. Hou, D. Chen, Y. Cheng and G. Shen, *Adv. Mater.*, 2013, **25**, 1479–1486.

16 C. Zhang, H. Yin, M. Han, Z. Dai, H. Pang, Y. Zheng, Y.-Q. Lan, J. Bao and J. Zhu, *ACS Nano*, 2014, **8**, 3761–3770.

17 S. R. Marri, S. Ratha, C. S. Rout and J. N. Behera, *Chem. Commun.*, 2017, **53**, 228–231.

18 A. M. Patil, A. C. Lokhande, N. R. Chodankar, J. H. Kim and C. D. Lokhande, *Int. J. Hydrogen Energy*, 2016, **41**, 17453–17461.

19 S. J. Patil, R. N. Bulakhe and C. D. Lokhande, *Chempluschem*, 2015, **80**, 1478–1487.

20 H. Quan, B. Cheng, D. Chen, X. Su, Y. Xiao and S. Lei, *Electrochim. Acta*, 2016, **210**, 557–566.

21 N. R. Chodankar, D. P. Dubal, G. S. Gund and C. D. Lokhande, *Electrochim. Acta*, 2015, **165**, 338–347.

22 S. Anandan, B. G. S. Raj, G.-J. Lee and J. J. Wu, *Mater. Res. Bull.*, 2013, **48**, 3357–3361.

23 R. B. Pujari, A. C. Lokhande, A. A. Yadav, J. H. Kim and C. D. Lokhande, *Mater. Des.*, 2016, **108**, 510–517.

24 X. Liu, J. Du, C. Li, X. Han, X. Hu, F. Cheng and J. Chen, *J. Mater. Chem. A*, 2015, **3**, 3425–3431.

25 N. Li, Y. Zhang, H. Zhao, Z. Liu, X. Zhang and Y. Du, *Inorg. Chem.*, 2016, **55**, 2765–2770.

26 K. Krishnamoorthy, P. Pazhamalai and S. J. Kim, *Electrochim. Acta*, 2017, **227**, 85–94.

27 K. Jeyasubramanian, T. S. Gokul Raja, S. Purushothaman, M. V. Kumar and I. Sushmitha, *Electrochim. Acta*, 2017, **227**, 401–409.

28 A. Rose, N. Raghavan, S. Thangavel, B. U. Maheswari, D. P. Nair and G. Venugopal, *Mater. Sci. Semicond. Process.*, 2015, **31**, 281–286.

29 Q. Peng, Y. Dong, Z. Deng, H. Kou, S. Gao and Y. Li, *J. Phys. Chem. B*, 2002, **106**, 9261–9265.

30 M. Wu, Y. Xiong, N. Jiang, M. Ning and Q. Chen, *J. Cryst. Growth*, 2004, **262**, 567–571.

31 F. Buciuman, F. Patcas, R. Craciun and D. R. T. Zahn, *Phys. Chem. Chem. Phys.*, 1999, **1**, 185–190.

32 S. Sahoo and C. S. C. S. Rout, *Electrochim. Acta*, 2016, **220**, 57–66.

33 M. Xu, L. Kong, W. Zhou and H. Li, *J. Phys. Chem. C*, 2007, **111**, 19141–19147.

34 V. Prabhakaran, B. L. Mehdi, J. J. Ditto, M. H. Engelhard, B. Wang, K. D. D. Gunaratne, D. C. Johnson, N. D. Browning, G. E. Johnson and J. Laskin, *Nat. Commun.*, 2016, **7**, 11399.

35 X. Wang, S. Kajiyama, H. Iinuma, E. Hosono, S. Oro, I. Moriguchi, M. Okubo and A. Yamada, *Nat. Commun.*, 2015, **6**, 1–6.

36 D. P. Dubal, S. H. Lee, J. G. Kim, W. B. Kim and C. D. Lokhande, *J. Mater. Chem.*, 2012, **22**, 3044.

37 T. Brezesinski, J. Wang, R. Senter, K. Brezesinski, B. Dunn and S. H. Tolbert, *ACS Nano*, 2010, **4**, 967–977.

38 X.-Y. Qiu, Q.-C. Zhuang, Q.-Q. Zhang, R. Cao, P.-Z. Ying, Y.-H. Qiang and S.-G. Sun, *Phys. Chem. Chem. Phys.*, 2012, **14**, 2617–2630.

39 X. Liu, J.-Z. Zhang, K.-J. Huang and P. Hao, *Chem. Eng. J.*, 2016, **302**, 437–445.

40 D. Zhang, X. Zhang, Y. Chen, P. Yu, C. Wang and Y. Ma, *J. Power Sources*, 2011, **196**, 5990–5996.

41 A. A. Yadav, S. N. Jadhav, D. M. Chougule, P. D. Patil, U. J. Chavan and Y. D. Kolekar, *Electrochim. Acta*, 2016, **206**, 134–142.

42 R. Ramachandran, M. Saranya, P. Kollu, B. P. C. Raghupathy, S. K. Jeong and A. N. Grace, *Electrochim. Acta*, 2015, **178**, 647–657.

43 K. Krishnamoorthy, S. Thangavel, J. Chelora Veetil, N. Raju, G. Venugopal and S. J. Kim, *Int. J. Hydrogen Energy*, 2016, **41**, 1672–1678.

44 C. C. Mayorga-Martinez, A. Ambrosi, A. Y. S. Eng, Z. Sofer and M. Pumera, *Electrochem. commun.*, 2015, **56**, 24–28.

45 C.-M. Chen, Q. Zhang, M.-G. Yang, C.-H. Huang, Y.-G. Yang and M.-Z. Wang, *Carbon N. Y.*, 2012, **50**, 3572–3584.

46 K. Krishnamoorthy, P. Pazhamalai, G. K. Veerasubramani and S. J. Kim, *J. Power Sources*, 2016, **321**, 112–119.

47 S. Vijayakumar, S. Nagamuthu and K.-S. Ryu, *Electrochim. Acta*, 2017, **238**, 99–106.

48 R. Wang, M. Han, Q. Zhao, Z. Ren, C. Xu, N. Hu, H. Ning, S. Song and J.-M. Lee, *Electrochim. Acta*, 2017, **243**, 152–161.

49 Y. Gao, Y. S. Zhou, M. Qian, X. N. He, J. Redepenning, P. Goodman, H. M. Li, L. Jiang and Y. F. Lu, *Carbon N. Y.*, 2013, **51**, 52–58.

50 K.-M. Lin, K.-H. Chang, C.-C. Hu and Y.-Y. Li, *Electrochim. Acta*, 2009, **54**, 4574–4581.

51 W. Xiong, M. Liu, L. Gan, Y. Lv, Y. Li, L. Yang, Z. Xu, Z. Hao, H. Liu and L. Chen, *J. Power Sources*, 2011, **196**, 10461–10464.

52 K. H. An, W. S. Kim, Y. S. Park, H. J. Jeong, Y. C. Choi, J.-M. Moon, D. J. Bae, S. C. Lim, Y. H. Lee and S. Saito, in *AIP Conference Proceedings*, AIP, 2001, vol. 590, pp. 241–244.

53 T. Zhu, B. Xia, L. Zhou and X. W. D. Lou, *J. Mater. Chem.*, 2012, **22**, 7851–7855.

54 A. D. Jagadale, V. S. Kumbhar, D. S. Dhawale and C. D. Lokhande, *Electrochim. Acta*, 2013, **98**, 32–38.

55 R. S. Kalubarme, H. S. Jadhav and C.-J. Park, *Electrochim. Acta*, 2013, **87**, 457–465.

56 K. Wang, H. Wu, Y. Meng, Y. Zhang and Z. Wei, *Energy Environ. Sci.*, 2012, **5**, 8384.

57 H. Wu, Z. Lou, H. Yang and G. Shen, *Nanoscale*, 2015, **7**, 1921–1926.

58 A. K. C. Gallegos and M. E. Rincón, *J. Power Sources*, 2006, **162**, 743–747.

59 M. A. Bissett, S. D. Worrall, I. A. Kinloch and R. A. W. Dryfe, *Electrochim. Acta*, 2016, **201**, 30–37.

CHAPTER – 4

Copper molybdenum sulfide: a novel pseudocapacitive electrode material for electrochemical energy storage device

Highlights

- The ever-growing demand for energy storage devices necessitates the development of novel energy storage materials with high performance.
- In this work, copper molybdenum sulfide (Cu_2MoS_4) nanostructures were prepared via a one-pot hydrothermal method and examined as an advanced electrode material for supercapacitor.
- Physico-chemical characterizations such as X-ray diffraction, laser Raman, field emission scanning electron microscope with elemental mapping, and X-ray photoelectron spectroscopy analyses revealed the formation of I-phase Cu_2MoS_4. Electrochemical analysis using cyclic voltammetry (CV), charge-discharge (CD) and electrochemical impedance spectroscopy (EIS) showed the pseudocapacitive nature of charge-storage via ion intercalation/de-intercalation occurring in the Cu_2MoS_4 electrode.
- The Cu_2MoS_4 electrode delivered a specific capacitance of 127 F g^{-1} obtained from the CD measured using a constant current density of 1.5 mA cm^{-2}. Further, Cu_2MoS_4 symmetric supercapacitor (SSC) device delivered a specific capacitance of 28.25 F g^{-1} at a current density of 0.25 mA cm^{-2} with excellent rate capability.
- The device acquired high energy and power density of 3.92 Wh kg^{-1} and 1250 W kg^{-1}, respectively. The Nyquist and Bode analysis further confirmed the pseudocapacitive nature of Cu_2MoS_4 electrodes.

4.1 Introduction

The scarcity of fossil fuels and increasing concerns about the greenhouse effect have greatly affected the world economy and environmental practices [1,2]. As such, there is a high demand for renewable and eco-friendly energy resources. Supercapacitors, fuel cells, and batteries play the crucial role to achieve the electrochemical energy conversion and storage easily [3,4]. Supercapacitor has captivated considerable interest in both academia and industrial sectors during the 21st century due to the ultrahigh power density, long cycle life (>100000 cycles), wide operation temperature range and high capacity for charge storage [5,6]. Supercapacitors provide a favorable route to encounter the growing power demands in commercial markets for portable electronics [7,8]. Depending on the charge storage mechanism, supercapacitors can be broadly classified into two categories (i) electric double layer capacitors (EDLCs) store charge via non-faradic ion adsorption/desorption on the electrode surface whereas (ii) pseudocapacitors store charge via a fast faradaic redox reaction [9,10]. Pseudocapacitive materials, including transition metal chalcogenides (TMCs) show better electrochemical performance compared to EDLC type materials, mainly due to the multiple oxidation states and rapid redox reactions of the transition metals. To date, researchers mainly focus on the fourth and fifth-period transition metal (Mn, Ni, Co, Cu, Mo and Fe) based oxides, hydroxides, selenides, and sulfides as electrode materials for pseudocapacitive energy storage devices [11,12]. Transition metal sulfides possess better electrical conductivity, and thermal stability than their corresponding metal oxides and hydroxides [13,14]. In metal sulfides, the sulfur ions generate more flexible structures than oxygen ions due to the higher electronegativity of sulfur, providing better electrochemical redox reactions. In the last decade, layered TMCs, such as WSe_2, MoS_2, $MoSe_2$, WS_2, TiS_2, and VS_2 have played a vital role in the field of energy storage and conversion due to their unique physical, structural, and chemical properties [15,16]. Recent

studies have highlighted that multi-component (binary/ternary) metal sulfides possess better electrochemical performance due to their higher electronic conductivity and richer redox chemistry, and the higher tunability of the inter-layer distance due to suitable substitution compared to single-component metal sulfides [17–19]. Further, multicomponent TMCs possess a large surface area which can be utilized for the efficient adsorption/desorption and transport of electrolyte ions, which are advantageous for charge storage and discharge processes [20].

In this scenario, the development of multicomponent TMC-based materials become an area of immense interest and new series of materials with the chemical formula Cu_2MX_4 (where 'M' belongs to transition metal and 'X' belongs to chalcogenide elements) has been developed recently by Pruss et al. followed by the works of Crossland et al. [21,22]. The Cu_2MX_4 materials possess two structural phases viz (i) P-phase (*Pm42* space group) and (ii) I-phase *Im42* space group in a tetragonal lattice [20,23]. In the Cu_2MX_4 family, Cu_2MoS_4 is a binary layered metal chalcogenide with intriguing properties such as being a wide-bandgap semiconductor with good photocatalytic and electrocatalytic properties for hydrogen evolution reaction (HER) with enhanced redox active sites [23,24]. At first, Tran et al. prepared P-phase Cu_2MoS_4 via refluxing approach and examined its use as an electrocatalyst for HER application [24]. Later, Zhang et al. synthesized Cu_2MoS_4 hollow spheres decorated on graphene sheets and examined their photocatalytic properties [25]. Further, Yu et al. demonstrated the lithium ion intercalation/de-intercalation properties of Cu_2MoS_4 (prepared by wet chemical route) with poor cyclic stability which was enhanced by the addition of graphene oxide sheets [26]. More recently, Ma et al. reported the application of Cu_2MoS_4/carbon dot hybrid materials as photocathodes for photo-electrochemical cells [27]. Further, it is expected that Cu_2MoS_4 might possess good electrochemical properties for electrochemical energy storage devices due to its layered crystal structure, which enhances more redox active sites, and it also has the advantages of being a low

cost, environmentally benign and earth-abundant materials [27]. In this study, we successfully synthesized tetragonal *P42m* symmetry copper molybdenum sulfide (Cu_2MoS_4) nanostructures via a facile hydrothermal method and investigated its use as an electrode material for supercapacitor. The electrochemical properties and charge storage mechanism of the Cu_2MoS_4 electrode were investigated using both three-electrode and two-electrode (via fabrication of symmetric supercapacitor (SSC) configurations in an aqueous solution containing 1 M Na_2SO_4 as the electrolyte.

4.2 Experimental section

4.2.1 Materials

Copper (II) sulfate pentahydrate ($CuSO_4 \cdot 5H_2O$), thioacetamide (CH_3CSNH_2), hydrazine monohydrate ($N_2H_4 \cdot H_2O$), sodium molybdate ($Na_2MoO_4 \cdot 2H_2O$), N-methyl pyrrolidone (NMP), ethylene glycol, and sodium sulfate (Na_2SO_4) were purchased from Daejung Chemicals Ltd., South Korea. Carbon black and polyvinylidene fluoride (PVDF) were purchased from Alfa Aesar and Sigma Aldrich, South Korea, respectively.

4.2.2 Preparation of Cu_2MoS_4 nanostructures

A facile hydrothermal route was carried out for the synthesis of Cu_2MoS_4 nanostructures similar to the previous report with minor modification [23,28]. In a typical approach, 60 mg of $Na_2MoO_4 \cdot 2H_2O$ and 120 mg of CH_3CSNH_2 were dissolved in 60 mL of ethylene glycol under ultra-sonication for 30 minutes. Then 40 mg of Cu_2O (co-precipitation method [29]) was added to the above precursor solution and kept under ultra-sonication for 1 h, causing a gradually change in the color of the solution to dark brown. Then, precursor solution was transferred to a 100 mL Teflon lined stainless steel autoclave and kept at 150 °C for 15 h. Upon completion of the reaction, the autoclave was then left to cool naturally to room temperature, and the precipitates

were collected by centrifugation and washed using water and absolute ethanol several times to remove any residuals. Finally, the collected product was dried at 60 °C for several hours.

4.2.3 Instrumentation

X-ray diffraction analysis of Cu_2MoS_4 nanostructures was conducted using a Rigaku X-ray diffractometer (Rigaku Instruments Co, Tokyo, Japan) at 40 kV and 40 mA with Cu-Kα radiation (λ = 1.54184 Å). Raman spectroscopy of Cu_2MoS_4 nanostructures was performed on a LabRam HR Evolution Raman spectrometer (Horiba Jobin-Yvon, France) with a laser excitation source of wavelength 514 nm at various laser powers. The surface morphology of the Cu_2MoS_4 nanostructures was analysed using field-emission scanning electron microscopy (TESCAN, MIRA3) under different magnifications. The chemical composition and oxidation state of elements present in the Cu_2MoS_4 was obtained by X-ray photoelectron spectroscopy (XPS) using an ESCA-2000, VG Microtech Ltd.

4.2.4 Electrochemical analysis

The working electrode was prepared using slurry coating method as reported in our earlier work [30]. Briefly, the working electrode was prepared by grinding the active material (Cu_2MoS_4 nanostructures), carbon black, and PVDF (mixture weight ratio 80:15:5) with an appropriate amount of NMP as solvent in an agate-mortar until a uniform slurry was obtained. Then, the as-prepared slurry was coated onto a pre-cleaned stainless-steel substrate (1×1 cm^2) and allowed to dry at 80 °C in an oven overnight. The electroactive mass of the Cu_2MoS_4 electrode on to the stainless-steel substrate is measured as 1 mg as calculated from the difference between the mass of the substrate before and after coating of the Cu_2MoS_4 electrode using Dual-range Semi-micro Balance (AUW-220D, SHIMADZU).

For the three-electrode measurement, Cu_2MoS_4 coated stainless steel electrode, platinum sheet and Ag/AgCl were used as working, counter and reference electrodes, respectively. The

Cu_2MoS_4 symmetric supercapacitor (SSC) device was fabricated by sandwiching polypropylene separator between two Cu_2MoS_4 coated stainless steel electrodes. An aqueous solution of 1 M Na_2SO_4 is used as the electrolyte. The electrochemical performance of Cu_2MoS_4 was investigated through cyclic voltammetry (CV), galvanostatic charge-discharge (CD), and electrochemical impedance spectroscopy (EIS) (in the frequency range of 0.1 Hz to 100 KHz) via three electrode system as well as SSC device using an AUTOLAB PGSTAT302N electrochemical workstation. The specific capacitance (C_{sp}), energy density (E) and power density (P) of the Cu_2MoS_4 electrode were calculated using the following relations:[30]

$$C_{sp} = [(\int I\,dV) / (s \times \Delta V \times m)] \quad \ldots\ldots\ldots (1)$$

$$C_{sp} = [(I \times \Delta t) / (\Delta V \times m)] \quad \ldots\ldots\ldots\ldots (2)$$

$$E = (0.5 \times C_{sp} \times \Delta V^2) \quad \ldots\ldots\ldots\ldots (3)$$

$$P = E / \Delta t \quad \ldots\ldots\ldots\ldots\ldots\ldots (4)$$

Here, "C_{sp}" is the specific capacitance (F g^{-1}), "I" is the current (A), "ΔV" is the potential window (V), "s" is the scan rate (mV s^{-1}), "Δt" is the discharge time (s), and "m" is the mass of the active material (g).

4.3 Results and Discussion

The crystal structure of as-prepared Cu_2MoS_4 is evaluated by the XRD pattern as shown in Figure 4.1 (A). The diffraction peaks obtained at 2θ = 17.22°, 18.63°, 23.90°, 29.27°, 31.85°, 33.02°, 37.69°, 46.67°, 47.98°,48.69°, 51.03°, 52.66°, 56.87°, 59.45°, 69.50°, 72.19°, 74.18° and 79.21° correspond to the (002), (011), (110), (112), (013), (020), (004), (123), (220), (015), (024), (222), (132), (033), (040), (042), (141) and (242) crystal planes of tetragonal Cu_2MoS_4 as previously reported [23]. In addition, three peaks (α) observed at 16.53°, 27.87°, and 41.44° are matched with the crystal planes of tetragonal Cu_2MoS_4 reported by Tran et al. [24]. The XRD pattern reveals that the sample corresponds to I-phase Cu_2MoS_4 crystal with tetragonal *P42m*

symmetry which is similar to the structure reported for Cu_2WS_4 [31]. Impurity peaks (MoO_3, Cu_2O, MoS_2, and Cu_2S) were not detected which confirms the high purity of prepared Cu_2MoS_4. Raman spectroscopy is known to be an effective and non-destructive tool to determine the intrinsic crystal structure and bonding nature of nanomaterials.

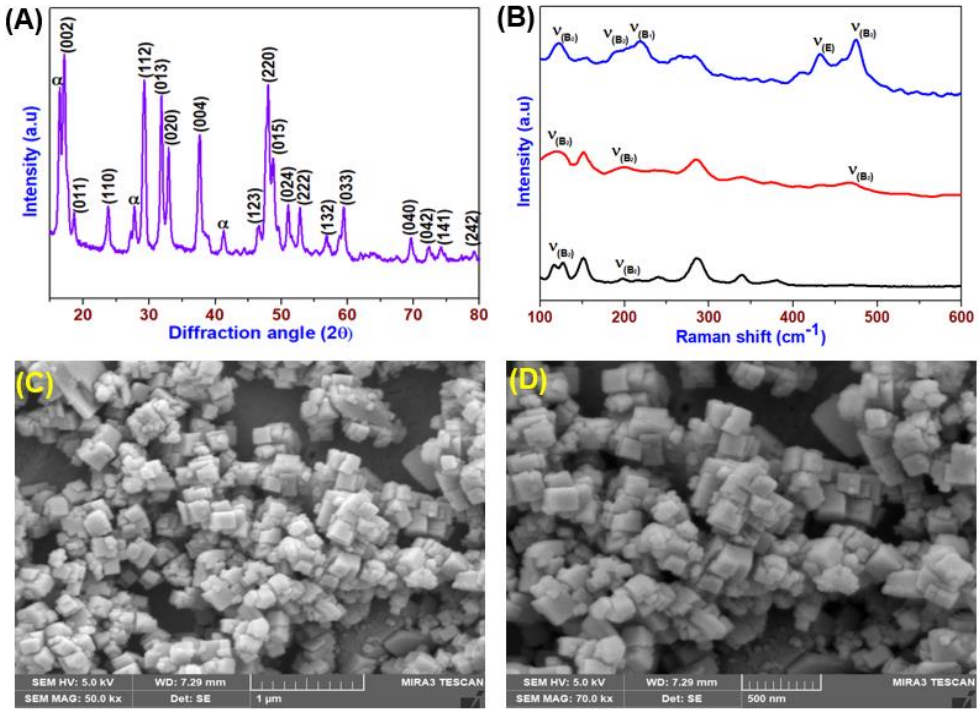

Figure 4.1 (A) X-ray diffraction pattern of Cu_2MoS_4 nanostructures and (B) laser Raman spectrum of Cu_2MoS_4 nanostructures at different laser powers. Field emission scanning electron micrographs of Cu_2MoS_4 nanostructures measured at different magnifications (C) 1 µm and (D) 500 nm.

Figure 4.1 (B) shows the Raman spectra of the Cu_2MoS_4 sample using different laser powers from 25 mW to 100 mW. There are five main peaks in the frequency range of 100-600 cm^{-1} which are well matched with the B_1, B_2 and E modes and are consistent with the previous report. The Raman peaks at 120 cm^{-1}, 200 cm^{-1} and 473 cm^{-1} belong to B_2 mode whereas 218 cm^{-1} and 431 cm^{-1} to B_1 mode and E stretching mode, respectively [28,32]. All the active modes arise due to stretching vibrations of Mo-S, Cu-S, and S-S in Cu_2MoS_4. With an increase in the

laser power, the peaks at 120 cm^{-1} and 473 cm^{-1} are broadening which is caused due to an increase in the bond length of the materials arises from the thermal effect of the laser [33,34]. It is clearly visible that with an increase in laser power (50 mW and 100 mW), a few weak bands appear, which signifies the dramatic change in sample nature. The weak bands at 156 cm^{-1} and 287 cm^{-1} appearing at the higher laser power correspond to the α-MoO_3, which is due to the surface oxidization of Cu_2MoS_4 [35].

Figure 4.1 (C and D) are FE-SEM micrographs of as-synthesized I-phase Cu_2MoS_4 at different magnification (50 Kx and 70 Kx). The FE-SEM micrographs of Cu_2MoS_4 reveals the formation of nanocubes with the average size in the range of 60-70 nm. To obtain the elemental distribution of the Cu_2MoS_4 nanostructures, elemental mapping has been performed, and the results are provided in Figure 4.2 (A-D). The elemental mapping indicates the homogenous distribution of Cu, Mo, and S in the prepared Cu_2MoS_4. XPS analysis was conducted to obtain detailed information on the elemental composition and surface oxidation states of the metals present in the Cu_2MoS_4 nanostructures and the results are shown in Figure 4.3.

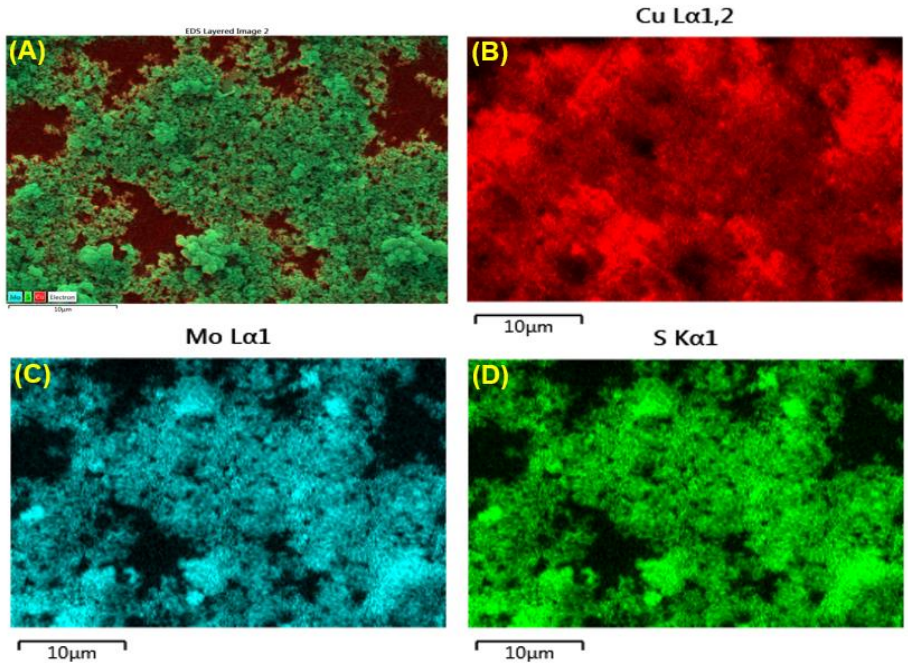

Figure 4.2 Elemental mapping of the Cu_2MoS_4 nanostructures: (A) FE-SEM micrographs for elemental mapping and corresponding elemental mapping (B) Cu, (C) Mo and (D) S.

The XPS survey spectrum of the Cu_2MoS_4 is represented by the binding energy range of 0 to 1200 eV as shown in Figure 4.3 (A). The survey spectrum indicates the presence of peaks corresponding to the Cu 2p, Mo 3d, S 2s, S 2p, C 1s and O 1s states. The existence of C and O in the survey spectrum is due to the exposure to air as seen in many reports [23]. The deconvoluted core level spectrum of Cu 2p is shown in Figure 4.3 (B), which indicates two strong peaks at 954.1 eV and 934.2 eV corresponding to Cu $2p_{1/2}$ and Cu $2p_{3/2}$, respectively. The deconvoluted core level spectrum of Mo 3d (Figure 4.3 (C)), reveals the presence of two major peaks at 233.5 eV and 230.6 eV corresponding to Mo $3d_{3/2}$ and Mo $3d_{5/2}$, respectively, with a minor peak around 226.5 eV due to the presence of the S 2s state. Figure 4.3 (D) represents the deconvoluted core level spectrum for S 2p state, which indicates the presence of two major peaks around 163.4 and 162.3 eV which can be attributed to the S $2p_{1/2}$ and S $2p_{3/2}$ states respectively. The observed peaks can be assigned to the Cu^{+}, $Mo^{6+,}$ and S^{2-} present in the Cu_2MoS_4 and these results are well matched with previous literature based on crystalline Cu_2MoS_4 [23,24].

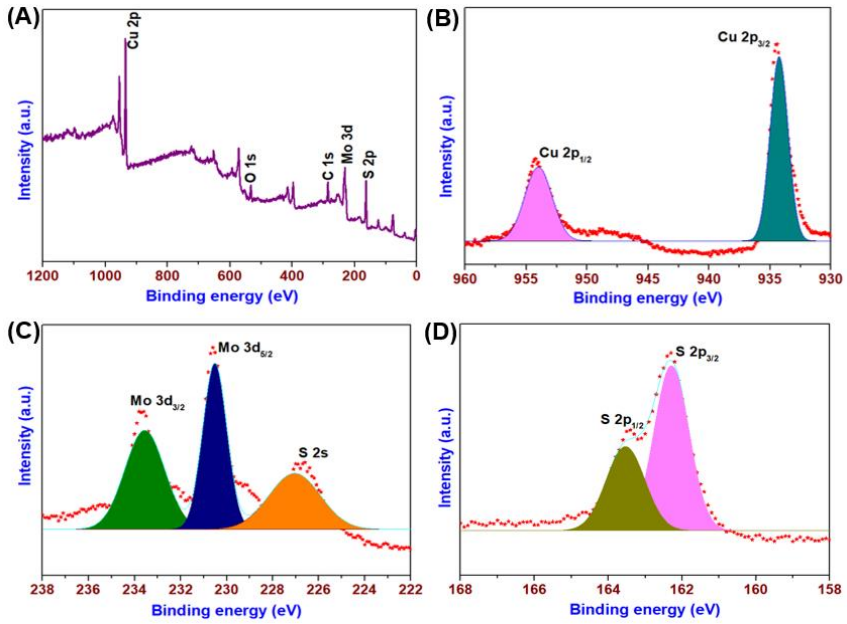

Figure 4.3 X-ray photoelectron spectrum of hydrothermally prepared Cu_2MoS_4 nanostructures (A) Survey spectrum in the range of 0 to 1200 eV, (B) core level spectrum of Cu 2p element present in Cu_2MoS_4, (C) core level spectrum of Mo 3d element present in Cu_2MoS_4, and (D) core level spectrum of S 2p element present in Cu_2MoS_4.

The electrochemical performance of Cu_2MoS_4 electrode was studied both in three-electrode and SSC configuration in an aqueous solution of 1 M Na_2SO_4 as the electrolyte. Figure 4.4 shows the electrochemical characterization of Cu_2MoS_4 electrode measured in a three-electrode configuration. The CV profiles of Cu_2MoS_4 electrode obtained using different scan rates ranging from 5 to 100 mV s^{-1} in the potential range of -0.8 to 0.2 V is provided in Figure 4.4 (A). The shape of the CV profiles depicts a quasi-rectangular behavior similar to that of MoS_2 electrodes, with no signs of any redox peaks, as observed in the CuS using Na_2SO_4 as electrolyte [36,37].

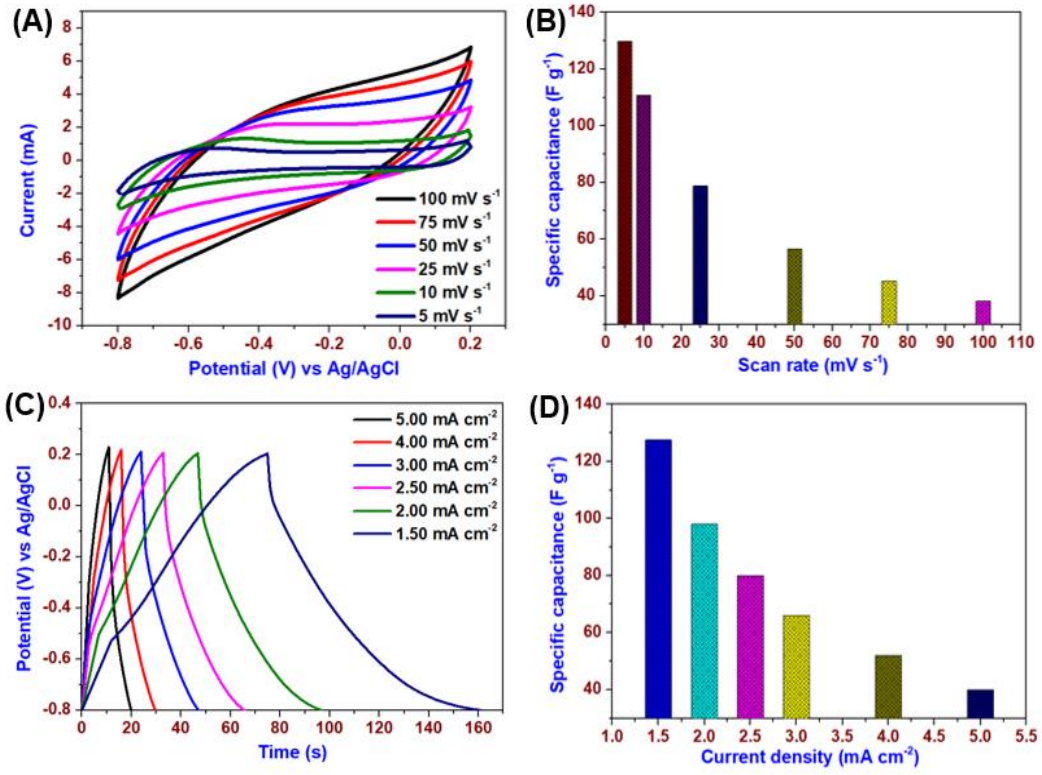

Figure 4.4 Electrochemical performance of Cu_2MoS_4 electrode in three electrode system. (A) Cyclic voltammetric profile of Cu_2MoS_4 electrode measured at various scan rate (5 to 100 mV s^{-1}), (B) effect of scan rate on the specific

capacitance of Cu_2MoS_4 electrode, (C) Galvanostatic charge-discharge profile of Cu_2MoS_4 electrode measured at various current densities (1.5 – 5 mA cm^{-2}) and (D) effect of current density on specific capacitance.

This suggested the presence of pseudocapacitance in the Cu_2MoS_4 electrode due to diffusion-assisted ion-intercalation/de-intercalation phenomenon similar to layered MoS_2 electrodes. Further, the current increases with increasing scan rate, which highlights the better capacitive nature of the Cu_2MoS_4 electrode. The charge storage mechanism can be attributed to the reversible intercalation/deintercalation of Na^+ ions occurring at the Cu_2MoS_4 electrode as follows [38].

$$Cu_2MoS_4 + Na^+ + e^- \leftrightarrow NaCu_2MoS_4 \ldots\ldots\ldots\ldots\ldots (5)$$

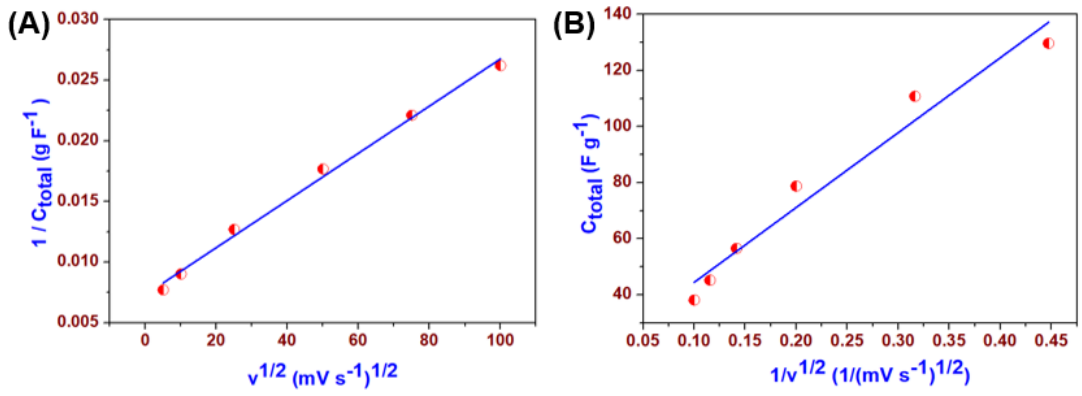

Figure 4.5 Trasatti plot for Cu_2MoS_4 electrode. (A) Dependence of 1 / C_{total} on $v^{1/2}$ and (B) dependence of C_{total} on $v^{-1/2}$ for Cu_2MoS_4 electrode in Na_2SO_4 electrolyte.

Here, during the charging process, the Na^+ ions from the electrolyte intercalate in the Cu_2MoS_4 electrode and liberate one electron, whereas while discharging, Na^+ ions are de-intercalated from the Cu_2MoS_4. The total amount of charge stored in the Cu_2MoS_4 electrode can be determined using Trasatti method [39]. In this method, the total charge (C_{total}) stored is equal to the summation of charge stored at the exterior surface of the electrode (C_{out}) and charge stored at the interior surface of the electrode (C_{in}). Here, charge storage at the exterior surface of the electrode (C_{out}) arises due to both electric double-layer and pseudocapacitive nature of electrode

material whereas charge stored at the interior surface of the electrode (C_{in}) can be attributed to ion diffusion into the bulk of electrode material. Figure 4.5 (A and B) shows the Trasatti plot for the Cu_2MoS_4 electrode. In the partition procedure, the y-intercept of the linear fit of $1/C_{total}$ vs $v^{1/2}$ at v = 0 illustrates the total quantity of charge stored in the electrode as shown in Figure 4.5 (A). At low scan rate, the stored amount of charge is very high, due to the electrolyte ions having sufficient time to interact with the electrode. On the other hand, the y-intercept of the linear fit of C_{total} vs. $v^{-1/2}$ at $v = \infty$ represents the quantity of charge stored at the outer surface of the electrode as shown in Figure 4.5 (B). At a high scan rate, the charge storage capability is very low because the electrolyte ions interact only with the outer surface of the electrode (insufficient of time). According to the Trasatti method, the percentage of charge stored in the outer and inner surface of the Cu_2MoS_4 electrode are 13 % and 87 %, respectively [39–41]. The Trasatti plot for the Cu_2MoS_4, clearly suggests that the mechanism of charge-storage is the presence of the ion-intercalation/de-intercalation process in the Cu_2MoS_4 electrode. Figure 4.4 (B) represents the effect of scan rate on the specific capacitance of Cu_2MoS_4 electrode which shows that the Cu_2MoS_4 electrode possesses a maximum specific capacitance of 129.68 F g^{-1} at a scan rate of 5 mV $s^{-1,}$ and a capacitance retention of about 43 and 29 % was retained with an increase of ten and twenty-fold in scan rate.

Figure 4.4 (C) displays the CD profiles of Cu_2MoS_4 electrode measured at various current densities (1.5 to 5 mA cm^{-2}) within the potential range -0.8 to 0.2 V. The CD profiles (Figure 4.4 (C)) reveal the non linear symmetric triangular charge-discharge nature, suggesting the pseudocapacitive nature of Cu_2MoS_4 electrode [42]. The time required for charging and discharging is increased with an increase in current density from 1.5 to 5 mA cm^{-2} and the Columbic efficiency (ratio of time required for discharging and charging) is above 90 % for all current densities, suggesting excellent electrochemical reversibility in the Cu_2MoS_4 electrode.

Figure 4.4 (D) represents the effect of current densities on the specific capacitance of Cu_2MoS_4 electrode which delivered a specific capacitance of 127.5 F g^{-1} for the Cu_2MoS_4 electrode at a constant current density of 1.5 mA cm^{-2} and with an increase in current density to 5 mA cm^{-2}, the specific capacitance is about 40 F g^{-1}. Further, the obtained specific capacitance of Cu_2MoS_4 electrode (127.5 F g^{-1}) is higher compared to the single component sulfides [MoS_2 (92.85 F g^{-1}), CuS (62.77 F g^{-1})] and oxides [MoO_3(108.88 F g^{-1}), CuO (88.5 F g^{-1})], respectively [36,37,43,44]. A summary of the performance metrics of the Cu_2MoS_4 electrode with other recently reported pseudocapacitive electrodes analyzed using three electrode systems is provided in Table 4.1. This clearly evidences the good electrochemical properties of the Cu_2MoS_4 electrode for energy storage applications which is due to the layered crystal structure which facilitating more active redox sites.

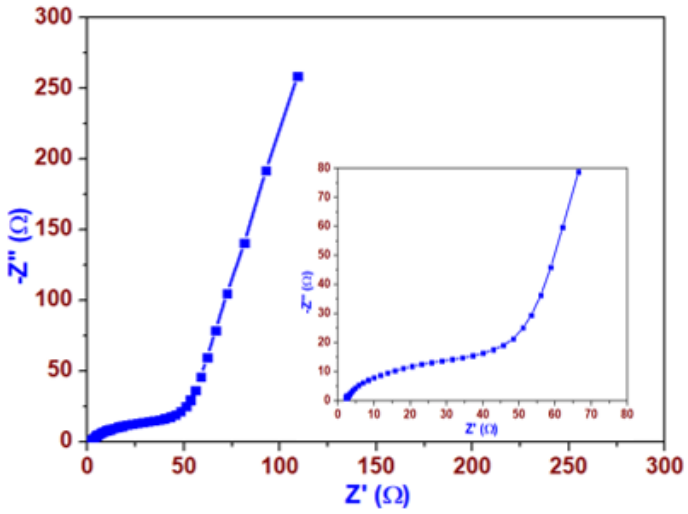

Figure 4.6 The Nyquist plot for Cu_2MoS_4 electrode (the inset shows the enlarged portion of Nyquist plot in the high-frequency region).

The Nyquist plot of the Cu_2MoS_4 electrode is provided in Figure 4.6 which shows the presence of semi-circle in the high-frequency region due to the charge transfer resistance followed by a straight line in the low-frequency region due to diffusion of electrolyte in the

electrode material. The straight line observed almost parallel to the y-axis is due to the frequency dependent diffusion kinetics of the electrolyte ions into the surface of the Cu_2MoS_4 electrode. The Cu_2MoS_4 electrode possesses a solution resistance (R_s) of about 2.1 Ω and charge-transfer resistance (R_{ct}) of about 48.2 Ω.

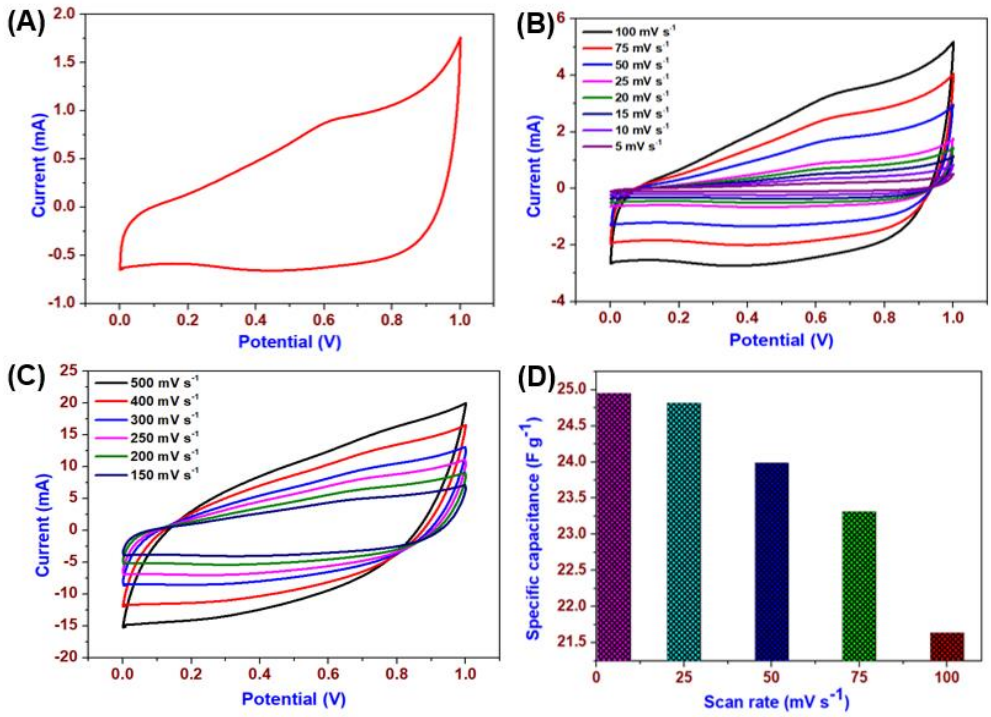

Figure 4.7 Electrochemical performance of Cu_2MoS_4 SSC device (A) cyclic voltammetric profile at 5 mV s^{-1}, (B) cyclic voltammetric profiles at different scan rates (5 – 100 mV s^{-1}) , (C) cyclic voltammetric profiles at different scan rates (150 – 500 mV s^{-1}), and (D) effect of scan rate on the specific capacitance of Cu_2MoS_4 SSC device.

It is known that electrochemical studies using three-electrode configuration are more useful for understanding the electrode properties whereas it is highly essential to test using in two-electrode configuration (symmetric supercapacitor devices) for understanding the device-specific properties of any electrode material. Therefore, we fabricated an SSC device using the Cu_2MoS_4 electrodes and examined their electrochemical properties in detail. Figure 4.7 (A, B

and C) shows the CV profiles of Cu_2MoS_4 SSC device measured at different scan rates from 5 to 500 mV s^{-1} in the potential window of 0 to 1 V. From Figure 4.7 (A and B) it is evident that the CV profiles are quasi-rectangular with small redox peaks observed at 0.62 and 0.37 V, which is due to the reversible intercalation/deintercalation of Na^+ ions at the Cu_2MoS_4 electrodes [45]. With the increase in scan rate from 5 to 100 mV s^{-1}, the anodic and cathodic peaks are shifted to higher and lower potential as well as the peak current increases which indicate the better polarization and faster electron transfer processes at high scan rates on the surface of Cu_2MoS_4 electrode [13,46]. With the increase in scan rate from 150 to 500 mV s^{-1} (Figure 4.7 (C)), the CV profiles become quasi-rectangular shaped, and the redox peaks are diminished which is due to the surface reaction at the higher scan rate. At lower scan rate the electrolyte ions have enough time to access the interior surface of the electrode materials, while this is limited at the high scan rates [45]. Figure 4.7 (D) represents the effect of scan rate on the specific capacitance of Cu_2MoS_4 SSC device. The Cu_2MoS_4 SSC device delivered a maximum specific capacitance of about 24.95 F g^{-1} from the CV profiles recorded at a scan rate of 5 mV s^{-1}. A capacitance retention of about 86.73 % (21.64 F g^{-1}) was measured with a twenty-fold increase in scan rate, suggesting better rate capability for the SSC device.

The galvanostatic CD measurements were performed in the potential window (0 to 1 V) at various current densities (0.25 – 2.5 mA cm^{-2}). Figure 4.8 (A) displays the CD profile of Cu_2MoS_4 SSC device measured at a constant current density of 0.5 mA cm^{-2} which indicates the presence of non-linear symmetric CD profiles and provides evidence of pseudocapacitive nature. The CD profiles recorded using different current densities are provided in Figure 4.8 (B) and exhibit a symmetric triangular shape for all current densities. The anodic peak observed in the CV profile is well reflected in the discharge curve shown in Figure 4.8 (B), further confirming the pseudocapacitive nature of the Cu_2MoS_4 electrode. The Cu_2MoS_4 SSC device delivered a

highest specific capacitance of 28.25 F g^{-1} at a current density of 0.25 mA cm^{-2} from the CD profile.

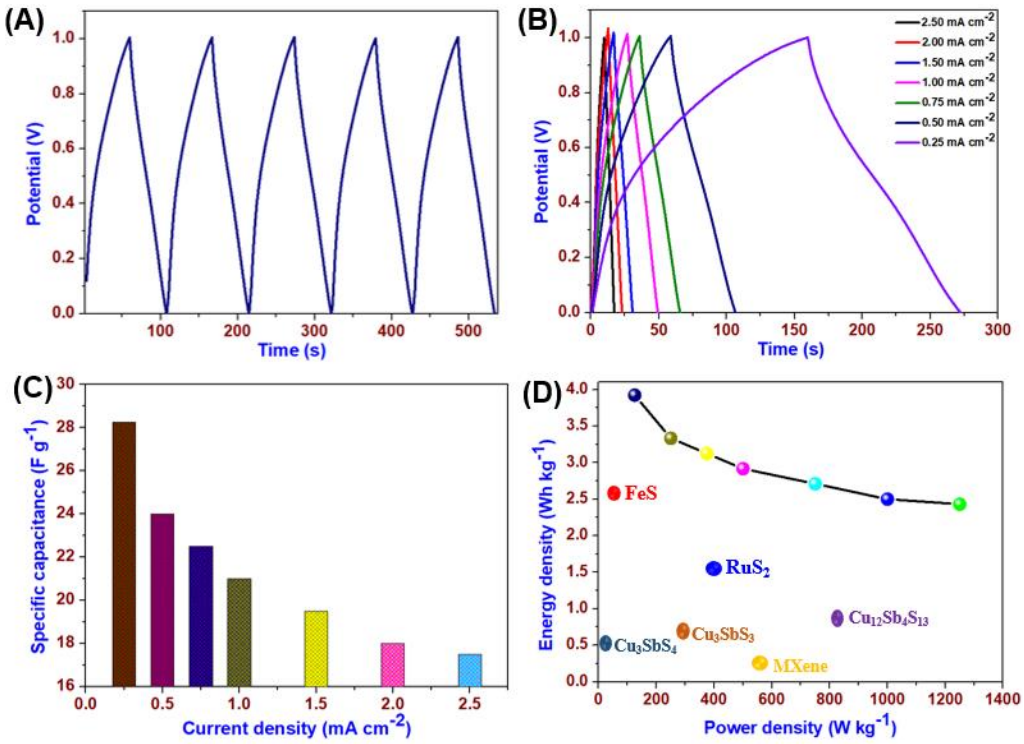

Figure 4.8 (A) Charge-discharge profile of Cu_2MoS_4 SSC device measured at constant current density of 0.5 mA cm^{-2}, (B) charge-discharge profiles measured at different current densities (0.25 – 2.5 mA cm^{-2}) , (C) effect of current density on specific capacitance and (D) Ragone plot of Cu_2MoS_4 SSC device.

The effect of current densities on specific capacitances of Cu_2MoS_4 SSC device is shown Figure 4.8 (C), which reveals that the specific capacitance decreases with increase in current density [47]. The acquired specific capacitance for the Cu_2MoS_4 SSC device is higher than that of other SSC device such as hydrothermally prepared RuS_2 (17 F g^{-1}), and with ionic layer adsorption method-prepared FeS (4.62 F g^{-1}) [30,48]. The Ragone plot of the Cu_2MoS_4 SSC device with the other reported SSC devices are shown in Figure 4.8 (D). The Cu_2MoS_4 SSC device possesses a maximum energy density of about 3.92 Wh kg^{-1} with a corresponding power density of about 125 W kg^{-1} from the CD profile at a discharge current density of 0.25 mA cm^{-2}. The

energy density decreases from 3.92 to 2.43 Wh kg^{-1}, while the power density increases from 125 to 1250 W kg^{-1} as the discharge current density increases from 0.25 to 2.5 mA cm^{-2}. The energy density of the Cu_2MoS_4 SSC device was higher than the reported energy density values of other SSC, such as RuS_2 (1.51 Wh kg^{-1}) and FeS (2.56 Wh kg^{-1}) [30,48]. A summary of the electrochemical performance of Cu_2MoS_4 SSC device with recently reported SSC device is provided in Table. 4.2.

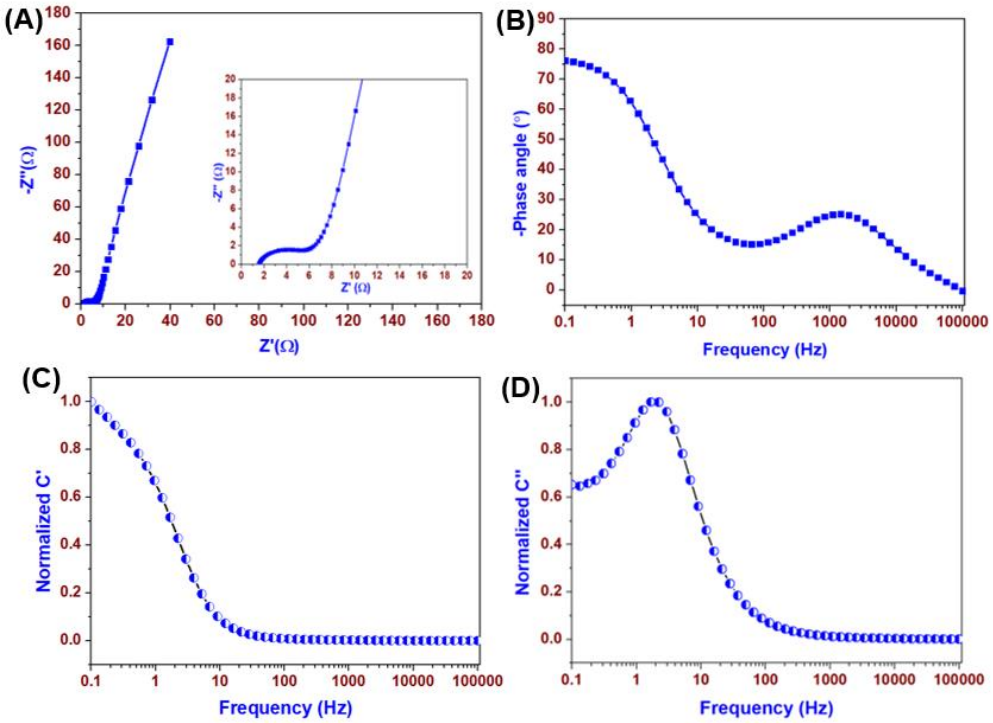

Figure 4.9. EIS analysis of Cu_2MoS_4 SSC device (A) Nyquist plot (the inset shown in Fig. 4.9 (A) represents the enlarged portion of Nyquist plot in the high-frequency region), (B) Bode phase angle plot, (C) Normalized real component of capacitance as a function of frequency and (D) Normalized imaginary component of capacitance as a function of frequency.

EIS is a prominent technique useful for understanding the charge-transfer mechanism and capacitive behavior of an electrolyte/electrode interfacial system [49]. The EIS analysis of Cu_2MoS_4 SSC device was performed in the frequency range of 0.1 Hz to 100 KHz at open circuit potential, and the results are analyzed using Nyquist and Bode phase angle plots. The

Nyquist plot of the Cu_2MoS_4 SSC device (Figure 4.9(A)) depicts the presence of a small semicircle in the high-frequency region (ideal resistor) and a vertically linear line (Warburg line) in the low-frequency region (ideal capacitor) [50]. The inset of Figure 4.9 (A) shows the enlarged portion of the high-frequency region from which the solution resistance (R_s), and charge-transfer resistance (R_{ct}) are found to be 1.53 and 4.83 Ω, respectively. The Warburg line observed at the low-frequency region is running almost parallel to the imaginary axis of the impedance, thus, suggesting the ideal capacitive nature of the Cu_2MoS_4 SSC device. From Figure 4.9 (B), the phase angle in the low-frequency region is about -76.23°, which further highlights the ideal capacitive nature of Cu_2MoS_4 SSC device [51]. Figure 4.9 (C and D) represents the plot of real (*C'*) and imaginary (*C"*) specific capacitance of the Cu_2MoS_4 SSC device with respect to the applied frequency using the given relations [30]:

$$C'(\omega) = - Z''(\omega)/ (\omega|Z(\omega)|)^2 \quad \ldots\ldots\ldots\ldots (6)$$

$$C'' (\omega) = Z' (\omega)/ (\omega|Z(\omega)|)^2 \quad \ldots\ldots\ldots\ldots (7)$$

Here, *C'* and *C"* represent the real and imaginary component of the specific capacitance of Cu_2MoS_4 SSC device. Figure 4.9 (C) shows that the real components of capacitance are higher at low frequencies, at which the Cu_2MoS_4 SSC device behaves like a capacitor, at high frequencies, the Cu_2MoS_4 SSC device instead behaves like a resistor [52]. Figure 4.9 (D) illustrates the imaginary components of capacitance (*C"*) against the applied frequencies, and it shows that the imaginary component of capacitance (*C"*) can reach maxima at a certain frequency, defining the relaxation time of the system [53]. The relaxation time constant represents the resistive behavior at frequencies above ($1/ \tau_o$) and capacitive behavior at frequencies below ($1/ \tau_o$) [54]. The time constant corresponds to the rate at which the system will be discharged; the relaxation time (τ) of the Cu_2MoS_4 SSC device was found to be 0.433 s.

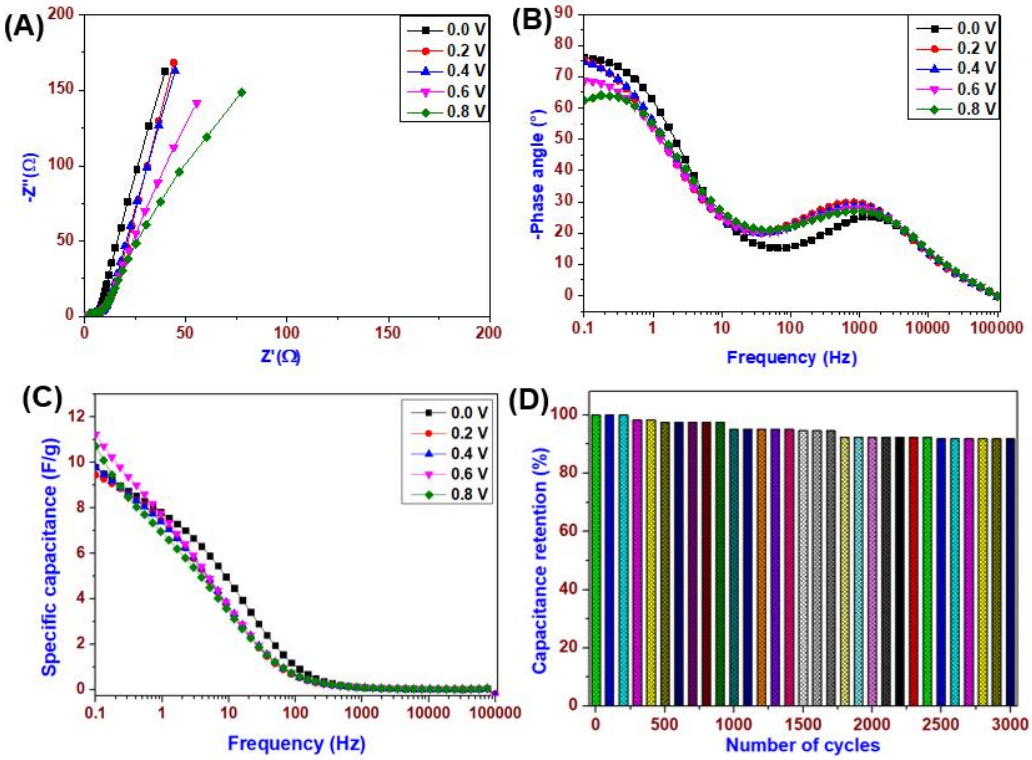

Figure. 4.10 (A) Nyquist plot at different applied potential, (B) Bode phase angle plot, (C) variation of specific capacitance concerning frequency of Cu_2MoS_4 SSC device and (D) The cyclic stability Cu_2MoS_4 SSC device over 3000 cycles.

Further, the EIS analysis of Cu_2MoS_4 SSC device as performed at a fixed electrode potential (0.0 to 0.8 V) is shown in Figure 4.10 (A). The Nyquist plot reveals that with an increase in applied potential the Warburg line deviated (away) from the imaginary axis (-Z'') gradually which might be due to faster ionic diffusion in the electrode material representing the higher contribution of pseudocapacitance [55]. The Bode phase angle plot in Figure 4.10 (B) shows the variation in phase angle in the low-frequency region (-76.23° to -62.49°) with an increase in the applied potential from 0.0 to 0.8 V, suggesting that contribution of pseudocapacitive nature is due to ion-intercalation/de-intercalation at the electrode. The variation of specific capacitance of Cu_2MoS_4 SSC device as a function of frequency with an increase in potential is shown in Figure 4.10 (C) using the relation [30]:

$$C_s = -1 / (2\pi f Z'') \ldots\ldots\ldots\ldots (8)$$

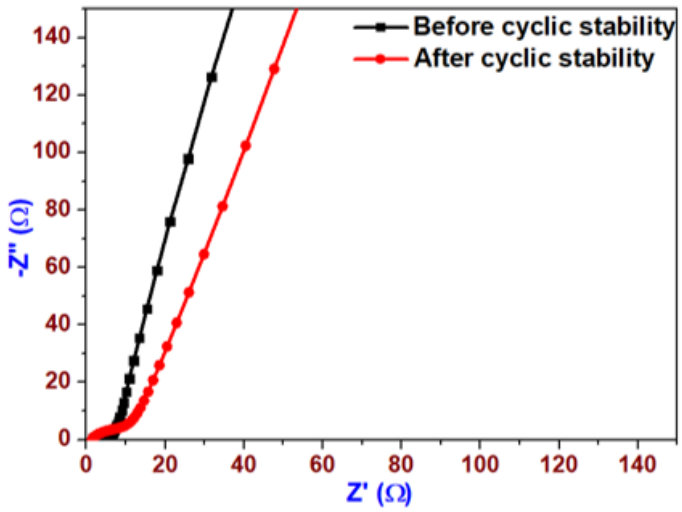

Figure 4.11. Nyquist plot of Cu_2MoS_4 SSC device before and after cyclic stability tests.

Here "C_s" is the specific capacitance of the SSC device, and "f" is the applied frequency, and "Z''" is the imaginary component of impedance. It represents that the specific capacitance of the Cu_2MoS_4 SSC device is initially about 9.23 F g^{-1} which is closer to that of the capacitance obtained from CV profiles. Further, the specific capacitance of the SSC device is increasing gradually from 9.23 to 11.4 F g^{-1} with an increase in applied potential from 0.0 to 0.8 V. These studies evidence the role of pseudocapacitance due to ion intercalation/de-intercalation phenomenon on the energy storage properties of Cu_2MoS_4 SSC device. The cyclic stability of a supercapacitor device is an important parameter which can determine its practical application [56]. The cyclic stability of the Cu_2MoS_4 SSC device was tested using continuous charge-discharge cycles at a constant current density of 1 mA cm^{-2} over 3000 cycles as displayed in Figure 4.10 (D). The capacitance retention of the SSC device after 3000 cycles is remarkable, ~ 91.78% of the initial capacitance. During the first few cycles (up to 200 cycles) the capacitance value is constant, after that it starts to decrease (up to 1700 cycles). After 1700 cycles, the specific capacitance value becomes constant without any degradation, confirming excellent cyclic

stability. Figure 4.11 shows the comparative Nyquist plot of the Cu_2MoS_4 SSC device measured before and after the cyclic tests. The solution resistance *(R_s)* and charge-transfer resistance *(R_{ct})* of the Cu_2MoS_4 SSC device changes from 1.53 to 1.42 Ω, and 4.83 to 7.4 Ω, respectively which might explain the observed capacitance decay of 9 % after 3000 cycles. The excellent electrochemical performance and better stability of Cu_2MoS_4 SSC device suggest that the Cu_2MoS_4 pseudocapacitive electrode material is a promising candidate for future-generation energy storage applications.

Table 4.1 Summary of electrochemical performance of Cu_2MoS_4 electrode and recently reported electrode materials using three-electrode configurations.

S. No	Material	Preparation method	Specific capacitance ($F\ g^{-1}$)	Reference
1	MoS_2	Hydrothermal	92.85	[36]
2	CuS	Sonochemically	62.77	[37]
3	CuO	Wet chemical method	88.5	[44]
4	MoO_3	Solution combustion method	108.88	[43]
5	RuO_2	Chemical synthesis	50	[57]
6	WS_2	Chemical exfoliation	40	[58]
7	ZnS	Solvothermal	32.8	[12]
8	$CuSbSe_2$	Colloidal method	34	[20]
9	$CuSbS_2$	Colloidal method	22	[20]
10	**Cu_2MoS_4**	**Hydrothermal**	**129.68**	**This work**

Table 4.2 Summary of electrochemical performance of Cu_2MoS_4 SSC device and recently reported SSC devices.

S. No	Material	Specific capacitance ($F\ g^{-1}$)	Energy density ($Wh\ kg^{-1}$)	Power density ($W\ kg^{-1}$)	Reference
1	FeS	4.62	2.56	1018	[48]
2	MXene	4.9	0.089	700	[59]
3	RuS_2	17	1.51	40	[30]

4	$Cu_{12}Sb_4S_{13}$	26	0.85	320	[60]
5	Cu_3SbS_3	19	0.7	380	[60]
6	Cu_3SbS_4	17.8	0.62	410	[60]
7	Porous carbon	-	2.2	300	[61]
8	Ni_2P	1.7	0.24	170	[62]
9	**Cu_2MoS_4**	**28.25**	**3.92**	**1250**	**This work**

4.4 Conclusions

In conclusion, we have successfully prepared Cu_2MoS_4 via a facile hydrothermal approach and investigated their electrochemical performance in three electrode system and SSC device in the aqueous Na_2SO_4 electrolyte. The physicochemical characterization such as XRD, FE-SEM, and laser Raman analyses confirmed the formation of I-phase Cu_2MoS_4 nanostructures with tetragonal *P42m* symmetry. The electrochemical analysis using three-electrode configuration revealed that the charge-storage mechanism in Cu_2MoS_4 electrode via the surface adsorption of electrolyte ions and the ion insertion/extraction phenomenon. The electrochemical performance of Cu_2MoS_4 SSC device indicates the pseudocapacitive nature of Cu_2MoS_4 with high specific capacitance 28.25 F g^{-1} at a current density of 0.25 mA cm^{-2} with excellent rate capability. The device acquired a high energy density and power density of 3.92 Wh kg^{-1} and 1250 W kg^{-1}, respectively. The charge storage mechanism of the Cu_2MoS_4 SSC device was investigated using EIS. Collectively, our research work not only recommends that Cu_2MoS_4 is a favorable electrode material for pseudocapacitance but also open a new horizon in the development of chalcogenide-based materials for energy storage application.

4.5 References

1 N. R. Chodankar, D. P. Dubal, G. S. Gund and C. D. Lokhande, *Electrochim. Acta*, 2015, **165**, 338–347.

2 D. P. Dubal, N. R. Chodankar, D.-H. Kim and P. Gomez-Romero, *Chem. Soc. Rev.*

3 T. Zhang, N. Imanishi, Y. Shimonishi, A. Hirano, Y. Takeda, O. Yamamoto and N. Sammes, *Chem. Commun.*, 2010, **46**, 1661–1663.

4 C. Galeano, C. Baldizzone, H. Bongard, B. Spliethoff, C. Weidenthaler, J. C. Meier, K. J. J. Mayrhofer and F. Schüth, *Adv. Funct. Mater.*, 2014, **24**, 220–232.

5 P. Pazhamalai, K. Krishnamoorthy and S. J. Kim, *Int. J. Hydrogen Energy*, 2016, **41**, 14830–14835.

6 S. Manoharan, S. Sahoo, P. Pazhamalai and S. J. Kim, *Int. J. Hydrogen Energy*, 2018, **43**, 1667–1674.

7 S. Sahoo, K. K. Naik and C. S. Rout, *Nanotechnology*, 2015, **26**, 455401.

8 K. Krishnamoorthy, P. Pazhamalai, S. Sahoo and S.-J. Kim, *J. Mater. Chem. A*, 2017, **5**, 5726–5736.

9 D. P. Dubal, P. Gomez-Romero, B. R. Sankapal and R. Holze, *Nano Energy*, 2015, **11**, 377–399.

10 G. K. Veerasubramani, K. Krishnamoorthy and S. J. Kim, *RSC Adv.*, 2015, **5**, 16319–16327.

11 K. Jeyasubramanian, T. S. Gokul Raja, S. Purushothaman, M. V. Kumar and I. Sushmitha, *Electrochim. Acta*, 2017, **227**, 401–409.

12 R. Ramachandran, M. Saranya, P. Kollu, B. P. C. Raghupathy, S. K. Jeong and A. N. Grace, *Electrochim. Acta*, 2015, **178**, 647–657.

13 S. Sahoo, K. K. Naik, D. J. Late and C. S. Rout, *J. Alloys Compd.*, 2017, **695**, 154–161.

14 S. Sahoo and C. S. Rout, *Electrochim. Acta*, 2016, **220**, 57–66.

15 G. A. Muller, J. B. Cook, H.-S. Kim, S. H. Tolbert and B. Dunn, *Nano Lett.*, 2015, **15**, 1911–1917.

16 X. Peng, L. Peng, C. Wu and Y. Xie, *Chem. Soc. Rev.*, 2014, **43**, 3303–3323.

17 S. S. Karade, D. P. Dubal and B. R. Sankapal, *ChemistrySelect*, 2017, **2**, 10405–10412.

18 S. S. Karade, D. P. Dubal and B. R. Sankapal, *RSC Adv.*, 2016, **6**, 39159–39165.

19 G. K. Veerasubramani, K. Krishnamoorthy, R. Sivaprakasam and S. J. Kim, *Mater. Chem. Phys.*, 2014, **147**, 836–842.

20 K. Ramasamy, R. K. Gupta, S. Palchoudhury, S. Ivanov and A. Gupta, *Chem. Mater.*, 2014, **27**, 379–386.

21 C. J. Crossland, P. J. Hickey and J. S. O. Evans, *J. Mater. Chem.*, 2005, **15**, 3452–3458.

22 E. A. Pruss, B. S. Snyder and A. M. Stacy, *Angew. Chemie Int. Ed.*, 1993, **32**, 256–257.

23 W. Chen, H. Chen, H. Zhu, Q. Gao, J. Luo, Y. Wang, S. Zhang, K. Zhang, C. Wang and Y. Xiong, *Small*, 2014, **10**, 4637–4644.

24 P. D. Tran, M. Nguyen, S. S. Pramana, A. Bhattacharjee, S. Y. Chiam, J. Fize, M. J. Field, V. Artero, L. H. Wong and J. Loo, *Energy Environ. Sci.*, 2012, **5**, 8912–8916.

25 K. Zhang, Y. Lin, C. Wang, B. Yang, S. Chen, S. Yang, W. Xu, H. Chen, W. Gan and Q. Fang, *J. Phys. Chem. C*, 2016, **120**, 13120–13125.

26 Y. W. Denis, R. L. Lee, R. Yi, S. Y. Chiam and P. D. Tran, *Electrochim. Acta*, 2014, **115**, 337–343.

27 N. Ma, B. Wei, W. Cao, H. Gao and L. Xu, *Mater. Lett.*, 2017, **197**, 79–82.

28 K. Zhang, W. Chen, Y. Lin, H. Chen, Y. A. Haleem, C. Wu, F. Ye, T. Wang and L. Song, *Nanoscale*, 2015, **7**, 17998–18003.

29 W. Wang, P. Zhang, L. Peng, W. Xie, G. Zhang, Y. Tu and W. Mai, *CrystEngComm*, 2010, **12**, 700–701.

30 K. Krishnamoorthy, P. Pazhamalai and S. J. Kim, *Electrochim. Acta*, 2017, **227**, 85–94.

31 X. Hu, W. Shao, X. Hang, X. Zhang, W. Zhu and Y. Xie, *Angew. Chemie Int. Ed.*, 2016, **55**, 5733–5738.

32 H. Chen, K. Zhang, W. Chen, I. Ali, P. Wu, D. Liu and L. Song, *AIP Adv.*, 2015, **5**, 37141.

33 A. Ahlawat and V. G. Sathe, *J. Raman Spectrosc.*, 2011, **42**, 1087–1094.

34 N. T. Liang, W. S. Tse, M. C. Chang, H. T. Chen and T. T. Chen, *J. Raman Spectrosc.*, 1993, **24**, 179–181.

35 T. Siciliano, A. Tepore, E. Filippo, G. Micocci and M. Tepore, *Mater. Chem. Phys.*, 2009, **114**, 687–691.

36 K. Krishnamoorthy, G. K. Veerasubramani, S. Radhakrishnan and S. J. Kim, *Mater. Res. Bull.*, 2014, **50**, 499–502.

37 K. Krishnamoorthy, G. K. Veerasubramani, S. Radhakrishnan and S. J. Kim, *J. Nanosci. Nanotechnol.*, 2015, **15**, 4409–4413.

38 K. V. Sankar, S. Surendran, K. Pandi, A. M. Allin, V. D. Nithya, Y. S. Lee and R. K. Selvan, *RSC Adv.*, 2015, **5**, 27649–27656.

39 S. Ardizzone, G. Fregonara and S. Trasatti, *Electrochim. Acta*, 1990, **35**, 263–267.

40 A. Fabre, T. Steur, W. G. Bouwman, M. T. Kreutzer and J. R. van Ommen, *J. Phys. Chem. C*, 2016, **120**, 20446–20453.

41 K. V. Sankar, R. K. Selvan and D. Meyrick, *RSC Adv.*, 2015, **5**, 99959–99967.

42 S. Vijayakumar, S. Nagamuthu, S.-H. Lee and K.-S. Ryu, *Int. J. Hydrogen Energy*, 2017, **42**, 3122–3129.

43 G. P. Nagabhushana, D. Samrat and G. T. Chandrappa, *RSC Adv.*, 2014, **4**, 56784–56790.

44 Y. X. Zhang, M. Huang, F. Li and Z. Q. Wen, *Int. J. Electrochem. Sci*, 2013, **8**, 8645–8661.

45 A. Devadas, S. Baranton, T. W. Napporn and C. Coutanceau, *J. Power Sources*, 2011, **196**, 4044–4053.

46 D. P. Dubal, N. R. Chodankar, G. S. Gund, R. Holze, C. D. Lokhande and P. Gomez-Romero, *Energy Technol.*, 2015, **3**, 168–176.

47 K. Krishnamoorthy, P. Pazhamalai, G. K. Veerasubramani and S. J. Kim, *J. Power Sources*, 2016, **321**, 112–119.

48 S. S. Karade, P. Dwivedi, S. Majumder, B. Pandit and B. R. Sankapal, *Sustain. Energy Fuels*, 2017, **1**, 1366–1375.

49 S. K. Shinde, D. P. Dubal, G. S. Ghodake and V. J. Fulari, *RSC Adv.*, 2015, **5**, 4443–4447.

50 S. Xu, T. Wang, Y. Ma, W. Jiang, S. Wang, M. Hong, N. Hu, Y. Su, Y. Zhang and Z. Yang, *ChemSusChem*, 2017, **10**, 4056–4065.

51 D. P. Dubal, N. R. Chodankar, A. Vinu, D.-H. Kim and P. Gomez-Romero, *ChemSusChem*, 2017, **10**, 2742–2750.

52 P. L. Taberna, P. Simon and J.-F. Fauvarque, *J. Electrochem. Soc.*, 2003, **150**, A292–A300.

53 G. Zhao, N. Zhang and K. Sun, *Mater. Res. Bull.*, 2013, **48**, 1328–1332.

54 J. M. Soon and K. P. Loh, *Electrochem. Solid-State Lett.*, 2007, **10**, A250–A254.

55 S. T. Senthilkumar, R. K. Selvan, J. S. Melo and C. Sanjeeviraja, *ACS Appl. Mater. Interfaces*, 2013, **5**, 10541–10550.

56 N. I. Chandrasekaran and M. Manickam, *Int. J. Hydrogen Energy*, 2017, **42**, 26475–26487.

57 V. D. Patake and C. D. Lokhande, *Appl. Surf. Sci.*, 2008, **254**, 2820–2824.

58 C. C. Mayorga-Martinez, A. Ambrosi, A. Y. S. Eng, Z. Sofer and M. Pumera, *Electrochem. commun.*, 2015, **56**, 24–28.

59 R. B. Rakhi, B. Ahmed, M. N. Hedhili, D. H. Anjum and H. N. Alshareef, *Chem. Mater.*, 2015, **27**, 5314–5323.

60 K. Ramasamy, R. K. Gupta, H. Sims, S. Palchoudhury, S. Ivanov and A. Gupta, *J. Mater. Chem. A*, 2015, **3**, 13263–13274.

61 D. Wang, F. Li, M. Liu, G. Q. Lu and H. Cheng, *Angew. Chemie*, 2008, **120**, 379–382.

62 W. Du, R. Kang, P. Geng, X. Xiong, D. Li, Q. Tian and H. Pang, *Mater. Chem. Phys.*, 2015, **165**, 207–214.

CHAPTER – 5

Copper molybdenum sulfide nanoparticles embedded on graphene sheets as advanced electrode for wide temperature-tolerant supercapacitor

Highlights

- A novel hybrid of Cu_2MoS_4 nanoparticles embedded on reduced graphene oxide (rGO) sheets is prepared via a one-pot hydrothermal method without any surfactants or templates.
- The electrochemical properties of the as-prepared Cu_2MoS_4-rGO electrode are investigated as an advanced electrode for supercapacitor application, and it exhibits higher specific capacitance (231.51 F g^{-1} at 5 mV s^{-1}) compare to the pristine Cu_2MoS_4 electrode (135.78 F g^{-1} at 5 mV s^{-1}).
- The Cu_2MoS_4-rGO electrode obtained an energy density of 31.92 Wh kg^{-1} at a constant current of 1.5 mA, which is higher than the pristine Cu_2MoS_4 electrode (17.91 Wh kg^{-1} at a constant current of 1.5 mA).
- Further, this work represents an extensive study about the effect of temperature (from 25 °C to 80 °C) on the Cu_2MoS_4-rGO electrode in aqueous Na_2SO_4 electrolyte.
- The effect of temperature on the electrochemical properties of Cu_2MoS_4-rGO electrode is investigated using cyclic voltammetry (CV), charge-discharge (CD) and electrochemical impedance spectroscopy (EIS).
- The electrochemical performance of the Cu_2MoS_4-rGO electrode exhibited ~ 128 % improvement at 80 °C compared to that at 25 °C in CD profile.

5.1 Introduction

Supercapacitors have considered as a vital energy storage device for the sustainable development of current and future societies and developing the industrial application.[1–3] It is well known that the traditional supercapacitors comprise of electric double-layer capacitors (EDLCs) arising from ion adsorption/desorption, and pseudocapacitors originating from fast Faradic reactions.[4,5] Whatever the type of supercapacitors, electrode materials play a key role in the energy storage performance of supercapacitor. Recently, Layered transition-metal chalcogenides (LTMCs) have concerned due to their potential applications in energy storage and conversions.[6,7] Precisely, LTMCs comprise of covalently bound layers of metal atoms bridged by sulfur atoms and have only weak van der Waals relations between these layers.[8] The literature on the energy storage performance of these LTMCs recommended more exertion are required to improve the specific capacitance and energy density of supercapacitors using these materials. Common strategies used for improving the performance metrics of LTMCs based supercapacitor by fabrication of composite electrode. In the past few years, self-assembling two-dimensional materials such as graphene, MXenes, siloxene, metalenes, LTMCs, and their mixed composite/hybrids electrode opens a new pathway for enhancing the performance of supercapacitor.[9–11] Moreover, as energy storage devices, the effect of operating temperature on supercapacitors play a crucial role in specific applications such as industrial, military, electric vehicles and space applications.[12,13] The temperature effects on the capacitive behavior of supercapacitors are not-completely understood up to date since most of the studies focused on their performance at room temperature and very few have done temperature-dependent studies. At first, Masarapu et al. have studied the electrochemical performance of carbon nanotube using 1 M $TEABF_4$ electrolyte at the temperature between 25 °C and 100 °C.[14] Later on, Zhang et al. performed the temperature dependent supercapacitor of carbon fiber@$NiCo_2O_4$@$Ni(OH)_2$

electrode in 1 M KOH electrolyte at different temperatures from 0 °C to 60 °C.[15] Similarly, Lee et al. and Wang et al. presented the effect of temperature on the specific capacitance of MnO_2 electrode at 0 °C to 75 °C temperature in aqueous Na_2SO_4 electrolyte.[16]

In this scenario, copper molybdenum sulfide (Cu_2MoS_4) is one of the most promising LTMCs with interesting properties such as electrochemical energy storage, photocatalysis and electrochemical hydrogen evolution.[17] In the structure of Cu_2MoS_4, the multi-valence of Mo can be a possibility of conversion reaction with S will give a high electrochemical performance.[18] Likewise, the presence of Cu in Cu_2MoS_4 can also be crucial for enhancing the electrochemical properties.[18] In 2012, Tran et al. demonstrated the electrocatalyst for hydrogen evolution reaction (HER) for Cu_2MoS_4 electrode in aqueous electrolyte solutions over a wide range of pH values (pH 0 to 7).[19] Later on, Chen et al. studied the electrocatalytic hydrogen evolution reaction (HER), photocatalytic degradation of rhodamine B (RhB) and conversion of benzyl alcohol of I-Cu_2MoS_4.[20] These investigations based on Cu_2MoS_4 recommended that few more captivating properties are expected in the field of energy storage and conversion. In our earlier study, our research group has been studied the electrochemical performance (as supercapacitor) of planner and a binder-free Cu_2MoS_4 electrode in the aqueous electrolyte at room temperature.[17,21] For enhancing the electrochemical performance of Cu_2MoS_4, the fabrication of composite/hybrid electrodes are required using the carbon-based material.[22] Graphene is the renowned two-dimensional carbon material consist of all-sp^2-hybridized carbon monolayers with some of the most interesting properties, such as high electrical and thermal conductivity, highly surface area and chemical stability.[23–25] In the case of graphene based hybrid supercapacitor electrode, graphene can provide excellent intrinsic electrical conductivity and large surface area for Cu_2MoS_4 in ion-transport kinetics during the electrochemical charging and discharging process.[18]

Therefore, we designed to investigate the electrochemical energy storage properties of Cu_2MoS_4-rGO hybrid with captivating the synergistic effect between Cu_2MoS_4 and graphene nanosheets in this work. Herein, we fabricated Cu_2MoS_4-rGO hybrid by one step hydrothermal approach and investigated their temperature dependent capacitive properties (25 °C to 80 °C) using a three-electrode configuration.

5.2 Experimental section

5.2.1 Materials

Copper (I) oxide (Cu_2O), sodium molybdate ($Na_2MoO_4{\cdot}2H_2O$), thioacetamide (CH_3CSNH_2), ethylene glycol, N-methyl pyrrolidone (NMP), Potassium permanganate ($KMnO_4$), sodium sulfate (Na_2SO_4), hydrogen peroxide (H_2O_2), ethanol (C_2H_5OH) and sulfuric acid (H_2SO_4) were bought from Daejung Chemicals Ltd., South Korea. Graphite powder and polyvinylidene fluoride (PVDF) were purchased Sigma Aldrich, South Korea. Carbon black is procured from Alfa aesar, South Korea.

5.2.2 Synthesis of Cu_2MoS_4 nanostructures

Cu_2MoS_4 nanostructures were synthesized using hydrothermal method as described in our previous report.[17] Briefly, Cu_2MoS_4 nanostructures were synthesized using $Na_2MoO_4{\cdot}2H_2O$ and CH_3CSNH_2 as the starting precursors. Initially, $Na_2MoO_4{\cdot}2H_2O$ (0.12 g) and CH_3CSNH_2 (0.24 g) were dissolved in ethylene glycol using ultra-sonication process. Then Cu_2O (0.08 g) was introduced to the above precursor solution and kept it for ultra-sonication. After ultra-sonication for 2 h, the mixture was transferred to an autoclave (100 mL Teflon lined stainless steel), and the hydrothermal reaction was carried out at 150 °C for 15 h. The resulted products were obtained by centrifugation using water and ethanol several times. Finally, the collected product (brown color) was dried at 60 °C overnight.

5.2.3 Synthesis of Cu_2MoS_4-rGO hybrid

The graphene oxide (GO) was synthesized by a modified Hummers method according to our previous report.[26] The obtained GO was dispersed in 60 mL ethylene glycol by ultra-sonication for 1 h to form homogeneous GO dispersion. Then $Na_2MoO_4 \cdot 2H_2O$ and CH_3CSNH_2 were added into GO aqueous solution and kept it for ultra-sonication for 30 min. After that Cu_2O was added into the above suspension solution. After sonicated for another 1 h, the blended solution was sealed into a 100 mL Teflon lined stainless steel autoclave and kept it in a hot air oven for hydrothermal reaction at 150 °C for 15 h. The Cu_2MoS_4-rGO precipitates were collected by centrifuging process using water and absolute ethanol and dried at 60 °C for 12 h.

5.2.4 Instrumentation

The crystal structure of Cu_2MoS_4 and Cu_2MoS_4-rGO hybrid was obtained using a Rigaku X-ray diffractometer (XRD) instrument (Bruker Co, Billerica, Massachussets, USA) using Cu-Kα radiation (λ = 1.54184 Å). Raman spectroscopy of Cu_2MoS_4 and Cu_2MoS_4-rGO hybrid was performed using LabRam HR Evolution Raman spectrometer (Horiba Jobin-Yvon, France, at laser excitation source of wavelength 514 nm). The morphological analysis of Cu_2MoS_4 and Cu_2MoS_4-rGO hybrid were performed using field-emission scanning electron microscopy (TESCAN, MIRA3) under different magnifications. The elemental chemical surface states of the Cu_2MoS_4 and Cu_2MoS_4-rGO hybrid were obtained by X-ray photoelectron spectroscopy (XPS) techniques using ESCA-2000, VG Microtech Ltd. The specific surface area for the Cu_2MoS_4 and Cu_2MoS_4-rGO hybrid were analysed using Particle and Pore Size Analysis System (UPA-150, ASAP2010, Autopore IV)

5.2.5 Electrochemical analysis

The fabrication of the working electrode is described in our earlier work.[27] In detail, the active material (Cu_2MoS_4 and Cu_2MoS_4-rGO hybrid), carbon black and PVDF were mixed in the weight ratio of 85:10:5 using N-methyl pyrrolidone (NMP) into the slurry form using an agate-

mortar. Then, the slurry was coated on pre-cleaned stainless-steel (MTI, South Korea) substrate (1×1 cm^2) and allowed to dry at 60 °C in an oven overnight. The electroactive mass of the Cu_2MoS_4, rGO and Cu_2MoS_4-rGO is about 1 mg loaded on to the stainless-steel substrate is used for the electrochemical characterization. The mass of the active material was calculated from the difference between the mass of the substrate before and after coating using Dual-range Semi-micro Balance (AUW-220D, SHIMADZU) with an approximation of five-decimal points.

For three electrode tests, Cu_2MoS_4 and Cu_2MoS_4-rGO coated stainless steel, platinum and Ag/AgCl is used as a working electrode, a counter electrode, and a reference electrode, respectively. An aqueous solution of 1 M Na_2SO_4 is used as the electrolyte. The electrochemical performance of Cu_2MoS_4 and Cu_2MoS_4-rGO was investigated through cyclic voltammetry (CV), galvanostatic charge-discharge (CD), and electrochemical impedance spectroscopy (EIS) via three electrode system using an AUTOLAB PGSTAT302N electrochemical workstation. The specific capacitance (C_{sp}), energy density (E) and power density (P) of the Cu_2MoS_4 and Cu_2MoS_4-rGO electrode were calculated using the following relations:[27]

$$C_{sp} = [(\int I\,dV) / (s \times \Delta V \times m)] \quad \ldots\ldots\ldots\ldots (1)$$

$$C_{sp} = [(I \times \Delta t) / (\Delta V \times m)] \quad \ldots\ldots\ldots\ldots\ldots (2)$$

$$E = (I \times \Delta t \times \Delta V) / (7.2 \times m) \quad \ldots\ldots\ldots\ldots (3)$$

$$P = (3.6 \times E) / \Delta t \quad \ldots\ldots\ldots\ldots\ldots (4)$$

Here, "C_{sp}" is the specific capacitance (F g^{-1}), "I" is the current (A), "ΔV" is the potential window of the Cu_2MoS_4 and Cu_2MoS_4-rGO electrode, "s" is the scan rate (mV s^{-1}), "Δt" is the discharge time (s), and "m" is the mass of the active material (g).

5.3 Results and Discussion

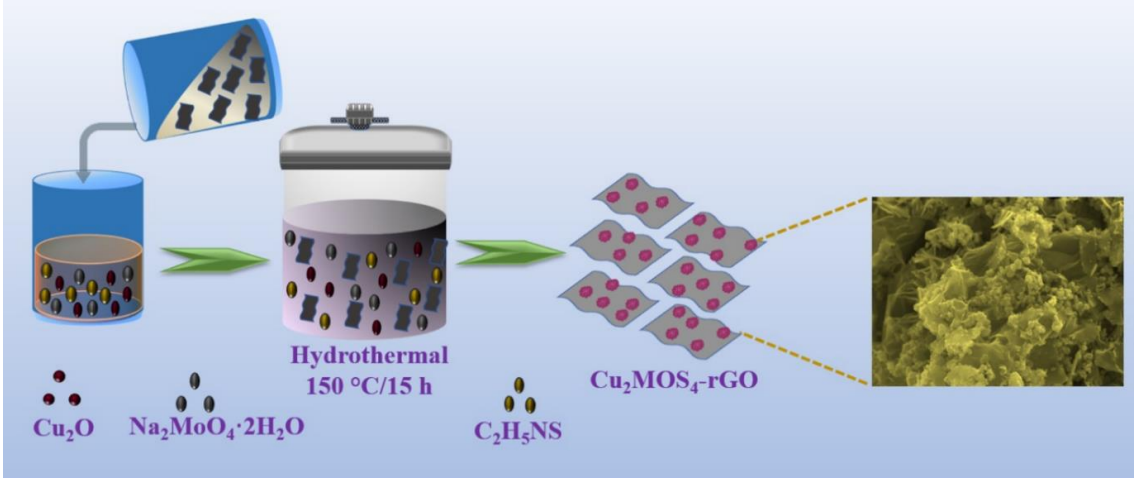

Figure 5.1 Schematic illustration of Cu_2MoS_4 nanoparticles embedded on graphene sheets by one-pot hydrothermal method.

The Cu_2MoS_4 and Cu_2MoS_4-rGO hybrid were prepared by facile hydrothermal approach (as displayed in Figure 5.1). Throughout the hydrothermal process, the MoO_4^{2-} ions and sulfur ions released from the sodium molybdate and thioacetamide precursors and reacts together, which consequence the formation of MoS_4^{2-} ions. Further, the Cu_2O reacts with the MoS_4^{2-} ions and forming the Cu_2MoS_4 nanostructure.[28] During the Cu_2MoS_4-rGO hybrid preparation, the Cu_2MoS_4 nanostructure not only interacted with the rGO sheets but also randomly decorated on the rGO sheets.[29] To explore the crystallinity and phase purities of the Cu_2MoS_4 and Cu_2MoS_4-rGO hybrid, we performed XRD analysis, and the corresponding result is demonstrated in Figure 5.2(A). As depicted in Figure 5.2(A) the distinctive peaks at 2θ =17.22°, 18.65°, 23.91°, 29.27°, 31.86°, 33.01°, 37.69°, 46.69°, 47.97°,48.69°, 51.01°, 52.67°, 56.89°, 59.42°, 69.50°, 72.18°, 74.17° and 79.20° correspond to the (002), (011), (110), (112), (013), (020), (004), (123), (220), (015), (024), (222), (132), (033), (040), (042), (141) and (242) crystal planes of tetragonal Cu_2MoS_4 as previously reported.[30] Additionally, three peaks (α) at 16.51°, 27.73°, and 41.23° can be successfully matched with the crystal planes of tetragonal Cu_2MoS_4 of another report.[19]

However, no other impurity peaks for MoS_2, NiS, and Cu_2S are noticed, signifying the formation of high purity and well crystalline Cu_2MoS_4. In the case of Cu_2MoS_4-rGO hybrid, the addition of rGO does not make any new crystal orientations of Cu_2MoS_4. Furthermore, no characteristic diffraction peak belongs to rGO is observed for Cu_2MoS_4-rGO hybrid, which might be due to less amount of rGO present in Cu_2MoS_4-rGO hybrid or relatively low diffraction intensity of rGO in the Cu_2MoS_4-rGO hybrid.[31] In the case of Cu_2MoS_4-rGO hybrid, few peaks are diminished due to the restacking inhibition of Cu_2MoS_4 by rGO nanosheets or a small amount of Cu_2MoS_4 might involve in the preparation of Cu_2MoS_4-rGO hybrid.[32,33]

Moreover, Cu_2MoS_4 and Cu_2MoS_4-rGO hybrid could be confirmed by Raman spectrum. Figure 5.2(B) displays the Raman spectrum for Cu_2MoS_4 and Cu_2MoS_4-rGO hybrid. The Cu_2MoS_4 and Cu_2MoS_4-rGO hybrid exhibit several characteristic Raman peaks in the frequency range of 100-2000 cm^{-1} belong to Cu_2MoS_4 and rGO. Mostly, the characteristic peaks of rGO are well referred to the D band and G band at 1354 and 1598 cm^{-1} respectively. The D-band is correlated to the edge defects, vacancies, and disordered carbon species in graphite layers, and G-band is owing to the plane vibration of sp^2 hybridized C-C atoms in the two-dimensional hexagonal lattice.[34,35] In case of Cu_2MoS_4 and Cu_2MoS_4-rGO hybrid, there are four small peaks visible in the frequency region of 100 to 800 cm^{-1} related to the Cu_2MoS_4. The Raman peaks located at 118 cm^{-1} belong to the B_2 mode, whereas 217 cm^{-1} belong to B_1 mode. It can be observed that the strongest peak at 430 cm^{-1} and weakest peak at 860 cm^{-1} can be assigned as a first-order and second-order peak. In the case of Cu_2MoS_4-rGO hybrid, the Raman peak at 430 cm^{-1} is disappeared compare to pristine Cu_2MoS_4. The disappearance of the Raman band at 430 cm^{-1} in the Cu_2MoS_4-rGO may be due to the generation of sulfur vacancies during the hydrothermal process of Cu_2MoS_4-rGO hybrid, which creates strain in the crystal structure and

changes in the restoring force constant in vibrational modes of the Cu_2MoS_4.[36,37] The observed Raman peaks are well matched with the crystalline Cu_2MoS_4.[31,38]

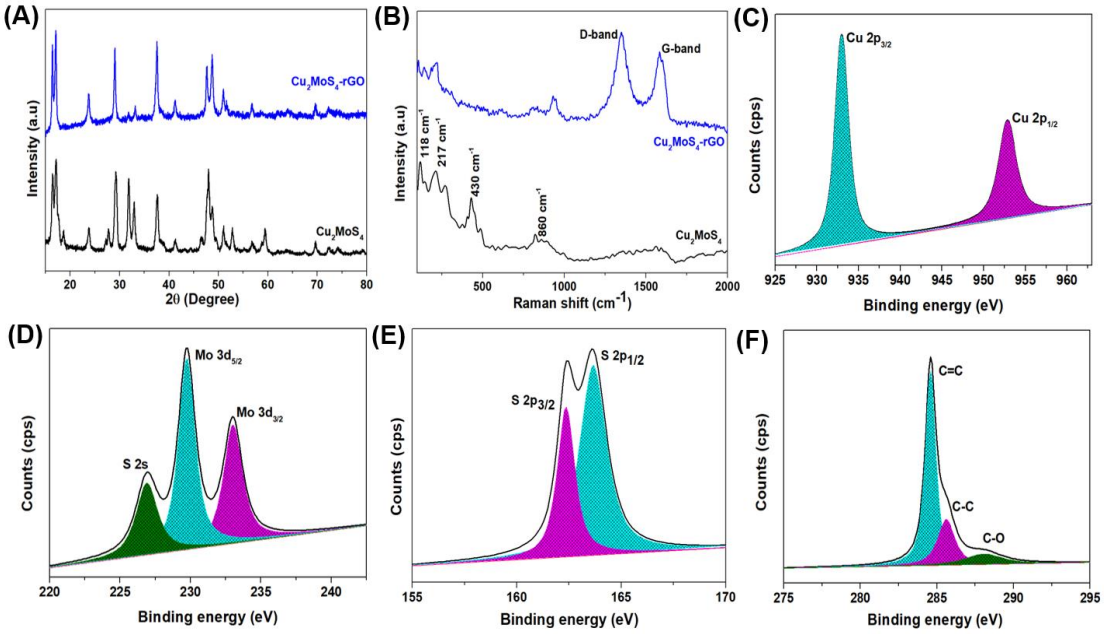

Figure 5.2 (A) X-ray diffraction pattern of as prepared Cu_2MoS_4 and Cu_2MoS_4-rGO hybrid and (B) laser Raman spectrum of Cu_2MoS_4 and Cu_2MoS_4-rGO hybrid. High resolution X-ray photoelectron spectrum (XPS) of as prepared Cu_2MoS_4-rGO hybrid (C) core level spectrum of Cu 2p state, (D) core level spectrum of Mo 3d state, (E) core level spectrum of S 2p state, and (F) core level spectrum of C 1s state.

To investigate the electronic state of the elements in compounds, XPS analysis of the Cu_2MoS_4-rGO and Cu_2MoS_4 was carried out and the results are shown in Figure 5.2, Figure 5.3 and Figure 5.4. Typical survey spectrum of Cu_2MoS_4-rGO hybrid confirmed the presence of Cu, Mo, S, C and O elements in the binding energy range of 0-1200 eV (shown in Figure 5.3(A). Figure 5.2 (C) represents the core level spectrum of Cu 2p and the binding energies noted at 932.94 eV, and 952.90 eV correspond to Cu $2p_{3/2}$ and Cu $2p_{1/2}$, respectively. As displayed in Figure 5.2(D), the deconvoluted spectra Mo 3d represent two strong peaks at the binding energy around 229.76 eV and 233.0 eV corresponding to the Mo^{4+} $3d_{5/2}$ and Mo^{4+} $3d_{3/2}$ states, respectively and a weak peak around 226 eV has been noticed which corresponds to the presence

of S 2s state. The core level spectrum (Figure 5.2(E)) for S 2p can be deconvoluted into two peaks (162.42 and 163.64 eV) correspond to the S $2p_{3/2,}$ and S $2p_{1/2}$ states, respectively. The XPS analysis suggests the successful formation of Cu_2MoS_4 in the Cu_2MoS_4-rGO hybrid, which is in good agreement with the previous literature.[21,31] The core-level spectrum of C 1s (as shown in Figure 5.2(F)) is deconvoluted into three peaks, which displayed an intense peak located at 284.61 eV is assigned to the functional groups of sp^2 bonded carbon C=C. Also, the low intense peaks noted at 285.69 eV and 288.28 eV correspond to the C-C and C-O, respectively. Figure 5.3(B) signifies the core level O 1s spectrum of Cu_2MoS_4-rGO hybrid, suggesting the presence of the O-C=O bond. The FE-SEM analysis was performed to analyze the morphology of the Cu_2MoS_4 and Cu_2MoS_4-rGO hybrid and the corresponding micrographs (at different magnification 30 Kx, 50 Kx and 200 Kx) are shown in Figure 5.4. The FE-SEM micrographs (Figure 5.4(A-C)) of Cu_2MoS_4 represent the formation of nanoparticle with the average size in the range of 50-60 nm. The FE-SEM micrographs of Cu_2MoS_4-rGO hybrid in Figure 5.4(D-F), identify that the Cu_2MoS_4 nanoparticles are uniformly distributed on the surfaces of graphene nanosheets.[39] In Cu_2MoS_4-rGO hybrid, the size of nanoparticles slightly decreases and the Cu_2MoS_4 nanoparticles are immersed into the rGO sheets, forming a 3D conductive network which enables the fast electron transport through the underlying rGO sheets to Cu_2MoS_4 nanoparticles and improving the electrochemical performance.[40] Energy dispersive X-ray (EDX) analysis (Figure 5.5) suggests that the five elements Cu, Mo, S, C, and O are there in Cu_2MoS_4-rGO hybrid. To know the homogenous distribution of Cu_2MoS_4 nanoparticles in the 3D graphene sheets, we performed the elemental mapping of Cu, Mo, S, C and O in Cu_2MoS_4-rGO hybrid (Figure 5.6(A–F)).

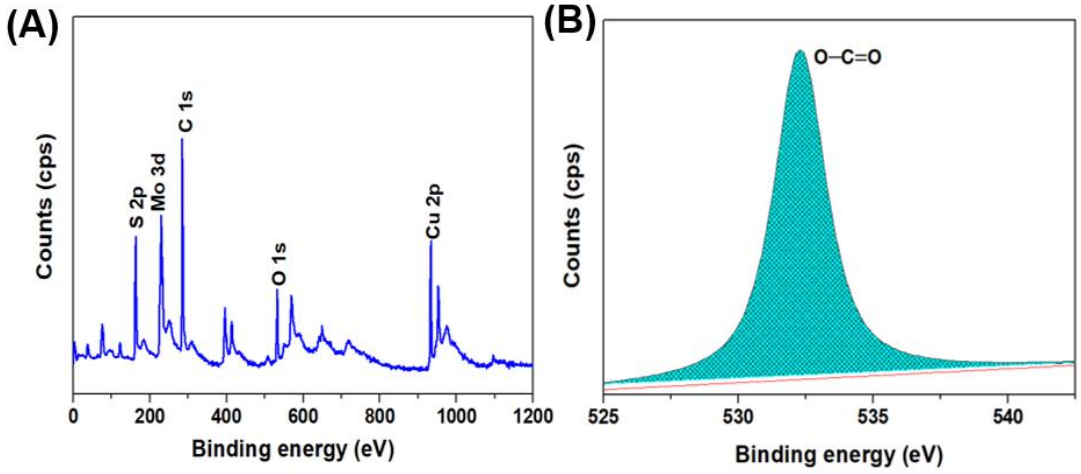

Figure 5.3 High resolution X-ray photoelectron spectrum (XPS) of as prepared Cu_2MoS_4-rGO hybrid (A) Survey spectrum in the range of 0 to 1200 eV, and (B) core level spectrum of O 1s state.

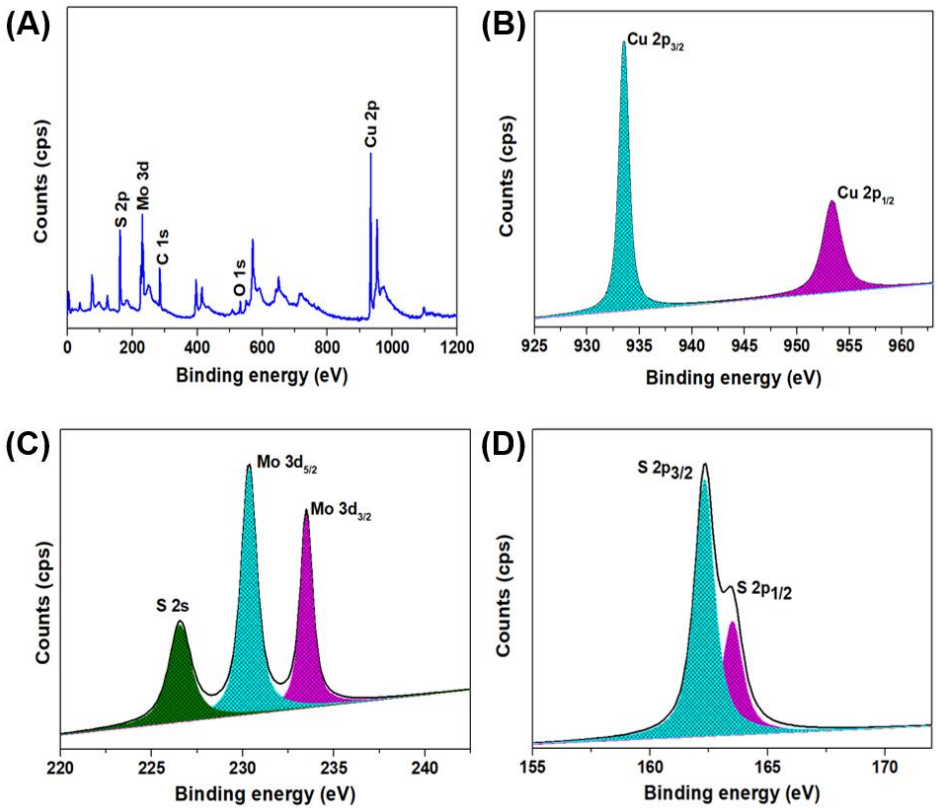

Figure 5.4 High resolution X-ray photoelectron spectrum (XPS) of as prepared Cu_2MoS_4 (A) Survey spectrum in the range of 0 to 1200 eV, (B) core level spectrum of Cu 2p state, (C) core level spectrum of Mo 3d state, (D) core level spectrum of S 2p state.

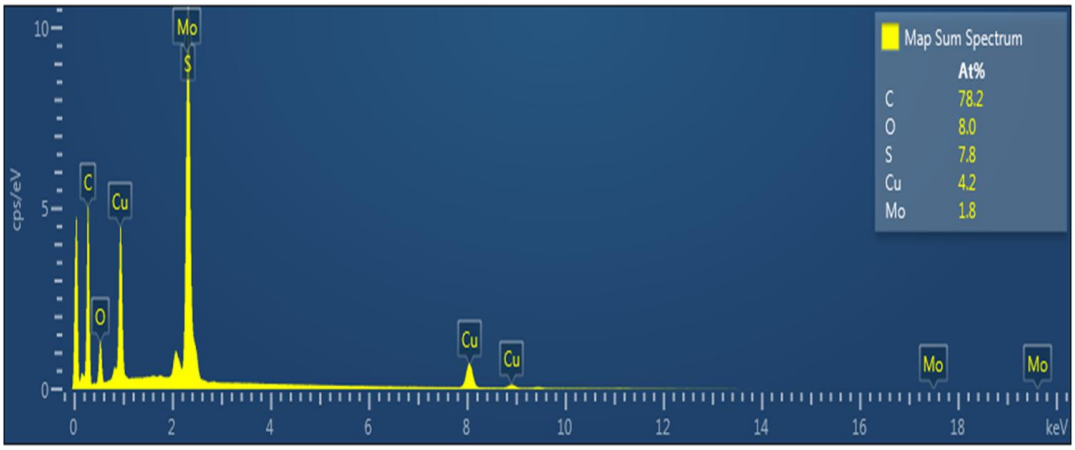

Figure 5.5. (A) Energy dispersive X-ray spectroscopic (EDS) analysis of Cu_2MoS_4-rGO hybrid.

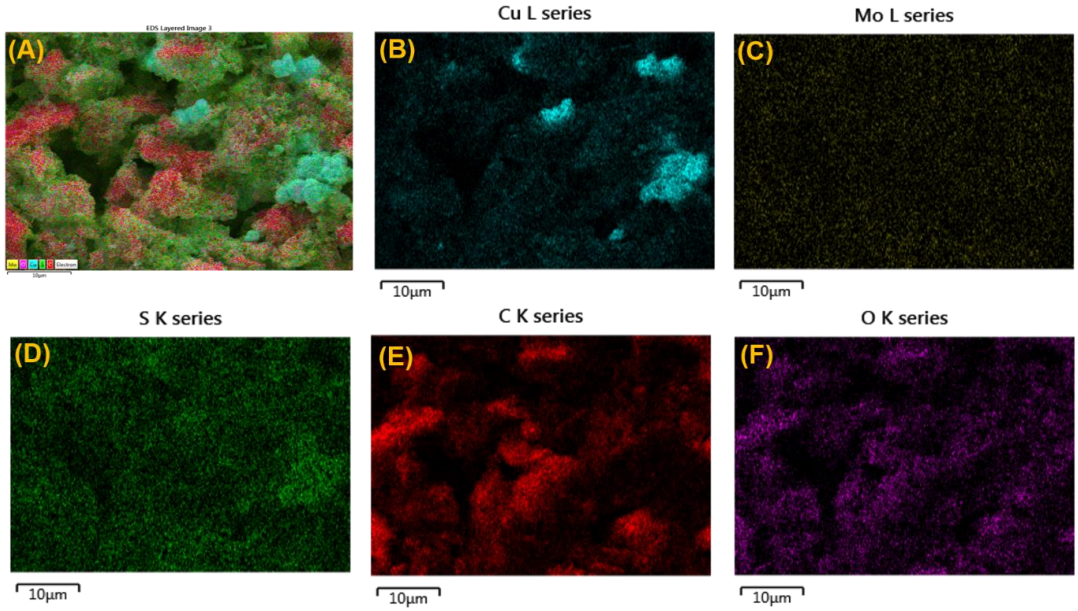

Figure 5.6 Elemental mapping of Cu_2MoS_4-rGO hybrid (A) FE-SEM micrographs for elemental mapping, (B) copper, (C) molybdenum, (D) sulfur, (E) carbon, and (F) oxygen.

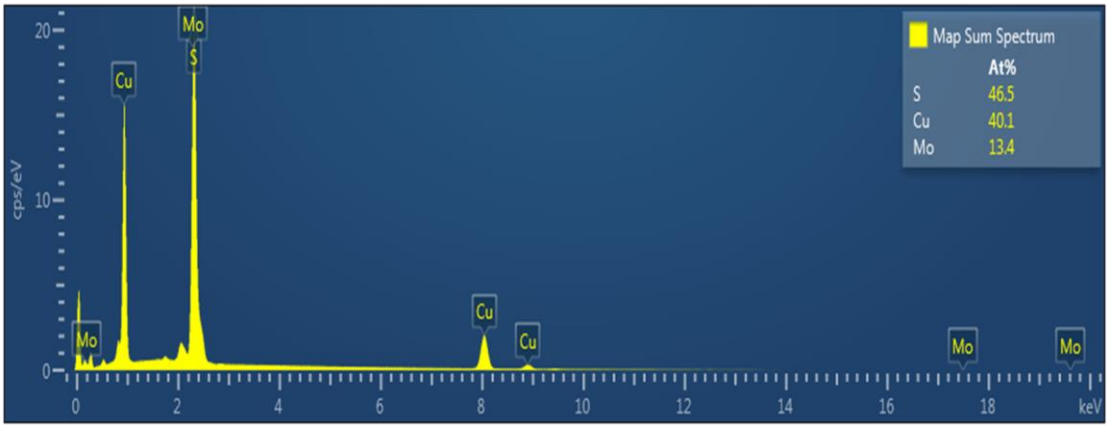

Figure 5.7. (A) Energy dispersive X-ray spectroscopic (EDS) analysis of as prepared Cu_2MoS_4.

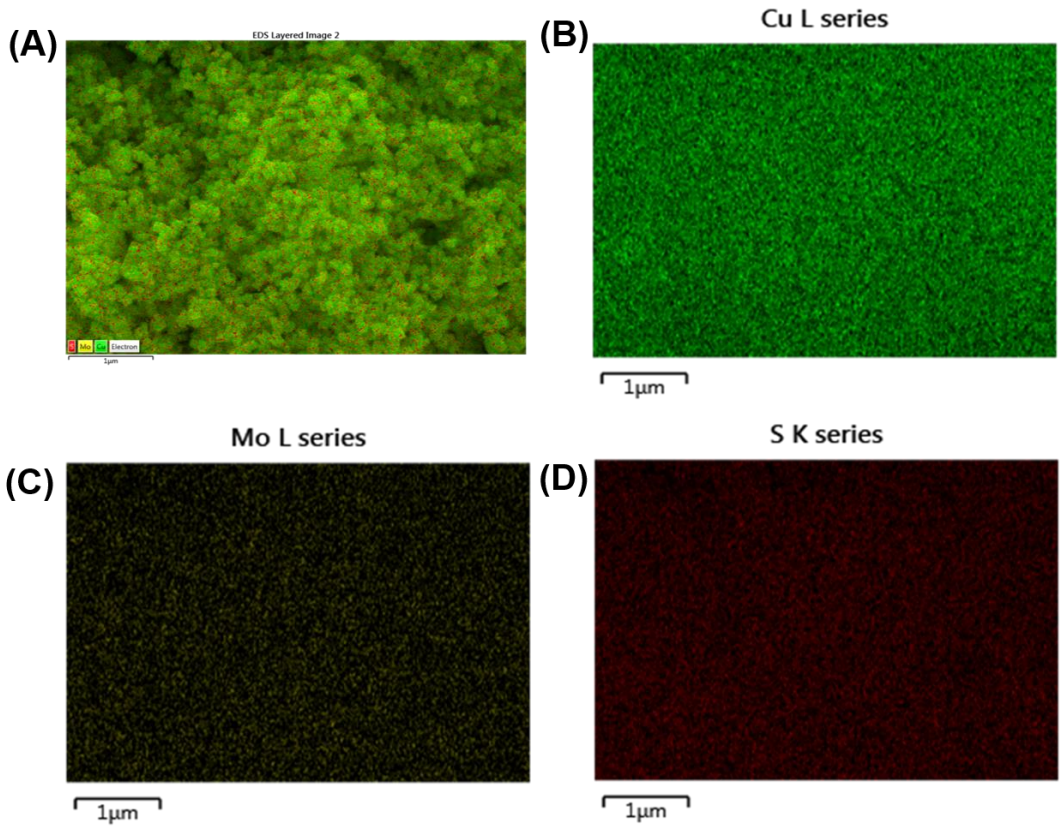

Figure 5.8 Elemental mapping of as prepared Cu_2MoS_4 (A) FE-SEM micrographs for elemental mapping, (B) copper, (C) molybdenum, (D) sulfur.

The Brunauer-Emmett-Teller (BET) and Barrett-Joyner-Halenda (BJH) analysis were performed to obtain the surface area and pore size analysis of the pristine Cu_2MoS_4 and Cu_2MoS_4-rGO hybrid (as shown in Figure 5.9). Figure 5.9(A and C) shows the N_2 adsorption-desorption isotherms of pristine Cu_2MoS_4 and Cu_2MoS_4-rGO hybrid respectively. The N_2 adsorption-desorption isotherms of both pristine Cu_2MoS_4 (Figure 5.9(A)) and Cu_2MoS_4-rGO hybrid (Figure 5.9(C)) represents the typical type (IV) adsorption-desorption isotherms according to the IUPAC definition, which is the characteristic isotherm of mesoporous materials.[41–43] The surface area of Cu_2MoS_4-rGO (17.41 m^2 g^{-1}) is 2.5 times higher than that of pristine Cu_2MoS_4 (6.4682 m^2 g^{-1}). In addition, the average pore diameter is calculated using the BJH analysis and provided in Figure 5.9(B and D). The average pore diameters of Cu_2MoS_4-rGO is 2.19 nm which is higher compared to the pristine Cu_2MoS_4 (1.7 nm). This result reveals that the Cu_2MoS_4-rGO has increased active sites and pore size compared to the pristine Cu_2MoS_4, which will more beneficial for facilitating the mobility of electrolyte ions during the electrochemical reaction of Cu_2MoS_4-rGO hybrid electrode.[44,45]

Electrochemical characterization of the Cu_2MoS_4 and Cu_2MoS_4-rGO are investigated by means of cyclic voltammogram (CV), galvanostatic charge-discharge (CD) and Electrochemical impedance spectroscopy (EIS) in a three-electrode configuration using aqueous Na_2SO_4 as the electrolyte. The comparative cyclic voltammetry (CV) profiles for Cu_2MoS_4 and Cu_2MoS_4-rGO electrodes are shown in Figure 5.10(A) at a sweep potential window of -0.8 to 0.2 V at a scan rate of 25 mV s^{-1}. Figure 5.10(B) represents the CV profiles of Cu_2MoS_4-rGO recorded at various scan rates (5 to100 mV s^{-1}). The quasi rectangular shaped CV curves of Cu_2MoS_4-rGO electrode implies the combination of the electrical double layer and pseudocapacitive behaviour of charge storage, which are resulted from the synergistic integration of Cu_2MoS_4 and rGO.[46]

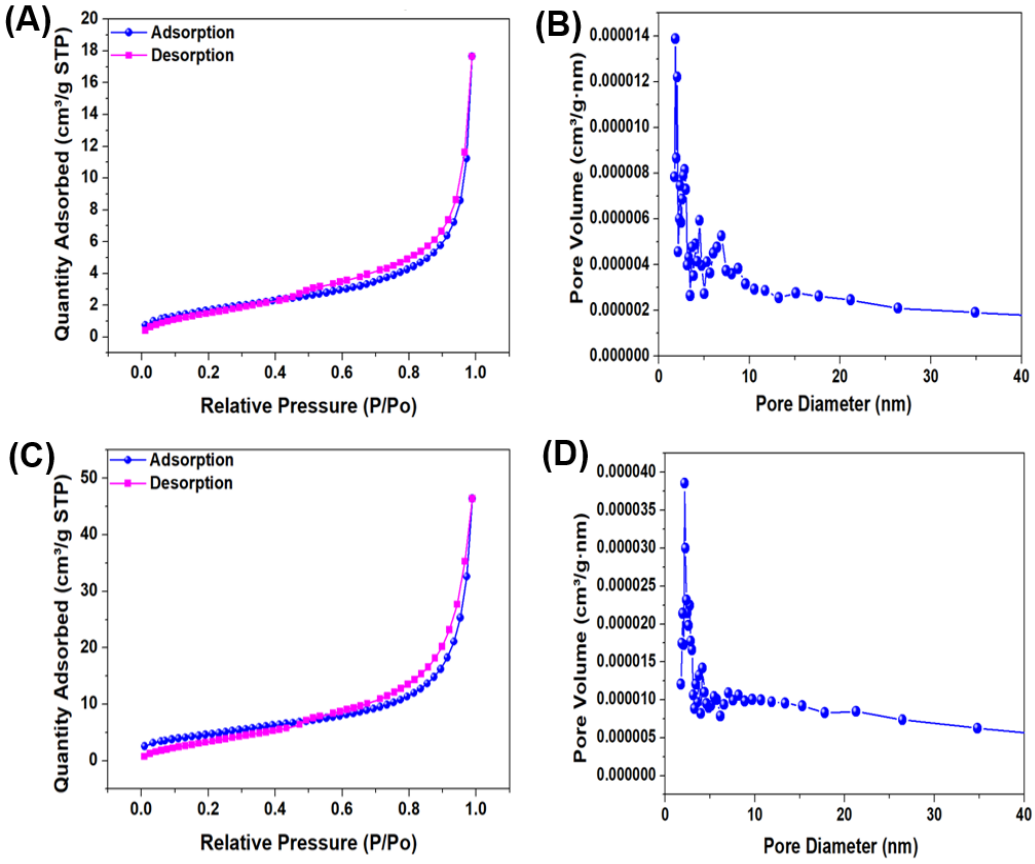

Figure 5.9 The Brunauer-Emmett-Teller (BET) and the Barrett-Joyner Halenda (BJH) analysis of pristine Cu_2MoS_4 and Cu_2MoS_4-rGO hybrid: (A) N_2 adsorption-desorption isotherms of pristine Cu_2MoS_4, (B) pore size distribution curve pristine Cu_2MoS_4, (C) N_2 adsorption-desorption isotherms of Cu_2MoS_4-rGO hybrid, and (D) pore size distribution curve of Cu_2MoS_4-rGO hybrid.

Figure 5.10(C) signifies the effect of scan rate on specific capacitance of Cu_2MoS_4-rGO electrode, which reveals that Cu_2MoS_4-rGO electrode exhibit a highest specific capacitance of 231.51 F g^{-1} at scan rate of 5 mV s^{-1}. The specific capacitance Cu_2MoS_4 and Cu_2MoS_4-rGO electrodes increase with increasing scan rates, which may be due to the dependence of electrochemical performance on the diffusion of electrolyte ions.[27,47] The specific capacitance of Cu_2MoS_4-rGO electrode substantially higher than the values obtained for the pristine Cu_2MoS_4 electrode (135.78 F g^{-1} at a scan rate of 5 mV s^{-1}). Moreover, the Cu_2MoS_4-rGO electrode exhibits a higher rate capability (44.6 %) than the pristane Cu_2MoS_4 electrode (28.14 %) with an

increase of twenty-fold in scan rate (5 to 100 mV s^{-1}). The enhanced electrochemical performance of Cu_2MoS_4-rGO electrode can be attributed to the nanoscale Cu_2MoS_4 nanoparticles and the residual oxygen-containing functional groups on the rGO sheets or van der Waals interactions between Cu_2MoS_4 and the rGO.[48]

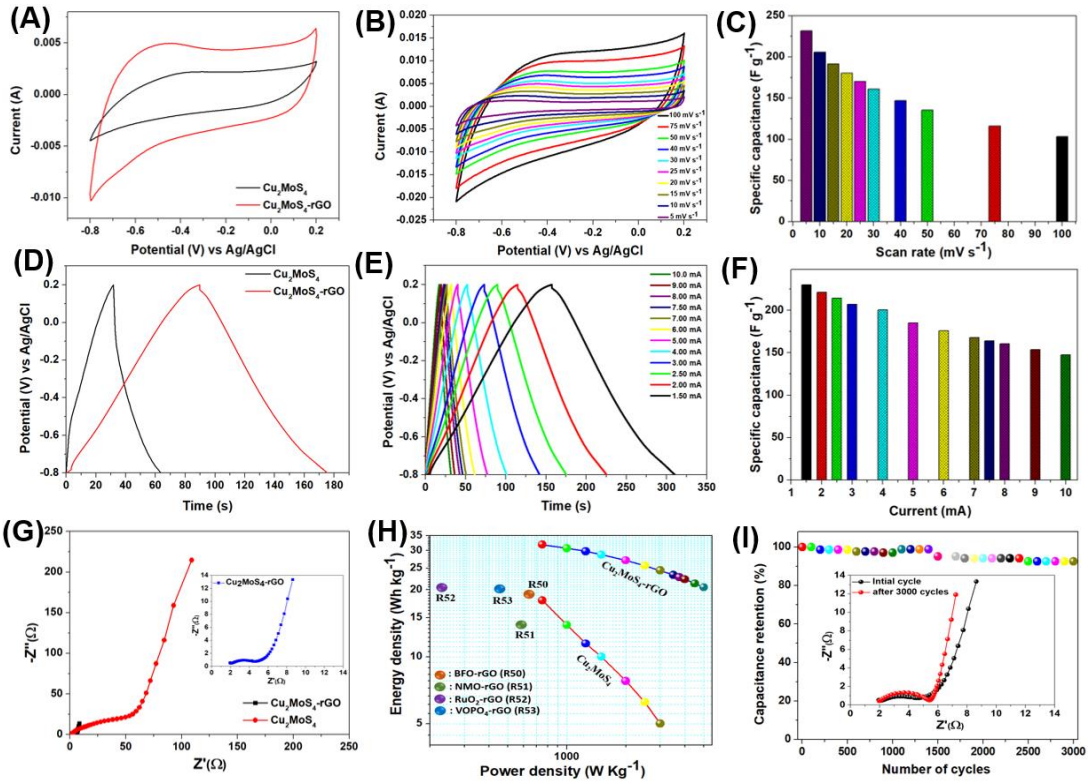

Figure 5.10 Electrochemical performance of as prepared Cu_2MoS_4 and Cu_2MoS_4-rGO electrode in three electrode system. (A) Cyclic voltammetric profile of Cu_2MoS_4 and Cu_2MoS_4-rGO electrode measured at constant scan rate of 25 mV s^{-1}, (B) cyclic voltammetric profile of the Cu_2MoS_4-rGO electrode at various scan rates (5 to 100 mV s^{-1}), (C) effect of scan rate on the specific capacitance of Cu_2MoS_4-rGO electrode, (D) Galvanostatic charge-discharge profile of Cu_2MoS_4 and Cu_2MoS_4-rGO electrode measured at constant current of 2.5 mA, (E) Galvanostatic charge-discharge profile of Cu_2MoS_4-rGO electrode measured at different current (1.5 to 10 mA), (F) effect of current on specific capacitance of Cu_2MoS_4-rGO electrode, (G) Nyquist plot of Cu_2MoS_4 and Cu_2MoS_4-rGO electrode with inset shows the enlarged portion of the Nyquist plot of Cu_2MoS_4-rGO electrode, (H) Ragone plot of Cu_2MoS_4, Cu_2MoS_4-rGO electrode and values reported for other rGO based hybrid supercapacitor electrodes are added for comparison

(References: R50-R53), and (I) The cyclic stability of Cu_2MoS_4-rGO electrode over 3000 cycles with inset shows the Nyquist plot of Cu_2MoS_4-rGO electrode initial and after cyclic stability test.

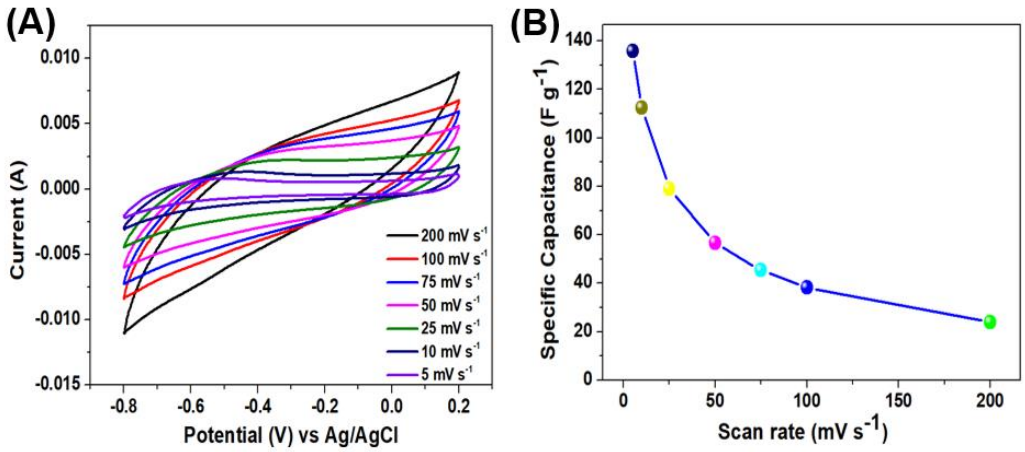

Figure 5.11 Electrochemical performance of as prepared Cu_2MoS_4 electrode, (A) cyclic voltammetric profile of the Cu_2MoS_4 electrode at various scan rates (5 to 200 mV s^{-1}), and (B) effect of scan rate on the specific capacitance of Cu_2MoS_4 electrode.

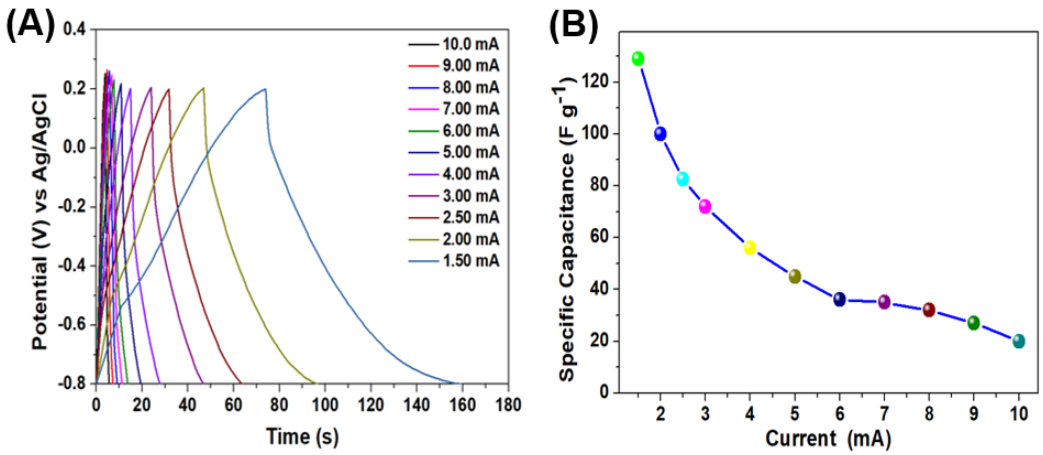

Figure 5.12 Electrochemical performance of as prepared Cu_2MoS_4 electrode, (A) Galvanostatic charge-discharge profile of Cu_2MoS_4 electrode measured at different current (1.5 to 10 mA) and (F) effect of current on the specific capacitance of Cu_2MoS_4 electrode.

To further understand the coulombic efficiency (ratio of time required for discharging and charging process) and calculate the specific capacitance of the pristane Cu_2MoS_4 and Cu_2MoS_4-rGO electrode, the galvanostatic charge-discharge (CD) measurements were

performed at various current, and the corresponding results are provided in Figure 5.10. The comparative charge-discharge (CD) profiles for Cu_2MoS_4 and Cu_2MoS_4-rGO electrodes are shown in Figure 5.10(D) at a sweep potential window of -0.8 to 0.2 V at a constant current of 2.5 mA. The Cu_2MoS_4-rGO electrode exposed longer charge-discharge time than the pristine Cu_2MoS_4 electrode at a constant current of 2.5 mA, indicating the higher specific capacitance. Figure 5.10(E) displays the CD profile of Cu_2MoS_4-rGO electrode at various current (10 mA to 1.5 mA) in the potential range of -0.8 to 0.2 V. It can be found that the CD profiles are non-linear Cu_2MoS_4-rGO electrode, suggesting the pseudocapacitive nature of charge storage.[17] Both Cu_2MoS_4 and Cu_2MoS_4-rGO electrodes exhibited a good coulombic efficiency (nearly 100 %). Figure 5.10(F) displays the variation of specific capacitance with respect to current for the Cu_2MoS_4-rGO electrode, which delivered a maximum specific capacitance of 229.83 F g^{-1} at a constant current of 1.5 mA. The detailed electrochemical performance of pristine Cu_2MoS_4 electrode is provided in Figure 5.11 and 5.12. A summary of the electrochemical performance of Cu_2MoS_4 and Cu_2MoS_4-rGO electrode with recently reported other electrodes is provided in Table 1.

To understand the charge transfer behavior of Cu_2MoS_4 and Cu_2MoS_4-rGO electrodes EIS measurement (Nyquist plot) is recorded between 0.1 Hz to 100 KHz frequency region as shown in Figure 5.10(G) and inset of Figure 5.10(G) shows the enlarged view of the Nyquist plot for Cu_2MoS_4-rGO electrode. From the Nyquist plot, it is visible that the solution resistance (R_s) for Cu_2MoS_4 and Cu_2MoS_4-rGO electrodes are 2.05 Ω and 1.94 Ω, respectively. An arc noticed at the low-frequency region of the Nyquist plot is a partial semi-circle whose diameter gives an approximate value of the charge transfer resistance (R_{ct}).[27]

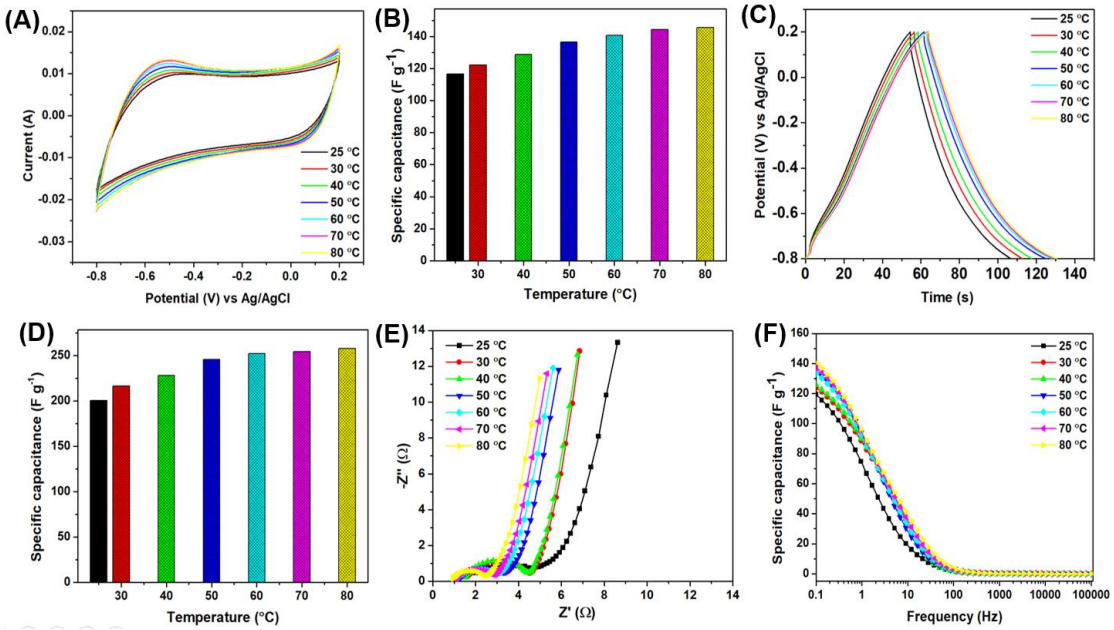

Figure 5.13 Electrochemical performance of as prepared Cu_2MoS_4-rGO electrode in three electrode system at different operating temperature (25 °C to 80 °C). (A) Cyclic voltammetric profile of Cu_2MoS_4-rGO electrode measured at various operating temperature, (B) effect of temperature on specific capacitance of Cu_2MoS_4-rGO electrode from cyclic voltammetric profile, (C) charge-discharge profiles of Cu_2MoS_4-rGO electrode measured at various operating temperature, (D) effect of temperature on the specific capacitance of Cu_2MoS_4-rGO electrode from charge-discharge profile, (E) Nyquist plot of Cu_2MoS_4-rGO electrode measured at different operating temperature, and (F) variation of specific capacitance with respect to frequency of Cu_2MoS_4-rGO electrode at different operating temperature.

A very low R_{ct} of 3 Ω was found out from the Nyquist plot for Cu_2MoS_4-rGO electrode compared to the pristine Cu_2MoS_4 electrode (53.36 Ω), which confirmed the incorporation graphene could enhance the electron transfer rate on the electrode surface.[49] The gravimetric energy and power densities for Cu_2MoS_4-rGO electrode at different applied current is represented by a Ragone plot as shown in Figure 5.10(H). The Cu_2MoS_4-rGO electrode exhibits a maximum energy density of about 31.92 Wh kg^{-1} with a corresponding power density of about 750 W kg^{-1} from the CD profile at a discharge current of 1.5 mA, which is higher than the pristine Cu_2MoS_4 electrode (17.91 Wh kg^{-1} at a constant current of 1.5 mA). The energy density

of Cu_2MoS_4-rGO electrode decreases from 31.92 to 20.5 Wh kg^{-1}, while the power density increases from 750 to 5000 W kg^{-1} as the discharge current increases from 1.5 to 10 mA in CD profiles. The energy density of the Cu_2MoS_4-rGO electrode was higher than the recently reported energy density values of other rGO hybrid supercapacitor electrodes, such as BFO-rGO (18.62 Wh kg^{-1}), NMO-rGO (14.25 Wh kg^{-1}), RuO_2-rGO (20.1 Wh kg^{-1}) and $VOPO_4$-rGO (21 Wh kg^{-1}).[50–53] The long-term cyclic stability of Cu_2MoS_4-rGO electrode was carried out using continuous charge-discharge cycles at a current of 10 mA over 3000 cycles (as shown in Figure 5.10(I)). Approximately 92.12 % of the specific capacitance of the Cu_2MoS_4-rGO electrode was retained at a current of 10 mA after 3,000 cycles. Inset of Figure 5.10(I) represents the Nyquist plot of the Cu_2MoS_4-rGO electrode investigated before and after the long cyclic tests. The obtained R_s values of the Cu_2MoS_4-rGO electrode before and after cyclic tests are 1.94 Ω and 2 Ω, respectively, suggesting the good conductivity of the electrolyte and low internal resistance of the electrode. The R_{ct} values increase from 3 Ω to 3.53 Ω after the cyclic tests, which might be a probable reason behind the observed capacitance decay.

Investigation of electrochemical supercapacitors as a function of different temperature is immensely required in future energy transfer and delivery in electric vehicles, large-scale grid storage, industry, and real-world applications.[54,55] The comprehensive electrochemical performance (CV, CD, and EIS) of Cu_2MoS_4-rGO electrode was performed at a different applied temperature and displayed in Figure 5.13. Figure 5.13(A) represents the CV profiles of Cu_2MoS_4-rGO electrode at a constant sweep rate of 75 mV s^{-1} in different applied temperature (25 °C, 30 °C, 40 °C, 50 °C, 60 °C, 70 °C and 80 °C). All the CV profiles represent the quasi-rectangular shapes without noticeable of redox peaks, suggesting the ideal pseudo-capacitive behaviors at different applied temperature. Notably, the size of the envelope (current of CV profile) increases with increase in the applied temperature, suggesting the higher specific

capacitance of Cu_2MoS_4-rGO electrode at higher temperature.[56] Figure 5.13(B) signifies the effect of operating temperature on the specific capacitance of Cu_2MoS_4-rGO electrode. At the temperature of 80 °C, the specific capacitance value of Cu_2MoS_4-rGO electrode exhibits as high as 145.65 F g^{-1}, which is increased by 125 % in contrast to the value at 25 °C (116.56 F g^{-1}). The increase in specific capacitance of Cu_2MoS_4-rGO electrode at different applied temperature can be explained as follows; the temperature effect may have an impact on the viscosity and the mobility of the aqueous electrolyte solution. It is well known that the viscosity of the aqueous electrolyte decreases with increase in temperatures from 25 °C to 80 °C. Hence, the resistive force of the electrode material to the adsorbed electrolyte ions becomes less; thus mobility of the adsorbed electrolyte ions is enhanced in case of higher applied temperature. Subsequently, the diffusion rate of electrolyte ions would be accelerated with less viscosity, which resulted in the increase of overall conductivity of the electrolyte with increasing temperature.[57] To further evaluate the temperature dependent electrochemical performance of Cu_2MoS_4-rGO electrode charge/discharge measurement was carried out at a constant applied current of 4 mA (as shown in Figure 5.13(C)). With the increase in the operating temperature, the charging and discharging time of Cu_2MoS_4-rGO electrode increases, suggesting the enhancement in the specific capacitance.[16] Figure 5.13(D) represents the variation of specific capacitance as a function of different operating temperature. The Cu_2MoS_4-rGO electrode delivers a capacitance of 200 F g^{-1} at 25 °C, which increases to 258 F g^{-1} at 80 °C (increased by 128 %). Moreover, the energy density of Cu_2MoS_4-rGO electrode 27.83 Wh Kg^{-1} to 35.83 Wh Kg^{-1} with an increase in the operating potential from 25 °C to 80 °C.

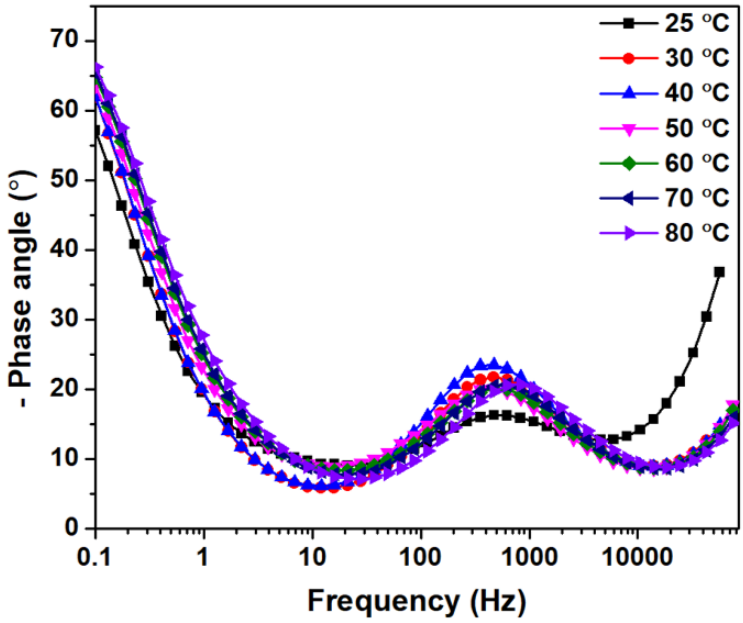

Figure 5.14 Variation of Bode phase angle concerning frequency of Cu_2MoS_4-rGO electrode at different operating temperature (25 °C to 80 °C).

To investigate the electrochemical performance of the Cu_2MoS_4-rGO electrode was strongly dependent on the operating temperature, the EIS measurement was carried out at a different operating temperature in the frequency range of 0.1 Hz to 100 KHz.[55] The typical Nyquist plot for Cu_2MoS_4-rGO electrode at different operating temperature was shown in Figure 5.13(E). All of the Nyquist plots consist of a compressed arc in the high-frequency region (ideal resistor) and a sloped line in the low-frequency region (ideal capacitor).[10] As observed from Nyquist plot the diameter of the Nyquist plot decreases gradually with an increase in operating temperature, suggesting the decrease in the value of R_s and R_{ct}, which represents the positive effect on enhancing the specific capacitance of Cu_2MoS_4-rGO electrode. The decrease in the value of R_s and R_{ct} with the increase in the temperature is caused by an increase in the conductivity of the electrolyte due to the enhanced mobility of the electrolyte ions in the electrolyte solution.[56] Additionally, the Bode phase angle plot in Figure 5.14 shows the variation

in phase angle in the low-frequency region (57.08° to 66.23°) with an increase in the applied temperature from 25 °C to 80 °C, suggesting the pseudocapacitive behavior of Cu_2MoS_4-rGO electrode at different applied temperature.[17] From the EIS analysis, the value of solution resistance (R_s), charge transfer resistance (R_{ct}) and Bode phase angle of Cu_2MoS_4-rGO electrode at different applied temperature is summarized in Table 5.2. Further, the variation of specific capacitance of Cu_2MoS_4-rGO electrode with respect to frequency is calculated from the impedance analysis employing the imaginary component of the impedance with an increase in the operating temperature (as shown in Figure 5.13(F)) by following equation:[58]

$$C_{sp} = -1 / (2\pi f Z''\mathrm{m}) \quad \ldots\ldots\ldots\ldots (5)$$

Where " f " is the applied frequency in Hz, " Z'' " is the imaginary component of impedance, " C_{sp} " is the specific capacitance and " m " is the mass of the Cu_2MoS_4-rGO electrode. The specific capacitance of the Cu_2MoS_4-rGO electrode increases from 119.38 F g^{-1} to 140.35 F g^{-1} (increased by 117 %) with an increase in the operating temperature from 25 °C to 80 °C. The obtained specific capacitance from the EIS analysis is well comparable with the CV profile specific capacitance (Figure 5.13(B)). The enhancement of specific capacitance of Cu_2MoS_4-rGO electrode as a function of operating temperature can be attributed to the enhanced diffusivity and mobility of the electrolyte ions at a higher temperature.

For comparison, the electrochemical performance of the rGO electrode was investigated using cyclic voltammetry (CV) and galvanostatic charge-discharge (CD) in 1 M aqueous Na_2SO_4 electrolyte using three electrode configurations (shown in Figure 5.15). Figure 5.15(A) shows the CV profiles of rGO electrodes measured at various scan rates (5-100 mV s^{-1}) over the operating potential window of -0.8 to 0.2 V. The CV profiles of rGO electrodes shows rectangularly shaped curve suggesting the electric double-layer capacitance. Figure 5.15(B)

represents the effect of scan rate on the specific capacitance of rGO electrodes. The rGO electrode possesses a specific capacitance of about 137.42 F g^{-1} obtained at a scan rate of 5 mV s^{-1}.

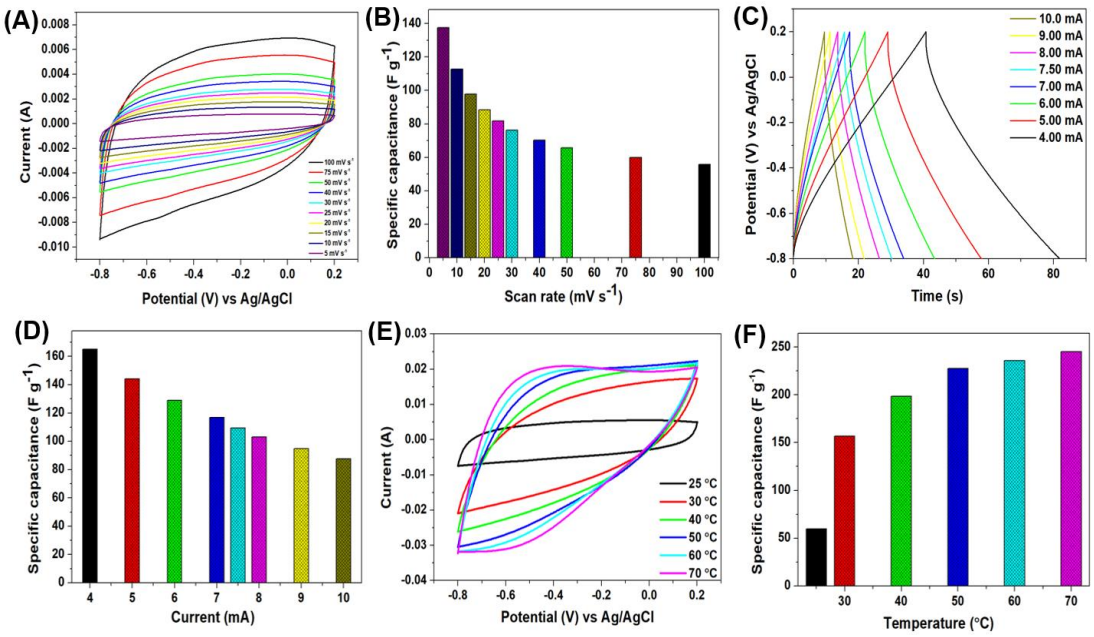

Figure 5.15 Electrochemical performance of as prepared rGO electrode in three electrode system. (A) Cyclic voltammetric profile of rGO electrode measured at various scan rates (5 to100 mV s^{-1}), (B) effect of scan rate on the specific capacitance of rGO electrode, (C) Galvanostatic charge-discharge profile of rGO electrode measured at different current (4 to 10 mA), (D) effect of current on specific capacitance of rGO electrode, (E) cyclic voltammetric profile of rGO electrode measured at various operating temperature, and (F) effect of temperature on specific capacitance of rGO electrode from cyclic voltammetric profile.

The galvanostatic charge/discharge (CD) profiles of rGO electrodes (Figure 5.15(C)) linear and symmetrical charge-discharge profiles over the current ranges from 4 to 10 mA, suggesting excellent electrochemical reversibility. Figure 5.15(D) represents the plot of specific capacitance with respect to the discharge current of rGO electrodes, which delivers a specific capacitance of about 164.92 F g^{-1} at a discharge current of 4 mA. The temperature dependent electrochemical performance of rGO electrode is provided in Figure 5.15(E and F). Figure

5.15(E) shows the temperature dependent CV profiles of rGO electrodes measured at various temperatures (25 °C to 70 °C) at a constant scan rate of 75 mV s^{-1}. The CV profiles display the increase in area with increase in the temperature from 25 °C to 70 °C suggesting the higher mobility of electrolyte ions at higher temperature results in enhanced charge storage capacity.[57] The specific capacitance of the rGO electrode increases from 59.97 F g^{-1} to 244.94 F g^{-1} with an increase in the operating temperature (from 25 °C to 70 °C), as shown in Figure 5.15(F). The enhanced electrochemical performance of Cu_2MoS_4-rGO electrode owed to the contribution of the synergistic effect between Cu_2MoS_4 and rGO. The rGO nanosheet offers conducting support for Cu_2MoS_4 nanoparticles to enhance the conducting properties of the hybrid electrode and reduce the electrode resistance. As a result of all the above aspects, the hybrid electrode (Cu_2MoS_4-rGO) exhibit better electrochemical performance compared to the pristine Cu_2MoS_4 and rGO electrode.

Table 5.1 The summary of electrochemical performances of Cu_2MoS_4 and Cu_2MoS_4-rGO electrode and reported electrodes for supercapacitor application using three-electrode configurations.

Material	**Preparation method**	**Specific capacitance (F g^{-1})**	**Reference**
CuO	Wet chemical method	88.5	[59]
RuO_2	Chemical synthesis	50	[60]
MoO_3	Solution combustion method	108.88	[61]
MoS_2	Hydrothermal	92.85	[62]
CuS	Sonochemically	62.77	[63]
ZnS	Solvothermal	32.8	[64]
WS_2	Chemical exfoliation	40	[65]
$CuSbS_2$	Colloidal method	22	[66]

$CuSbSe_2$	Colloidal method	34	[66]
Cu_2MoS_4	**Hydrothermal**	**135.78**	**This work**
Cu_2MoS_4-rGO	**Hydrothermal**	**231.51**	**This work**

Table 5.2 The summary of EIS parameters of Cu_2MoS_4-rGO electrode at different operating temperatures.

Temperature (°C)	**Solution resistance (R_s, Ω)**	**charge transfer resistance (R_{ct}, Ω)**	**Bode phase angle (°)**
25 °C	1.90	3	57.08
30 °C	1.51	2.96	61.91
40 °C	1.38	2.89	61.64
50 °C	1.16	2.1	63.53
60 °C	1.08	1.9	64.77
70 °C	1.01	1.8	65.36
80 °C	0.92	1.6	66.23

5.4 Conclusions

In conclusion, a novel hybrid electrode comprising Cu_2MoS_4 nanoparticles decorated on rGO sheets has been successfully synthesized via a one-step hydrothermal method. The as prepared Cu_2MoS_4-rGO hybrid electrode shows better electrochemical performance compared to the pristine Cu_2MoS_4 electrode and rGO electrode. The Cu_2MoS_4-rGO electrode exhibits a specific capacitance of 231.51 F g^{-1} at a scan rate of 5 mV s^{-1} in cyclic voltammetry analysis.

Moreover, the electrochemical performance of the Cu_2MoS_4-rGO electrode using 1 M Na_2SO_4 aqueous electrolyte was systematically studied in a temperature window ranging from 25 °C to 80 °C. An improvement of electrochemical performance such as specific capacitance (116.56 F g^{-1} to 145.65 F g^{-1}) was observed on increasing the operating temperature from 25 °C to 80 °C for Cu_2MoS_4-rGO electrode. The specific capacitance enhancement as a function of temperature can be attributed to the enhanced diffusivity and mobility of the electrolyte ions at a higher temperature. The utilization of such a hybrid supercapacitor electrode enables wide-ranging advances in industrial, military and space applications.

5.5 References

1 D. P. Dubal, N. R. Chodankar, D.-H. Kim and P. Gomez-Romero, *Chem. Soc. Rev.*

2 S. Sahoo and C. S. C. S. Rout, *Electrochim. Acta*, 2016, **220**, 57–66.

3 Y. Yan, T. Wang, X. Li, H. Pang and H. Xue, *Inorg. Chem. Front.*, 2017, **4**, 33–51.

4 B. Li, M. Zheng, H. Xue and H. Pang, *Inorg. Chem. Front.*, 2016, **3**, 175–202.

5 T.-H. Ko, S. Radhakrishnan, M.-K. Seo, M.-S. Khil, H.-Y. Kim and B.-S. Kim, *J. Alloys Compd.*, 2017, **696**, 193–200.

6 S. R. Marri, S. Ratha, C. S. Rout and J. N. Behera, *Chem. Commun.*, 2017, **53**, 228–231.

7 Z. Guo, F. Sun and W. Yuan, *Cryst. Growth Des.*, 2017, **17**, 2238–2253.

8 C. J. Crossland, P. J. Hickey and J. S. O. Evans, *J. Mater. Chem.*, 2005, **15**, 3452–3458.

9 K. Krishnamoorthy, P. Pazhamalai and S.-J. Kim, *Energy Environ. Sci.*

10 K. Krishnamoorthy, P. Pazhamalai, S. Sahoo and S.-J. Kim, *J. Mater. Chem. A*, 2017, **5**, 5726–5736.

11 R. Ramachandran, K. Rajavel, W. Xuan, D. Lin and F. Wang, *Ceram. Int.*

12 X. Lin, M. Salari, L. M. R. Arava, P. M. Ajayan and M. W. Grinstaff, *Chem. Soc. Rev.*, 2016, **45**, 5848–5887.

13 K. Hung, C. Masarapu, T. Ko and B. Wei, *J. Power Sources*, 2009, **193**, 944–949.

14 C. Masarapu, H. F. Zeng, K. H. Hung and B. Wei, *ACS Nano*, 2009, **3**, 2199–2206.

15 J. Zhang, H. Gao, Q. Yang, X. T. Zhang, M. Y. Zhang and L. L. Xu, *Appl. Surf. Sci.*, 2015, **356**, 167–172.

16 J.-G. Wang, Y. Yang, Z.-H. Huang and F. Kang, *J. Power Sources*, 2013, **224**, 86–92.

17 S. Sahoo, K. Krishnamoorthy, P. Pazhamalai, V. K. Mariappan and S.-J. Kim, *Int. J. Hydrogen Energy*, , DOI:10.1016/j.ijhydene.2018.04.143.

18 Y. W. Denis, R. L. Lee, R. Yi, S. Y. Chiam and P. D. Tran, *Electrochim. Acta*, 2014, **115**, 337–343.

19 P. D. Tran, M. Nguyen, S. S. Pramana, A. Bhattacharjee, S. Y. Chiam, J. Fize, M. J. Field, V. Artero, L. H. Wong and J. Loo, *Energy Environ. Sci.*, 2012, **5**, 8912–8916.

20 B.-B. Chen, D.-K. Ma, Q.-P. Ke, W. Chen and S.-M. Huang, *Phys. Chem. Chem. Phys.*, 2016, **18**, 6713–6721.

21 S. Sahoo, K. Krishnamoorthy, P. Pazhamalai and S.-J. Kim, *Nanoscale*, 2018, **10**, 13883–13888.

22 C. Liu, Z. Yu, D. Neff, A. Zhamu and B. Z. Jang, *Nano Lett.*, 2010, **10**, 4863–4868.

23 L. L. Zhang, R. Zhou and X. S. Zhao, *J. Mater. Chem.*, 2010, **20**, 5983–5992.

24 J. Zhang, J. Jiang, H. Li and X. S. Zhao, *Energy Environ. Sci.*, 2011, **4**, 4009–4015.

25 S. Radhakrishnan and J. Mathiyarasu, in *Graphene-Based Electrochemical Sensors for Biomolecules*, Elsevier, 2019, pp. 187–205.

26 G. Venugopal and S.-J. Kim, *J. Nanosci. Nanotechnol.*, 2012, **12**, 8522–8525.

27 S. Sahoo, P. Pazhamalai, K. Krishnamoorthy and S.-J. Kim, *Electrochim. Acta*, , DOI:10.1016/j.electacta.2018.02.116.

28 K. Zhang, W. Chen, Y. Lin, H. Chen, Y. A. Haleem, C. Wu, F. Ye, T. Wang and L. Song, *Nanoscale*, 2015, **7**, 17998–18003.

29 R. Rameshbabu, R. Vinoth, M. Navaneethan, Y. Hayakawa and B. Neppolian, *CrystEngComm*, 2017, **19**, 2475–2486.

30 W. Chen, H. Chen, H. Zhu, Q. Gao, J. Luo, Y. Wang, S. Zhang, K. Zhang, C. Wang and Y. Xiong, *Small*, 2014, **10**, 4637–4644.

31 R. Rameshbabu, R. Vinoth, M. Navaneethan, S. Harish, Y. Hayakawa and B. Neppolian, *Appl. Surf. Sci.*, 2017, **418**, 128–137.

32 Y. Zhou, G. Liu, X. Zhu and Y. Guo, *Sensors Actuators B Chem.*, 2017, **251**, 280–290.

33 K. Chang, Z. Mei, T. Wang, Q. Kang, S. Ouyang and J. Ye, *ACS Nano*, 2014, **8**, 7078–7087.

34 A. Gopalakrishnan, R. Krishnan, S. Thangavel, G. Venugopal and S.-J. Kim, *J. Ind. Eng. Chem.*, 2015, **30**, 14–19.

35 S. Thangavel and G. Venugopal, *Powder Technol.*, 2014, **257**, 141–148.

36 A. Mondal, A. Paul, D. N. Srivastava and A. B. Panda, *ACS Appl. Nano Mater.*, 2018, **1**, 4622–4632.

37 J. Jiang, S. Lu, W.-K. Wang, G.-X. Huang, B.-C. Huang, F. Zhang, Y.-J. Zhang and H.-Q. Yu, *Nano Energy*, 2018, **43**, 300–309.

38 N. Raghavan, S. Thangavel, Y. Sivalingam and G. Venugopal, *Appl. Surf. Sci.*, 2018, **449**, 712–718.

39 K. Zhang, Y. Lin, C. Wang, B. Yang, S. Chen, S. Yang, W. Xu, H. Chen, W. Gan and Q. Fang, *J. Phys. Chem. C*, 2016, **120**, 13120–13125.

40 Y.-M. Fan, Y. Liu, X. Liu, Y. Liu and L.-Z. Fan, *Electrochim. Acta*, 2017, **249**, 1–8.

41 R. Rameshbabu, R. Vinoth, M. Navaneethan, Y. Hayakawa and B. Neppolian, *CrystEngComm*, 2017, **19**, 2475–2486.

42 G. Ali, S. H. Oh, S. Y. Kim, J. Y. Kim, B. W. Cho and K. Y. Chung, *J. Mater. Chem. A*, 2015, **3**, 10258–10266.

43 P. Pazhamalai, K. Krishnamoorthy, M. S. P. Sudhakaran and S. J. Kim, *ChemElectroChem*, 2017, **4**, 396–403.

44 G. Yuan, J. Xiang, H. Jin, Y. Jin, L. Wu, Y. Zhang, A. Mentbayeva and Z. Bakenov, *Electrochim. Acta*, 2018, **259**, 647–654.

45 H. Jiang, Y. Dai, Y. Hu, W. Chen and C. Li, *ACS Sustain. Chem. Eng.*, 2014, **2**, 70–74.

46 N. R. Chodankar, D. P. Dubal, S.-H. Ji and D.-H. Kim, *Electrochim. Acta*.

47 R. Ramachandran, C. Zhao, D. Luo, K. Wang and F. Wang, *Electrochim. Acta*, 2018, **267**, 170–180.

48 J. Shen, M. Shi, B. Yan, H. Ma, N. Li and M. Ye, *J. Mater. Chem.*, 2011, **21**, 7795–7801.

49 K. P. Singh, D. Bhattacharjya, F. Razmjooei and J.-S. Yu, *Sci. Rep.*, 2016, **6**, 31555.

50 D. Moitra, C. Anand, B. K. Ghosh, M. Chandel and N. N. Ghosh, *ACS Appl. Energy Mater.*, 2018, **1**, 464–474.

51 P. Kakvand, M. S. Rahmanifar, M. F. El-Kady, A. Pendashteh, M. A. Kiani, M. Hashami, M. Najafi, A. Abbasi, M. F. Mousavi and R. B. Kaner, *Nanotechnology*, 2016, **27**, 315401.

52 Z. Wu, D. Wang, W. Ren, J. Zhao, G. Zhou, F. Li and H. Cheng, *Adv. Funct. Mater.*, 2010, **20**, 3595–3602.

53 N. Chen, J. Zhou, Q. Kang, H. Ji, G. Zhu, Y. Zhang, S. Chen, J. Chen, X. Feng and W. Hou, *J. Power Sources*, 2017, **344**, 185–194.

54 P. Zhang, J. Wang, W. Sheng, F. Wang, J. Zhang, F. Zhu, X. Zhuang, R. Jordan, O. G. Schmidt and X. Feng, *Energy Environ. Sci.*

55 X. Xia, Y. Zhang, D. Chao, Q. Xiong, Z. Fan, X. Tong, J. Tu, H. Zhang and H. J. Fan, *Energy Environ. Sci.*, 2015, **8**, 1559–1568.

56 A. Singh, M. A. Akhtar and A. Chandra, *Electrochim. Acta*, 2017, **229**, 291–298.

57 M. Miah, S. Bhattacharya, D. Dinda and S. K. Saha, *Electrochim. Acta*, 2018, **260**, 449–458.

58 K. Krishnamoorthy, P. Pazhamalai and S. J. Kim, *Electrochim. Acta*, 2017, **227**, 85–94.

59 Y. X. Zhang, M. Huang, F. Li and Z. Q. Wen, *Int. J. Electrochem. Sci*, 2013, **8**, 8645–8661.

60 V. D. Patake and C. D. Lokhande, *Appl. Surf. Sci.*, 2008, **254**, 2820–2824.

61 G. P. Nagabhushana, D. Samrat and G. T. Chandrappa, *RSC Adv.*, 2014, **4**, 56784–56790.

62 K. Krishnamoorthy, G. K. Veerasubramani, S. Radhakrishnan and S. J. Kim, *Mater. Res. Bull.*, 2014, **50**, 499–502.

63 K. Krishnamoorthy, G. K. Veerasubramani, S. Radhakrishnan and S. J. Kim, *J. Nanosci. Nanotechnol.*, 2015, **15**, 4409–4413.

64 R. Ramachandran, M. Saranya, P. Kollu, B. P. C. Raghupathy, S. K. Jeong and A. N. Grace, *Electrochim. Acta*, 2015, **178**, 647–657.

65 C. C. Mayorga-Martinez, A. Ambrosi, A. Y. S. Eng, Z. Sofer and M. Pumera, *Electrochem. commun.*, 2015, **56**, 24–28.

66 K. Ramasamy, R. K. Gupta, S. Palchoudhury, S. Ivanov and A. Gupta, *Chem. Mater.*, 2014, **27**, 379–386.

CHAPTER – 6

Copper molybdenum sulfide anchored nickel foam: A high performance, binder-free, negative electrode for supercapacitor

Highlights

- Herein, we are demonstrating the use of a binder-free electrode based on copper-molybdenum-sulfide nanostructures grown on nickel foam (CMS/Ni) as a novel negative electrode for supercapacitor.
- The cyclic voltammetry and charge-discharge analysis reveal the pseudocapacitive nature of the CMS/Ni electrode with a high specific capacity of 633 mAh g^{-1} (~20-fold higher than binder-based CMS electrode) which is mainly due to their superior electronic conductivity and short ion transport pathways.
- Further, the fabricated symmetric supercapacitor using CMS/Ni electrode delivered a high device capacitance (265.62 F g^{-1}), high energy density (23.61 Wh kg^{-1}) and long cycle-life.
- The results ensure that CMS/Ni binder-free electrode will be a promising negative electrode for high-performance supercapacitors.

6.1 Introduction

Electrode materials play a key role on the energy storage performance of supercapacitor devices, which are considered as a prime energy storage device to meet out the depletion of fossil fuels as well as the global energy crisis/demands.[1–3] Recent advances in electrode materials focused on the use of 2D materials beyond graphene such as transition metal chalcogenides (MoS_2, $MoSe_2$, TiS_2, VS_2), layered MXenes (Ti_3C_2, Ti_2C), and layered transition metal oxides/hydroxides.[4] The literature on the electrochemical properties of these layered materials suggested much efforts are needed to improve the energy density of supercapacitors using these electrodes. General strategies used for improving the energy density can be achieved via (i) use of ionic or organic electrolytes which can widen the operating potential window of the supercapacitor up to 3.5 V, and (ii) enhance the specific capacitance/capacity of the electrode.[5] The former relating the use of ionic or organic electrolytes might be looks promising strategy to enhance the energy density, their limitations towards the fabrication of flexible devices, and high-cost of organic/ionic electrolytes hinders the practical applications.[6,7] The latter focused on improving the specific capacitance/capacity of electrode becomes more promising and can be achieved via several methods including (i) increasing the electrical conductivity of the electrode via doping, or using multi-component system, (ii) developing high surface area materials, (iii) designing binder-free electrodes via direct integration of electroactive-material with current collectors, and (iv) use of redox-additive electrolytes, etc.[8–11] The development of novel electrode materials by keeping the above-mentioned perceptions might provide improved electrochemical properties, thereby increases the energy density of supercapacitor.

In this scenario, copper molybdenum sulfide (CMS) which is one of the families of layered ternary transition metal sulfide possesses interesting electrochemical properties, high

electrical conductivity with wide band gap makes them a high-performance electrode for electrocatalytic hydrogen evolution reaction, and visible-light driven photocatalysis.[12] The physical and chemical properties of CMS nanostructures are not-completely understood well up to date since only few-researchers investigated the properties of CMS as follows: Tran et al. reported the use of CMS electrode as an efficient electrocatalyst for hydrogen production from water.[13] Later on, Chen et al. demonstrated the mechanistic investigation of via nanoscale Kirkendall effect and Ostwald ripening process in the solvothermal preparation of CMS nanostructures.[14] A recent study by Zhang et al. showed the presence of room-temperature ferromagnetism in CMS nanosheets.[15] These studies suggested that few more interesting properties are expected from CMS on the energy storage-conversion and harvesting sectors which are needed to elucidate. The structure of CMS with sulfur ligands covalently bonded with copper and molybdenum sites can provide more reactive sites sufficient for ion-transport kinetics during the electrochemical charging and discharging. Therefore, we aimed to investigate the energy storage properties of CMS nanostructures in this work. Herein, we fabricated CMS grown on Ni foam and investigated their capacitive properties using a three-electrode configuration and symmetric supercapacitor design.

6.2 Experimental section

6.2.1 Materials

Sodium molybdate ($Na_2MoO_4.2H_2O$), hydrazine monohydrate ($N_2H_4.H_2O$), thioacetamide (CH_3CSNH_2), copper (II) sulfate pentahydrate ($CuSO_4.5H_2O$), ethylene glycol, and sodium sulfate (Na_2SO_4) were purchased from Daejung Chemicals Ltd., South Korea. Nickel Foam (110 PPI, Thickness: 1.0 mm) obtained from HEZE JIAOTONG GROUP (China) were used as the substrate for direct to grow CMS nanostructure. All used Ni foam substrates were thoroughly cleaned with absolute ethanol and DI water many times by ultra-sonication.

Then they were dried in an electric oven at 60 °C temperature for 3 h. Afterwards used as the substrate for hydrothermal growth of CMS nanostructure.

6.2.2 Hydrothermal growth of CMS anchored on Ni foam

A one-pot hydrothermal method was used for the preparation of CMS nanostructure on Ni foam. In a typical synthesis, 60 mg of $Na_2MoO_4.2H_2O$ and 120 mg of CH_3CSNH_2 was dissolved in 60 mL of ethylene glycol by ultra-sonication for one hour. Then 40 mg of Cu_2O was added slowly to the above precursor solution (synthesized using the process given in literature [16]) and kept it for ultra-sonication for two h to form a dark brown solution. After that, the precursor solution was transferred to a 100 mL Teflon lined stainless steel autoclave. The cleaned piece of Ni foam was immersed in the dark brown solution and kept at 150 °C for 15 h. After completion of the hydrothermal reaction, the autoclave was allowed to cool to room temperature naturally and collected the obtained precursor grown on Ni foam. Ni foam was cleaned by ultrasonication approach using repeated rinses of water and absolute ethanol. Finally, the collected Ni foam was dried at 60 °C for 4 h.

6.2.3 Instrumentation

The as-grown CMS nanostructure on Ni foam were used for different physical characterizations to confirm the structural and morphological analysis. The morphologies of the as prepared binder free CMS nanostructure on Ni foam was analysed using field-emission scanning electron microscopy (TESCAN, MIRA3) under different magnifications. The chemical elements and its states were analyzed using X-ray photoelectron spectroscopy (XPS) techniques (ESCA-2000, VG Microtech Ltd, Al Kα (1486.6 eV) and binding energies (B.E.) were evaluated using C 1 s (B.E.=284.6 eV) as the reference. The XRD analysis were analysed using X-Ray Diffractometer System (X'pert pro MPD) with Cu-Kα radiation (λ=1.5418 Å) (KBSI, Busan Center). The UV-vis spectroscopy analysis was performed using Optical Spectrometer

(UV/VIS/NIR spectrophotometer) Cary 5G, KBSI, Daegu centre). The specific surface area for the CMS/Ni and CMS powder were analysed using Particle and Pore Size Analysis System (UPA-150, ASAP2010, Autopore IV, KBSI, Jeonju Center)

6.2.4 Electrochemical analysis

The electrochemical performance of as synthesized binder free CMS nanostructure anchored on Ni foam was investigated through cyclic voltammetry (CV), galvanostatic charge–discharge (CD), and electrochemical impedance spectroscopy (EIS) in three electrode system and symmetric device using an AUTOLAB PGSTAT302N electrochemical workstation in 1 M aqueous solution of sodium sulfate (Na_2SO_4) as the electrolyte. For three electrode system freshly prepared a piece of CMS anchored on Ni foam (1×1 cm^2) was used as working electrode, platinum as the counter electrode, and Ag/AgCl as the reference electrode. The electroactive mass of the CMS anchored on Ni foam current collector is measured as 1 mg which was calculated from the difference between the mass of the substrate before and after growing of the CMS using Dual-range Semi-micro Balance (AUW-220D, SHIMADZU) with an approximation of five-decimal points.

The binder-free CMS anchored on Ni foam SSC device was fabricated by sandwiching polypropylene separator between two CMS anchored on Ni foam. An aqueous solution of 1 M Na_2SO_4 is used as the electrolyte. The electrochemical performance of SSC device was investigated through cyclic voltammetry (CV), galvanostatic charge-discharge (CD), and electrochemical impedance spectroscopy (EIS) using an AUTOLAB PGSTAT302N electrochemical workstation.

Electrochemical parameter: The evaluation of specific capacitance (*Csp*) of CMS/Ni electrode was obtained from cyclic voltammetry (CV) and galvanostatic charge-discharge (CD) is given by following relations:[17]

$$Csp = [(\int I\,dV) / (s \times \Delta V \times m)] \ldots\ldots\ldots\ldots\ldots\ldots\ldots\ldots \quad (1)$$

$$Csp = [(I \times \Delta t) / (\Delta V \times m)] \ldots\ldots\ldots\ldots\ldots\ldots\ldots\ldots \quad (2)$$

The specific capacity (*Qs*) of CMS/Ni electrode was obtained from CV and CD profile using the following relations:[18]

$$Qs = [(\int I\,dV) / (s \times m)] \ldots\ldots\ldots\ldots\ldots\ldots\ldots\ldots \quad (3)$$

$$Qs = (I \times \Delta t) / (m \times 3.6) \ldots\ldots\ldots\ldots\ldots\ldots\ldots\ldots \quad (4)$$

Here, "*Csp*" is the specific capacitance (F g^{-1}), specific capacity "*Qs*" in (mAh g^{-1}), "*I*" is the current (A), "Δ*V*" is the potential window, "s" is the scan rate (mV s^{-1}), "Δ*t*" is the discharge time (s), and "*m*" is the mass of the active material (mg).

The energy density (*E*) and power density (*P*) of the CMS/Ni SSC device were calculated using the following relations:[19]

$$E = (I \times \Delta t \times \Delta V) / (7.2 \times m) \ldots\ldots\ldots\ldots\ldots\ldots\ldots \quad (5)$$

$$P = (3.6 \times E) / \Delta t \ldots\ldots\ldots\ldots\ldots\ldots\ldots \quad (6)$$

Here, "*E*" is the energy density (Wh kg^{-1}), "*P*" is the power density (W kg^{-1}), "*I*" is the current (A), "Δ*V*" is the potential window, "Δ*t*" is the discharge time (s), and "*m*" is the mass of the active material (mg).

The variation of specific capacitance of CMS/Ni electrode with respect to frequency was obtained from the EIS analysis using the relation:[20]

$$Cs = -1/2\pi f z'' \ldots\ldots\ldots\ldots\ldots\ldots\ldots \quad (7)$$

Here "*Cs*" is the specific capacitance of the device, and "*f*" is the applied frequency, and "*z*′′" is the imaginary plot of impedance.

3. Results and discussion

The CMS nanostructures were grown directly on the surface of Ni foam via a hydrothermal reaction (see Electronic Supplementary Information given in ESI) using sodium

molybdate, thioacetamide and copper oxide as starting materials. Figure 6.1(A) shows the digital photograph of the bare and CMS grown on Ni foam after the hydrothermal reaction which showed the change in color from grey into black color indicates the growth of CMS on Ni foam.

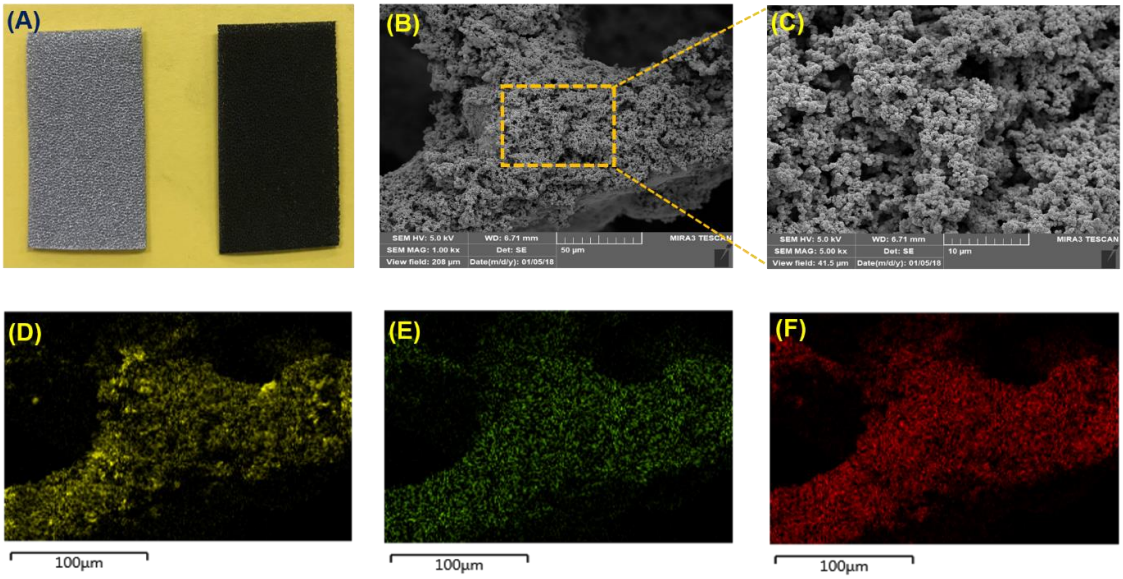

Figure 6.1 (A) Digital photographs of bare Ni Foam and CMS nanostructure anchored on Ni foam, Field emission-scanning electron micrographs of CMS nanostructure anchored on Ni foam measured at different magnifications (B) 50 µm and (C) 10 µm. The elemental mapping of (D) copper, (E) molybdenum and (F) sulfur elements present in CMS nanostructure anchored on Ni foam.

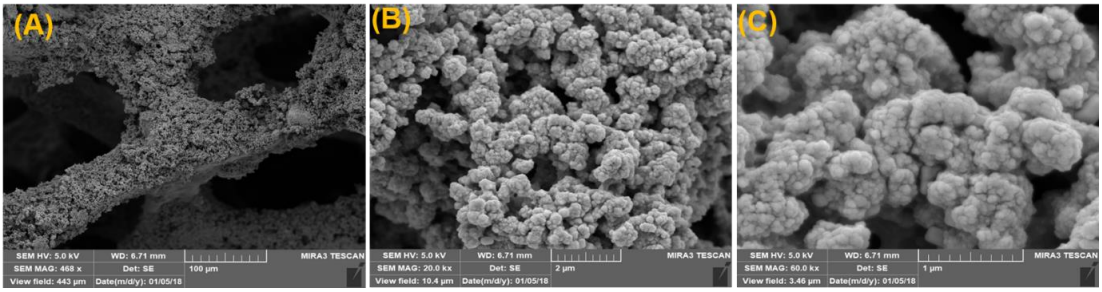

Figure 6.2 FE-SEM image of CMS anchored on Ni foam.

The field emission-scanning electron microscope (FE-SEM) analysis of CMS grown on Ni foam (under different locations) is shown in Figure 6.1(B, C) and Figure 6.2. The FE-SEM micrographs given in Figure 6.1(B, C) shows the homogeneous growth of CMS nanostructures

on the surface of Ni foam with size in the range of 100 to 200 nm. The formation of CMS nanostructure can be explained as follows: During the hydrothermal reaction, the MoO_4^{2-} ions and sulfur ions (released from the sodium molybdate and thioacetamide) reacts together which results in the formation of MoS_4^{2-} ions via nanoscale Kirkendall effect. Later, the Cu_2O particles reaction with the MoS_4^{2-} ions which results in the formation of CMS anchored on Ni foam.[14]

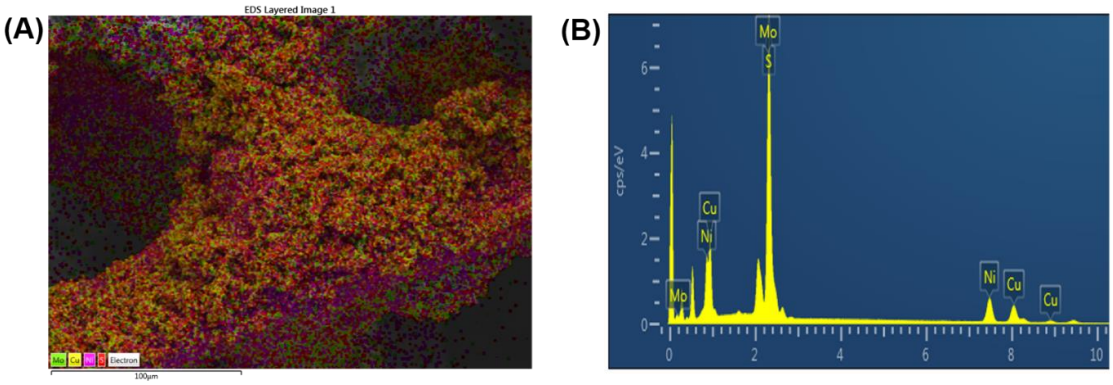

Figure 6.3 (A) FE-SEM micrographs for elemental mapping and (B) EDS spectrum for CMS anchored on Ni foam.

The overlay elemental mapping of copper, molybdenum and sulfur element present in the CMS grown on Ni foam is shown in Figure 6.3(A). The EDS spectrum for the CMS grown on Ni foam is provided in Figure 6.3(B). Figure 6.1(D-F) shows the elemental mapping of copper, molybdenum and sulfur elements which are homogeneously distributed on the individual CMS anchored on Ni foam. Typical XPS survey spectrum of CMS nanostructure (given in Figure 6.4(A)) anchored on Ni foam shows the presence of Cu 2p, Mo 3d, S 2p, Ni 2p, C 1s and O 1s states of elements, respectively. The presence of C and O element in the survey spectrum due to the exposure to air before the experiment. The presence of Ni-auger peaks is also observed in the survey spectrum which is due to the CMS nanostructures directly grown on Ni foam.[21] The core-level spectrum of Cu 2p states is presented in Figure 6.4(B) which shows the presences of two major peaks at 953.13 eV and 933.40 eV corresponding to the Cu $2p_{1/2}$ and Cu $2p_{3/2}$ states respectively.[22] The core-level XPS spectrum for Mo 3d is provided in Figure 6.4(C),

which revealed the presence of two strong peaks at 234.28 eV for Mo $3d_{3/2}$ and 231.17 eV for Mo $3d_{5/2}$ states present in the CMS grown on Ni foam.[22] Figure 6.4(D) represents the core-level spectrum for S 2p state, which indicated the presence of a major peak around 162.14 eV due to the S $2p_{3/2}$ state. The appearance of an additional peak at about 167.1 eV which can be ascribed to the shake-up satellites (identified as "Sat."). The observed peaks are well matched with a previous report based on Cu_2MoS_4 and the valence states of Cu, Mo, and S in CMS nanostructure on Ni foam is +1, +6, and -2 valences, respectively.[23]

Figure 6.5 represents the XRD pattern of CMS grown on Ni foam. The diffraction peaks obtained at 2θ = 16.73°, 21.87°, 29.12°, 31.02°, 37.54°, 46.20°, 48.54°, and 55.40°, corresponding to the (002), (110), (112), (013), (004), (123), (220) and (132) crystal planes of tetragonal Cu_2MoS_4 as reported in the previous literature.[13,14] The XRD pattern reveals that the CMS grown on Ni foam corresponds to I-phase Cu_2MoS_4 crystal with tetragonal *P42m* symmetry.[13,14] In addition, three extra peaks (*) observed at 2θ = 44.32°, 51.69° and 76.14° correspond to the Ni foam (current collector).

The UV-vis spectrum for the as-prepared CMS is shown in Figure 6.6. The UV-vis spectrum for the CMS nanostructures exhibiting a strong light absorption in the wavelength range of 300-800 nm.[24] The optical band gap of CMS nanostructures is calculated using the Tauc' s method and the band gap is around 1.65 eV.[25,26]

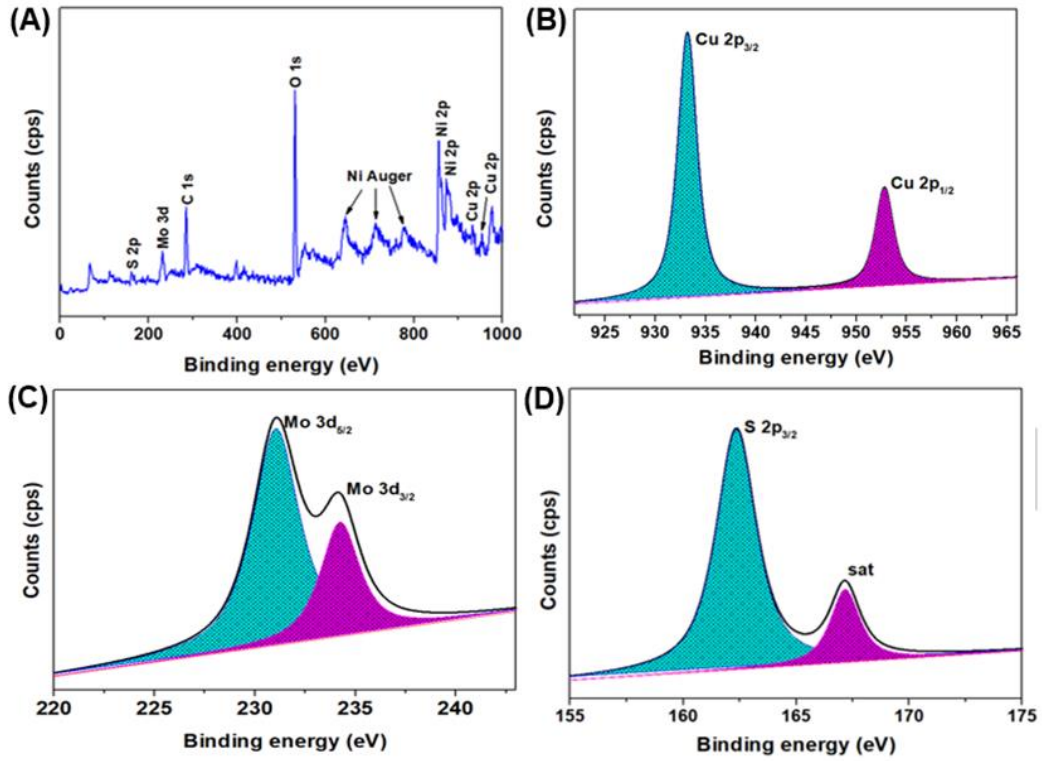

Figure 6.4 X-ray photoelectron spectrum of CMS nanostructure anchored on Ni foam (A) survey spectrum, (B) core level spectrum of Cu 2p state (C) core level spectrum of Mo 3d state, and (D) core level spectrum of S 2p state present in CMS nanostructure.

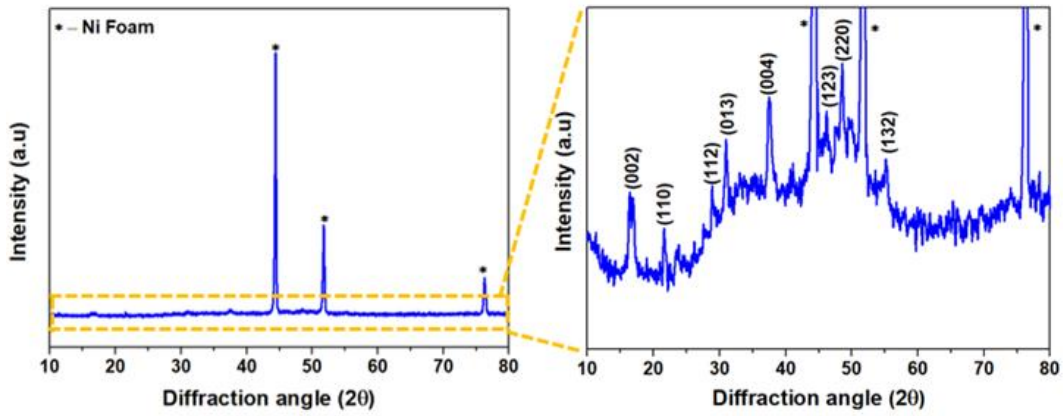

Figure 6.5 XRD pattern of CMS grown on Ni foam, peaks denoted to (*) correspond to Ni foam.

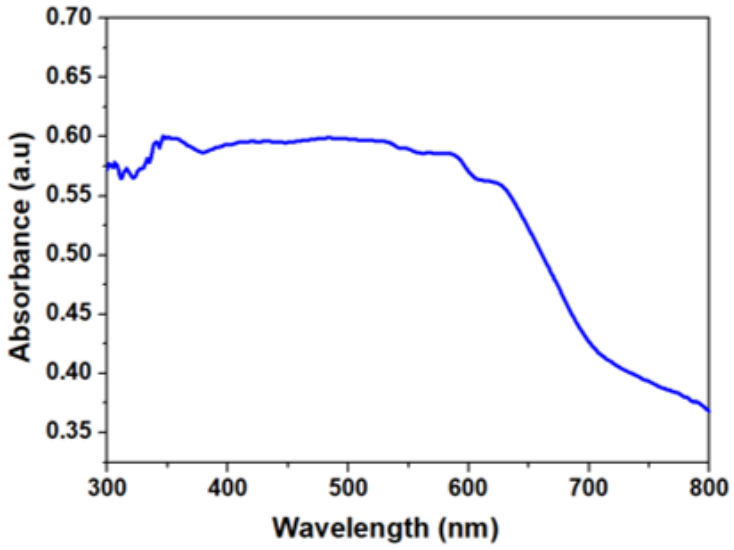

Figure 6.6 (A) UV–vis absorption spectrum for the CMS nanostructures.

The Brunauer-Emmett-Teller (BET) investigation was performed to obtain the specific surface area of the nanostructures. The BET surface area for CMS powder and CMS/Ni foam is about 6.4682 m^2 g^{-1} and 30.6913 m^2 g^{-1}, respectively. The surface area for the CMS/Ni foam is higher compared to the CMS powder due to the porous nature of Ni foam as shown in Figure 6.7.

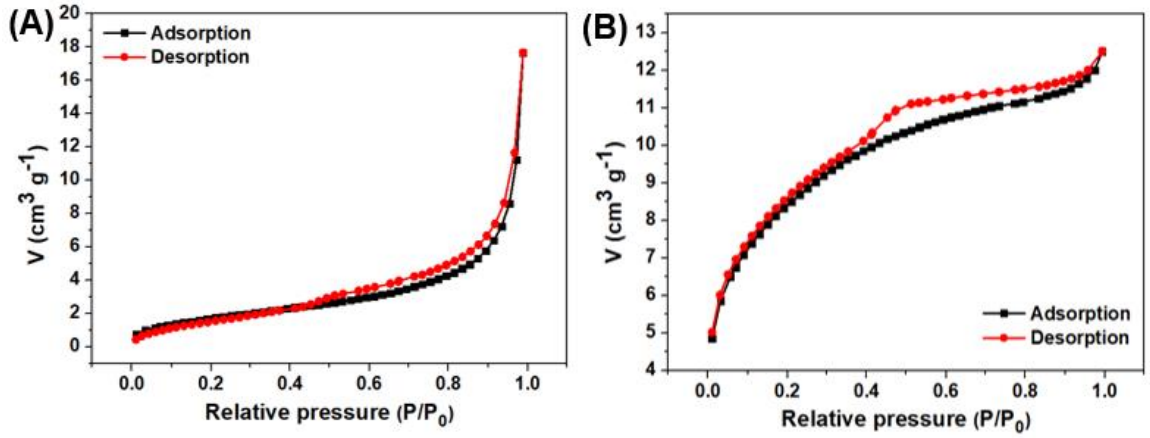

Figure 6.7 (A) Nitrogen adsorption-desorption isotherm for CMS powder and (B) CMS/Ni foam.

The as-prepared CMS anchored on Ni foam is examined as an electrode material for supercapacitor using three-electrode configuration and symmetric cell using 1 M Na_2SO_4

solution as an electrolyte. Figure 6.8(A) shows the cyclic voltammetric (CV) profiles of CMS/Ni electrode recorded using different scan rates (from 5 to 25 mV s^{-1}). The CV profiles showed the presence of a pair of redox peaks signifying the mechanism of charge-storage is due to the pseudocapacitive nature of CMS/Ni electrode.[27] Further, the current is increased with respect to an increase in scan rates suggesting the better capacitive nature of the CMS/Ni electrode. Figure 6.8(B) shows the effect of scan rate on the specific capacity of CMS/Ni electrode. A high specific capacity of 633 mAh g^{-1} (equivalent to a specific capacitance of 2278.83 F g^{-1}) was obtained for the CMS/Ni electrode at a low scan rate of 5 mV s^{-1}. From Figure 6.9 (in ESI), it is clear that the contribution of Ni foam is negligible on the overall specific capacitance of CMS/Ni electrode.

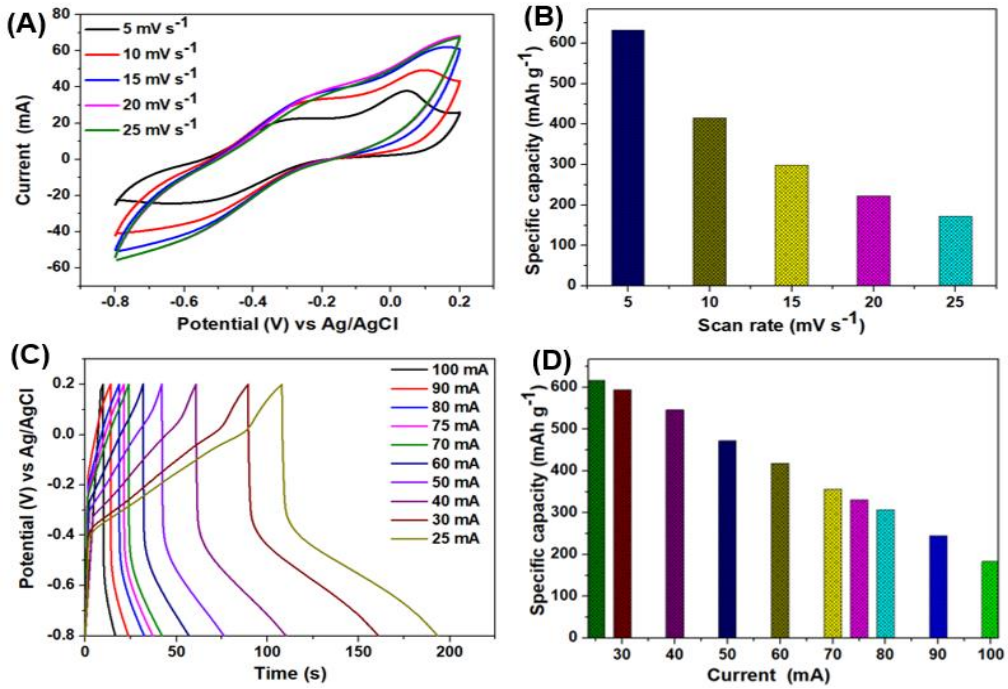

Figure 6.8 Electrochemical performance of CMS/Ni electrode using three-electrode configuration. (A) cyclic voltammetric profiles of CMS/Ni electrode measured at various scan rate, (B) effect of scan rate on the specific capacity of CMS/Ni electrode, (C) galvanostatic charge-discharge profile of CMS/Ni electrode measured at various current, and (D) effect of current on specific capacity of CMS/Ni electrode.

Figure 6.10 represents the electrochemical performance of binder-based CMS electrode. Further, the specific capacity of CMS/Ni electrode (633 mAh g^{-1}) is nearly 19.28-fold higher than that of the binder-based CMS electrode (32.83 mAh g^{-1}). Figure 6.8(C) shows the galvanostatic charge-discharge (CD) profiles of CMS/Ni electrode obtained at various current (25 to 100 mA). The CD profiles indicate the presence of distinct plateau regions, demonstrating the pseudocapacitive nature of CMS/Ni electrode and is in close agreement with the CV profiles given in Figure 6.8(A).

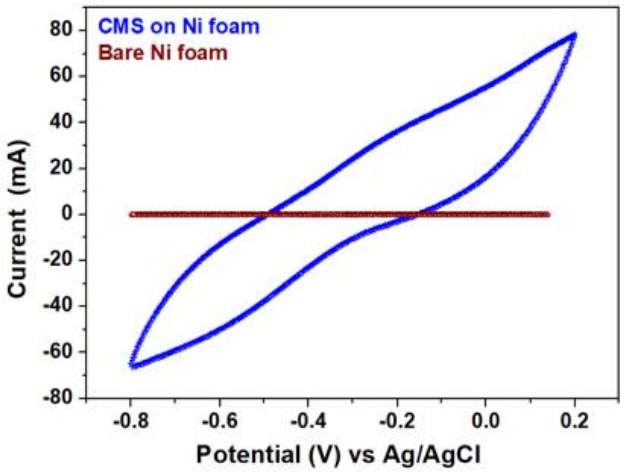

Figure 6.9 Cyclic voltammetry analysis of bare Ni foam and CMS/Ni electrode in three electrode configuration.

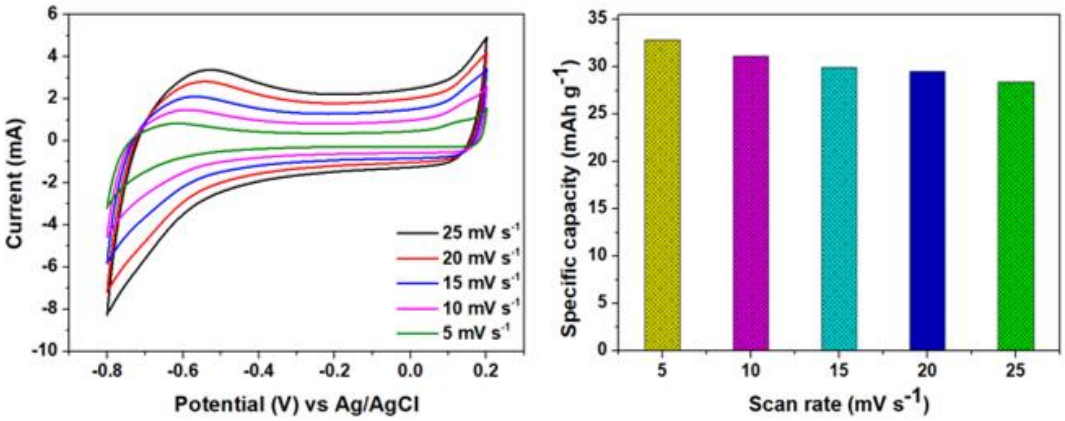

Figure 6.10 Electrochemical performance of binder-based CMS electrode in three electrode configuration. The three-electrode configuration test of binder-based CMS electrode was performed according to the method reported in our earlier literature.[20]

The columbic efficiency is about 85 % for all the tested current which indicated the good electrochemical capacitive nature of CMS/Ni electrode.[28] The existence of ohmic drop of about 0.13 V at a current of 25 mA for the CMS/Ni electrode due to the internal resistance of the active electrode material and the contact resistance between the electrode and electrolyte solution.[29] The effect of current on the specific capacity of CMS/Ni electrode is provided in Figure 6.8(D). Figure 6.11 shows the variation of specific capacitance of CMS/Ni electrode with respect to scan rates and current. A high specific capacity of 617.36 mAh g^{-1} (specific capacitance of 2222.50 F g^{-1}) was obtained for the CMS/Ni electrode from the CD profile obtained at a current of 25 mA. Table 6.1 shows the performance superiority of the CMS/Ni electrode over the recently reported binder-free electrodes. Further, the CMS/Ni electrode operates as a negative electrode which is an added advantage for supercapacitor devices since only few electrode materials can work as a negative electrode.[30]

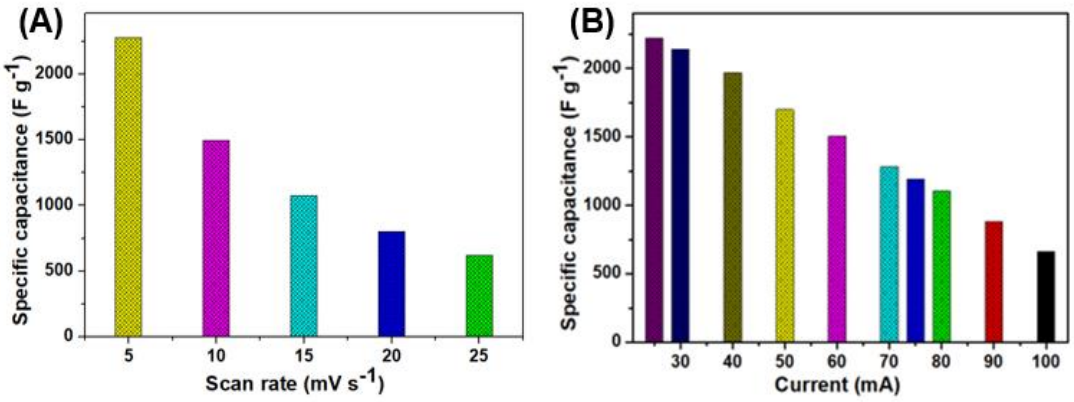

Figure 6.11 (A) Effect of specific capacitance of CMS/Ni electrode with respect to scan rate, and (B) Effect of specific capacitance of CMS/Ni electrode with respect to current.

The device specific properties of the CMS/Ni electrode were examined by the fabrication and testing of a SSC. Figure 6.12 shows the CV profiles of the CMS/Ni SSC with different operating potential window (OPW) which revealed an increase in current for CMS/Ni SSC with an increase in OPW, suggesting the ideal capacitive nature.[31] The CV profiles of the CMS/Ni SSC obtained using different scan rates is shown in Figure 6.13(A) which displayed a typical rectangular behavior, thus indicating the ideal capacitive properties of the CMS/Ni SSC.[32] The effect of scan rate on the specific capacitance for CMS/Ni SSC is illustrated in Figure 6.13(B).

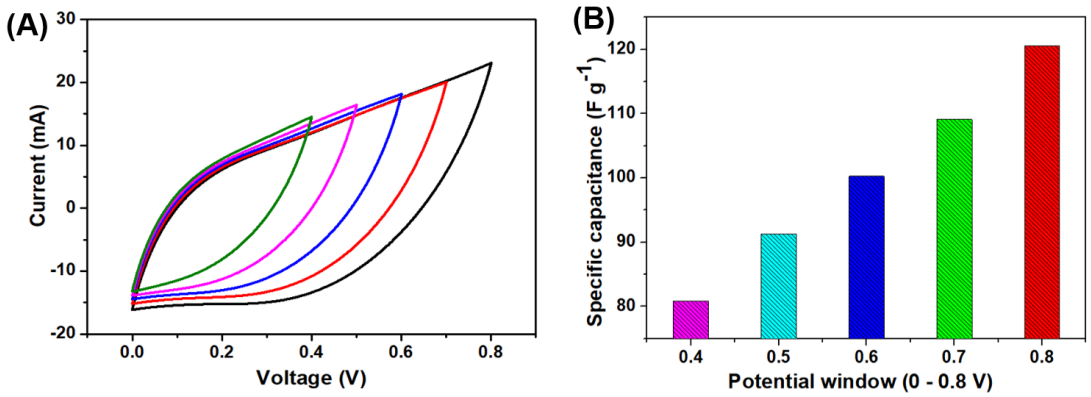

Figure 6.12 Potential window optimization of CMS/Ni SSC device using cyclic voltammetry: (A) cyclic voltammetric profile at different potential window, and (B) effect of specific capacitance of CMS/Ni SSC device with respect to different operating potential window (OPW).

The CMS SSC device possesses a high specific capacitance of about 219.91 F g^{-1} obtained from the CV profiles recorded at 5 mV s^{-1}. Further, the CMS/Ni SSC still holds a specific capacitance of about 120.53 and 60.85 F g^{-1} with an increase in scan rate up to ten- and twenty-fold, suggesting their better rate capability. EIS measurement is carried out to understand the charge-transfer behavior and capacitive characteristic of the CMS/Ni SSC device.

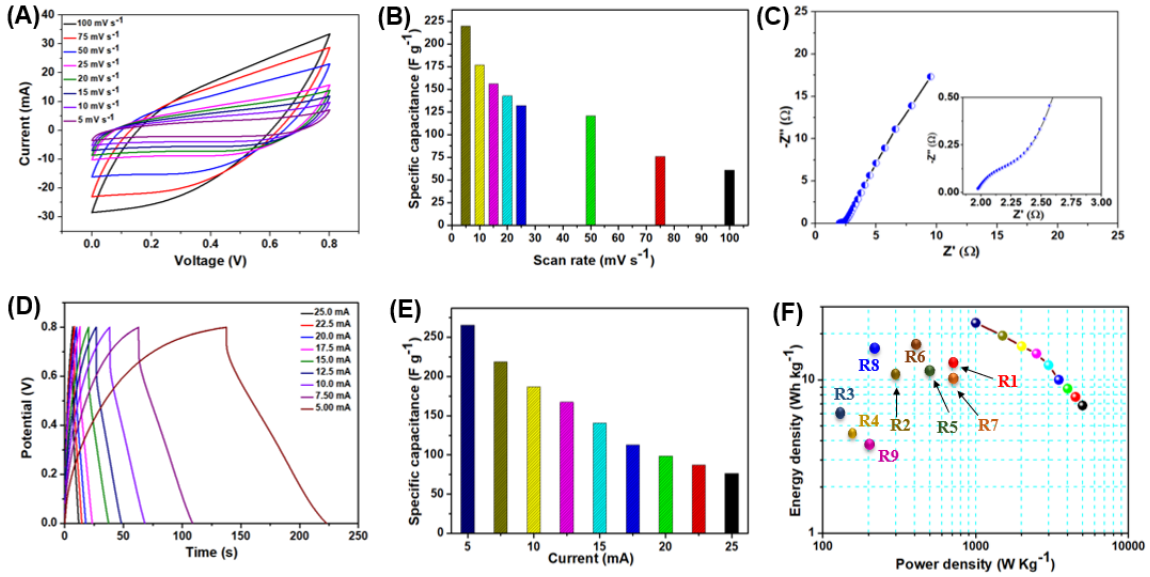

Figure 6.13 Electrochemical performance of CMS/Ni SSC. (A) cyclic voltammetric profiles at different scan rate, (B) effect of scan rate on the specific capacitance of CMS/Ni SSC, (C) Nyquist plot of CMS/Ni SSC (inset shows the enlarged view of the Nyquist plot), (D) charge-discharge profiles of CMS/Ni SSC measured at different current, (E) effect of current on specific capacitance of CMS/Ni SSC, (F) Ragone plot of CMS/Ni SSC and the references R1-R9 are provided in Table 6.2.

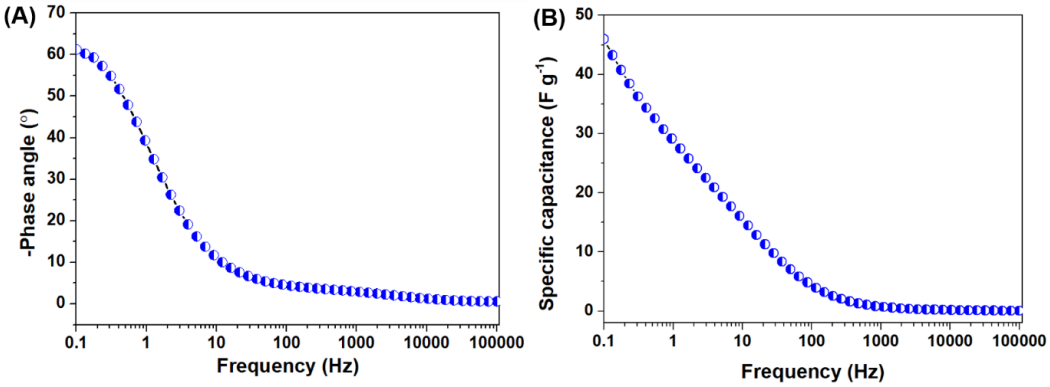

Figure 6.14 EIS analysis of CMS/Ni SSC device (A) Bode phase angle plot, and (B) Plot of variation of specific capacitance of CMS/Ni SSC device with respect to frequency.

Figure 6.13(C) depicted the Nyquist plot of CMS/Ni SSC which revealed the presence of a semicircle at high-frequency region and a straight line at the low-frequency region. From the enlarged view of the Nyquist plot (inset of Figure 6.13(C)), it is clearly noticeable that the

solution resistance (R_s) and charge transfer resistance (R_{ct}) is about 1.97 Ω and 0.33 Ω, respectively.[33] The obtained slope (~45°) in Nyquist plot nearly parallel to the imaginary axis is due to the Warburg impedance as a result of frequency-dependent fast ion diffusion kinetics of the electrolyte into the CMS/Ni SSC device.[33] Figure 6.14(A) represent the Bode plots of phase angle against the frequency for the CMS/Ni SSC. The phase angle at the tail is nearly 61.27° at low frequency region indicating the pseudocapacitive behavior of CMS/Ni SSC.[28] The effect of applied frequency on the specific capacitance of CMS/Ni SSC is provided in Figure 6.14(B) which revealed a maximum capacitance of about 45.94 F g^{-1} at a frequency of 0.1 Hz, and the capacitance decreases with an increase in frequency.

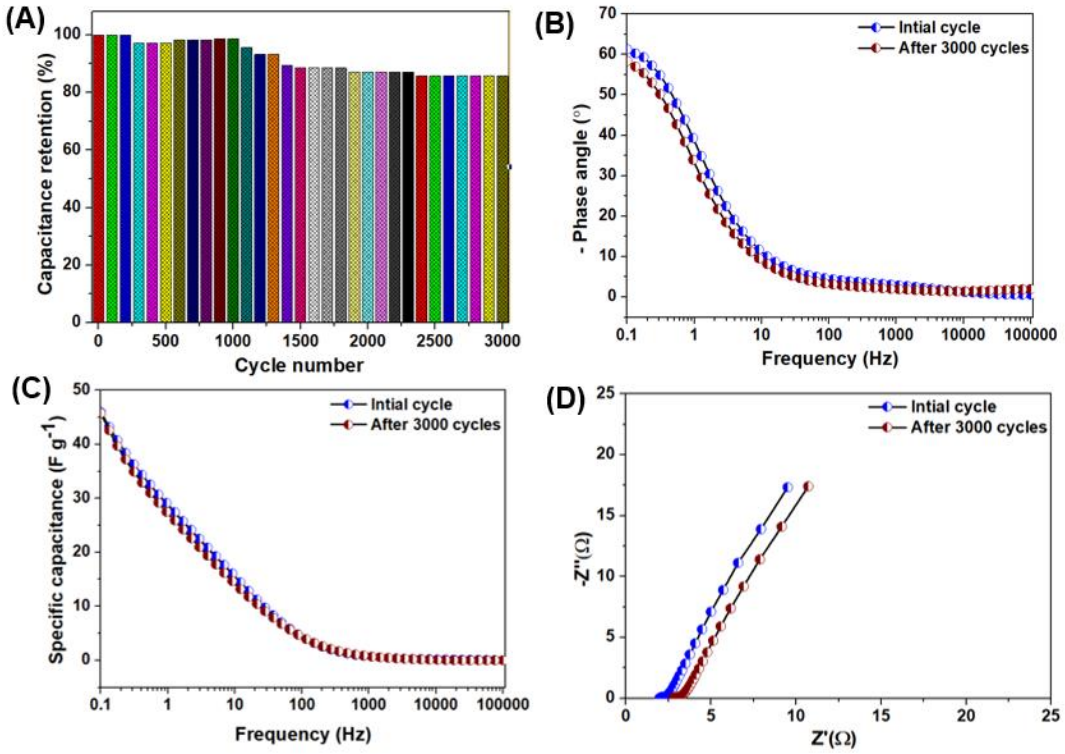

Figure 6.15 (A) Cyclic stability performance for CMS/Ni SSC device, (B) Bode phase angle plot initial and after 3000 cycles for CMS/Ni SSC device, (C) Plot of variation of specific capacitance of CMS/Ni SSC device with respect to frequency initial and after 3000 cycles for CMS/Ni SSC device, and (D) Nyquist plot of CMS/Ni SSC device measured during initial and after 3000 cycles.

The CD profiles of CMS/Ni SSC recorded using different current of 5 to 25 mA is presented in Figure 6.13(D). The CD profiles revealed the presence of sloppy-symmetric triangular shaped nature as evidence of pseudocapacitive nature of CMS/Ni SSC. The effect of current on the specific capacitance of CMS/Ni SSC is provided in Figure 6.13(E) which shows a high specific capacitance of about 265.62 F g^{-1} was obtained for the CMS/Ni SSC from the discharge profile recorded using 5 mA. The energy and power density of the CMS/Ni SSC was determined from the CD profiles and is represented in the form of Ragone plot (Figure 6.13(F)). The CMS/Ni SSC possesses a high energy density of 23.61 Wh kg^{-1} with a corresponding power density of 1000 W kg^{-1} obtained from the CD profile recorded using a current of 5 mA. With a five-fold increase in current, the CMS/Ni SSC still holds an energy density of 6.80 Wh kg^{-1} whereas the power density increases up to 5000 W kg^{-1}, respectively. The specific capacitance and energy density of the CMS/Ni SSC is quite higher compared to the state of art of symmetric supercapacitors as evidenced from the Ragone plot and Table 6.2.

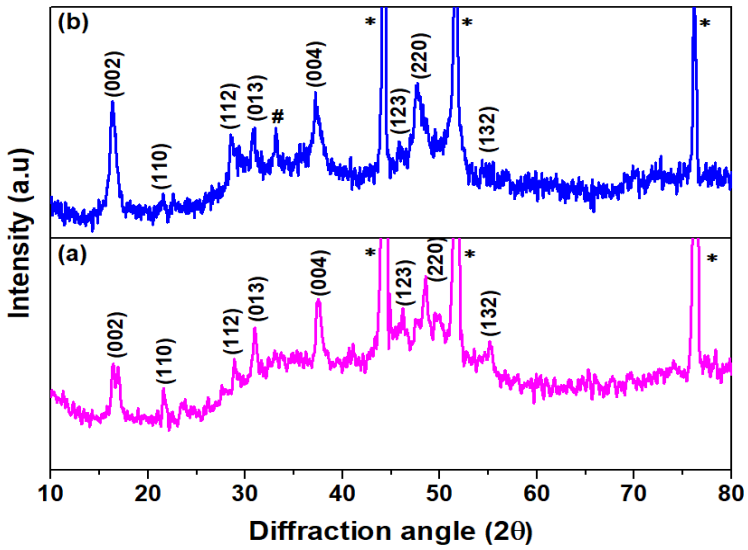

Figure 6.16 Comparison of XRD spectra for CMS/Ni foam (a) initial and (b) after the cyclic test. The peaks denoted to (*) correspond to Ni foam and (#) to Na_2SO_4.

The electrochemical stability of the CMS/Ni SSC over 3000 cycles of charge-discharge is presented in Figure 6.15(A) (in ESI) which showed capacitance retention of about 85.73 % of its initial capacitance. The EIS analysis is recorded after the cyclic tests, and the results are provided in Figure 6.15(B-D). Figure 6.15(B and C) shows that the phase angle at the tail decreases from 61.27° to 58.38° and the specific capacitance values decrease from 45.94 to 45.74 F g^{-1} after the cyclic test. The Nyquist plot of the CMS/Ni SSC measured after 3000 cycles (Figure 6.15(D)) showed an increase in R_s (from 1.97 to 2.78 Ω) and R_{ct} (0.33 to 0.48 Ω,) of CMS/Ni SSC, which might be one of the reason for the observed small decay in capacitance.[28,32]

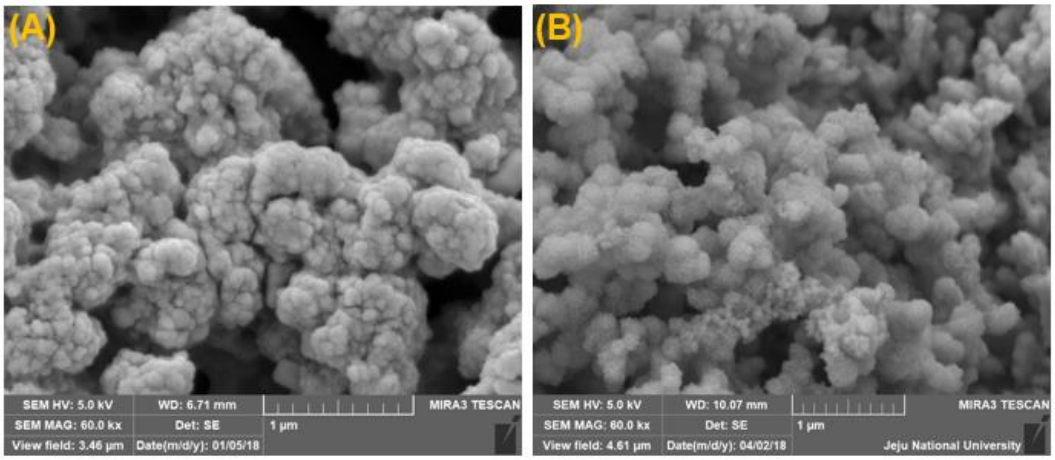

Figure 6.17 FE-SEM micrograph for CMS/Ni SSC (A) before and (B) after cyclic stability performance.

The XRD and FESEM analysis for the CMS/Ni electrode before and after cyclic stability are provided in Figure 6.16 and 6.17. The XRD pattern (Figure 6.16) before and after cyclic test shows that there is no phase change has been observed after cyclic stability. In addition, a small peak corresponds to the Na_2SO_4 has been observed which might be due to the ion-intercalation/de-intercalation into the CMS/Ni electrode during the electrochemical reaction[34]. This observation in XRD is confirmed from the FESEM micrograph (Figure 6.17) which reveals that there is a slight increase in the volume of the electrode material after 3000 cycles, which may be due to reaction with electrolyte ions over prolonged charged discharge

cycles. The increase in the volume of the electrode material may also be a reason for the observed capacitance decay after 3000 cycles.[35]

Table 6.1 Summary of electrochemical performances of binder-free CMS/Ni electrode and recently reported binder free electrode materials using three-electrode configurations.

S. No.	Material	Preparation method	Specific capacity (mAh g^{-1})	Specific capacitance (F g^{-1})	Ref
1.	CuS/Ni foam	Hydrothermal	-	1124	[36]
2.	MoS_2/Ni foam	SILAR	-	661	[37]
3.	MoS_2/Mo foil	Hydrothermal	-	192.7	[38]
4.	Ni_3S_2/Ni foam	Hydrothermal	-	1293	[17]
5.	Co_9S_8/Ni foam	Hydrothermal	-	1775	[39]
6.	NCS/Ni foam	Electrodeposition	-	1712	[40]
7	Co-Mn S/ Ni foam	Electrodeposition	53.4	1000	[41]
8	Ni_3S_2@β-NiS/Ni foam	Solvothermal	-	1158	[42]
9	$ZnCo_2O_4$ /Ni foam	Hydrothermal	-	1620	[43]
10.	Ni-Mo oxide/ Ni foam	Hydrothermal	-	1189	[44]
11.	**CMS/Ni foam**	**Hydrothermal**	**633**	**2278.83**	**This work**

Table 6.2 Summary of electrochemical performances of CMS/Ni SSC device and recently reported binder-free SSC device.

S. No.	Material	Potential window (V)	Specific capacitance (F g^{-1})	Energy density (Wh kg^{-1})	Power density (W kg^{-1})	Reference
1	$ZnCo_2O_4$/Ni foam	0.8	568	12.5	800	R1[45]
2	Co_3O_4@$CoMoO_4$/Ni foam	0.8	107	10.1	200	R2[46]

3	MoS_2/Carbon cloth	0.8	368	5.42	128	R3[47]
4	MnO_2/ Ni coated porous AAO	0.8	194.23	4.2	151	R4[48]
5	MnO_2/Carbon fiber	1	79	11	529.3	R5[49]
6	$CuCo_2O_4$/Ni foam	1.2	50.75	17	480	R6[50]
7	$Cd(OH)_2$/SS	1.9	51	11.09	799	R7[51]
8	$Co(OH)_2$/GF	1.2	69	13.9	-	R8[52]
9	$Co(OH)_2$/SS	1.2	44	3.96	-	R9[53]
10	**CMS/Ni SSC device**	**0.8**	**265.625**	**23.61**	**1000**	**This work**

6.4 Conclusions

The key findings of this contribution demonstrated the use of a novel copper-molybdenum-sulfide nanostructures grown on nickel foam (CMS/Ni) as a promising binder-free, negative electrode with a high specific capacity (633 mAh g^{-1}) for supercapacitor devices. The electrochemical analysis of the CMS/Ni SSC revealed the superior charge-storage performance with a high specific capacitance (265.62 F g^{-1}), high energy density (23.61 Wh kg^{-1}), and excellent cyclic stability. Collectively, this study demonstrated the potential use of binder-free CMS/Ni electrode as a high-performance negative electrode towards the development of next-generation supercapacitors.

6.5 References

1 C. Jiang, Y. Fang, J. Lang and Y. Tang, *Adv. Energy Mater.* 2017, **7**, 1700913.

2 S. Zhang, M. Wang, Z. Zhou and Y. Tang, *Adv. Funct. Mater.* 2017, **27**, 1703035.

3 M. Huang, X. L. Zhao, F. Li, W. Li, B. Zhang, Y. X. Zhang, , *J. Mater. Chem. A*, 2015, **3**, 12852–12857.

4 S. R. Marri, S. Ratha, C. S. Rout and J. N. Behera, *Chem. Commun.*, 2017, **53**, 228–231.

5 C. Zhong, Y. Deng, W. Hu, J. Qiao, L. Zhang and J. Zhang, *Chem. Soc. Rev.*, 2015, **44**,

7484–7539.

6 A. M. Navarro-Suárez, K. L. Van Aken, T. Mathis, T. Makaryan, J. Yan, J. Carretero-González, T. Rojo and Y. Gogotsi, *Electrochim. Acta*, 2018, **259**, 752–761.

7 K. Krishnamoorthy, P. Pazhamalai and S.-J. Kim, *Energy Environ. Sci.*, 2018, **11**, 1595–1602.

8 G. K. Veerasubramani, K. Krishnamoorthy, P. Pazhamalai and S. J. Kim, *Carbon N. Y.*, 2016, **105**, 638–648.

9 H. Wang, M. Wang and Y. Tang, *Energy Storage Mater.*

10 M. Huang, F. Li, J. Y. Ji, Y. X. Zhang, X. L. Zhao and X. Gao, *CrystEngComm*, 2014, **16**, 2878–2884.

11 M. Huang, X. L. Zhao, F. Li, L. L. Zhang and Y. X. Zhang, *J. Power Sources*, 2015, **277**, 36–43.

12 E. A. Pruss, B. S. Snyder and A. M. Stacy, *Angew. Chemie Int. Ed.*, 1993, **32**, 256–257.

13 P. D. Tran, M. Nguyen, S. S. Pramana, A. Bhattacharjee, S. Y. Chiam, J. Fize, M. J. Field, V. Artero, L. H. Wong and J. Loo, *Energy Environ. Sci.*, 2012, **5**, 8912–8916.

14 W. Chen, H. Chen, H. Zhu, Q. Gao, J. Luo, Y. Wang, S. Zhang, K. Zhang, C. Wang and Y. Xiong, *Small*, 2014, **10**, 4637–4644.

15 K. Zhang, R. Khan, H. Guo, I. Ali, X. Li, Y. Lin, H. Chen, W. Yan, X. Wu and L. Song, *Phys. Chem. Chem. Phys.*, 2017, **19**, 1735–1739.

16 W. Wang, P. Zhang, L. Peng, W. Xie, G. Zhang, Y. Tu and W. Mai, *CrystEngComm*, 2010, **12**, 700–701.

17 K. Krishnamoorthy, G. K. Veerasubramani, S. Radhakrishnan and S. J. Kim, *Chem. Eng. J.*, 2014, **251**, 116–122.

18 V. K. Mariappan, K. Krishnamoorthy, P. Pazhamalai, S. Sahoo and S. J. Kim,

Electrochim. Acta.

19 K. Krishnamoorthy, P. Pazhamalai, S. Sahoo, J. H. Lim, K. H. Choi and S. J. Kim, *ChemElectroChem*.

20 K. Krishnamoorthy, P. Pazhamalai and S. J. Kim, *Electrochim. Acta*, 2017, **227**, 85–94.

21 D. He, G. Liu, A. Pang, Y. Jiang, H. Suo and C. Zhao, *Dalt. Trans.*, 2017, **46**, 1857–1863.

22 K. Zhang, Y. Zheng, Y. Lin, C. Wang, H. Liu, D. Liu, C. Wu, S. Chen, Y. Chen and L. Song, *Phys. Chem. Chem. Phys.*, 2017, **19**, 557–561.

23 I. Ali, Z. Ullah, I. Rehan, A. Khalil, M. Habib, H. T. Masood, Y. Sohail and M. Waseem, *J. Mater. Sci. Mater. Electron.*, 2017, **28**, 15936–15941.

24 K. Zhang, W. Chen, Y. Lin, H. Chen, Y. A. Haleem, C. Wu, F. Ye, T. Wang and L. Song, *Nanoscale*, 2015, **7**, 17998–18003.

25 K. Krishnamoorthy, R. Mohan and S.-J. Kim, *Appl. Phys. Lett.*, 2011, **98**, 244101.

26 R. Rameshbabu, R. Vinoth, M. Navaneethan, Y. Hayakawa and B. Neppolian, *CrystEngComm*, 2017, **19**, 2475–2486.

27 G. K. Veerasubramani, M. S. P. Sudhakaran, N. R. Alluri, K. Krishnamoorthy, Y. S. Mok and S. J. Kim, *J. Mater. Chem. A*, 2016, **4**, 12571–12582.

28 K. Krishnamoorthy, P. Pazhamalai, S. Sahoo and S.-J. Kim, *J. Mater. Chem. A*, 2017, **5**, 5726–5736.

29 K. Wang, H. Wu, Y. Meng, Y. Zhang and Z. Wei, *Energy Environ. Sci.*, 2012, **5**, 8384–8389.

30 X.-J. Ma, W.-B. Zhang, L.-B. Kong, Y.-C. Luo and L. Kang, *RSC Adv.*, 2015, **5**, 97239–97247.

31 S. Lehtimäki, A. Railanmaa, J. Keskinen, M. Kujala, S. Tuukkanen and D. Lupo, *Sci. Rep.*, 2017, **7**, 46001.

32 K. Jeyasubramanian, T. S. Gokul Raja, S. Purushothaman, M. V. Kumar and I. Sushmitha, *Electrochim. Acta*, 2017, **227**, 401–409.

33 L. Wang, X. Zhang, Y. Ma, M. Yang and Y. Qi, *J. Phys. Chem. C*, 2017, **121**, 9089–9095.

34 X. Wu, M. Fan, S. Cui, G. Tan and X. Shen, *Sol. Energy Mater. Sol. Cells*, 2018, **178**, 280–288.

35 Y. Li, Y. Zheng, J. Yao, J. Xiao, J. Yang and S. Xiao, *RSC Adv.*, 2017, **7**, 31287–31297.

36 Y. Zhang, J. Xu, Y. Zheng, X. Hu, Y. Shang and Y. Zhang, *RSC Adv.*, 2016, **6**, 59976–59983.

37 R. N. Bulakhe and J.-J. Shim, *New J. Chem.*, 2017, **41**, 1473–1482.

38 K. Krishnamoorthy, G. K. Veerasubramani, P. Pazhamalai and S. J. Kim, *Electrochim. Acta*, 2016, **190**, 305–312.

39 J. Pu, Z. Wang, K. Wu, N. Yu and E. Sheng, *Phys. Chem. Chem. Phys.*, 2014, **16**, 785–791.

40 S. Sahoo, K. K. Naik, D. J. Late and C. S. Rout, *J. Alloys Compd.*, 2017, **695**, 154–161.

41 S. Sahoo and C. S. Rout, *Electrochim. Acta*, 2016, **220**, 57–66.

42 W. Li, S. Wang, L. Xin, M. Wu and X. Lou, *J. Mater. Chem. A*, 2016, **4**, 7700–7709.

43 B. Guan, D. Guo, L. Hu, G. Zhang, T. Fu, W. Ren, J. Li and Q. Li, *J. Mater. Chem. A*, 2014, **2**, 16116–16123.

44 D. Cheng, Y. Yang, Y. Luo, C. Fang and J. Xiong, *Electrochim. Acta*, 2015, **176**, 1343–1351.

45 S. Wang, J. Pu, Y. Tong, Y. Cheng, Y. Gao and Z. Wang, *J. Mater. Chem. A*, 2014, **2**, 5434–5440.

46 J. Wang, X. Zhang, Q. Wei, H. Lv, Y. Tian, Z. Tong, X. Liu, J. Hao, H. Qu and J. Zhao, *Nano Energy*, 2016, **19**, 222–233.

47 M. S. Javed, S. Dai, M. Wang, D. Guo, L. Chen, X. Wang, C. Hu and Y. Xi, *J. Power Sources*, 2015, **285**, 63–69.

48 A. Kumar, A. Sanger, A. Kumar, Y. Kumar and R. Chandra, *Electrochim. Acta*, 2016, **222**, 1761–1769.

49 Y. Wen, T. Qin, Z. Wang, X. Jiang, S. Peng, J. Zhang, J. Hou, F. Huang, D. He and G. Cao, *J. Alloys Compd.*, 2017, **699**, 126–135.

50 Y. Wang, D. Yang, J. Lian, T. Wei and Y. Sun, *J. Alloys Compd.*

51 S. Patil, S. Raut, R. Gore and B. Sankapal, *New J. Chem.*, 2015, **39**, 9124–9131.

52 U. M. Patil, S. C. Lee, J. S. Sohn, S. B. Kulkarni, K. V Gurav, J. H. Kim, J. H. Kim, S. Lee and S. C. Jun, *Electrochim. Acta*, 2014, **129**, 334–342.

53 A. D. Jagadale, V. S. Kumbhar, D. S. Dhawale and C. D. Lokhande, *Electrochim. Acta*, 2013, **98**, 32–38.

CHAPTER – 7

High performance self-charging supercapacitor using porous PVDF-ionic liquid electrolyte sandwiched between two-dimensional graphene electrodes

Highlights

- The research on the development of all-in-one self-charging supercapacitor power cell (SCSPC) received increasing attention during recent years.
- Herein, we reported a novel SCSPC device comprising two-dimensional graphene sheets as electrodes for energy storage and porous PVDF incorporated $TEABF_4$ electrolyte as a solid-like piezo-polymer separator.
- Initially, the energy harvesting properties of porous PVDF films and energy storage performance of graphene based SCSPC device were evaluated separately.
- The porous PVDF film generated a voltage from 4 to 11 V when subjected to compressive forces of 5 and 20 N, respectively.
- The graphene SCSPC device delivered a highest specific device capacitance of 28.46 F g^{-1} (31.63 mF cm^{-2}) with a specific energy of 35.58 Wh kg^{-1} and high-power density of 7500 W Kg^{-1}, respectively.
- Strikingly, the graphene SCSPC device can be charged up to 112 mV under a compressive force of 20 N within 250 seconds and the mechanism of self-charging via piezo-electrochemical energy conversion process- discussed in detail.

7.1 Introduction

The increasing development of portable and wearable electronic device have resulted in tremendous research interest in developing new energy harvesting- and storage systems during recent decades.[1] In order to meet the energy requirements of modern society, researchers have persistently devoted their immense efforts to build efficient energy harvesting and storage devices that can act as a sustainable energy source.[2,3] Classically, energy harvesting and energy storage are two well-defined phenomena utilizing different mechanisms and individual physical units.[4,5] For modern electronics, design and development of a single device capable of energy harvesting-, conversion- and storage properties are highly essential for day-to-day applications.[6,7] Among the energy harvesting devices, piezoelectric and triboelectric nanogenerators possess wide interests since they can convert mechanical energy into electrical energy without any restriction from the weather, and location.[8–10] Further, the harvested electrical energy is needed to be stored in an energy storage device (such as Li-ion batteries and supercapacitors).[11,12] The recent studies reported the integration of these energy harvesting and storage devices using extrinsic and internal integration methods. The extrinsic integration of the nanogenerators and batteries/supercapacitors required additional power management circuits whereas the internal integration possesses the advantage of reducing the cost of additional power management circuits. [13–15] Thus, the development of an internally integrated self-charging power cell is of high interest.

The self-charging power cell (SCPC) device is capable of simultaneous converting mechanical to electrical energy and stores them in an energy storage device without the aid of external circuitry via a novel “piezo-electrochemical process”.[15] This novel concept of piezo-electrochemical process is used for self-charging the power cell was initially demonstrated by Xue et al. in 2012. In this study, they reported a novel SCPC using a lithium ion battery

(containing $LiCoO_2$ cathode, TiO_2 anode) via replacing the commercial polymeric separator by polyvinylidene fluoride (PVDF) based piezo-separator.[6] Following on, several reports on SCPC devices using the battery as energy storage devices have been demonstrated by a few researchers from 2012 to till date. In the most recent study, Xue et al. demonstrated the improved self-charging properties of SCPC via using $LiPF_6$ incorporated porous PVDF piezo-polymer separator.[16] However, the self-charging efficiencies of SCPCs are still needed to be improved to meet out the essential criterions for practical applications. Hitherto, SCPC devices utilizing supercapacitors as energy storage unit can be termed as SCSPCs (self-charging supercapacitor power cell) which was initially demonstrated by our group in 2015 using pseudocapacitive MnO_2 electrode sandwiched in between a ZnO-PVDF piezo-polymer separator.[17] Following this work, Song et al. represented the self-charging properties of functionalized carbon cloth based SCSPC using PVDF separator.[12] Later on, Parida et al. demonstrated fast charging self-powered electric double layer capacitor based on carbon nanotube as supercapacitor electrode integrated with PVDF-TrFE as piezo-separator, and polymethyl methacrylate/$LiClO_4$ as an electrolyte.[18] In our recent study, we have demonstrated the high performance SCSPC device using 2D $MoSe_2$ based electrodes with ionogel-PVDF piezo-separator.[15] The detailed analysis of this literature suggested that the mechanism of self-charging properties of the SCPC and SCSPC devices are still under debate which is due to the structural complexity of the devices.

The selection of appropriate individual components (or materials) for the SCSPC devices is highly essential to achieve high performance as well as in-depth fundamental understanding of the mechanism. Considering the individual components of the SCSPC devices, the electrode material, electrolyte type, and piezo-polymer separator plays a vital role in the self-charging properties of SCSPC devices.[19–21] Without any competition, PVDF based co-polymers becomes the ideal piezo-polymer separator used in SCSPCs.[5] Upto date, only a few electrode

materials such as MnO_2, carbon cloth, CNTs, and $MoSe_2$ are examined as electrodes for SCSPC devices. [12,15,17,18] In this scenario, graphene sheets become a widely used supercapacitor electrode with high energy and power capabilities owing to their high electrical conductivity, surface area and sheet-like morphologies.[22,23] However, there were no studies on SCSPC devices utilizing graphene sheets as electrodes have been reported up to date. The presence of double layer capacitance in graphene sheets might provide new insights on the self-charging properties or piezo-electrochemical energy conversion properties. Therefore, in this study, we focused on developing SCSPC utilizing graphene sheets as ideal electrodes using a low-cost table salt derived porous PVDF as piezo-separator incorporated with $TEABF_4$ electrolyte. The self-charging performance metrics of the graphene SCSPC device is evaluated in detail with the use of various levels of compressive forces, and the self-charging performance was analyzed in detail.

7.2. Experimental section

7.2.1 Materials

Graphite powder and polyvinylidene fluoride (PVDF) were purchased Sigma Aldrich, South Korea. Potassium permanganate ($KMnO_4$), N-methyl pyrrolidone (NMP), N, N-dimethylformamide (DMF), hydrogen peroxide (H_2O_2), sulfuric acid (H_2SO_4), sodium hydroxide (NaOH), acetone (C_3H_6O), hydrazine hydrate (N_2H_4) and ethanol (C_2H_5OH) and were bought from Daejung Chemicals Ltd., South Korea. Carbon black and tetraethylammonium tetrafluoroborate ($TEABF_4$) is procured from Alfa aesar, South Korea. Table salt was purchased from Sajo supplier (South Korea).

7.2.2 Sonochemical reduction of graphene oxide (GO) into reduced graphene sheets (rGO):

At first, the graphene oxide (GO) sheets were prepared in accordance with the modified Hummers method (using graphite powders, $KMnO_4$ and H_2SO_4) as reported in literature.[24,25]

After that, the de-oxygenation of GO sheets into reduced graphene sheets were achieved via a sonochemical process similar to that of the method reported in our earlier work.[26] Briefly, GO powders were dispersed in aqueous solution (with a concentration of 1 mg/mL) via ultrasound irradiation and the pH of the solution was adjusted into 10 using the addition of NaOH followed by the drop-wise addition of 2 mL of hydrazine hydrate solution. The ultrasound irradiation process was continued for 2 h which result in the change in brownish yellow color (GO) into black graphene sheets color indicating the de-oxygenation of GO leading to the formation of graphene sheets. Then, the resulting graphene dispersion was thoroughly washed with water and ethanol via repeated centrifugation process. Finally, the graphene sheets powders were dried at 60 °C for 12 h and used for further studies.

7.2.3 Fabrication and analysis of free-standing porous PVDF piezo-polymer separator

The free-standing porous PVDF films were prepared through solvent-based film casting method.[27] Briefly, 2 g of PVDF powders were dispersed in DMF solution and subjected to ultrasound irradiation process for 2 h which result in the formation of a homogeneous and transparent solution. Following this, 2.5 g of mechanically grounded table salt powders was added into the PVDF solution using the magnetic stirring process for 24 h at a temperature of 80 °C. After that, the solution was poured into a Petri dish and kept it in a hot air oven at 70 °C for overnight for removing the solvent (DMF). Then, the PVDF-table salt composite film was peeled off from the Petri dish and the salt was removed by immersing the film in deionized water for 72 h which result in the formation of porous PVDF. The prepared porous PVDF are allowed to dry at a temperature of 80 °C for 6 h and used for further characterization. The table-salt incorporated PVDF film was prepared with the addition of table salt using the similar process. The piezoelectric properties of the free-standing porous PVDF film were measured under various external mechanical forces with the aid of a linear motor (E1100), and a Keithley

Electrometer (Model no: 6514) was adopted to test the short-circuit current and open circuit voltage.

7.2.4 Instrumentation

The crystal structure of GO and graphene sheets were obtained using an Empyrean X-ray diffractometer (XRD) instrument (Malvern Panalytical, UK) using Cu-Kα radiation (λ = 1.54184 Å). The laser Raman spectroscopy of GO, graphene (rGO) and porous PVDF were performed using Lab Ram HR Evolution Raman spectrometer (Horiba Jobin-Yvon, France, at laser excitation source of wavelength 514 nm). The morphological analysis of graphene sheets, table salt induced PVDF and porous PVDF were performed using field-emission scanning electron microscopy (TESCAN, MIRA3) under different magnifications with energy dispersive X-ray (EDS) spectroscopy. The Fourier transform infrared spectrum (FT-IR) was measured using Thermo scientific, Nicolet-6700 FT-IR spectrometer. The chemical elements and its states were analyzed using X-ray photoelectron spectroscopy (XPS) techniques using ESCA-2000, VG Microtech Ltd, (Al Kα (1486.6 eV)).

7.2.5 Fabrication of self-charging supercapacitor power cell (SCSPC):

The self-charging supercapacitor power cell (SCSPC) in this work was constructed using graphene sheets as energy storage electrodes and porous PVDF incorporated $TEABF_4$ electrolyte as the separator.

7.2.5.1. Preparation of graphene electrodes for SCSPC:

The rGO electrodes were fabricated using the slurry coating method as described in literature.[28] Briefly, the active material (graphene), carbon black and PVDF were taken in the weight ratio of 85:10:5 and grounded well using NMP dispersant until a uniform slurry was formed. Then, the slurry was coated on stainless-steel (SS) coin cell substrate (with a dimension of 15.4 mm × 0.2 mm) using slurry coating method and allowed to dry at 70 °C in an oven

overnight. The mass loading of the graphene on SS substrate is about 1 mg which was determined using the difference between the mass of graphene coated SS to that of the bare SS substrate.

7.2.5.2. Incorporation of $TEABF_4$ electrolyte into porous PVDF matrix:

The piezo-polymer separator used for the graphene SCSPC device was prepared by immersing the porous PVDF in a 1 M solution of $TEABF_4$ electrolyte in an argon filled glove box for 24 h. This process leads to the entrapment of electrolyte into the pores of the prepared porous PVDF and followed by drying which results in a formation solid-like piezo polymer separator films.

7.2.5.3. Construction of graphene based SCSPC:

The graphene based SCSPC device was fabricated in symmetric supercapacitor with coin-cell (CR2032) type configuration using two ideal graphene electrodes separated by the solid-like piezo-polymer separator. The fabricated SCSPC device was crimped using an electric coin-cell crimping machine (MTI, Korea). All this fabrication process was performed in a glove box with less than 1 ppm of moisture and oxygen.

7.2.5.4. Electrochemical analysis of graphene based SCSPC:

The electrochemical performance of graphene based SCSPC device was investigated using cyclic voltammetry (CV), galvanostatic charge-discharge (CD), and electrochemical impedance spectroscopy (EIS), and long-term cyclic stability tests. The self-charging characterization of the graphene based SCSPC device was performed under an external mechanical force with the aid of a linear motor. All the electrochemical measurements were carried out using AUTOLAB PGSTAT302N electrochemical workstation. The specific capacitance (Csp), energy density (E) and power density (P) of the graphene SCSPC device were calculated using the following relations; [29–31]

$$C_{sp} = [(\int I\, dV) / (s \times \Delta V \times m)] \quad \ldots\ldots\ldots\ldots (1)$$

$$C_{sp} = [(I \times \Delta t) / (\Delta V \times m)] \quad \ldots\ldots\ldots\ldots\ldots (2)$$

$$E = (I \times \Delta t \times \Delta V) / (7.2 \times m) \quad \ldots\ldots\ldots\ldots (3)$$

$$P = (3.6 \times E) / \Delta t \quad \ldots\ldots\ldots\ldots\ldots (4)$$

Here, *"C_{sp}"* is the specific capacitance (F g^{-1}), "*I*" is the applied current (A), "Δ*V*" is the operating potential window, "*s*" is the scan rate (mV s^{-1}), "Δ*t*" is the discharge time (s), and "*m*" is the combined mass of the electro-active material (g) in both electrodes.

7.3 Results and Discussion

Figure 7.1(A) shows the schematic annotation of the work process involved in the preparation of porous PVDF film which is used as the piezo-polymer separator for the graphene SCSPC device. Here, the commercially available table salt powder is mixed with the prepared PVDF solution and allowed to cast in a Petri dish. The free-standing porous PVDF film was prepared via selective extraction of table salt from the composite film via immersing in hot water followed by drying process.[27] Figure 7.2(A-B) represents the FE-SEM micrographs of table salt incorporated PVDF film which shows the presence of table salt microstructures in the PVDF matrix. This was later confirmed by the EDX spectrum (Figure 7.2(C)) which shows the presence of Na and Cl components (from table salt) along with the C and F components (from PVDF). The elemental mapping of table salt powders incorporated PVDF film (given in Figure 7.3(A-D)) evidenced the uniform and homogeneous distribution of Na and Cl in the polymer matrix. After extraction of table salt from the prepared composite films using hot water, the FE-SEM and EDX analysis were performed to study the formation of porous nature in the PVDF and the efficiency of salt removal.

Figure 7.1(B-D) shows the FE-SEM micrographs of the prepared free-standing PVDF film which shows the presence of interconnected 3D framework of PVDF chains with irregular

pores in the film. The EDX mapping of the porous PVDF film (given in Figure 7.1(E-G)) shows the homogenous distribution of C and F components of PVDF (as seen in Figure 7.1(F, G)). The EDX spectrum of porous PVDF film (Figure 7.2(A)) indicated the absence of Na and Cl components and preservation of C and F, thus, indicating the successful removal of table salt from the PVDF film which also results in the formation of PVDF film with porous nature. Previous works on the preparation of porous PVDF films for SCPC devices using solvent casting followed by dissolution reactions such as the dissolution of ZnO and/or SiO_2 from PVDF using hydrofluoric acid.[16,32] Compared to these methods, the preparation of porous PVDF using table salt involved herein provides us a cost-effective and environmentally safe over them.

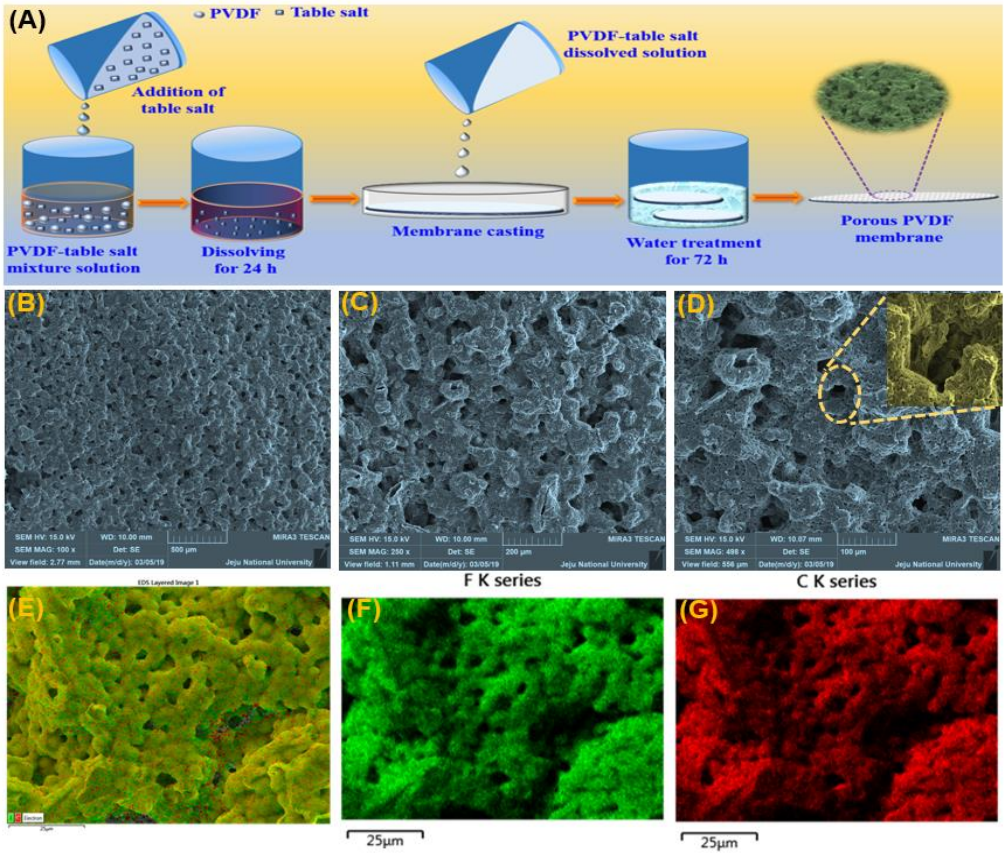

Figure 7.1 (A) Schematic illustration for fabrication of porous PVDF film via table salt incorporated method. (B-D) Field emission-scanning electron micrographs of porous PVDF film obtained under different magnifications. (E-G)

Elemental mapping micrographs of porous PVDF film in which (E) shows the overlay map, (F, G) represents the elemental maps of fluorine (F) and carbon (G) elements in the porous PVDF film.

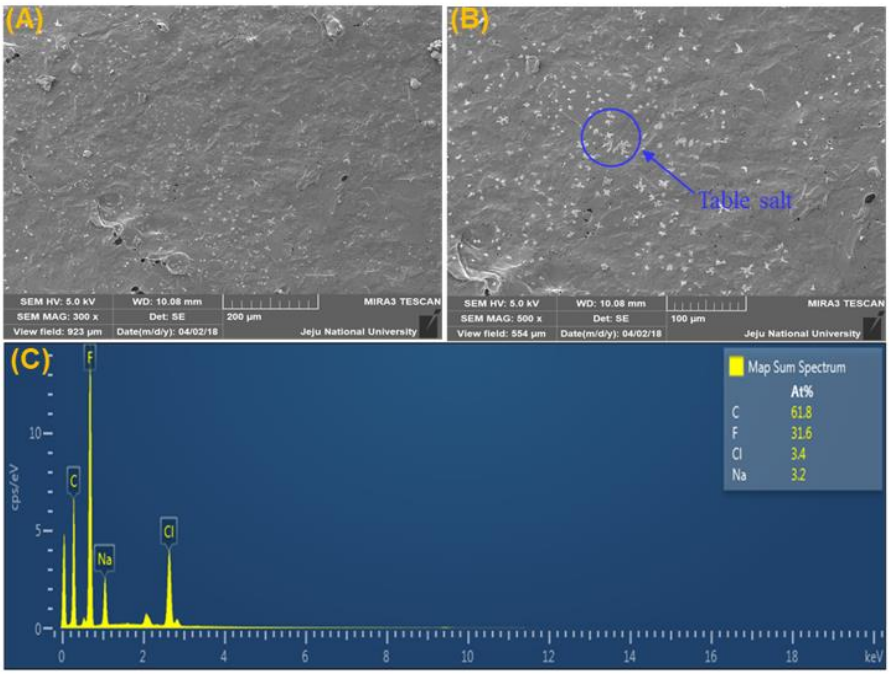

Figure 7.2. FE-SEM micrographs of table salt-induced PVDF film at magnification of (A) 200 µm and (B) 100 µm. (C) EDX spectrum of table salt-induced PVDF film with an atomic percentage.

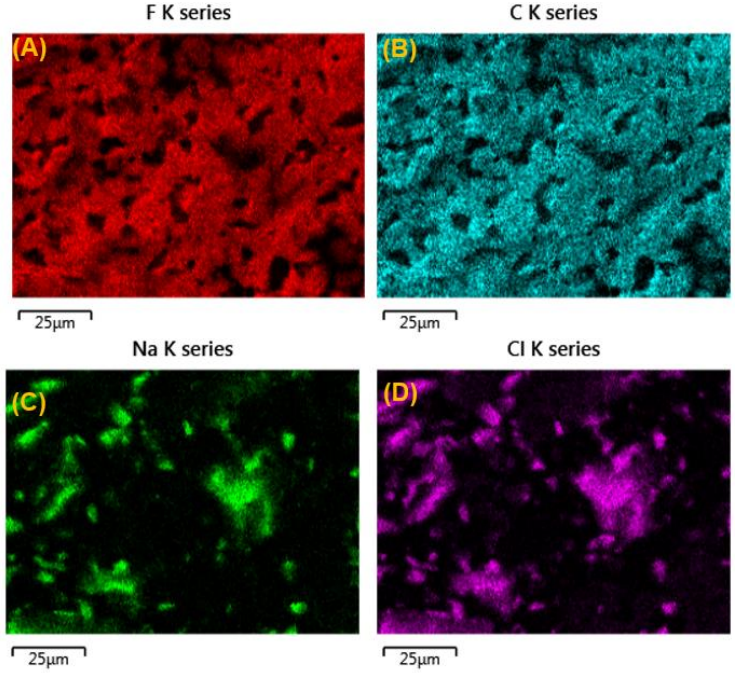

Figure 7.3 Elemental mapping micrographs of table salt incorporated PVDF film. The elemental maps of (A) fluorine, (B) carbon, (C) sodium and (D) Chlorine elements present in table salt incorporated PVDF film.

It is well known that the presence of pores in the PVDF film makes them ideal separator for electrochemical energy storage devices (such as supercapacitors and batteries).[33] Whereas in case of SCPC or SCSPC devices, in addition to porous nature, the piezoelectric properties of the PVDF separator play a vital role in the piezo-electrochemical energy conversion process when the device is subjected to mechanical force.[32,33] The PVDF film can be formed in a variety of phases such as α and β-phases in which the latter is highly essential for making them as piezoelectric polymer.[34]

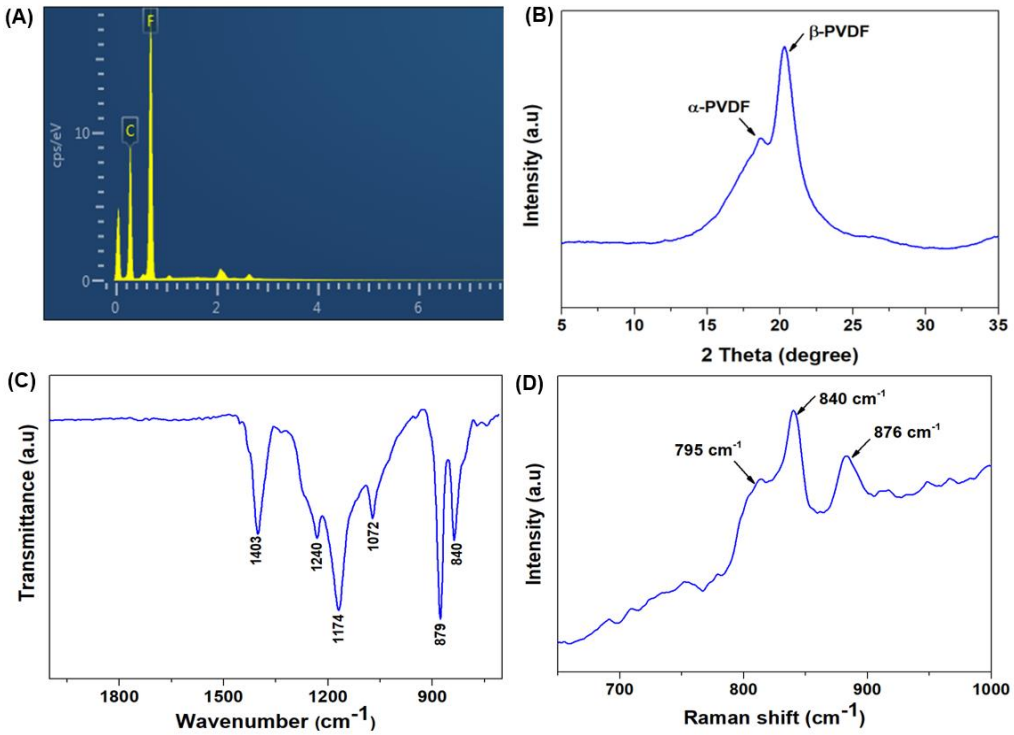

Figure 7.4 (A) EDX spectrum of porous PVDF film showing the presence of C and F elements. (B) X-ray diffraction pattern of porous PVDF film. (C) Fourier transform- infrared spectrum of porous PVDF film. (D) Laser Raman spectrum of porous PVDF film.

Therefore, characterizations such as XRD, FT-IR, and laser Raman spectroscopic studies were used to examine the formation of β-phase or not in the prepared porous PVDF films.

The XRD pattern of the prepared porous PVDF (shown in Figure 7.4(B)) indicated the presence of a broad diffraction peak at 2θ=20.28° which corresponds to the β-phase and the minor peak at 2θ=18.75° indicated the presence of α phase in the prepared film.[35,36] Figure 7.4(C) represents the Fourier transform infrared (FTIR) spectrum of the prepared porous PVDF film. The presence of characteristic bands at 840 cm^{-1} in the FT-IR spectrum confirmed the presence of β-phase in the prepared PVDF film.[37] The other absorption bands observed at 1403 cm^{-1} and 1176 cm^{-1} belongs to -CF_2- and -CH_2- presented in PVDF.[38]

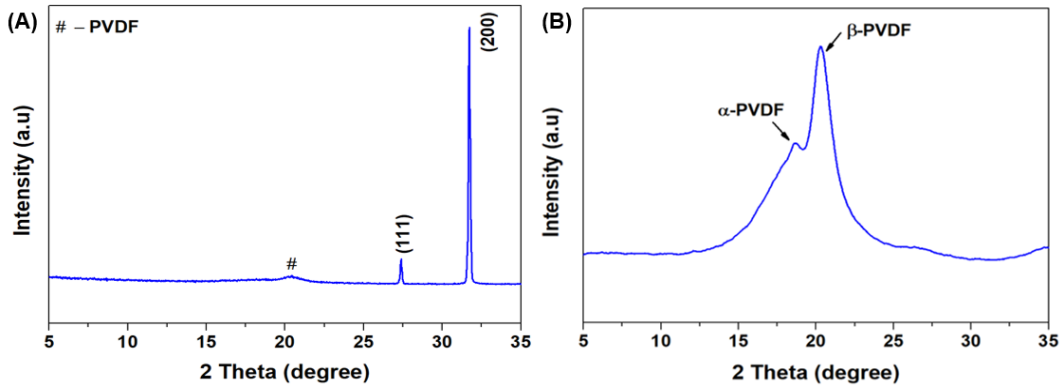

Figure 7.5 XRD pattern of (A) table salt incorporated PVDF film (JCPDS No:05-0628) and (B) porous PVDF film.

Figure 7.4(D) shows the laser Raman spectrum of the prepared porous PVDF which revealed the presence of three Raman bands 795, 840 and 876 cm^{-1}, respectively [39]. The small band at 795 and 876 cm^{-1} corresponds to the presence of α- phase, whereas the other strong band observed at 840 cm^{-1}, indicated the presence of β- phase in the prepared porous PVDF film.[40] The comparative physico-chemical characterizations of salt-PVDF composite and the porous PVDF films are provided in Figure 7.5-7.7.

These studies suggested the presence of porous nature and β-phase in the prepared PVDF film, thus making them as a suitable candidate as a piezo-polymer separator for SCSPC devices.[32] Figure 7.8 represents the piezoelectric energy harvesting properties of the prepared

porous PVDF film subjected to various levels of applied compressive forces. From Figure 7.8(A), it is evidenced that the voltage output of the porous PVDF film is increasing with an increase in applied compressive force. The effect of various levels of applied compressive forces on the electrical outputs of the porous PVDF film is shown in Figure 7.8(B).

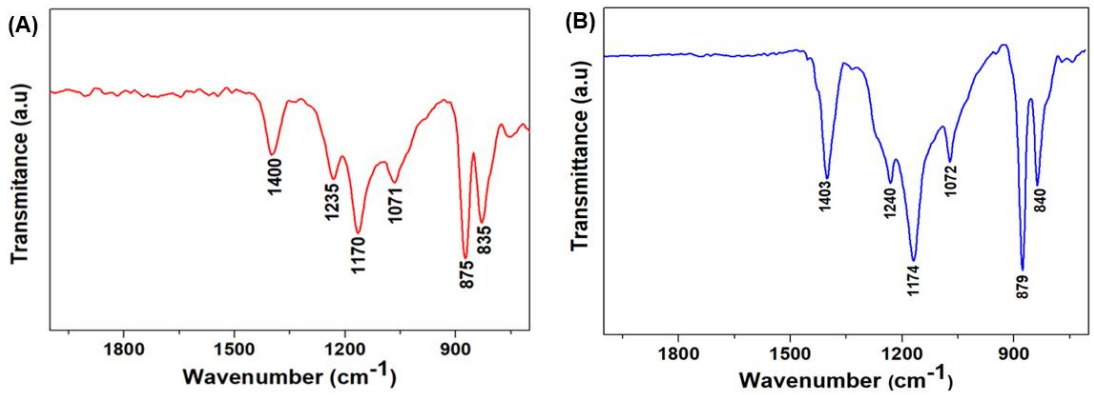

Figure 7.6 FT-IR spectra of (A) table salt incorporated PVDF film and (B) porous PVDF film.

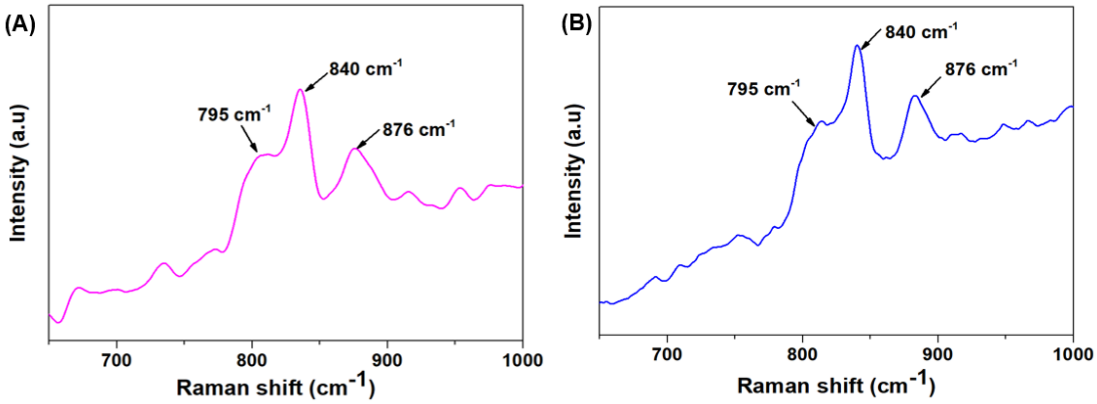

Figure 7.7 Raman spectra of (A) table salt incorporated PVDF film and (B) porous PVDF film.

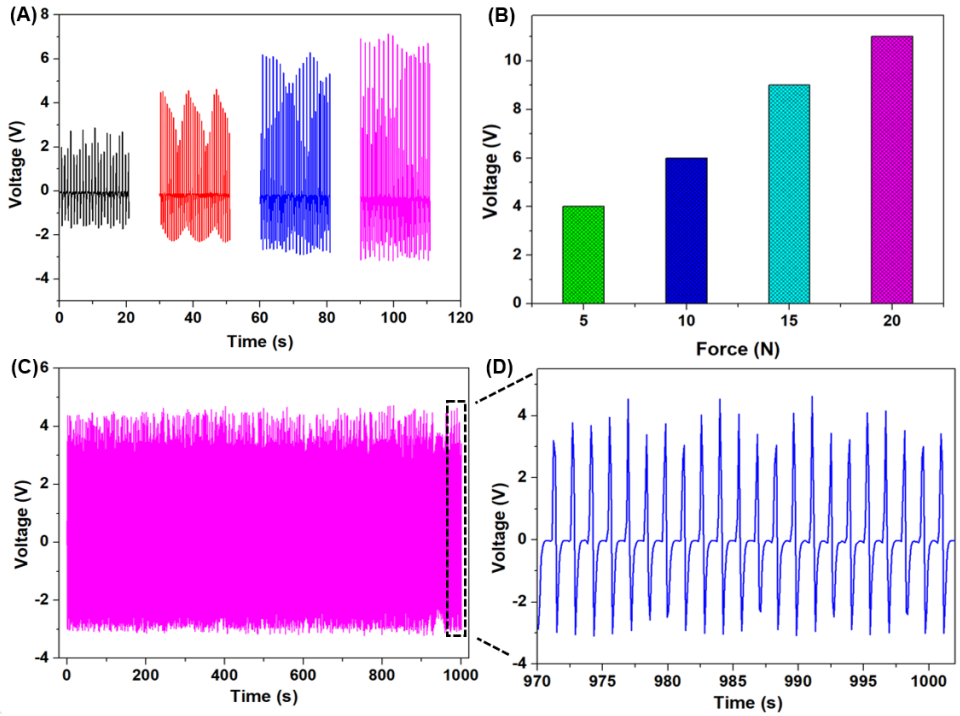

Figure 7.8 Piezoelectric energy harvesting properties of porous PVDF film. (A) Output voltage profile of the porous PVDF film obtained using various compressive forces from 5 to 20 N, (B) Variation of the output voltage of the porous PVDF film under different magnitude (5 to 20 N) of applied force, (C) electromechanical stability of the porous PVDF film under continuous applied force of 10 N over 1000 seconds, (D) the enlarged view (last 30 seconds) of the output voltage profile given in Figure 7.8(C).

The output voltage of porous PVDF film is found to be 4 V at a compressive force of 5 N and it was increased upto 11 V with an increase in force level up to 20 N. Figure 7.9 shows the current outputs of the porous PVDF film measured using different levels of compressive forces which shows the generated current in the range of 20 to 90 nA. The electromechanical stability of the piezoelectric porous PVDF film is an important criterion required for the long-term practical applications.[41] Figure 7.8(C) represents the electrochemical stability of the porous PVDF film 1000 seconds subject to a compressive force of 10 N. The porous PVDF film showed excellent electromechanical stability over 1000 seconds with consistent and stable electrical outputs (as seen from Figure 7.8(D)). The electrical performances of the porous PVDF

separators in this work are comparable to that of the other reported PVDF separators used for SCPC or SCSPC devices in literatures.[6,42,43]

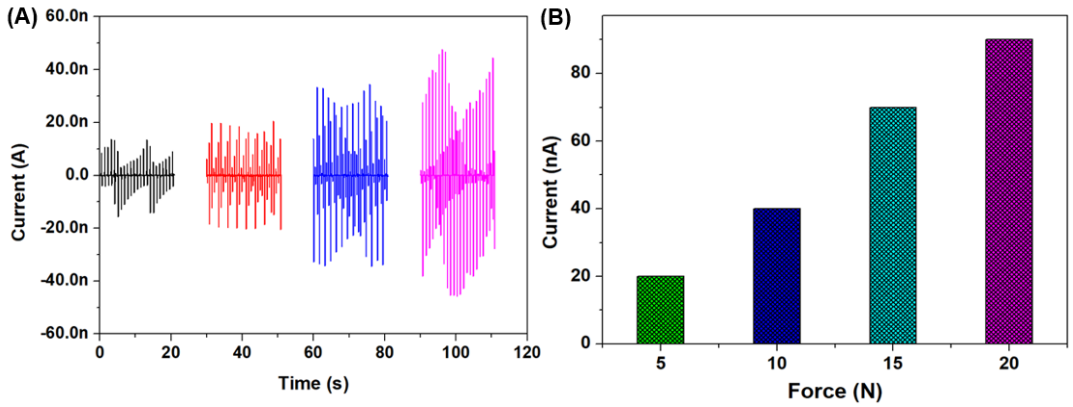

Figure 7.9 (A) Current profile of the porous PVDF film based nanogenerator device under various compressive forces from 5 to 20 N. (B) Variation of the output current of the porous PVDF film under different magnitude (5 to 20 N) of the applied force.

Figure 7.10 depicts the physico-chemical characterization of graphene sheets prepared via deoxygenation of GO sheets using the sonochemical method. The XRD pattern of GO and sonochemically prepared graphene sheets is provided in Figure 7.10(A). The disappearance of diffraction pattern at $2\theta = 11.44°$ confirms the removal of oxygenated functional groups in GO and formation of the new broad peak at $2\theta = 23.21°$ confirms the re-graphitization process leading to the formation of graphene sheets via sonochemical reduction method.[26]

The nature of oxygenated functional groups in GO and the reduced counterparts are studied by FT-IR spectroscopy (as shown in Figure 7.10(B)). The FT-IR spectrum of GO sheets shows the presence of various oxygenated functional groups such as carboxyl (1734 cm^{-1}), C-C (1640,1621, and 1515 cm^{-1}), hydroxyl (1405 cm^{-1}), epoxyl (1250 cm^{-1}), and carbonyl (1050 cm^{-1}) skeleton, respectively.[26] After sonochemical reduction reaction, peaks due to these functional groups are diminished and only peaks due to C-C skeleton (1640 and 1621 cm^{-1}) and hydroxyl skeleton (1405 cm^{-1}) is preserved in the FT-IR spectrum of graphene sheets.[26]

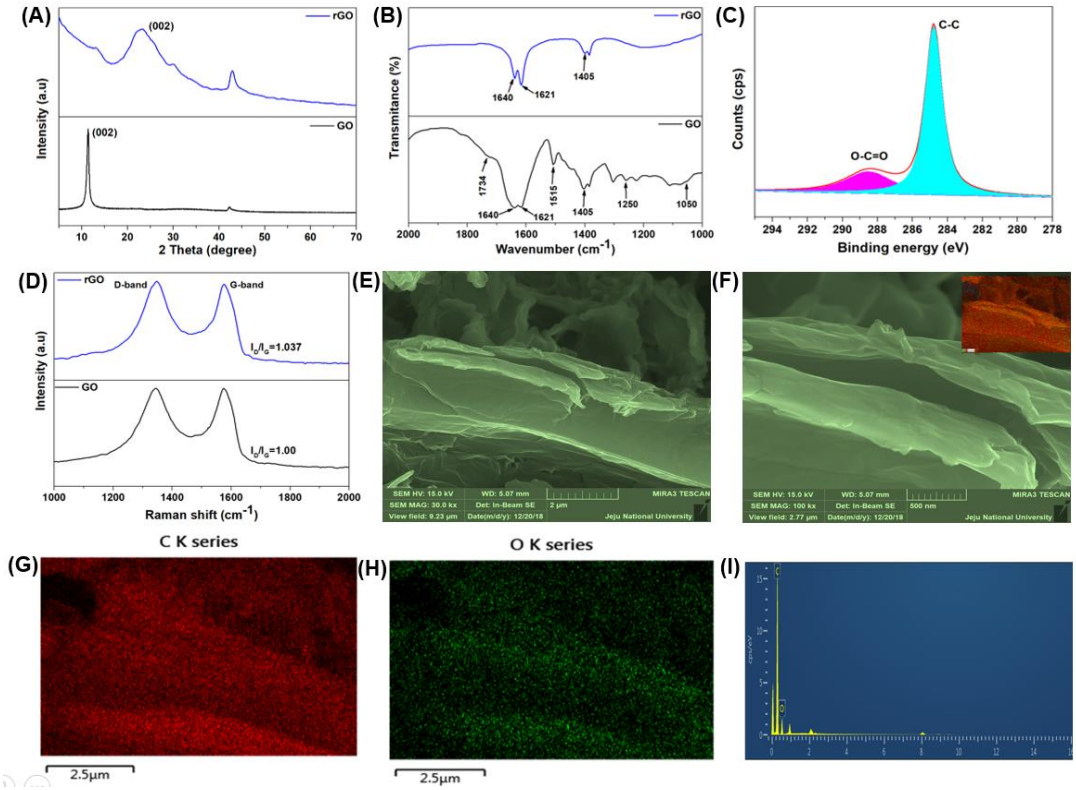

Figure 7.10 Physico-chemical characterization of sonochemically prepared graphene sheets. (A) The x-ray diffraction pattern of GO and graphene(rGO) sheets. (B) Fourier transform- infrared spectra of GO and graphene sheets. (C) C 1s core-level spectrum X-ray photoelectron spectrum of graphene sheets. (D) Laser Raman spectra of GO and graphene sheets. (E-F) Field emission-scanning electron micrographs of graphene sheets measured at different magnifications. The inset in Figure 7.10(E) shows the FE-SEM overlay micrograph used for elemental mapping analysis, and (G-H) represents the elemental maps of carbon and oxygen elements present in graphene sheets, (I) EDX spectrum of graphene sheets.

The core-level C 1s XPS spectrum of sonochemically prepared graphene sheets is provided in Figure 7.10(C) which shows the presence of C-C skeleton (284.5 eV) with little amounts of O-C=O groups (288.5 eV). In comparison to the C 1s spectrum of GO sheets,[44] the spectrum of graphene sheets indicated the removal of oxygenated functional groups via the sonochemical reduction reaction. Figure 7.10(D) represents the laser Raman spectra of GO and graphene sheets to further understand the crystallinity, defects of these materials. The Raman

spectrum of the GO nanosheets displays the occurrence of G band at 1596 cm^{-1}, and D band at 1359 cm^{-1}, respectively.[45] After the sonochemical reduction reaction, the G band is shifted to 1584 cm^{-1} justifying the removal of oxygenated functional groups and restoration of sp^2 domains in the prepare graphene sheets.[26] There is no significant change occurred in the peak position of the D band. Further, the intensity ratio of D- and G-band (I_D/I_G) is used to characterize the crystallinity and disorder degree of carbon-based materials, i.e., the higher the I_D/I_G, the larger disorder degree of the carbon-based materials.[46] The calculated I_D/I_G ratio for the GO and rGO are 1.00 and 1.037 respectively, which indicates the good reduction of GO occurred after the sonochemical reaction. The FE-SEM micrograph of graphene sheets obtained at different magnification levels are presented in Figure 7.10 (E and F) which revealed that the edges of graphene sheets were crumpled with overlapping of several individual sheets on each other. The overlay image of graphene sheets (given in inset of Figure 7.10(F)) used for EDX mapping analysis can be convoluted into two components such as carbon mapping (Figure 7.10(G)) and oxygen mapping (Figure 7.10 (H)). The EDX spectrum of graphene sheets provided in Figure 7.10(I) indicated the presence of C and O elements in the ratio of 83.4:16.6. This indicated the presence of residual oxygen groups in the sonochemically prepared graphene sheets which is in good agreement with the previous studies on chemically derived graphene.[47,48]

The graphene symmetric SCSPC device is fabricated in CR2032 coin-cell type configuration using two ideal graphene electrodes separated by $TEABF_4$-porous PVDF separator. At first, we have evaluated the operating potential window (OPW) of the graphene SCSPC device as shown in Figure 7.11(A-E), which showed that the device could operate over an OPW of 3.0 V without any sign of evolution. The plot of specific device capacitance against different OPWs (shown in Figure 7.11(F)) indicated the linear increase in capacitance with a corresponding increase in OPW in accordance with the Power law.[49] Figure 7.12(A and B)

represents the cyclic voltammetric (CV) profiles of the graphene SCSPC device recorded using different applied scan rates ranging from 5 to 500 mV s^{-1} over an OPW of 3.0 V. The shape of the CV profiles of graphene SCSPC shows typical rectangular behaviour which can be classified as Type A curve (EDLC) in accordance with the editorial note contributed by Prof. R. M. Penner and Prof. Y. Gogotsi. [50]

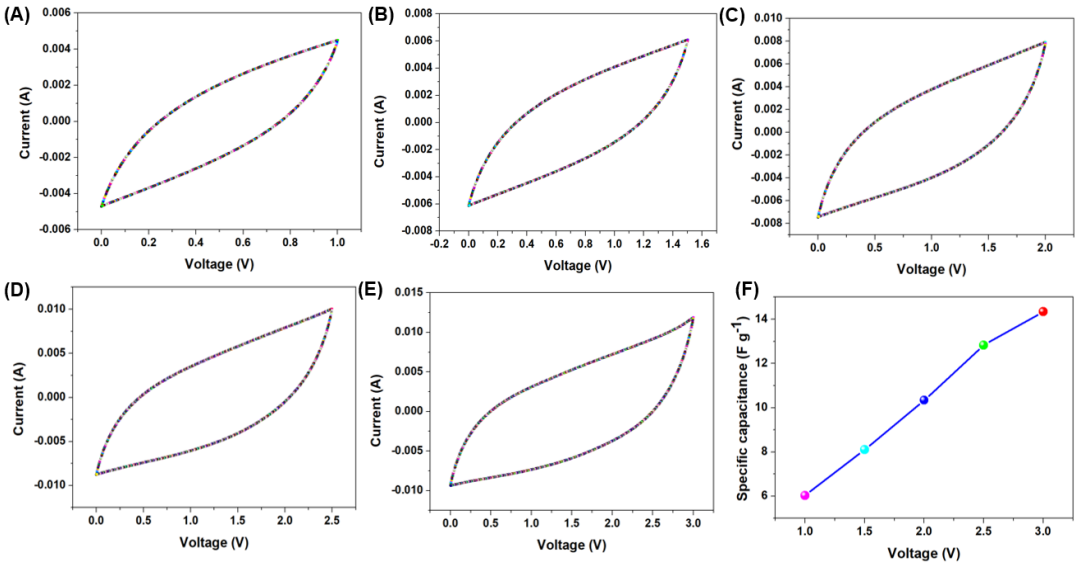

Figure 7.11 Electrochemical analysis of the graphene SCSPC (CR2032 coin cell) in $TEABF_4$ electrolyte. (A-E) Cyclic voltammetric profiles of the graphene SCSPC measured at the different operating potential window (1.0 to 3.0 V) using a scan rate of 200 mV s^{-1}. (F) Effect of specific capacitance of graphene SCSPC with respect to the different operating potential window (1.0 to 3.0 V).

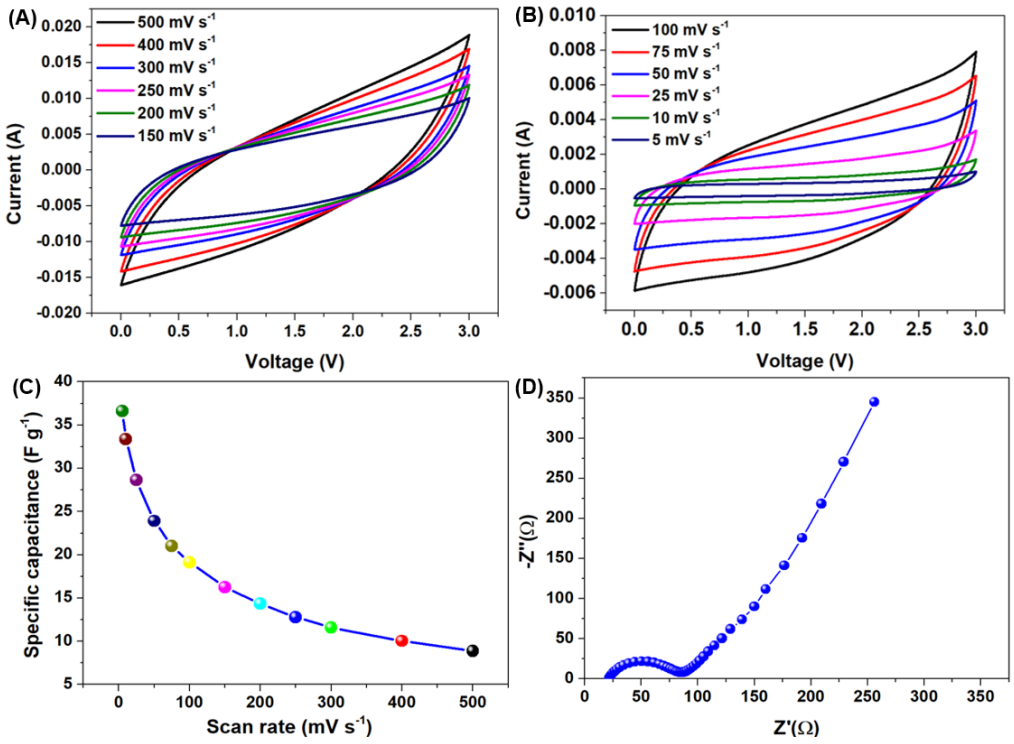

Figure 7.12 Electrochemical analysis of the graphene SCSPC (CR2032 coin cell) using porous PVDF incorporated $TEABF_4$ electrolyte. (A-B) Cyclic voltammetric profiles of the graphene SCSPC measured at scan rates (from 5 to 500 mV s^{-1}). (C) Effect of gravimetric specific device capacitance of graphene SCSPC with respect to applied scan rates. (D) Nyquist plot of graphene SCSPC.

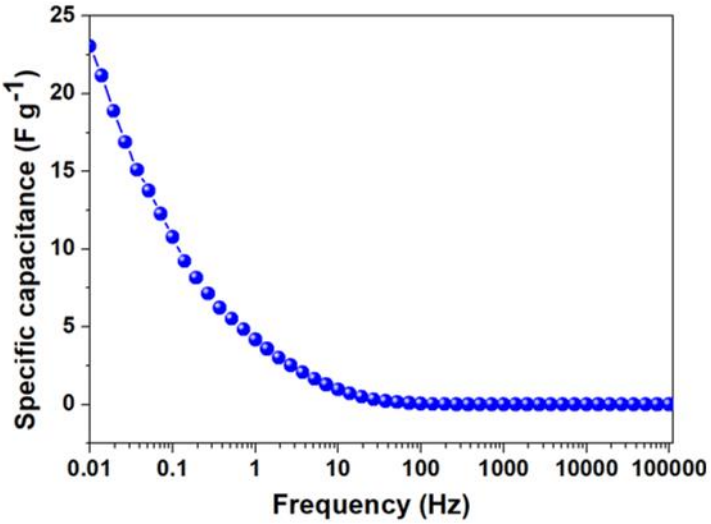

Figure 7.13 The plot of variation of specific capacitance of graphene SCSPC with respect to frequency.

From Figure 7.12(A and B), it is well noticeable that an increase in scan rate results in increase in current ranges which can be attributed to be better capacitive properties.[51] Further, the shape of the CV profiles is close to ideal rectangular shape upto a scan rate of 100 mV s^{-1} whereas further increase in scan rate up to 500 mV s^{-1}, the shape of the CV profiles becomes quasi parallelogram which might be due to the intrinsic resistance of the stacked graphene sheets.[52] Figure 7.12(C) represents the relationship between specific device capacitance with applied scan rates, which showed that the graphene SCSPC device possesses a specific device capacitance of 36.62 F g^{-1} (40.69 mF cm^{-2}) at a scan rate of 5 mV s^{-1}. Additionally, the graphene SCSPC still holds a specific device capacitance of about 8.87 F g^{-1} (9.85 mF cm^{-2}) as the scan rate increased by about 100 times (500 mV s^{-1}), signifying the good rate capability of the graphene SCSPC. In order to understand the fundamental charge-storage behaviour and capacitive nature of the graphene SCSPC, electrochemical impedance spectroscopy (EIS) measurements were carried out in this work. Figure 7.12(D) represents the Nyquist plot of graphene SCSPC which showed the presence of a semi-circle arc at the high- frequency region followed by a straight line at the low- frequency region.[49] The equivalent series resistance (ESR) and charge-transfer resistance (R_{ct}) resistance of the graphene SCSPC were determined as 21.39 and 59.53 Ω from the Nyquist plot. These values are higher compared to the graphene-based supercapacitor devices fabricated using an aqueous electrolyte which is mainly due to the low ionic conductivity and higher ionic radii of the TEA^+ and BF_4^- electrolyte ions.[53] The straight line observed at the low- frequency region running parallel to the imaginary axis of the impedance can be termed as “Warburg line” which is due to the diffusion of electrolyte ions on to the surface of electroactive materials.[54] Figure 7.13 shows the plot of specific device capacitance as a function of an applied frequency determined using the EIS spectrum. It showed

that the specific device capacitance is higher (23.02 F g^{-1}) at a low- frequency of 0.01 Hz and decreasing with an increase in applied frequency.

The galvanostatic charge-discharge (CD) profile of the graphene SCSPC obtained using a constant current of 2.5 mA in the OPW of 0.0-3.0 V is demonstrated in Figure 7.14(A), which shows the existence of almost symmetric charge-discharge behavior which is in good agreement with CV behavior. The CD profiles of graphene SCSPC recorded using various applied current ranges (from 1 to 10 mA) is illustrated in Figure 7.14(B). The CD profiles recorded using different applied currents revealed the presence of symmetric triangular shaped nature, thus, confirming that the charge storage is due to the double layer capacitance.[52] The effect of discharge current on the gravimetric specific device capacitance of the graphene SCSPC is provided in Figure 7.14(C).

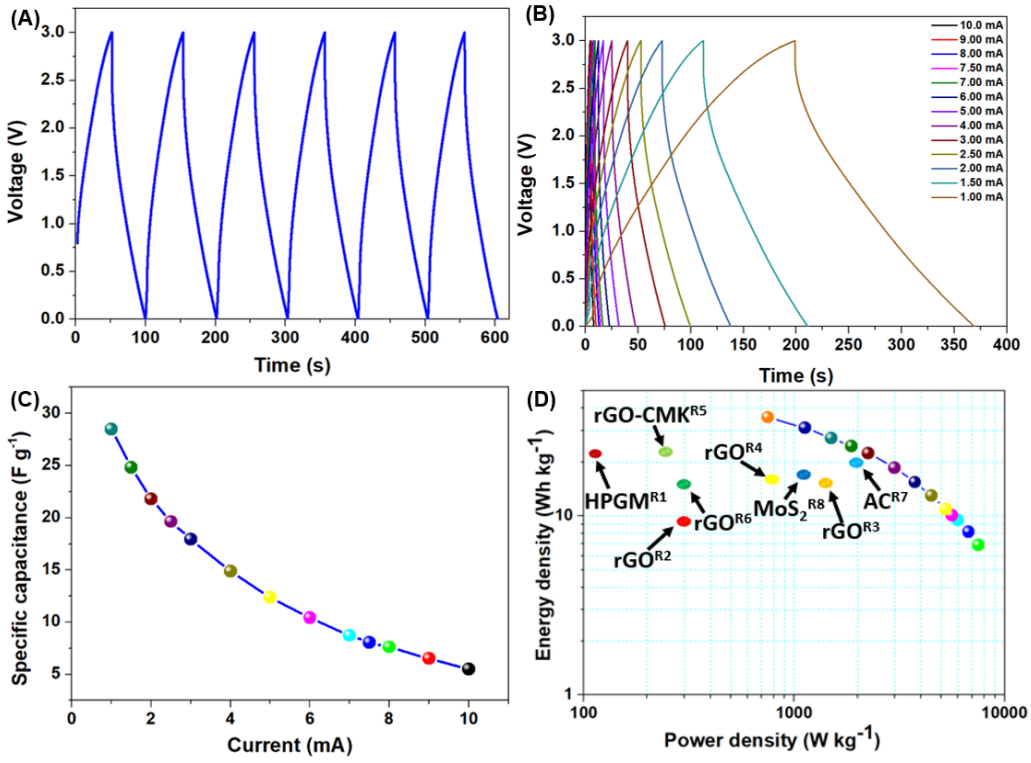

Figure 7.14 Electrochemical analysis of the graphene SCSPC device. (A) Galvanostatic charge-discharge profiles of graphene SCSPC measured at a constant current of 2.5 mA in the operating potential window from 0.0 to 3.0 V. (B) Charge-discharge profiles of graphene SCSPC obtained in different applied current ranges from 1 to 10 mA. (C) Effect of discharge current on the gravimetric specific device capacitance of graphene SCSPC, (D) Ragone plot of graphene SCSPC showing their superior performance metrics over the reported supercapacitors using ionic liquid electrolytes. The references (R^1-R^8) in Fig. 7.14(D) are provided in Table 7.1.

A high gravimetric specific device capacitance of about 28.46 F g^{-1} (corresponding to an areal capacitance of about 31.63 mF cm^{-2}) was obtained for the graphene SCSPC from the discharge profile recorded using 1 mA. A specific capacitance of 5.5 F g^{-1} (6.11 mF cm^{-2}) for the graphene SCSPC is retained with an increase in the applied current up to10-fold (10 mA) suggests their better rate capability.[55]

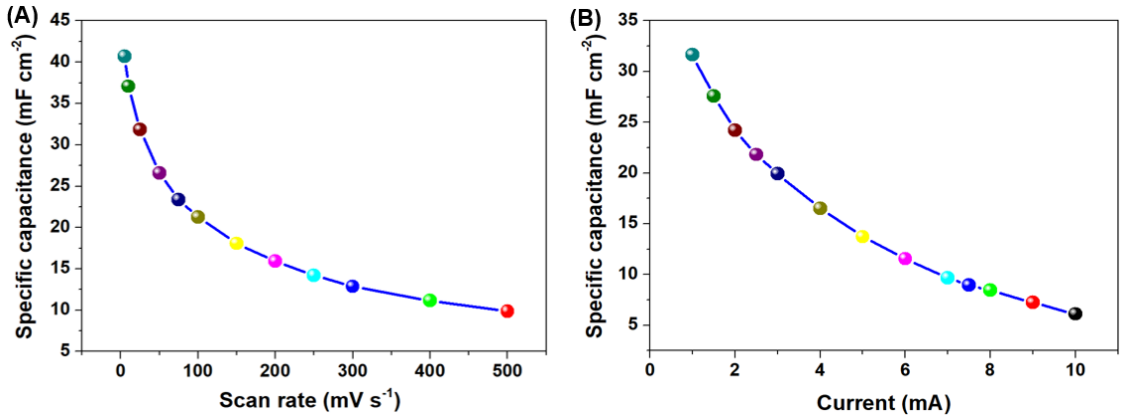

Figure 7.15 (A) Effect of areal specific capacitance of graphene SCSPC with respect to scan rate. (B) Effect of areal specific capacitance of graphene SCSPC with respect to the discharge current.

The effect of areal specific capacitance of graphene SCSPC with respect to scan rate (from CV analysis) and applied current ranges (from CD analysis) are provided in Figure 7.15. The energy and power densities of the graphene SCSPC was determined from the CD profiles and symbolized in the form of Ragone plot (shown in Figure 7.14(D)). The graphene SCSPC device delivered a high energy density of about 35.58 Wh kg^{-1} with a corresponding power density of about 750 W kg^{-1} from the CD profile recorded at a constant discharge current of 1

mA. With an increase of discharge current range of ten-fold (discharge current 10 mA), the device still holds an energy density of about 6.87 Wh kg^{-1} whereas the power density increases up to 7500 W kg^{-1}. The energy density and power density of the graphene SCSPC are quite higher compared to the state of art of other supercapacitor devices as evidenced from the Ragone plot and Table 7.1.

The long-term cyclic stability of the graphene SCSPC has recorded over 10,000 continuous cycles of charge-discharge using CD measurements (applied current of 10 mA). Figure 7.16(A) shows the capacitance retention of graphene SCSPC device over 10,000 cycles which showed retention of 91 % to their initial capacitance. The Nyquist plot of graphene SCSPC (inset of Figure 7.16(A)) recorded after cyclic tests shows the increase in ESR (from 21.39 to 27.47 Ω) and R_{ct} (59.53 to 70.09 Ω) values which might be a reason for the observed capacitance decay over prolonged cycles.

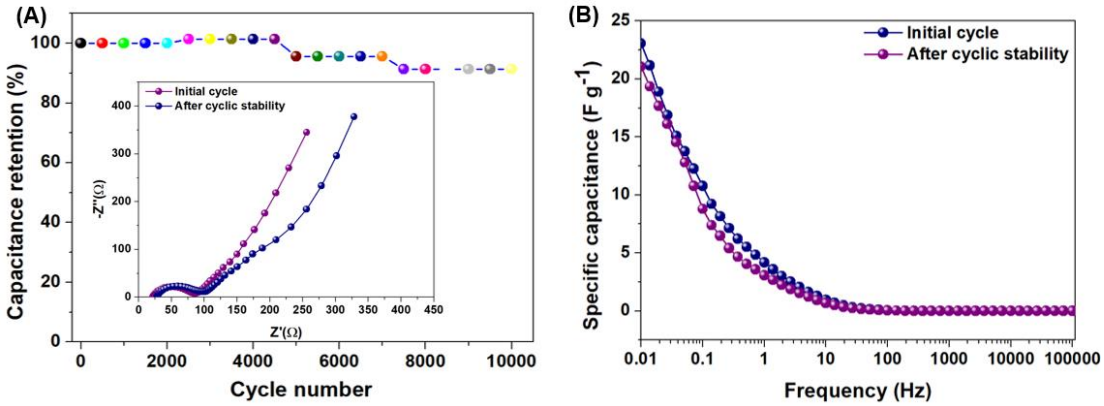

Figure 7.16 (A) Cyclic stability performance for graphene SCSPC over 10000 cycles with inset, shows the Nyquist plot of graphene SCSPC measured during initial and after 10000 cycle. (B) The plot of variation of specific capacitance of graphene SCSPC with respect to frequency initial and after 10000 cycles.

Figure 7.17(B) shows the decrease in specific device capacitance from 23.02 F g^{-1} to 21.06 F g^{-1} (at low- frequency of 0.01 Hz) after the cyclic tests. These long-term stability tests

showed better stability of the graphene SCSPC over reported supercapacitor devices in literature.[56–58] Figure 7.18 represents the practical application of the fabricated graphene SCSPC. Initially, the graphene based SCSPC was fully charged upto 3.0 V using a constant current of 1 mA, then the stored energy in the graphene SCSPC can be utilized to glow night lamp.

Figure 7.18 shows the self-charging performance of the graphene SCSPC device using porous piezoelectric PVDF (incorporated with $TEABF_4$) polymeric separator under various applied compressive forces (5 to 20 N), respectively. When the graphene SCSPC device is subjected to a compressive force of 5 N, the device was able to self-charge from 115 to 176 mV (Figure 7.18(A)) within a time duration of 250 seconds followed by discharging using a constant current of 25 μA. Thus, the graphene SCSPC device was able to self-charging up to 61 mV when subjected to a compressive force of 5 N. The effect of various applied compressive force from 10 to 20 N on the self-charging performances of graphene SCSPC device is provided in Figure 7.18(B-D), respectively. The graphene SCSPC device was able to self-charge up to 70, 77, and 112 mV when the device was subjected to compressive forces of 10, 15, and 20 N, respectively.

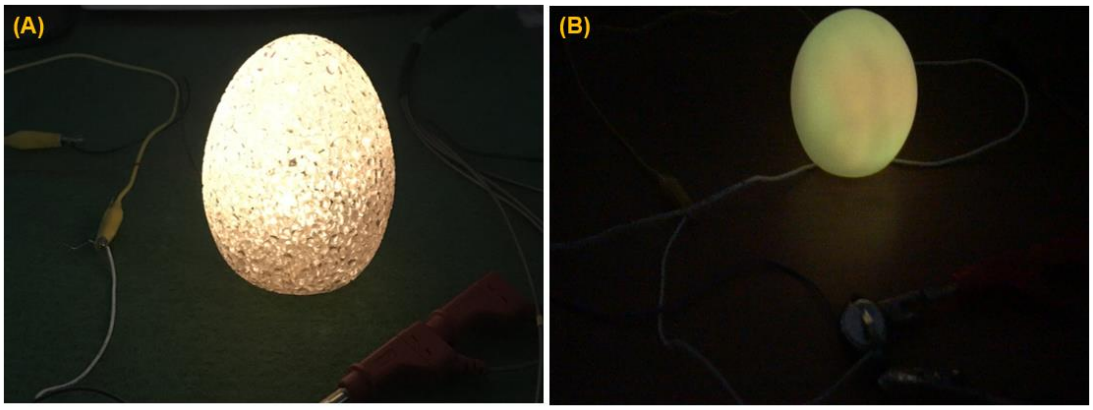

Figure 7.17 The practical application of fully charged graphene SCSPC to glow (A) a white LED-based night lamp, and (B) a blue LED-based night lamp.

A self-charging performance of graphene SCSPC is higher (112 mV) using a compressive force of 20 N which can be ascribed to the higher piezo-electric output of the porous PVDF separator at the same force (as seen in Figure 7.8(A and B)). This study suggested that the self-charging properties of the graphene SCSPC device are directly related to the piezoelectric properties of the separator.[5] Figure 7.19 represents the effect of different applied forces on the self-charging performance of the graphene SCSPC device.

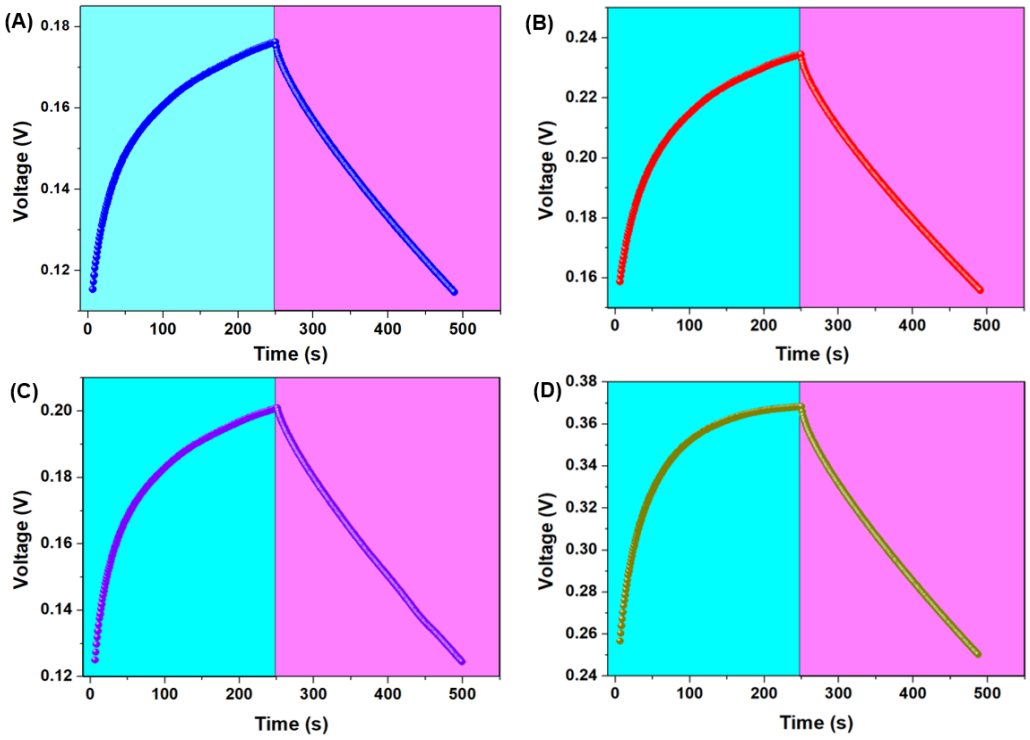

Figure 7.18 Self-charging behaviour of the graphene SCSPC. (A-D) Self-charging properties of graphene SCSPC subjected to different levels of applied compressive force from 5 to 20 N showing a maximum self-charging of graphene SCSPC device up to 112 mV using a compressive force of 20 N.

Figure 7.20 represents the underlying working mechanism on the self-charging properties of the graphene SCSPC device when subject to compressive force. At the initial state or discharge state (Figure 7.20(A)), the graphene SCSPC device is at the equilibrium state in which there is no electrochemical reaction occurred (i.e., the absence of double layer

capacitance). When the graphene SCSPC device is subjected to an applied compressive force (Figure 7.20(B)), the generation of piezo-potential on the surface of porous PVDF separator occurred similar to that of Figure 7.8(A).

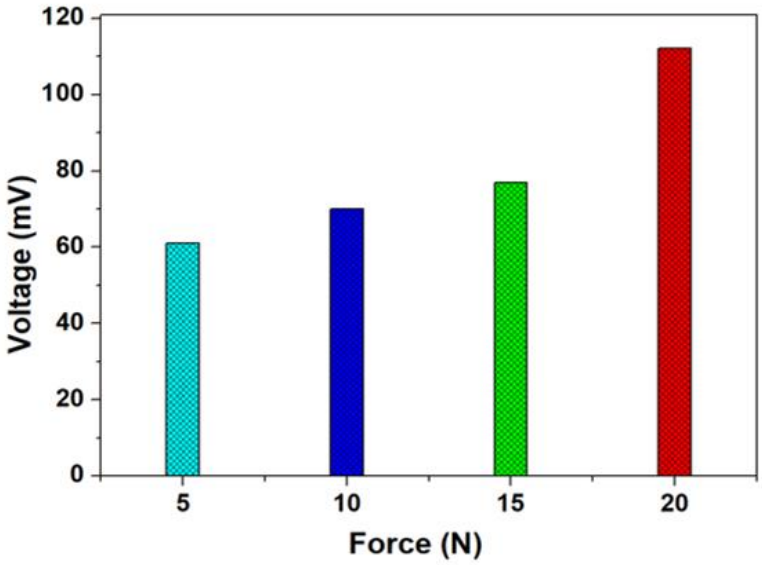

Figure 7.19 The effect of different applied forces on the self-charging performance of the graphene SCSPC.

The generated piezo-electric potential was accessed by the two ideal graphene electrodes in SCSPC device making them an ideal positive and negative electrode, thus, in turn, leads to the formation of electric double layer capacitance on their surface of graphene electrodes (Figure 7.20(C)).[59] The presence of pores in the prepared PVDF film provide sufficient ion transport pathways for ease of electrolyte ion migration towards the electrode surface until an equilibrium state is reached (Figure 7.20(D)).[32] When the applied compressive force is stopped, the distribution of ions reaches the balance point as seen in Figure 7.20(E).

The overall process can be termed as “piezo-electrochemical energy conversion and storage process” as initially demonstrated by Prof. Z. L. Wang using self-charging Li-ion battery base power cell.[7,60] Further, the self-charging performance of the graphene SCSPC device is also compared with literature in this work. The self-charging output of 112 mV obtained in this work

using graphene electrodes is higher compared to the previous works on carbon (electrode) based SCSPC devices such as (i) functionalized carbon cloth (90 mV) and (ii) CNT based electrode (70 mV), respectively.[12,18]

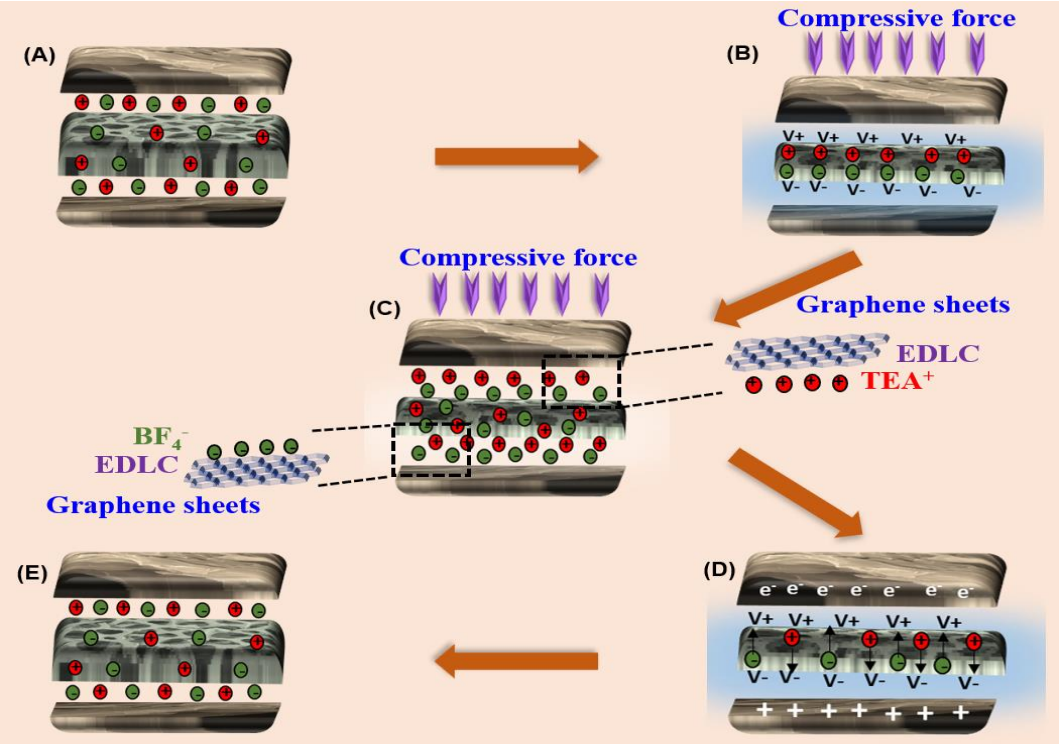

Figure 7.20 Schematic representation for the underlying working mechanism for the self-charging process involved in graphene SCSPC when subjected to compressive force. (A) The normal (or uncharged) state of the graphene SCSPC with no applied compressive force (rest condition), (B) The graphene SCSPC is under compressive force. Piezoelectrical polarization produced by the porous PVDF separator, which migrates the electrolyte ions. (C) Migration of TEA^+ and BF_4^- ions towards the graphene electrode. (D) An equilibrium state has been reached between piezoelectric potential created by the porous PVDF separator and the electrochemical reaction of the graphene SCSPC. (E) Completion of one self-charging cycle upon releasing of an external force and the piezoelectric potential disappeared in the graphene SCSPC.

However, the self-charging profile of the graphene SCSPC device is closely matched with the findings of Song et al.[12] whereas the work by Parida et al. shows immediate charging

upon the device is subjected to mechanical force.[18] In general, the performance metrics of any energy harvesting and storage device is needed to be analysed in detail.[29,41] A straight-forward reason for improved self-charging performances or comparison analysis is critical at this stage since there are several factors such as (i) nature of supercapacitor electrode,[61] (ii) mechanical to electrical energy conversion efficiency of PVDF separator,[62] (iii) the role of electrolyte ions to migrate between the separator to reach the electrode surface,[53] and so on, which are needed to be evaluated in more detail. Altogether, the collective experimental findings demonstrated high performance self-charging properties of graphene based SCSPC device using porous PVDF separator compared to the state of art of SCSPCs using EDLC electrode and further works are needed to improve the piezo-electrochemical energy conversion process.

Table 7.1. Summary of electrochemical performances of graphene SCSPC and recently reported supercapacitor devices using an ionic liquid as electrolyte.

Si. No.	**Electrode material**	**Electrolyte**	**Potential window (V)**	**Energy density (Wh kg^{-1})**	**Power density (W kg^{-1})**	**Reference**
1	HPGM	$TEABF_4$	2.5	23.5	62.5	R1[63]
2	rGO	$LiClO_4$/PC	1.6	9.4	678	R2[64]
3	rGO	BMIBF4	4	16.5	1600	R3[65]
4	rGO	[SET3][TFSI]-GO	2.5	17.7	875	R4[66]
5	rGO-CMK-5	$LiPF_6$	2.5	23.1	-	R5[67]
6	rGO	Et_4NBF_4	2.5	16	-	R6[68]
7	Activated carbon	$PYR_{14}TFSI$	3.5	20	2000	R7[69]

8	MoS_2 sheets	$TEABF_4$	3	18.43	1125	R8[70]
9	**rGO**	**$TEABF_4$**	**3**	**35.58**	**7500**	**This work**

7.4 Conclusion:

The key findings of this study demonstrated the fabrication of graphene based SCSPC devices using porous PVDF (incorporated with ionic liquid electrolyte) piezo-polymer separator. The ability of graphene SCSPC device for direct conversion and storage of mechanical energy to electrical energy in an integrated device has been demonstrated in this work. The performance metrics are superior to that state of the art of EDLC electrode based SCSPCs reported till date. The collective findings of this work provide us an important step towards ongoing research on SCSPC devices which will be useful for the development of next-generation all-in-one energy conversion and storage devices.

7.5 References

1 T. G. Yun, M. Park, D.-H. Kim, D. Kim, J. Y. Cheong, J. G. Bae, S. M. Han and I.-D. Kim, *ACS Nano*, 2019, **13**, 3141–3150.

2 M. Liu, Z. Cong, X. Pu, W. Guo, T. Liu, M. Li, Y. Zhang, W. Hu and Z. L. Wang, *Adv. Funct. Mater.*, 2019, 1806298.

3 J. Deng, X. Kuang, R. Liu, W. Ding, A. C. Wang, Y.-C. Lai, K. Dong, Z. Wen, Y. Wang, L. Wang, H. J. Qi, T. Zhang and Z. L. Wang, *Adv. Mater.*, 2018, **30**, 1705918.

4 A. Maitra, S. K. Karan, S. Paria, A. K. Das, R. Bera, L. Halder, S. K. Si, A. Bera and B. B. Khatua, *Nano Energy*, 2017, **40**, 633–645.

5 N. Wang, W. Dou, S. Hao, Y. Cheng, D. Zhou, X. Huang, C. Jiang and X. Cao, *Nano*

energy, 2019, **56**, 868–874.

6 X. Xue, P. Deng, S. Yuan, Y. Nie, B. He, L. Xing and Y. Zhang, *Energy Environ. Sci.*, 2013, **6**, 2615.

7 X. Xue, S. Wang, W. Guo, Y. Zhang and Z. L. Wang, *Nano Lett.*, 2012, **12**, 5048–5054.

8 M. Xu, T. Zhao, C. Wang, S. L. Zhang, Z. Li, X. Pan and Z. L. Wang, *ACS Nano*, 2019, acsnano.8b08274.

9 X. Hu, X. Yan, L. Gong, F. Wang, Y. Xu, L. Feng, D. Zhang and Y. Jiang, *ACS Appl. Mater. Interfaces*, 2019, **11**, 7379–7386.

10 S. Qin, Q. Zhang, X. Yang, M. Liu, Q. Sun and Z. L. Wang, *Adv. Energy Mater.*, 2018, **8**, 1800069.

11 X. Xue, P. Deng, B. He, Y. Nie, L. Xing, Y. Zhang and Z. L. Wang, *Adv. Energy Mater.*, 2014, **4**, 1301329.

12 R. Song, H. Jin, X. Li, L. Fei, Y. Zhao, H. Huang, H. L.-W. Chan, Y. Wang, Y. Chai, R. Song, Y. Wang, Y. Chai, H. Lai-Wa Chan, H. Huang, X. Li, Y. Zhao and L. Fei, *J. Mater. Chem. A*, 2015, **3**, 14963–14970.

13 A. Maitra, S. Paria, S. K. Karan, R. Bera, A. Bera, A. K. Das, S. K. Si, L. Halder, A. De and B. B. Khatua, *ACS Appl. Mater. Interfaces*, 2019, **11**, 5022–5036.

14 K. Zhao, Y. Yang, X. Liu and Z. L. Wang, *Adv. Energy Mater.*, 2017, **7**, 1700103.

15 P. Pazhamalai, K. Krishnamoorthy, V. K. Mariappan, S. Sahoo, S. Manoharan and S. Kim, *Adv. Mater. Interfaces*, 2018, 1800055.

16 H. He, Y. Fu, T. Zhao, X. Gao, L. Xing, Y. Zhang and X. Xue, *Nano Energy*, 2017, **39**,

590–600.

17 A. Ramadoss, B. Saravanakumar, S. W. Lee, Y.-S. Kim, S. J. Kim and Z. L. Wang, *ACS Nano*, 2015, **9**, 4337–4345.

18 K. Parida, V. Bhavanasi, V. Kumar, J. Wang and P. S. Lee, *J. Power Sources*, 2017, **342**, 70–78.

19 X. Pu, W. Hu and Z. L. Wang, *Small*, 2018, **14**, 1702817.

20 K. Zhao, Y. Wang, L. Han, Y. Wang, X. Luo, Z. Zhang and Y. Yang, *Nano-Micro Lett.*, 2019, **11**, 19.

21 Y. Yang, L. Xie, Z. Wen, C. Chen, X. Chen, A. Wei, P. Cheng, X. Xie and X. Sun, *ACS Appl. Mater. Interfaces*, 2018, **10**, 42356–42362.

22 J. R. Miller, R. A. Outlaw, B. C. Holloway, K. J. Ganesh, W. Cai, P. J. Ferreira, A. Pirkle, R. M. Wallace, K. A. Cychosz, M. Thommes, D. Su, E. A. Stach and R. S. Ruoff, *Science (80-.).*, 2010, **329**, 1637–1639.

23 L. Que, L. Zhang, C. Wu, Y. Zhang, C. Pei and F. Nie, *Carbon N. Y.*, 2019, **145**, 281–289.

24 K. Krishnamoorthy, M. Veerapandian, K. Yun and S.-J. Kim, *Carbon N. Y.*, 2013, **53**, 38–49.

25 S. Pei, J. Zhao, J. Du, W. Ren and H.-M. Cheng, *Carbon N. Y.*, 2010, **48**, 4466–4474.

26 K. Krishnamoorthy, G.-S. Kim and S. J. Kim, *Ultrason. Sonochem.*, 2013, **20**, 644–649.

27 F. Chen, Y. Lu, X. Liu, J. Song, G. He, M. K. Tiwari, C. J. Carmalt and I. P. Parkin, *Adv. Funct. Mater.*, , DOI:10.1002/adfm.201702926.

28 N. S. A. Manaf, M. S. A. Bistamam and M. A. Azam, *ECS J. Solid State Sci. Technol.*, 2013, **2**, M3101–M3119.

29 S. Zhang and N. Pan, *Adv. Energy Mater.*, 2015, **5**, 1401401.

30 S. Sahoo, P. Pazhamalai, K. Krishnamoorthy and S.-J. Kim, *Electrochim. Acta*, , DOI:10.1016/j.electacta.2018.02.116.

31 P. Pazhamalai, K. Krishnamoorthy, V. K. Mariappan, S. Sahoo, S. Manoharan and S.-J. Kim, *Adv. Mater. Interfaces*, 2018, **5**, 1800055.

32 Y.-S. Kim, Y. Xie, X. Wen, S. Wang, S. J. Kim, H.-K. Song and Z. L. Wang, *Nano Energy*, 2015, **14**, 77–86.

33 X. Xue, S. Wang, W. Guo, Y. Zhang and Z. L. Wang, *Nano Lett.*, 2012, **12**, 5048–5054.

34 A. J. Lovinger, *Science (80-.).*, 1983, **220**, 1115–1121.

35 K. Krishnamoorthy, V. K. Mariappan, P. Pazhamalai, S. Sahoo and S.-J. Kim, *Nano Energy*, 2019, **59**, 453–463.

36 P. Singh, H. Borkar, B. P. Singh, V. N. Singh and A. Kumar, *AIP Adv.*, 2014, **4**, 87117.

37 Y. Mao, P. Zhao, G. McConohy, H. Yang, Y. Tong and X. Wang, *Adv. Energy Mater.*, 2014, **4**, 1301624.

38 L. Chen, Y. Si, H. Zhu, T. Jiang and Z. Guo, *J. Memb. Sci.*, 2016, **520**, 760–768.

39 E. H. Abdelhamid, O. D. Jayakumar, V. Kotari, B. P. Mandal, R. Rao, V. M. Naik, R. Naik and A. K. Tyagi, *RSC Adv.*, 2016, **6**, 20089–20094.

40 S. K. Pradhan, A. Kumar, A. N. Sinha, P. Kour, R. Pandey, P. Kumar and M. Kar,

Ferroelectrics, 2017, **516**, 18–27.

41 J. Briscoe, N. Jalali, P. Woolliams, M. Stewart, P. M. Weaver, M. Cain and S. Dunn, *Energy Environ. Sci.*, 2013, **6**, 3035–3045.

42 Y.-S. Kim, Y. Xie, X. Wen, S. Wang, S. J. Kim and H.-K. Song, *Nano Energy*, 2015, **14**, 77–86.

43 L. Xing, Y. Nie, X. Xue and Y. Zhang, *Nano Energy*, 2014, **10**, 44–52.

44 F. T. Johra and W. G. Jung, *Appl. Surf. Sci.*, 2015, **357**, 1911–1914.

45 S. Thangavel and G. Venugopal, *Powder Technol.*, 2014, **257**, 141–148.

46 E. F. Antunes, A. O. Lobo, E. J. Corat, V. J. Trava-Airoldi, A. A. Martin and C. Veríssimo, *Carbon N. Y.*, 2006, **44**, 2202–2211.

47 G. Eda and M. Chhowalla, *Adv. Mater.*, 2010, **22**, 2392–2415.

48 J. D. Fowler, M. J. Allen, V. C. Tung, Y. Yang, R. B. Kaner and B. H. Weiller, *ACS Nano*, 2009, **3**, 301–306.

49 K. Krishnamoorthy, P. Pazhamalai and S.-J. Kim, *Energy Environ. Sci.*, 2018, **11**, 1595–1602.

50 Y. Gogotsi and R. M. Penner, *ACS Nano*, 2018, **12**, 2081–2083.

51 V. K. Mariappan, K. Krishnamoorthy, P. Pazhamalai, S. Sahoo, S. S. Nardekar and S.-J. Kim, *Nano Energy*, 2019, **57**, 307–316.

52 Q. Shao, J. Tang, Y. Lin, J. Li, F. Qin, K. Zhang, J. Yuan and L.-C. Qin, *Electrochim. Acta*, 2015, **176**, 1441–1446.

53 C. Zhong, Y. Deng, W. Hu, J. Qiao, L. Zhang and J. Zhang, *Chem. Soc. Rev.*, 2015, **44**, 7484–7539.

54 P. Pazhamalai, K. Krishnamoorthy, S. Sahoo, V. K. Mariappan and S.-J. Kim, *ACS Appl. Mater. Interfaces*, 2019, **11**, 624–633.

55 K. Krishnamoorthy, P. Pazhamalai, S. Sahoo and S.-J. Kim, *J. Mater. Chem. A*, 2017, **5**, 5726–5736.

56 C. Ogata, R. Kurogi, K. Hatakeyama, T. Taniguchi, M. Koinuma and Y. Matsumoto, *Chem. Commun.*, 2016, **52**, 3919–3922.

57 Z. Li, S. Gadipelli, Y. Yang, G. He, J. Guo, J. Li, Y. Lu, C. A. Howard, D. J. L. Brett, I. P. Parkin, F. Li and Z. Guo, *Energy Storage Mater.*, 2019, **17**, 12–21.

58 L.-B. Xing, Z. Li, J. Zhou, J.-L. Zhang, S. Zhuo, S.-F. Hou and W. Si, *J. Nanosci. Nanotechnol.*, 2016, **16**, 8451–8459.

59 B. E. Conway, 1999, 481–505.

60 L. Xing, B. He, Z. L. Wang, X. Xue, Y. Nie, P. Deng and Y. Zhang, *Adv. Energy Mater.*, 2013, **4**, 1301329.

61 F. Wang, X. Wu, X. Yuan, Z. Liu, Y. Zhang, L. Fu, Y. Zhu, Q. Zhou, Y. Wu and W. Huang, *Chem. Soc. Rev.*, 2017, **46**, 6816–6854.

62 S. K. Karan, R. Bera, S. Paria, A. K. Das, S. Maiti, A. Maitra and B. B. Khatua, *Adv. Energy Mater.*, 2016, **6**, 1–12.

63 Y. Tao, X. Xie, W. Lv, D.-M. Tang, D. Kong, Z. Huang, H. Nishihara, T. Ishii, B. Li and D. Golberg, *Sci. Rep.*, 2013, **3**, 2975.

64 Z. Liu, H. Zhang, Q. Yang and Y. Chen, *Electrochim. Acta*, 2018, **287**, 149–157.

65 Y. Chen, X. Zhang, D. Zhang and Y. Ma, *Mater. Lett.*, 2012, **68**, 475–477.

66 N. das M. Pereira, J. P. C. Trigueiro, I. de F. Monteiro, L. A. Montoro and G. G. Silva, *Electrochim. Acta*, 2018, **259**, 783–792.

67 Z. Lei, Z. Liu, H. Wang, X. Sun, L. Lu and X. S. Zhao, *J. Mater. Chem. A*, 2013, **1**, 2313–2321.

68 A. M. Navarro-Suárez, K. L. Van Aken, T. Mathis, T. Makaryan, J. Yan, J. Carretero-González, T. Rojo and Y. Gogotsi, *Electrochim. Acta*, 2018, **259**, 752–761.

69 A. Balducci, R. Dugas, P.-L. Taberna, P. Simon, D. Plee, M. Mastragostino and S. Passerini, *J. Power Sources*, 2007, **165**, 922–927.

70 P. Pazhamalai, K. Krishnamoorthy, S. Manoharan and S.-J. Kim, *J. Alloys Compd.*, 2019, **771**, 803–809.

CHAPTER – 8

Conclusions and Future Work

8.1. Conclusions

This chapter describes general conclusions of overall thesis and future directions of this work.

- In this thesis, Chapter 1 describes the detailed introduction about the energy storage systems, electrochemical capacitors, mechanism of the different types of electrochemical capacitors and energy harvesting system.
- Chapter 2 provides details of the chemicals and reagents, experimental setups and methods used in the thesis. Also deals with the different characterization engaged in the analysis of materials properties like structural, optical, composition, morphological and electrochemical properties.
- Chapter 3 discuss the synthesis of α-MnSe nanoparticles using hydrothermal approach and investigated as an electrode material for supercapacitors in three-electrode system and SSC device. The electrochemical performance of the α-MnSe SSC device shows that the specific capacitance of the device is about 23.44 F g^{-1} at a current density of 0.1 mA cm^{-2}, with an optimized window of 0.8 V.
- Chapter 4 describes the preparation of copper molybdenum sulfide (Cu_2MoS_4) nanostructures via hydrothermal approach and examined as a novel electrode material for supercapacitor in three-electrode configuration and symmetric supercapacitor device. The Cu_2MoS_4 SSC device received high energy and power density of 3.92 Wh kg^{-1} and 1250 W kg^{-1}, respectively. The Nyquist and Bode investigation further confirmed the pseudocapacitive nature of Cu_2MoS_4 electrodes.
- Chapter 5 discuss the preparation of novel hybrid of Cu_2MoS_4 nanoparticles embedded on reduced graphene oxide (rGO) sheets via hydrothermal approach and performed

temperature dependent supercapacitor study. The electrochemical performance of the Cu_2MoS_4-rGO electrode exhibited ~ 128 % enhancement at 80 °C compared to that at 25 °C in CD profile. The experimental results specify a vital knowledge of the temperature dependent supercapacitor electrodes for industrial-, military- and space- applications.

- Chapter 6 presents the binder-free electrode based on copper-molybdenum-sulfide nanostructures formed on nickel foam (CMS/Ni) via hydrothermal approach and performed supercapacitor study. The fabricated SSC device using CMS/Ni electrode obtained a high device capacitance (265.62 F g^{-1}), high energy density (23.61 Wh kg^{-1}) and long cycle-life.
- Chapter 7 describes the fabrication of Self-Charging Supercapacitor Power Cell (SCSPC) using porous PVDF as a piezo-separator and graphene as electrochemically active materials for positrode and negatrode, respectively for the first time. The fabrication and working mechanism of a SCSPC was discussed in detail. The graphene SCSPC device can be self-charged up-to 112 mV under an applied force of 20 N within 250 seconds. The self-charging mechanism for graphene SCSPC is discussed in detail via piezo-electrochemical energy conversion process-. The SCSPC provide a new promising direction in the supercapacitor research for the development of future generation self-powered sustainable power source for portable and flexible electronic devices.

8.2. Suggestions for future work

Energy storage has increasingly been recognized as a crucial technology to enable the global transformation towards low-carbon, resilient power systems. In addition to enabling more efficient uptake of renewable resources, energy storage can directly service the power grid, enhancing grid operations and safety. In the present study, enhancement on energy

storage performance of supercapacitor was accomplished by designing novel electrode materials through modifying the nano-structures. Further, we have prepared an innovative SCSPC device consisting two-dimensional graphene sheets as supercapacitor electrodes and porous PVDF merged $TEABF_4$ electrolyte as a solid-like piezo-polymer separator. So, the ultimate aim is to design a self-charging power cell.

- The construction of miniaturized electrochemical energy storage systems is crucial for the growth of next-generation wearable and portable electronic devices for Internet of Things (IOTs) applications where associated devices are increasingly deployed in our regular life without decaying performance metrics.
- To improve the self-charging performance of SCSPC for portable and wearable electronics applications.

APPENDIX A: List of Publications

1. **Surjit Sahoo**, K. Krishnamoorthy, P. Pazhamalai, V. K. Mariappan, S. Manoharan, S.-J. Kim, "High performance self-charging supercapacitor using porous PVDF-ionic liquid electrolyte sandwiched between two-dimensional graphene electrodes". **Journal of Materials Chemistry A** 7 (2019) 21693-21703. "Article featured as 2019 Journal of Materials Chemistry A HOT Papers with front cover page" **I.F. 10.733**
2. **Surjit Sahoo,** P. Pazhamalai, V. K. Mariappan, Ganesh Kumar Veerasubramani, Nam-Jin Kim, S.-J. Kim, "Hydrothermally synthesized Chalcopyrite platelets as electrode material for symmetric supercapacitors". **Inorg. Chem. Front., (just accepted)**
3. P. Pazhamalai, K. Krishnamoorthy, **Surjit Sahoo**, V. K. Mariappan, S.-J. Kim, "Supercapacitive properties of amorphous MoS3 and crystalline MoS2 nanosheets in an organic electrolyte". **Inorg. Chem. Front.,** 6 (2019) 2387-2395. **I.F. 5.93**
4. Sudhakaran M.S.P. G. Gnanasekaran, P. Pazhamalai, **Surjit Sahoo**, Md. Mokter Hossain, Roshan Mangal Bhattarai, Sang-Jae Kim, Young Sun Mok* "Hierarchically Porous Nanostructured Nickel Phosphide with Carbon Particles Embedded by Dielectric Barrier Discharge Plasma Deposition as a Binder-Free Electrode for Hybrid Supercapacitors" **ACS Sustainable Chem. Eng.** 17 (2019) 14805-14814 **I.F. 6.97**
5. V. K. Mariappan, K. Krishnamoorthy, P. Pazhamalai, **Surjit Sahoo**, S.-J. Kim, "Carbyne-enriched carbon anchored on nickel foam: A novel binder-free electrode for supercapacitor application". **Journal of colloid and interface science** 556 (2019) 411-419 **I.F. 6.36**
6. **Surjit Sahoo**, K. Krishnamoorthy, P. Pazhamalai, V. K. Mariappan, S.-J. Kim, "Copper molybdenum sulfide nanoparticles embedded on graphene sheets as advanced electrodes for wide temperature-tolerant supercapacitors". **Inorg. Chem. Front.,** 6 (2019) 1775-1784 **I.F. 5.934**
7. V. K. Mariappan, K. Krishnamoorthy, P. Pazhamalai, **Surjit Sahoo**, D. Kesavan S.-J. Kim, "Two dimensional famatinite sheets decorated on reduced graphene oxide: A novel electrode for high performance supercapacitors". **Journal of Power Sources** 433 (2019) 126648 **I.F. 7.46**
8. P. Pazhamalai, K. Krishnamoorthy, **Surjit Sahoo**, V. K. Mariappan, S.-J. Kim, "Copper tungsten sulfide anchored on Ni-foam as a high-performance binder free negative electrode for asymmetric supercapacitor". **Chemical Engineering Journal** 359 (2019) 409-418. **I.F. 8.355**

9. K. Krishnamoorthy, V. K. Mariappan, P. Pazhamalai, **Surjit Sahoo**, S.-J. Kim, "Mechanical energy harvesting properties of free-standing carbyne enriched carbon film derived from dehydrohalogenation of polyvinylidene fluoride". **Nano Energy** 59 (2019) 453-463. **I.F. 15.54**
10. P. Pazhamalai, K. Krishnamoorthy, **Surjit Sahoo**, V. K. Mariappan, S.-J. Kim," Understanding the thermal treatment effect of two dimensional siloxene sheets and the origin of superior electrochemical energy storage performances". **ACS Applied Materials and Interface** 11 (1) (2019) 624-633. **I.F. 8.097**
11. P. Pazhamalai, K. Krishnamoorthy, **Surjit Sahoo**, S.-J. Kim, "Two-dimensional molybdenum diselenide nanosheets as a novel electrode material for symmetric supercapacitors using organic electrolyte". **Electrochimica Acta** 295 (2019) 591-598. **I.F. 5.116**
12. V. K. Mariappan, K. Krishnamoorthy, P. Pazhamalai, **Surjit Sahoo**, S.-J. Kim, "Nanostructured ternary metal chalcogenide-based binder-free electrodes for high energy density asymmetric supercapacitors". **Nano Energy** 57 (2019) 307-316. **I.F. 15.54**
13. P. Pazhamalai, K. Krishnamoorthy, **Surjit Sahoo**, S.-J. Kim, "High-energy aqueous Li-ion hybrid capacitor using metal organic framework mimicking insertion-type copper hexacyanoferrate and capacitive-type graphitic carbon electrodes". **Journal of Alloys and compounds** 765 (2018)1041-1048. **I.F. 3.779**
14. **Surjit Sahoo**, K. Krishnamoorthy, P. Pazhamalai, S.-J. Kim, "Copper molybdenum sulfide anchored nickel foam: A high performance, binder-free, negative electrode for supercapacitor". **Nanoscale** 10 (29) (2018) 13883-13888. **I.F. 6.93**
15. V. K. Mariappan, K. Krishnamoorthy, P. Pazhamalai, **Surjit Sahoo**, S.-J. Kim, "Layered famatinite nanoplates as an advanced pseudocapacitive electrode material for supercapacitor applications". **Electrochimica Acta** 275 (2018) 110-118. **I.F. 5.383**
16. **Surjit Sahoo**, K. Krishnamoorthy, P. Pazhamalai, V. K. Mariappan, S.-J. Kim, "Copper molybdenum sulfide: A novel pseudocapacitive electrode material for electrochemical energy storage device". **International Journal of Hydrogen Energy** 43 (27) (2018) 12222-12232. **I.F. 4.229**
17. P. Pazhamalai, K. Krishnamoorthy, V. K. Mariappan, **Surjit Sahoo**, S. Manoharan, S.-J. Kim, "A high efficacy self-charging $MoSe_2$ solid state supercapacitor using electrospun

nanofibrous piezoelectric separator with ionogel electrolyte". **Advanced Materials and Interface** 5 (2018) 1800055. **I.F. 4.834**

18. V. K. Mariappan, K. Krishnamoorthy, P. Pazhamalai, **Surjit Sahoo**, S.-J. Kim, "Electrodeposited molybdenum selenide sheets on nickel foam as a binder-free electrode for supercapacitor application". **Electrochimica Acta** 265 (2018) 514-522. **I.F. 5.383**
19. **Surjit Sahoo**, P. Pazhamalai, K. Krishnamoorthy, S.-J. Kim, "Hydrothermally prepared α-MnSe nanoparticles as a new pseudocapacitive electrode material for supercapacitor". **Electrochimica Acta** 268 (2018) 403-410. **I.F. 5.383**
20. S. Manoharan, **Surjit Sahoo**, P. Pazhamalai, S.-J. Kim, "Supercapacitive properties of activated carbon electrode using ammonium-based proton conducting electrolytes", **International Journal of Hydrogen Energy** 43 (3) (2018) 1667-1674. **I.F. 4.229**
21. K. Krishnamoorthy, P. Pazhamalai, **Surjit Sahoo**, J. H. Lim, K. H. Choi, S.-J. Kim, "A High-Energy Aqueous Sodium-Ion Capacitor with Nickel Hexacyanoferrate and Graphene Electrodes", **ChemElectroChem** 4 (12) (2017) 3302-3308. **I.F. 4.446**
22. K. Krishnamoorthy, P. Pazhamalai, **Surjit Sahoo**, S.-J. Kim, "Titanium carbide sheet based high performance wire type solid state supercapacitors", **Journal of Materials Chemistry A** 5 (12) (2017) 5726-5736. "*Article featured as* ***2017 Journal of Materials Chemistry A HOT Papers****"* **I.F. 10.731**
23. **Surjit Sahoo**, K. Naik, D. J. Late, C. S. Rout, "Electrodeposited Nickel Cobalt Manganese based mixed sulfide nanosheets for high performance supercapacitor application", **Microporous and Mesoporous Materials** 244 (2017) 101-108. **I.F. 4.18**
24. **Surjit Sahoo**, K. Naik, D. J. Late, C. S. Rout, "Electrochemical synthesis of a ternary transition metal sulfide nanosheets on nickel foam and energy storage application", **Journal of Alloys and Compounds** 695 (2017) 154-161. **I.F. 4.17**
25. K. Naik, **Surjit Sahoo**, C. S. Rout, "Facile electrochemical growth of spinel copper cobaltite nanosheets for non-enzymatic glucose sensing and supercapacitor applications", **Microporous and Mesoporous Materials** 244 (2017) 226-234. **I.F. 4.18**
26. **Surjit Sahoo**, C. S. Rout, "Spinel NiCo2O4 And Single Walled Carbon Nanotube Nanocomposites For High Performance Supercapacitor Application", **Adv. Mater. Lett.,** 2017, 8 (8), pp 847-851
27. **Surjit Sahoo**, C. S. Rout, "Facile Electrochemical Synthesis of Porous Manganese-Cobalt-Sulfide Based Ternary Transition Metal Sulfide Nanosheets Architectures for High

Performance Energy Storage Applications", **Electrochimica Acta** 220 (2016) 57–66. **I.F. 5.383**

28. R. V Gelamo, G. de S Augusto, L. GB Machuno, S. Moshkalev, A. R Vaz, C. S Rout, **Surjit Sahoo**, "Plasma-Treated Multilayer Graphene: Synthesis and Applications", **2016 31st Symposium on Microelectronics Technology and Devices (IEEE Conference)** 978-1-5090-2788-0/16/$31.00 ©2016 IEEE.
29. K. S. Samantaray, **Surjit Sahoo**, C. S. Rout, "Hydrothermal Synthesis of CuWO4-Reduced Graphene Oxide Hybrids and Supercapacitor Application", **American Journal of Engineering and Applied Sciences** 2016, 9 (3): 584.590.
30. R. Mondal, **Surjit Sahoo**, C. S. Rout, "Mixed nickel cobalt manganese oxide nanorods for supercapacitor application", **American Journal of Engineering and Applied Sciences** 2016, 9 (3): 540.546.
31. **Surjit Sahoo**, K. Naik, C. S. Rout, "Electrodeposition of spinel $MnCo_2O_4$ nanosheets for supercapacitor applications", **Nanotechnology** 26 (2015) 455401. **I.F. 3.39**
32. **Surjit Sahoo**, S. Ratha, C. S. Rout, "Spinel $NiCo_2O_4$ Nanorods for Supercapacitor Applications", **American Journal of Engineering and Applied Sciences** 8 (3), (2015) 371-379.

APPENDIX-B: Conference presentations:

1. P. Pazhamalai, K. Krishnamoorthy, **Surjit Sahoo**, S.-J. Kim, "Biopolymer derived graphitic carbon nanoparticles as an electrode for supercapacitor", The 19th Korean MEMS Conference-2017, Jeju, Korea. **(Poster presentation)**
2. P. Pazhamalai, **Surjit Sahoo**, K. Krishnamoorthy, V. K. Mariappan, S. Manoharan, S.-J. Kim, "Development of polymer based self-charging supercapacitor", The 4th International Conference on Advanced Electromaterials (ICAE 2017), Jeju, Korea. **(Poster presentation).**
3. P. Pazhamalai, K. Krishnamoorthy, **Surjit Sahoo**, V. K. Mariappan, S. Manoharan, S.-J. Kim, "Development of high-energy aqueous sodium ion capacitors using metal hexacyanoferrate and graphene", The 4th International Conference on Advanced Electromaterials (ICAE 2017), Jeju, Korea. **(Poster presentation).**
4. **Surjit Sahoo**, P. Pazhamalai, K. Krishnamoorthy, S. Manoharan, V. K. Mariappan, S.-J. Kim "A Facile and Template-Free Synthesis of α-MnSe Microspheres as electrodes for high performance supercapacitor", The 4th International Conference on Advanced Electromaterials (ICAE 2017), Jeju, Korea. **(Poster presentation).**
5. V. K. Mariappan, P. Pazhamalai, **Surjit Sahoo**, S. Manoharan, K. Krishnamoorthy, S.-J. Kim, "Duo-facet molybdenum selenide as a binder free electrode for supercapacitor application", The 4th International Conference on Advanced Electromaterials (ICAE 2017), Jeju, Korea. **(Poster presentation).**
6. P. Pazhamalai, K. Krishnamoorthy, **Surjit Sahoo**, V. K. Mariappan, S. Manoharan, S.-J. Kim, "Development of high-energy aqueous Li-ion capacitors using metal hexacyanoferrate", The 10th International Conference on Advanced Materials and Devices (ICAMD 2017), Jeju, Korea. **(Poster presentation).**
7. P. Pazhamalai, K. Krishnamoorthy, **Surjit Sahoo**, S.-J. Kim, "Preparation of graphene based conductive paint", The 10th International Conference on Advanced Materials and Devices (ICAMD 2017), Jeju, Korea. **(Poster presentation).**
8. **Surjit Sahoo**, P. Pazhamalai, K. Krishnamoorthy, S. Manoharan, V. K. Mariappan, S.-J. Kim "Electrochemically deposited FeS as new electrode material for supercapacitors", The 10th International Conference on Advanced Materials and Devices (ICAMD 2017), Jeju, Korea. **(Poster presentation).**
9. S. Manoharan, **Surjit Sahoo**, P. Pazhamalai, K. Krishnamoorthy, V. K. Mariappan, S.-J. Kim, "Ammonium based proton conducting electrolytes for supercapacitor applications",

The 10th International Conference on Advanced Materials and Devices (ICAMD 2017), Jeju, Korea. **(Poster presentation)**.

10. P. Pazhamalai, K. Krishnamoorthy, **Surjit Sahoo**, V. K. Mariappan, S. Manoharan, S.-J. Kim, "Cobalt hexacyanoferrate as the intercalative type electrode for Li-ion capacitors", The 20th Korean MEMS Conference-2018, Jeju, Korea. **(Poster presentation)**
11. V. K. Mariappan, K. Krishnamoorthy, P. Pazhamalai, **Surjit Sahoo**, S. Manoharan, Suk-Jun Ko, and S.-J. Kim, "Layered famatinite nanoplates as an advanced pseudocapacitive electrode material", The 20th Korean MEMS Conference-2018, Jeju, Korea. **(Poster presentation)**
12. **Surjit Sahoo**, P. Pazhamalai, K. Krishnamoorthy, S. Manoharan, V. K. Mariappan, Nam-Jin Kim, and S.-J. Kim, "Electrochemically deposited FeS nanosheet arrays as electrode material for high performance supercapacitors", The 20th Korean MEMS Conference-2018, Jeju, Korea. **(Poster presentation)**
13. P. Pazhamalai, K. Krishnamoorthy, **Surjit Sahoo**, V. K. Mariappan, S. Manoharan, S.-J. Kim, "Development of self-charging supercapacitor using polymer composites", 4th International Conference on Nanogenerators and Piezotronics (NGPT 2018), Seoul, Korea. **(Poster presentation)**
14. **Surjit Sahoo**, K. Krishnamoorthy, P. Pazhamalai, S.-J. Kim, "Binary metal sulfide-based supercapacitors for self-powered Nanosystems", 4th International Conference on Nanogenerators and Piezotronics (NGPT 2018), Seoul, Korea. **(Poster presentation)**
15. P. Pazhamalai, K. Krishnamoorthy, **Surjit Sahoo**, S.-J. Kim, "Two-dimensional titanium carbide sheets based high performance flexible wire type solid state supercapacitors", The 19th International Symposium on the Physics of Semiconductors and Applications (ISPSA 2018), Jeju, Korea **(Oral Presentation)**
16. **Surjit Sahoo**, P. Pazhamalai, V. K. Mariappan, S.-J. Kim, "Copper molybdenum sulfide: a novel pseudocapacitive electrode material for electrochemical energy storage device", The 19th International Symposium on the Physics of Semiconductors and Applications (ISPSA 2018), Jeju, Korea. **(Poster presentation)**
17. K. Krishnamoorthy, **Surjit Sahoo**, P. Pazhamalai, S.-J. Kim, "Copper molybdenum sulfide anchored on nickel foam: binder-free electrodes for high-performance symmetric supercapacitors", The 23th Annual Joint Workshop on Advanced Electronic Technology and Application, Jeju, Korea. **(Poster presentation)**

18. P. Pazhamalai, K. Krishnamoorthy, **Surjit Sahoo**, S.-J. Kim, "Two-dimensional molybdenum diselenide nanosheets as high-performance symmetric supercapacitor in organic electrolyte", International Conference on Electronic Materials and Nanotechnology for Green Environment-2018(ENGE-2018), Jeju, Korea. **(Poster presentation)**
19. **Surjit Sahoo**, P. Pazhamalai, K. Krishnamoorthy, S.-J. Kim, "Direct Growth of Copper molybdenum sulfide Nanostructures on Nickel Foam as High-Performance Binder-Free Negative Electrodes for Supercapacitors", International Conference on Electronic Materials and Nanotechnology for Green Environment-2018(ENGE-2018), Jeju, Korea. **(Poster presentation)**
20. P. Pazhamalai, K. Krishnamoorthy, **Surjit Sahoo**, V. K. Mariappan, S.-J. Kim, "Reliability of layered TiO_2 nanosheets as a high-performance electrode material for supercapacitors", 대한기계학회 신뢰성부문 2018 년도 춘계학술대회, Jeju, Korea. **Feb 26 -28, 2019 (Poster presentation)**
21. **Surjit Sahoo**, K. Krishnamoorthy, P. Pazhamalai, V. K. Mariappan, S.-J. Kim, "Reliability of temperature-dependent supercapacitor electrodes using copper molybdenum sulfide-reduced graphene oxide composite", 대한기계학회 신뢰성부문 2018 년도 춘계학술대회, Jeju, Korea. **Feb 26 -28, 2019 (Poster presentation)**
22. V. K. Mariappan, P. Pazhamalai, K. Krishnamoorthy, **Surjit Sahoo**, S.-J. Kim, "Reliability of high-performance supercapacitor electrodes using two dimensional famatinite sheets decorated reduced graphene oxide sheets", 대한기계학회 신뢰성부문 2018 년도 춘계학술대회, Jeju, Korea. **Feb 26 -28, 2019 (Poster presentation)**
23. S. Manoharan, K. Krishnamoorthy, P. Pazhamalai, **Surjit Sahoo**, V. K. Mariappan, S.-J. Kim, "Reliability of Cobalt based metal organic framework as an effective binder free supercapacitor electrode", 대한기계학회 신뢰성부문 2018 년도 춘계학술대회, Jeju, Korea. **Feb 26 -28, 2019 (Poster presentation)**
24. K. Krishnamoorthy, Parthiban Pazhamalai, **Surjit Sahoo**, V. K. Mariappan, S. -J Kim. "Energy storage performance of mechanically exfoliated few layered molybdenum disulfide nanosheets in organic electrolyte", The 21th Korean MEMS Conference-2019, Jeju, Korea. **(Poster presentation)**

25. P. Pazhamalai**,** K. Krishnamoorthy**,** **Surjit Sahoo**, V. K. Mariappan, S. -J Kim. "A novel 2D siloxene sheet electrode for a high-performance supercapacitor", The 21th Korean MEMS Conference-2019, Jeju, Korea. **(Poster presentation)**
26. **Surjit Sahoo**, K. Krishnamoorthy, P. Pazhamalai, V. K. Mariappan, S. -J Kim. "Fabrication of copper molybdenum sulfide nanoparticles embedded on graphene sheets.", The 21th Korean MEMS Conference-2019, Jeju, Korea. **(Poster presentation)**
27. V. K. Mariappan, P. Pazhamalai, K. Krishnamoorthy, **Surjit Sahoo**, S. -J Kim. "Interlayer engineered famatinite-graphene nanohybrid sheets as an advanced electrode for high performance supercapacitors.", The 21th Korean MEMS Conference-2019, Jeju, Korea. **(Poster presentation)**
28. P. Pazhamalai, K. Krishnamoorthy, **Surjit Sahoo**, V. K. Mariappan, S.-J. Kim, "Binder-free copper tungsten sulfide anchored on Ni-foam: An advanced negative electrode for high-performance asymmetric supercapacitor", Materials Challenges in Alternative and Renewable Energy 2019 (MCARE 2019), Jeju, Korea. Aug 19-23, 2019 **(Poster Presentation)**.
29. **Surjit Sahoo**, K. Krishnamoorthy, P. Pazhamalai, V. K. Mariappan, S. Manoharan, S.-J. Kim, "High performance supercapacitor using ionic liquid electrolyte sandwiched between two-dimensional graphene electrodes", Materials Challenges in Alternative and Renewable Energy 2019 (MCARE 2019), Jeju, Korea. Aug 19-23, 2019 **(Poster Presentation)**.
30. V. K. Mariappan, K. Krishnamoorthy, P. Pazhamalai, **Surjit Sahoo**, S. -J Kim, "Microwave irradiated binder free copper antimony sulfide as high performances asymmetric supercapacitor", Materials Challenges in Alternative and Renewable Energy 2019 (MCARE 2019), Jeju, Korea. Aug 19-23, 2019 **(Poster Presentation)**.
31. P. Pazhamalai, K. Krishnamoorthy, **Surjit Sahoo**, V. K. Mariappan, S.-J. Kim, "Two Dimensional Siloxene Sheets: Heat Treatment and Origin of Superior Electrochemical Energy Storage Performances", The 5th International Conference on Advanced Electromaterials (ICAE 2019), Jeju, Korea. Nov 5-8, 2019 **(Oral Presentation)**
32. S. S. Nardekar, P. Pazhamalai, K. Krishnamoorthy, **Surjit Sahoo**, V. K. Mariappan, S.-J. Kim, "MoS_2 Quantum Sheets as the Advanced Electrode Material for High-performance Solid-state Symmetric Supercapacitors", The 5th International Conference on Advanced Electromaterials (ICAE 2019), Jeju, Korea. Nov 5-8, 2019 **(Oral Presentation)**

33. **Surjit Sahoo**, K. Krishnamoorthy, P. Pazhamalai, V. K. Mariappan, S. Manoharan, S.-J. Kim, "A High-performance Self-Charging Supercapacitor Device for Energy Harvesting and Storage", The 5th International Conference on Advanced Electromaterials (ICAE 2019), Jeju, Korea. Nov 5-8, 2019 **(Oral Presentation)**
34. S. Manoharan, P. Pazhamalai, K. Krishnamoorthy, **Surjit Sahoo**, S.-J. Kim, "Metal Organic Framework: Based Energy Harvesting and Storage Device towards Self-Charging Supercapacitor Power Cell", The 5th International Conference on Advanced Electromaterials (ICAE 2019), Jeju, Korea. Nov 5-8, 2019 **(Oral Presentation)**
35. S. Manoharan, K. Krishnamoorthy, P. Pazhamalai, **Surjit Sahoo**, V. K. Mariappan, S.-J. Kim, "Metal organic framework: Cobalt based porous co-ordination polymer as supercapacitor electrode with neutral and alkaline electrolytes", 5th International Conference on Materials and Reliability (ICMR 2019), Jeju, Korea. Nov 27-29, 2019 **(Poster Presentation)**
36. V. K. Mariappan, K. Krishnamoorthy, P. Pazhamalai, **Surjit Sahoo**, S. -J Kim. "Carbyne-enriched carbon- A novel binder-free electrode for supercapacitor application", 5th International Conference on Materials and Reliability (ICMR 2019), Jeju, Korea. Nov 27-29, 2019 (**Poster presentation)**
37. **Surjit Sahoo**, K. Krishnamoorthy, P. Pazhamalai, V. K. Mariappan, S.-J. Kim, "One-step synthesis of binder-free Copper molybdenum sulfide for high-performance symmetric supercapacitor", 5th International Conference on Materials and Reliability (ICMR 2019), Jeju, Korea. Nov 27-29, 2019 **(Poster Presentation)**
38. S. S. Nardekar, P. Pazhamalai, K. Krishnamoorthy, **Surjit Sahoo**, V. K. Mariappan, S.-J. Kim, "Two-dimensional MoS_2 quantum sheet embedded PVDF as flexible piezoelectric nanogenerator for self-powered system", The 11th International Conference on Advanced Materials and Devices (ICAMD 2019), Jeju, Korea. Dec 10-13, 2019 **(Poster Presentation)**
39. **Surjit Sahoo**, P. Pazhamalai, K. Krishnamoorthy, V. K. Mariappan, S.-J. Kim, "Hydrothermally synthesized Chalcopyrite as electrode material for supercapacitors", The 11th International Conference on Advanced Materials and Devices (ICAMD 2019), Jeju, Korea. Dec 10-13, 2019 **(Poster Presentation)**
40. D. Kesavan, K. Krishnamoorthy, P. Pazhamalai, V. K. Mariappan, S. Manoharan, **Surjit Sahoo**, S.-J. Kim, "Shrimp-shell derived chitosan as an efficient energy harvester for self-

powered applications", The 11th International Conference on Advanced Materials and Devices (ICAMD 2019), Jeju, Korea. Dec 10-13, 2019 **(Poster Presentation)**

41. S. Manoharan, P. Pazhamalai, K. Krishnamoorthy, V. K. Mariappan, **Surjit Sahoo**, S.-J. Kim, "Cobalt based metal organic framework synthesis with surfactants and their electrochemical property analysis as supercapacitors" The 11th International Conference on Advanced Materials and Devices (ICAMD 2019), Jeju, Korea. Dec 10-13, 2019 **(Poster Presentation)**

DECLARATION

I, Surjit Sahoo, hereby declare that the thesis entitled **"Development of Nanostructured Electrode Materials for Self-Charging Supercapacitor Power Cell"**, submitted to Jeju National University, in the partial fulfilment of the requirements for the award of the **Degree of Doctor of Philosophy in the Department of Mechatronics Engineering** is a record of original and independent research work done and published by me during the period of September 2016 to February 2020 under the supervision and guidance of **Prof. Sang-Jae Kim,** Department of Mechatronics Engineering, Jeju National University. This thesis is based on our publication in reputed journals and it has not been formed for the award of any other Degree/Diploma/Associateship/Fellowship to any candidate of any university.

Surjit Sahoo